

S&G 3688

RESEARCH REPORT

Interpretation of Piezocone Data and its Use in Estimating Seismic Soil Liquefaction Potential

Roger Anton Vreugdenhil

November 1995

95-7

Department of Civil Engineering

**University of Canterbury
Christchurch New Zealand**

**INTERPRETATION OF PIEZOCONE DATA
AND ITS USE IN ESTIMATING
SEISMIC SOIL LIQUEFACTION POTENTIAL**

by

Roger Anton VREUGDENHIL

This report is identical to a thesis of the same name
submitted to the University of Canterbury in partial
fulfilment of the requirements for the degree of
Doctor of Philosophy in Civil Engineering

Research Report 95-7

November 1995

Department of Civil Engineering
University of Canterbury
New Zealand

*For my whanau
and for my Father*

"Lo these are parts of His ways but how little a portion is heard of Him"
Job 26:14

Abstract

The first half of this report documents an investigation of level ground sites of liquefaction during the 17 October, 1989, Loma Prieta earthquake. Field testing at ten liquefaction sites included piezocone probes (CPTU) and Standard Penetration Tests (SPT). Based on the comparison of ejecta and SPT sample mean grain size, liquefaction appeared to be shallow for the Loma Prieta event.

The performance of five liquefaction prediction models is assessed using the Loma Prieta CPTU data. The five models include two energy-based methods, two methods based on cyclic stress ratio, and one purely empirical method. Results from this analysis indicate that, for this data set, no single model clearly out-performed the others; the predictions of four of the five models were highly conservative. The CPT-SPT correlation is examined, as part of a wider study of model sensitivity to parameter variation.

Previously developed corrections to piezocone data for pore water pressure effects are examined, along with methods for CPTU data normalisation. Pore pressure effects, however, are far outweighed by effects of soil layering on cone resistance. An investigation of layering effects on cone resistance and sleeve friction is detailed in the second half of this report.

A simple approximate analysis is presented for interpretation of cone penetration results when cone resistance is affected by layering of soils with different stiffnesses. It is argued that the cone senses the presence of a nearby layer elastically, and an approximate elastic analysis is developed to quantify the effect on cone resistance. The approximate solution compares favourably with an exact elastic solution for the case of two layers, and with multilayered calibration chamber experimental results. The problem of misclassification of thin stiff layers embedded in softer materials is illustrated by application of the approximate solution to sections of cone resistance records from the Loma Prieta data.

Results from an investigation of layering effects on sleeve friction indicate that, when probing in asymmetrical soil layering configurations, sleeve friction resolution may exceed that of cone resistance. Values for lag between cone resistance and sleeve friction are suggested, based on results from a statistical cross-correlation analysis performed on the Loma Prieta CPTU data. Lag is found to increase with increasing soil stiffness.

An attempt is made to invert sections of real cone resistance records for layer thicknesses and stiffness ratios, by employing a Genetic Algorithm to optimise the approximate solution. Sections of cone resistance from Loma Prieta field records are successfully inverted for stiffness ratios. Partial inversion is favoured due to computation time considerations.

*"This new learning amazes me, Sir Bedemir. Explain again how
sheep's bladders may be employed to prevent earthquakes."*

King Arthur

Monty Python's Quest for the Holy Grail

Acknowledgements

I am greatly indebted to many people who have supported me throughout the course of my PhD research. I wish to express my gratitude to my supervisors, Dr John Berrill and Dr Rob Davis, for their invaluable advice, timely encouragement, patience and hospitality. Their conscientious and enthusiastic approach to research has been a constant source of motivation.

The assistance of the Department of Civil Engineering academic and technical staff is gratefully acknowledged. I extend my thanks to John Van Dyk, Siale Pasa, Frank Greenslade, and Gordon and Val Grey. Their cheerful cooperation and expertise were much appreciated.

The cooperation of the United States Geological Survey (USGS) is acknowledged. I am grateful to Mike Bennett, John Tinsley III and Tom Holzer for their hospitality, and for making investigation of the Loma Prieta liquefaction sites a rewarding experience.

The companionship of my fellow graduate students has made my time as a PhD student highly enjoyable. I thank my friend Wayne Munro for his endless assistance and good (sic) humour. Also deserving of special mention are Steve Christensen and Nathan Schmidt, along with Jose Restrepo and Joe Maffei who endured my idiosyncrasies while sharing the same office.

I extend heartfelt thanks to members of my whanau (extended family) who, by supporting me in countless ways, have contributed to this work. In particular, I thank Fraser and Lyn, Dirk and Mandy, James, Mike, Chris, Raewyn, and Alison and Andy.

I gratefully acknowledge the financial assistance of the New Zealand Earthquake Commission (EQC) for jointly funding the testing of Loma Prieta liquefaction sites with the USGS. Direct financial assistance of the EQC, the New Zealand National Society for Earthquake Engineering, the New Zealand Geomechanics Society and the University Grants Committee is also gratefully acknowledged. The calibration chamber results were obtained within the joint French-United States-New Zealand *Projet Piézocône*, funded principally by the French Ministry of Research and Technology, but also by the New Zealand Ministry of Energy, Transit New Zealand and the EQC.

Finally, I sincerely thank my parents, Tony and Trudi, for the many sacrifices they have made for the sake of my education; I thank my wife, Joanna, for her enduring love, support and encouragement; and I thank God for our daughter, Zeniya.

Contents

<i>Abstract</i>	iii
<i>Acknowledgements</i>	v
1 Introduction and Overview	1
2 Piezocone Investigation of Loma Prieta Liquefaction Sites	5
2.1 Introduction	5
2.2 The Loma Prieta Earthquake	5
2.3 Geotechnical Considerations	7
2.4 Liquefaction Damage during Loma Prieta	7
2.5 Description of California Test Sites	8
2.5.1 Moss Landing	10
2.5.2 Pajaro Dunes	12
2.5.3 Miller's Farm	12
2.5.4 Airport, Watsonville	13
2.5.5 Jefferson	15
2.5.6 Scattini	15
2.5.7 Sea Mist	15
2.5.8 Leonardini	16
2.5.9 SPR Bridge	16
2.5.10 Marina District	18
3 Piezocone Data Correction and Standardisation	21
3.1 General Considerations	21
3.2 CPTU Procedure	21
3.3 Error Sources during California Testing	24
3.4 Pore Pressure Effects	25
3.4.1 Cone Resistance	25
3.4.2 Sleeve Friction	27
3.4.3 Pore Water Pressure	28
3.5 The Influence of Soil Layering	28
4 Performance of Liquefaction Prediction Models	29
4.1 Introduction	29
4.2 Liquefaction Prediction Models	29
4.2.1 Davis and Berrill	31
4.2.2 Seed <i>et al.</i>	32

4.2.3	Shibata and Teparaksa	34
4.2.4	Zhou	35
4.2.5	Liao, Veneziano and Whitman	36
4.3	Model Performance	37
4.4	Parameter Influence and Sources of Error	43
4.5	Summary	49
5	Interpretation of Cone Resistance: the Two Layer Case	51
5.1	Introduction	51
5.2	Point Loads in Elastic Spaces	52
5.2.1	Classical Elasticity Solutions	52
5.2.2	Simulating the Elastic Effects of Layering	53
5.3	The Plevako Solution	54
5.3.1	Mathematical Development	54
5.3.2	Features of the Plevako Solution	57
5.3.3	Application to Two-Layer Soil Systems	59
5.4	Comparison with Calibration Chamber Test Data	60
5.5	Towards a More General Model	62
6	Interpretation of Cone Resistance: the Multilayer Case	63
6.1	Introduction	63
6.2	Development of Approximate Solution	64
6.2.1	The Solution for Two Layers	64
6.2.2	Extending the Solution to Several Layers	66
6.2.3	Comparison with Plevako Solution	69
6.3	Comparison with Experimental Data	70
6.4	Solution Response for Symmetric Layering	73
6.5	Application of Solution to CPTU Records	77
6.5.1	Soil Type Misclassification	77
6.5.2	Soil Strength Misclassification	79
6.6	Ramifications of Model	81
6.7	Summary	82
7	Resolution of Sleeve Friction and Cone Resistance	83
7.1	Introduction	83
7.2	Sleeve Friction Response to Soil Layering	83
7.3	Resolution of Sleeve Friction and Cone Resistance	84
7.3.1	Cone Resistance Behaviour for Asymmetric Layering	85
7.3.2	Analysis of CPTU Data for Test 19	86
7.4	The Question of Lag	89

8	Optimisation of Approximate Solution by Genetic Algorithm	95
8.1	Introduction	95
8.2	The Genetic Algorithm	96
8.2.1	Implicit Parallelism	98
8.2.2	Factors Affecting GA Performance	100
8.3	GA Application to Cone Resistance Modelling	102
8.3.1	The Approximate Solution in a GA Framework	102
8.3.2	Preliminary Results from an Artificial Record	103
8.3.3	Results from GA Application to Field q_c Records	106
8.4	Summary	112
9	Conclusions and Future Research	113
	<i>References</i>	119
	<i>Appendix A</i>	125
	<i>Appendix B</i>	171
	B.1 Development of Plevako Solution	171
	B.2 Development of Approximate Solution	176

1

Introduction and Overview

Although liquefaction is recognised as a major contributor to earthquake damage, the process itself remains poorly understood. The effect of increasing fines content on liquefaction susceptibility is unclear, due to the conflicting consequences of increasing effective cohesion and decreasing permeability. In addition, the variation of liquefaction susceptibility with depth remains equivocal. In spite of the tragic nature of the event, the Loma Prieta earthquake represented a unique opportunity to study several aspects of the liquefaction phenomenon.

The initial, primary aim of this research project was to document sites of liquefaction during the Loma Prieta earthquake. Thus, in 1990 the author joined a United States Geological Survey (USGS) reconnaissance team, investigating level ground sites of liquefaction associated with the Loma Prieta earthquake. The visit to California was arranged as a cooperative research venture by the Department of Civil Engineering at the University of Canterbury, New Zealand, and the Western Region Headquarters of the USGS, California, with the financial support of the New Zealand Earthquake Commission (EQC) and the USGS.

Field testing at ten Loma Prieta liquefaction sites commenced in June, 1990. At each site, cone penetration tests with pore water pressure measurements (CPTU) were conducted in regions of failure and non-failure. At the same sites the USGS carried out conventional boring, standard penetration testing (SPT) and sampling. The author returned to New Zealand in July, 1990, with the intention of using the Loma Prieta field data to assess the performance of selected liquefaction prediction models, develop an improved prediction model, and commence an experimental investigation into the effect of increasing fines content on liquefaction susceptibility.

However, on examination of the CPTU and SPT data, a systematic error in the cone penetrometer data became apparent. Evidence from samples recovered from several sites suggested that clearly defined interfaces existed between soil layers at certain depths in the soil

column. The corresponding cone resistance q_c records, however, displayed each of these distinct interfaces between soils of different stiffnesses as a gradual change in resistance with depth. This observation led to a change of focus for the research project, from a study of the liquefaction process and prediction model performance, towards a fundamental investigation of cone resistance response in layered soils.

It has long been accepted that stiffness changes across soil layer interfaces affect measured cone resistance. Sanglerat (1972) recognised that only resistance measured by a penetrometer of infinitesimal diameter would not be influenced by layering effects. Early calibration chamber studies revealed that cone resistance is influenced by soil properties several diameters ahead and behind the cone tip (Treadwell, 1975). Minimum layer thickness values for stiff layers embedded in softer materials have been suggested by some researchers (Robertson and Campanella (1983); Meigh (1987)); CPT users are cautioned that for less thick layers the measured resistance will underestimate the true resistance of the soil. However, in spite of a common appreciation of the existence of this systematic error in cone resistance records, it appears little progress has been made to quantify the effects of soil layering on the development of cone resistance in more complex stratigraphy. Instead, researchers have tended to focus on the mechanics of cone penetration and the interpretation of cone resistance in a single material. Konrad and Law (1987), and Campanella and Robertson (1988), present brief reviews of existing theories on cone resistance. The research presented here will provide an understanding of piezocone response in heavily interbedded soils, and help improve the accuracy of soil classification using cone penetrometer data. The content of each Chapter of this report is reviewed below.

Chapter 2 summarizes the investigation of Loma Prieta liquefaction sites in California. An overview is provided of the effects of the earthquake, along with a brief discussion of geotechnical considerations and liquefaction damage. Selection criteria are outlined for the ten liquefaction sites chosen for testing. A description of the geographical characteristics of each of the sites is included, along with maps showing the locations of the 35 probes conducted. Values for epicentral distance, Modified Mercalli Intensity and peak ground acceleration are provided for each site in Table 2.1.

In Chapter 3, the correction and standardisation of piezocone data is discussed. The piezocone test procedure followed in California is outlined, including the technique chosen for de-airing. Sources of error in the data are discussed briefly. Previously developed corrections to cone resistance and sleeve friction for pore water pressure effects are examined, along with normalisation methods.

The performance of five liquefaction prediction models is assessed in Chapter 4, using the Loma Prieta CPTU liquefaction data set. The five models include two energy-based methods, two

methods based on cyclic stress ratio, and one purely empirical method. The strengths and weaknesses of each model are discussed, and model sensitivity to parameter variation is investigated. The relationship between CPT cone resistance and SPT blowcount is critically examined, along with the observed and implied variation of liquefaction susceptibility with depth.

In Chapter 5, a model based on linear elasticity is developed to investigate cone resistance response for the situation of a cone approaching an interface between two soils of different stiffness. The effect of varying the ratio of stiffnesses for the two layers is examined. Dimensionless resistance predicted by the model is compared with calibration chamber data.

An approximate model is presented in Chapter 6 which extends the investigation of layering effects on cone resistance to cases of multilayered soils. The performance of the approximate solution for the two layer case is assessed using the elastic model presented in Chapter 5. The solution is then compared with results from multilayered calibration chamber tests. Development of cone resistance in symmetric soil layering configurations is examined, and important behavioural trends are revealed and quantified. Examples of application of the approximate solution to cone resistance records from Loma Prieta liquefaction test sites are also presented. Ramifications of the approximate solution behaviour, with regard to soil type and soil strength misclassification, are discussed.

In Chapter 7, layering effects on raw sleeve friction are investigated, and friction ratio is examined as a derived parameter. Artificial and actual cases of asymmetric soil layering are investigated to illustrate the relative resolution of cone resistance and sleeve friction. Results are presented from a statistical cross-correlation analysis, performed on the Loma Prieta CPTU data to determine the variation with soil stiffness of the lag between cone resistance and sleeve friction.

A potential method for inverting cone resistance records is investigated in Chapter 8. The Genetic Algorithm, a powerful and robust optimisation technique, is outlined. Factors affecting the performance of a Genetic Algorithm are discussed. Optimisation of the approximate solution by Genetic Algorithm is described. Results are presented from full inversion attempts of a simple, short, artificial cone resistance record, and partial inversion attempts of sections of real cone resistance data from California. Comparisons are made between the perceived resistance profiles and the stiffness ratio profiles determined by inversion.

Conclusions and recommendations for future research are presented in Chapter 9. Finally, there are two appendices. The raw and corrected California piezocone data is presented in Appendix A. Lines of critical cone resistance from the five liquefaction prediction models outlined in Chapter 4 are included on each cone resistance trace. Also included in Appendix A

are data from SPT conducted alongside a number of the CPTU probes, with maps detailing the locations of sampled sand boils relative to the probes conducted at each site. Appendix B contains details of the mathematical derivations of the exact and approximate solutions for dimensionless cone resistance.

2

Piezocone Investigation of Loma Prieta Liquefaction Sites

2.1 INTRODUCTION

The purpose of this Chapter is to describe aspects of the fieldwork undertaken by the author in the United States of America during June 1990. The main aim of the visit was to document sites of liquefaction, on level ground, associated with the Loma Prieta earthquake of 17 October, 1989. Selected sites were investigated using the piezocone (CPTU). At the same sites, the United States Geological Survey (USGS) carried out conventional boring, standard penetration testing (SPT) and sampling.

The visit to California was arranged as a cooperative research venture by the Department of Civil Engineering at the University of Canterbury, and the Western Region Headquarters of the USGS. The piezocone and associated data logging equipment were provided by the University of Canterbury; the drilling rig and other testing equipment were supplied by the USGS.

2.2 THE LOMA PRIETA EARTHQUAKE

On Tuesday, 17 October, 1989, at 5:04pm (local, Pacific Daylight Time), a moderately large earthquake with a surface-wave magnitude of $M_s = 7.1$ rocked Northern California for approximately 15 seconds. The epicentre of the tremor was near Loma Prieta Mountain, about 30 km south of San Jose. Although centred in a sparsely populated area, and in spite of the relatively short duration of strong ground shaking, the earthquake claimed the lives of 62 people

and left thousands of others injured and homeless in its wake. Property damage and recovery costs were estimated to exceed six billion US dollars (Plafker and Galloway, 1989).

A 40 km long segment of the San Andreas fault beneath the Santa Cruz mountains ruptured during the Loma Prieta event. The fault mechanism consisted of nearly equal components of right-lateral strike-slip and reverse-slip on a steeply inclined fault plane, dipping 70 degrees to the southwest. Figure 2.1 shows the epicentre (star), the surface projection of the rupture plane (hatched area), and the zone of aftershocks (dotted line). The depth to the hypocentre, located at the midpoint of the ruptured segment, was approximately 18 km. As determined by the spatial distribution of aftershocks, the rupture spread from the hypocentre upwards and bilaterally along the strike of the fault to the northwest and southeast, 20 km in each direction (Plafker and Galloway, 1989).

The earthquake caused structural and nonstructural damage throughout an 8000 square kilometre area of central California. The bilateral rupture mechanism strongly influenced the resulting damage patterns, focusing the released energy to the north and south of the epicentre. Other major factors that controlled and confined the earthquake damage were the relative remoteness and depth of the main shock, the short duration of strong ground motion and the subsurface soil conditions. Unquestionably, the effects of the earthquake would have been even more devastating if strong ground shaking had continued for a few more seconds.

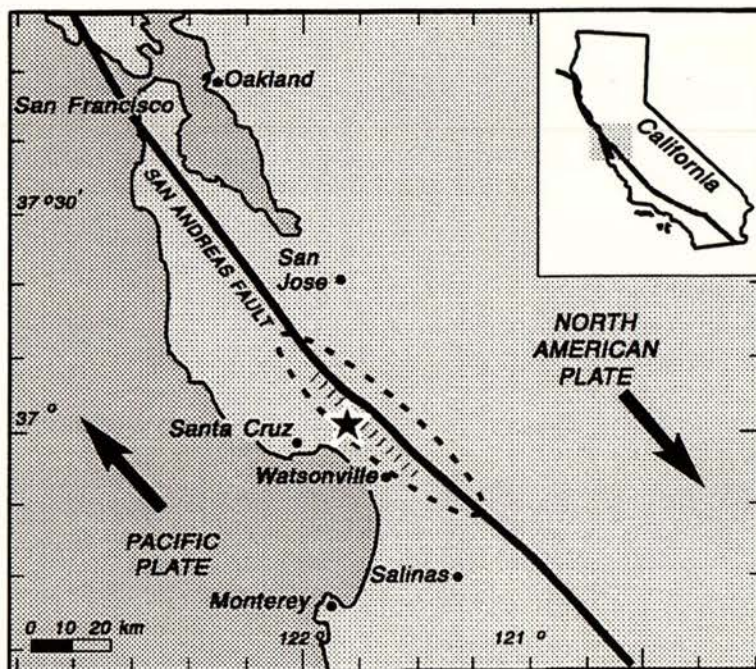


Figure 2.1 Fault rupture of the Loma Prieta earthquake: hatched area beside the epicentre (star) indicates surface projection of fault plane; dotted line outlines zone of aftershocks.

(After Benuska, 1990)

2.3 GEOTECHNICAL CONSIDERATIONS

Geotechnical considerations of the Loma Prieta earthquake were important. In particular, subsurface soil conditions played a significant role in regulating the intensity of ground motion felt throughout central California during the tremor, and the amount of damage incurred.

The comparatively large hypocentral depth of the earthquake, about twice the average value for this portion of the San Andreas fault, contributed to an unusual absence of surface faulting. However, evidence of significant ground deformation (primarily extensional ground cracking) was found at the northern end of the ruptured fault segment. More than 1000 landslides and rock falls were triggered by the earthquake, one of the largest blocking a portion of State Highway 17 for nearly one month with approximately 1000 cubic metres of rock and soil debris (Benuska, 1990).

Site amplification of ground accelerations was significant, particularly in the San Francisco Bay area, regions of which are located on deep, soft, cohesive soils. Although the epicentral Modified Mercalli (MM) intensity was rated at VIII, a higher level of intensity was assigned to the Marina district of northern San Francisco, 98 km from the epicentre, as a result of this site amplification. There was widespread evidence of liquefaction in the Santa Cruz and central Monterey Bay regions, relatively close to the epicentre. Isolated instances of liquefaction occurred further to the north, within the Marina district, and parts of the east San Francisco Bay shore.

2.4 LIQUEFACTION DAMAGE DURING LOMA PRIETA

Liquefaction of natural dune and river sand deposits along with artificial fills contributed greatly to damage resulting from the Loma Prieta event. Typically, ground shaking during the earthquake initiated densification of these loose, saturated sediments, causing a rapid increase in pore water pressure. Instability in the soil column arose at sites where the excess pore water pressure, unable to drain away freely due to the fineness of the soil and the rapid nature of the cyclic loading, increased to balance the overburden stress. At that instant, the effective stress reduced to zero in the sandy soil and contact between soil particles was lost (National Research Council, 1985; Ishihara, 1993).

The presence of liquefied layers in the soil column caused large scale lateral spreading along the banks of several rivers, in most cases towards the river centreline. This caused crack damage to river levees, and in some instances resulted in the compression of bridge structures and the tilting of bridge piers. Lateral spreading also initiated failures of coastal retaining walls and caused damage to piled port facilities.

Airport runways and highways were damaged as liquefaction caused disruption of these paved surfaces. Many structures suffered large differential settlements due to the liquefaction of subsurface layers. In many instances these settlement failures were complicated by secondary factors such as a loss of services as a result of gas, electricity and water mains shearing directly or failing under their self-weight. Flotation of empty ground storage tanks and pipelines also contributed to the damage (Shephard *et al.*, 1990).

2.5 DESCRIPTION OF CALIFORNIA TEST SITES

In June 1990, the author joined a USGS reconnaissance team investigating sites of liquefaction associated with the Loma Prieta earthquake. Ten sites of liquefaction were tested using the University of Canterbury Fugro piezocone, with a total of 35 probes undertaken. Two of the sites were located on sand spits, seven were alongside the banks of either the Pajaro or Salinas Rivers, and one was located in the Marina District of San Francisco. The sites are shown in Figure 2.2. The cone was de-aired and a full piezocone test was carried out in all but three cases; test results can be found in Appendix A. A summary of site characteristics is provided in Table 2.1. The intensity values listed in Table 2.1 have been deduced from the report of Plafker and Galloway (1989). Values for epicentral distance have been provided by J.C. Tinsley III (USGS Menlo Park, personal communication, 1990).

Site	Epicentral Distance (km)	Modified Mercalli Intensity	Peak Ground Acceleration (fraction of g)
Moss Landing	27.1	7	0.267
Pajaro Dunes	21.1	7	0.323
Millers Farm	18.7	8	0.528
Airport Watsonville	19.5	8	0.379
Jefferson Castroville	35.5	7	0.205
Scattini	31.1	7	0.229
Sea Mist	33.5	7	0.214
Leonardini	34.3	7	0.214
SPR Bridge	18.8	8	0.488
Marina District	98	9	0.21

Table 2.1 Test site characteristics

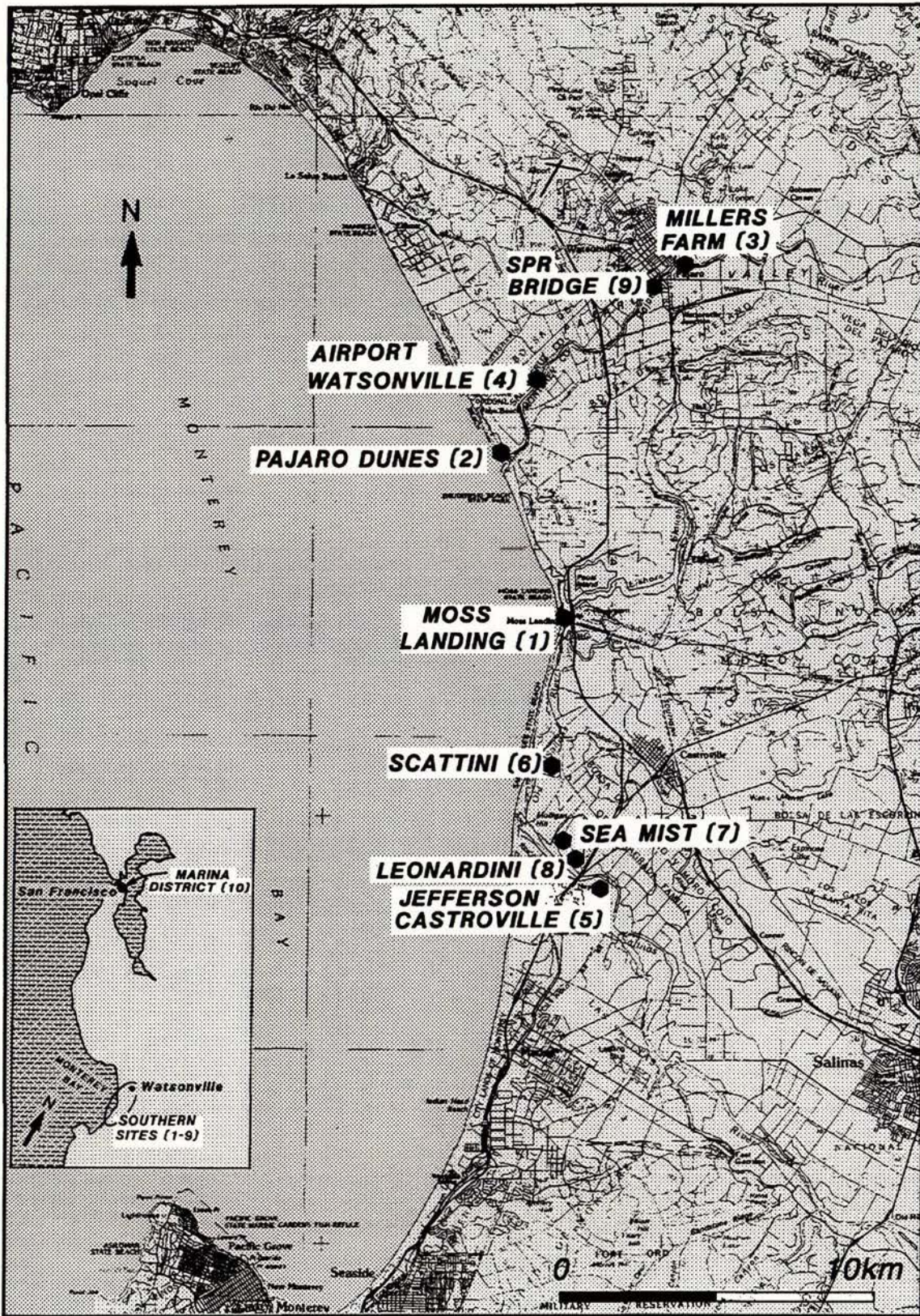


Figure 2.2 Piezocone test sites

Values for peak ground-surface accelerations have been estimated using an attenuation relationship (Boore *et al.*, 1993), with the exception of $a_{\max} = 0.21g$ for the Marina District. Although no strong motion seismogram was recorded at the Marina District, estimates of peak surface acceleration for this site have been proposed by Hanks and Brady (1991), and Boatwright *et al.* (1991). Boatwright *et al.* suggest that the peak accelerations in the Marina District reached or exceeded 0.25g, a value similar to peak accelerations recorded at stations sited on older Bay mud in Emeryville (0.25g) and Oakland (0.29g). However, Hanks and Brady suggest that the peak acceleration of 0.16g recorded at Treasure Island is a more appropriate substitute value for the Marina District. The value of 0.21g used in this report is a representative average, taking the above estimates into consideration.

During reconnaissance investigations immediately following the earthquake, many areas of liquefaction were discovered. The ten sites selected for testing were regions of substantial liquefaction, as evidenced by large-scale lateral spreading and the presence of many sand boils. At each site, the positioning of the probes was arranged so that data were collected from regions of failure and non-failure. The reason for this was to provide a distinction between these regions, to assist in identifying the layers which failed by liquefaction. The geographical locations and major features of the ten sites are described below.

2.5.1 Moss Landing

Moss Landing is located on the California coast, 40 km southwest of Santa Cruz, approximately midway between the mouths of the Pajaro and Salinas Rivers. Part of the small township occupies a one-kilometre-long sand spit, zones of which liquefied during the Loma Prieta event. The spit is more accurately described as an island, since the Old Salinas River separates this land from the mainland.

Testing was carried out near the end of the spit at the locations shown in Figure 2.3, in the vicinity of a cluster of four Chevron oil and gasoline tanks (refer Figure 2.4) that underwent a foundation failure as subsurface layers liquefied. According to an eye-witness, moderate ground cracking began in a west to east direction just outside the northwest corner of the tank enclosure, approximately four seconds after the shaking commenced. The opening of these ground cracks was accompanied by an ejection of a mixture of sand and water, which rose to a height of two metres, level with the bow of a boat on a trailer parked adjacent to the enclosure.

The cone was de-aired for two of the three tests conducted here. A CPT and a CPTU were performed side by side in a region of no apparent liquefaction, approximately 30 metres to the south of the tank enclosure. A second CPTU was conducted in the vicinity of the reported ground cracking.

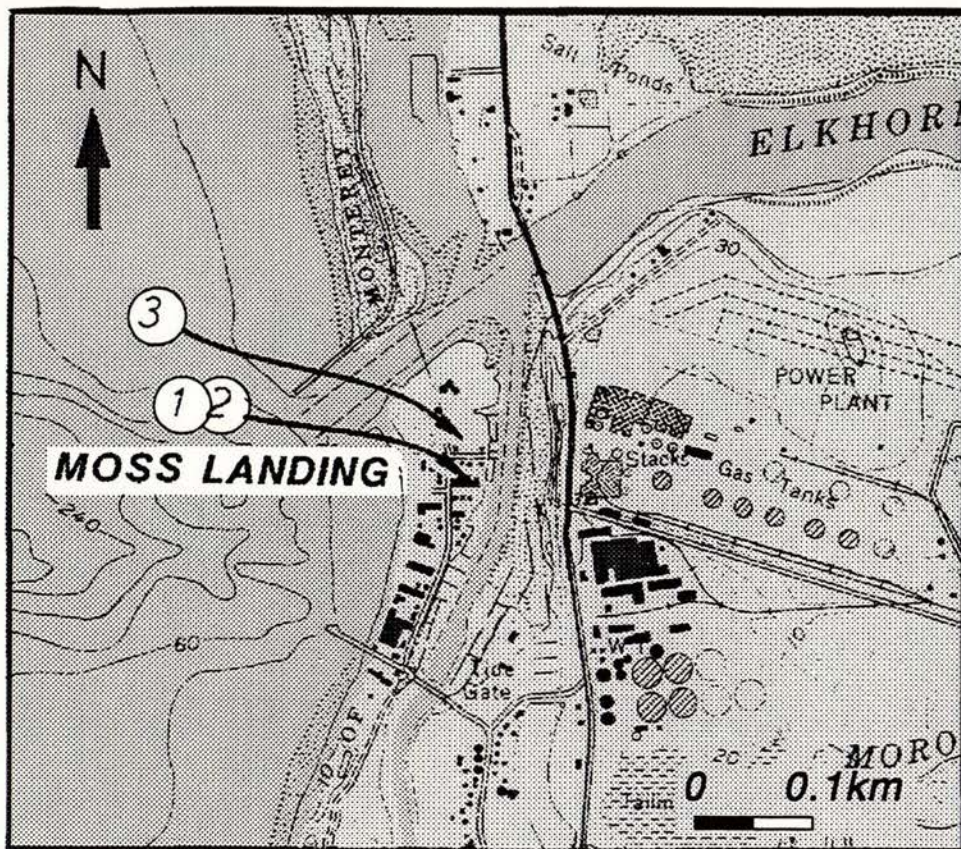


Figure 2.3 Moss Landing test site



Figure 2.4 Moss Landing test site, viewed NW (SPT in progress). The oil tanks in the background underwent a foundation failure during the earthquake.

2.5.2 Pajaro Dunes

Pajaro Dunes is a relatively small, modern holiday retreat situated inside the dunes of Sunset State Beach, just north of the Pajaro River mouth. The complex is bordered to the east by the Watsonville Slough, and is therefore effectively built on a sand spit. The development comprises several holiday homes and large four-storey condominiums.

Liquefaction during the Loma Prieta event caused the disruption of pavements and services to buildings at the southern end of the complex. There was also settlement of some of the larger buildings in this region, and a small lateral spread which resulted in partial failure of a retaining wall constructed along the north bank of the Pajaro River. Two de-aired tests were conducted here, the first inside the east tip of the island within the south car parking lot, which was covered with ejected sand after the earthquake. The second probe was performed further north, along the slough side of the access road that is in parallel alignment with the Watsonville Slough. This test ended at a comparatively shallow depth due to very high resistance to penetration of the dense sandy soil. Test locations are shown in Figure 2.5.

2.5.3 Miller's Farm

Miller's Berry Farm is situated to the east of Watsonville, on the north side of San Juan Road. The farm occupies an area of 19.5 hectares (48.1 acres), and is bounded to the north by the south levee of the Pajaro River. As with many of the berry and produce farms in the Pajaro Valley, the fields had been ploughed and levelled using laser-guided graders shortly before the day of the earthquake. The earthquake caused significant deformation and disruption of the ground surface, creating bands of subsidence. Large areas of sand boils indicated that there had been liquefaction of one or more of the sub-surface soil layers.

A total of eight de-aired tests were conducted at this site, as shown in Figure 2.6. These were arranged in three north-to-south lines, to cover as much of the deformed ground area as possible and to provide some contrast between areas of failure and non-failure. Lines of three tests were conducted at the east and west ends of the farm, and a line of two tests was conducted in the centre. Figure 2.7 is a photo of Test 14 in progress at the Miller's Farm site.

There appeared to be some confinement of ground water at this site. The ground water level consistently rose by approximately half a metre after drilling through a comparatively dry layer of clay at an average depth of 4.4 metres. This could be a result of a seasonal variation in the water table depth, rather than an excess, artesian pressure. Nevertheless, it is possible that pore water pressures at this site were naturally elevated before the earthquake, aiding the liquefaction process.

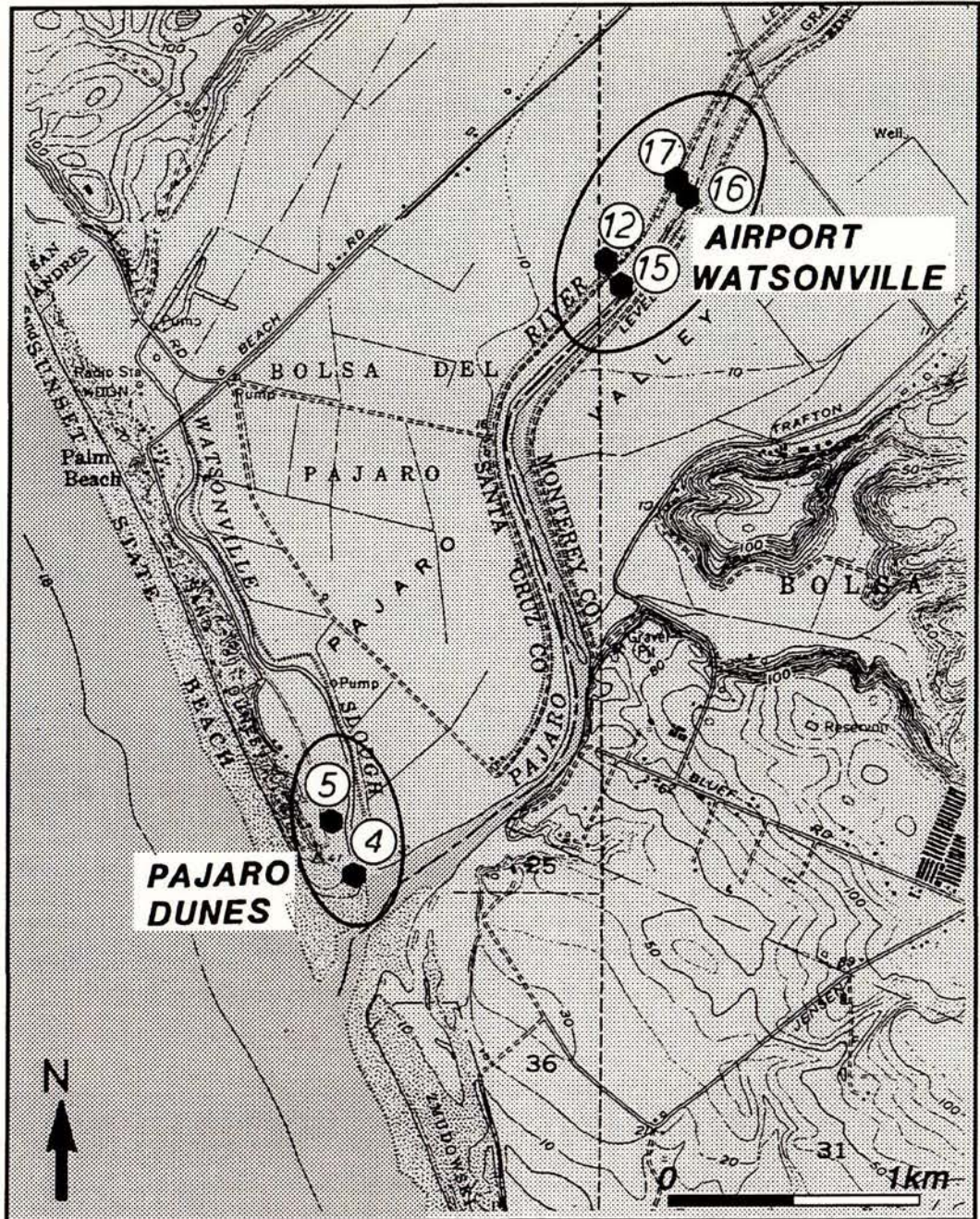


Figure 2.5 Pajaro Dunes and Airport Watsonville test sites

2.5.4 Airport, Watsonville

Model aeroplane enthusiasts in the Pajaro Valley make use of a small runway constructed inside the north levee of the Pajaro River, situated approximately midway between Watsonville and Pajaro Dunes. The runway is parallel to the river and levee. Lateral spreading of the Pajaro River banks disrupted the asphalt surface of the runway, causing cracking and changes in elevation throughout its cross-section (refer Figure 2.8).

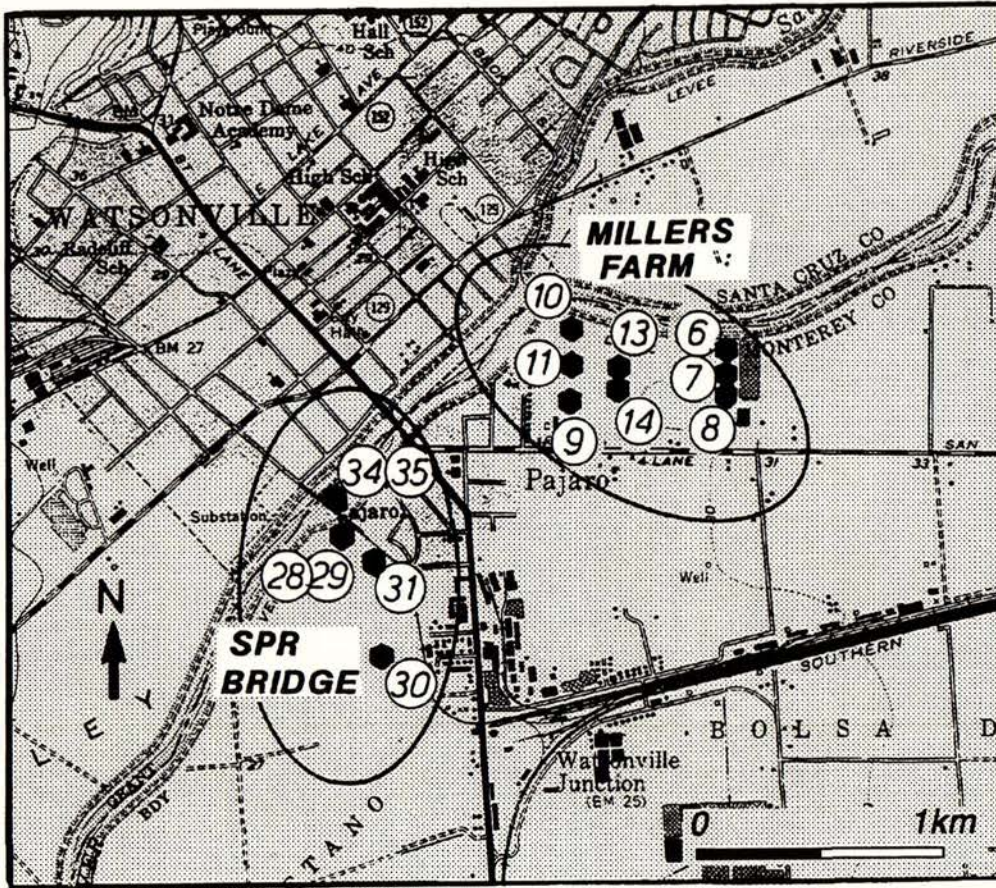


Figure 2.6 Miller's Farm and Southern Pacific Railroad Bridge test sites

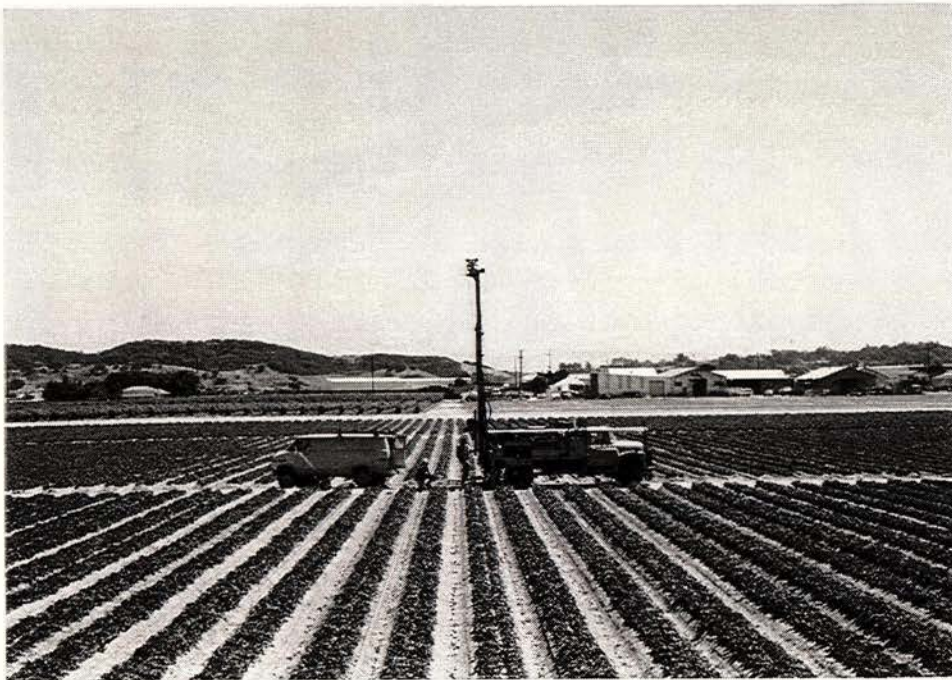


Figure 2.7 Test 14 in progress at Miller's Farm (viewed S from levee of Pajaro River)

Four tests, located in Figure 2.5, were conducted here, one outside and three inside the levee; the cone was de-aired for all of these tests. The test outside the levee, and one between the runway and the river, were conducted at the southwest end of the runway; the other two tests were conducted at the northeast end of the runway, one between the levee and the runway, and one between the runway and the river. The two tests conducted between the runway and the river were within the lateral spread failure zone.

2.5.5 Jefferson

The Jefferson produce farm is bordered on its north side by the south levee of the Salinas River. It is situated to the east of Highway 1, approximately 4 km south of the township of Castroville. The Loma Prieta earthquake caused significant subsidence of approximately one third of the 50 hectare (124 acre) farm, reducing the elevation of some regions by as much as half a metre. This disrupted the drainage of the fields, making it necessary for them to be re-levelled. Subsidence had not ceased at the time of the piezocone testing, some seven months after the earthquake, and was causing on-going problems for the land owner.

The cone was de-aired for all four tests conducted here. Two probes were performed inside the levee, on a track which led to the river. The other two were conducted on the tracks dividing the fields, one close to the levee and one further away on higher ground, outside the failure zone. Locations are shown in Figure 2.9.

2.5.6 Scattini

The Scattini site is nestled into a loop of the Old Salinas River, a few hundred metres east of the coast, between the present dunes and the pre-1906 channel of the Salinas River. The Loma Prieta earthquake initiated a large lateral spread at this site, the slide block moving to the north by a half to one metre. Two de-aired tests were conducted here along the centreline of the spread. The first was within 20 metres of the slough towards which the spreading occurred, and the second was approximately 200 metres away from the slough, outside the apparent failure zone. Probe locations are shown in Figure 2.9.

2.5.7 Sea Mist

The Sea Mist property is less than 2 km south of the Scattini site, and is bounded to the south by the north bank of the Salinas River. At this site, a large lateral spread towards the Salinas River occurred. In this instance the slide block moved to the south-west, perpendicular to the axis of the river. The cumulative movement totalled approximately two metres. Two CPTU were conducted here, one inside and one outside the lateral spreading limit (refer Figure 2.9).

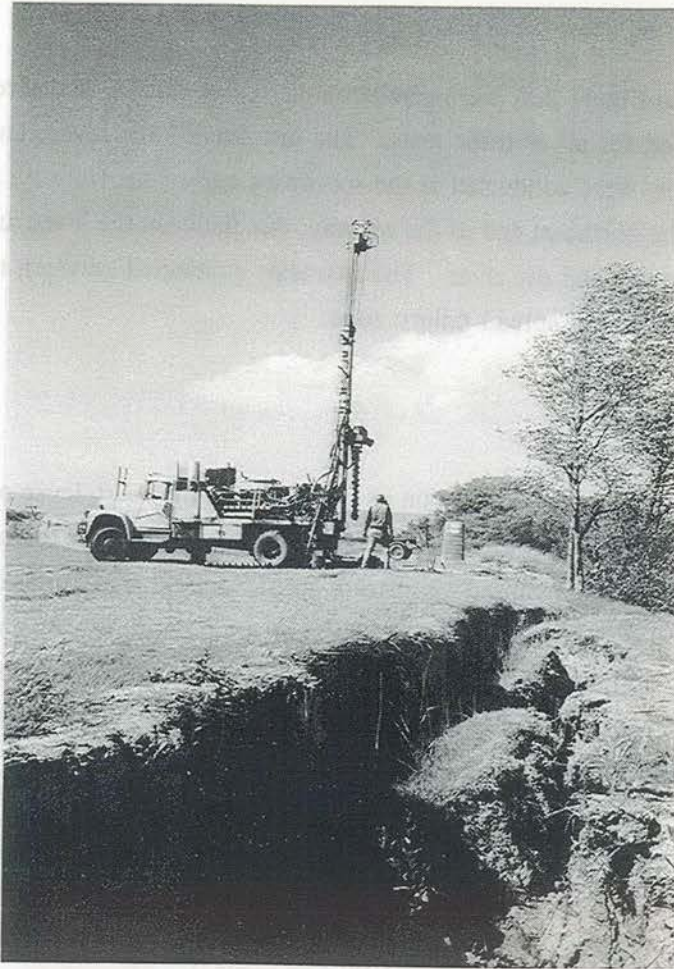


Figure 2.8 SPT in progress at Airport, Watsonville site (viewed NE, Pajaro River on right)

2.5.8 Leonardini

This site is almost identical to the Sea Mist site. It is located 500 metres further upstream along the Salinas River. As with Sea Mist, the southern boundary of the Leonardini property is the north bank of the Salinas River. The farm is bordered to the east by Highway 1. Two de-aired probes were conducted here, as shown in Figure 2.9, again one inside and one outside the limit of a large lateral spread.

2.5.9 SPR Bridge

The Southern Pacific Railroad bridge crosses the Pajaro River approximately 400 metres downstream of the Watsonville Main Street bridge. The bridge was subjected to both compression due to lateral spreading and shaking during the Loma Prieta earthquake. A concrete pier on the south bank failed by overturning, and was replaced with braced steel columns before the piezocone work was undertaken. Extensive ground cracking was evident inside and outside the south levee.

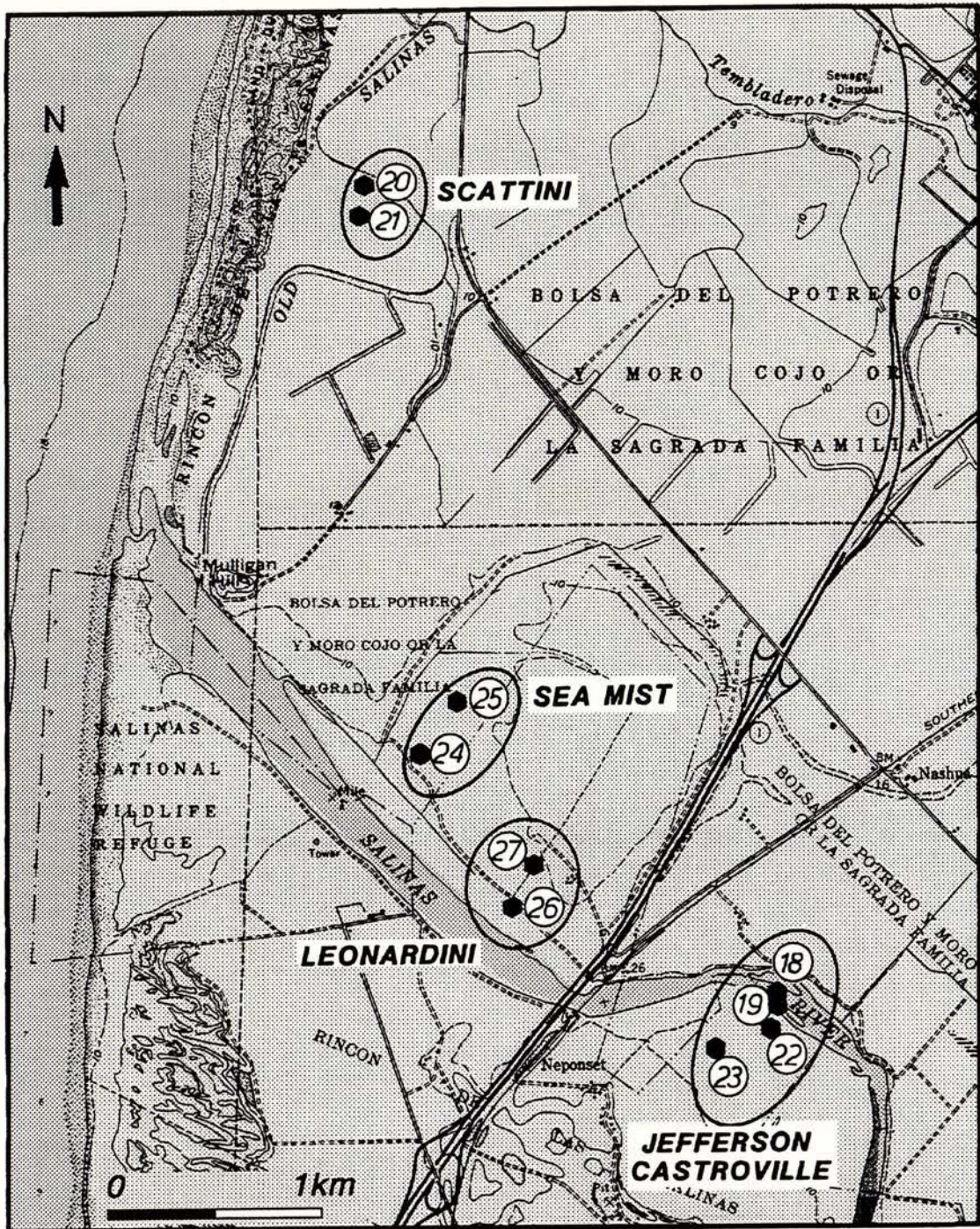


Figure 2.9 Jefferson, Scattini, Sea Mist and Leonardini test sites

A total of six tests were conducted at this site, as shown in Figure 2.6. The cone was only de-aired for four of these tests. A CPT and a CPTU were conducted side by side inside the south levee, to the north side of the bridge. These tests were inside the zone of ground cracking associated with the primary lateral spread. Another CPT and CPTU were conducted outside the south levee, to the south side of the bridge, outside the primary lateral spread. Two

additional tests were conducted, one 30 metres further down the railway in line with an apparent secondary lateral spread, and one approximately 1 km due south of the bridge along a track centreline, away from the failure zone and in a different geological deposit (J.C. Tinsley III, USGS Menlo Park, personal communication, 1990). Figure 2.11 is a photo of Test 29 in progress.

2.5.10 Marina District

The Marina district is situated at the very northern tip of the San Francisco peninsula and suffered much damage from liquefaction during the earthquake, despite its large epicentral distance. The district is residential and consists mainly of three to four storey timber-framed buildings, with some smaller single dwellings.

Two probes were conducted here, one in the centre of Marina Green, in line with the centre of Filmore Street (refer photo, Figure 2.12), and the other in the courtyard of Winfield Scott School. The cone was de-aired for both tests. The first hole went to a depth of almost 20 metres, and could have been taken further if more rods had been available. The second hole only went to a depth of 4.7 metres due to complications with the drilling rig lifting as the cone encountered a dense layer. Test locations are shown in Figure 2.10.

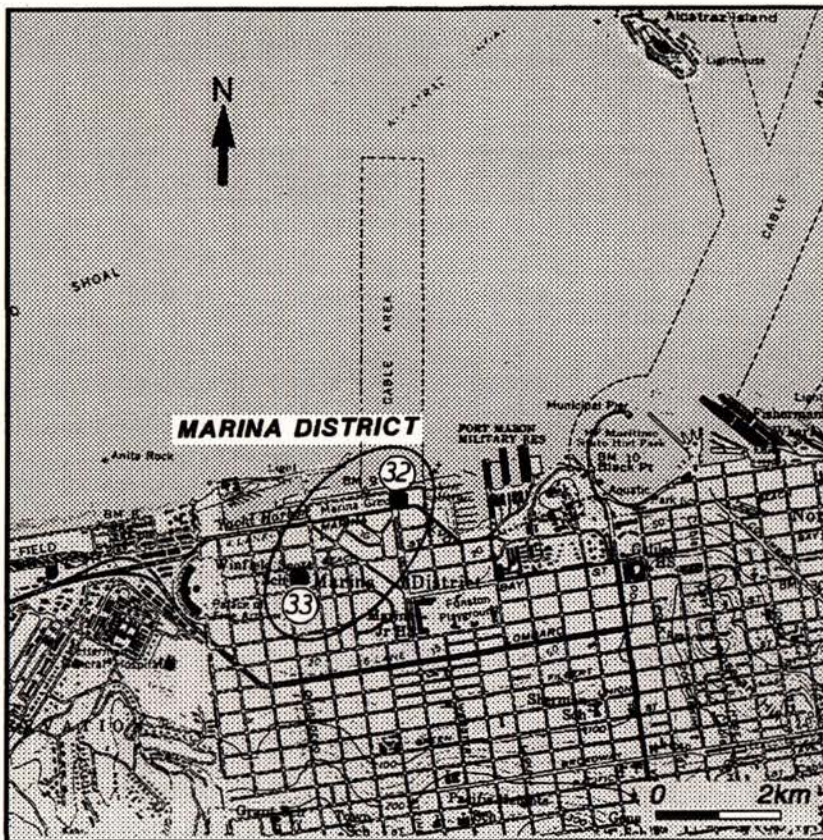


Figure 2.10 Marina District test site



Figure 2.11 Test 29 in progress at SPR Bridge site
(viewed S from SW end of bridge)



Figure 2.12 Test 32 in progress at the Marina Green (Marina District, San Francisco)

CPTU and SPT raw data relating to each of the sites detailed above can be found in Appendix A. In addition, values for median grain size (D_{50}) of ejecta samples recovered at each site is provided on site plots at the end of Appendix A.

3

Piezocone Data Correction and Standardisation

3.1 GENERAL CONSIDERATIONS

In spite of care taken during piezocone testing, data retrieved contain both random errors, and systematic errors that stem from standard cone design. Cone calibration factors and zero readings should be checked for drift between tests, and the accuracy of depth measurements should be monitored while a test is in progress. The parameters cone resistance (q_c) and sleeve friction (f_s) may require correction due to pore water pressure effects. Total stresses q_t and f_t are derived from these corrections, which are significant for probes conducted in fine-grained soils. Raw friction ratio (R_f) should be calculated using an appropriate lag between the two parameters q_c and f_s . In addition to the above corrections, it may be useful to normalise cone resistance, friction ratio and pore water pressure results in a standard way to make test results from different cones comparable. This Chapter addresses issues of piezocone data collection, correction and normalisation.

3.2 CPTU PROCEDURE

A piezocone probe is conducted as a standard cone penetration test with the addition of pore water pressure measurements, and excess pore pressure dissipation recordings. Each probe conducted in California followed the international reference test procedure, as outlined by De Beer *et al.* (1988). A four-channel Fugro piezocone was used for the California fieldwork, with projected tip area of ten square centimetres and friction sleeve surface area of 150 square centimetres. The Fugro cone was of the subtraction type, with sleeve friction (f_s) measured

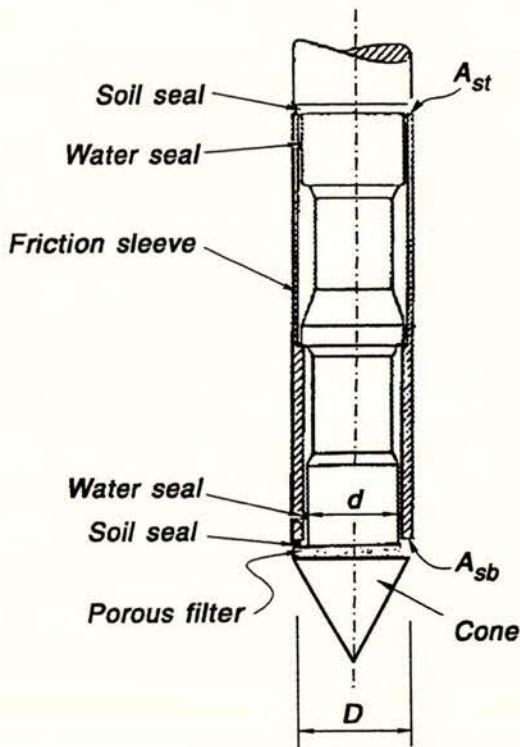


Figure 3.1 Diagram of piezocone (after Robertson, 1990)

indirectly by subtracting tip resistance (q_c) from combined tip and sleeve resistance. The remaining two channels measured cone inclination and pore water pressure (u). Inclination measurements are useful for checking the accuracy of recorded depths, and for differentiating between thin, stiff soil layers, and embedded objects within the soil column such as large stones or buried organic matter. A schematic of a typical piezocone is shown in Figure 3.1.

Unfortunately, the integrity of the piezocone pore-pressure-transducer response is compromised if the pore pressure measuring system is not rigid. Even a very small quantity of air entrained in the cavity below the pore-water-pressure transducer will significantly increase the compressibility of the pore fluid and the response time of the system along with it (Smits, 1982; Meigh, 1987).

To achieve a rigid measuring system, the piezocone was subjected to a standard de-airing procedure when accurate pore water pressure and dissipation test records were required. The cavity behind the pressure transducer was injected with water while the cone was submerged in a tank. Following this, the cone, the porous filter and the cone-tip were placed under a vacuum of approximately 70 kPa under water for 30 minutes. After this time, the vacuum was released and the cavity behind the transducer was re-injected, under water, with de-aired water. The piezocone was then assembled under water, and a latex sheath slipped over the tip and part

of the shaft, covering the porous filter. Figure 3.2 shows the de-airing process in operation. Considerations of speed and simplicity influenced the choice of de-aired water as cavity fluid, in favour of glycerin or silicon oil. The above method of de-airing consistently yielded a rigid pore pressure measuring system.

A clean polypropylene filter was used for each test. Such filters are relatively permeable (0.1mm/sec) and have a high resistance to abrasion, important attributes when probing sandy soils. Although plastic filters are compressible, the location of the filter behind the shoulder of the cone would have minimised the likelihood of filter squeeze effects corrupting the recorded pore pressure (Campanella and Robertson, 1988).

During the de-airing procedure, a hole was augered to the water table, and the drilling rig used to push the cone was positioned over the hole. Upon completion of the set-up, the cone was removed from the vacuum tank and connected to the rods. This was always the final connection made, so that the cone maintained saturation for as long as possible.



Figure 3.2 Piezocone de-airing in progress (Miller's Farm, Test 7)

When this connection was secure, the power to the cone was switched on for several minutes, allowing the electronics to warm up. After zero readings were recorded, the cone was lowered down the hole and allowed to rest on the ground at the base. A starting depth below ground level was recorded, and penetration testing initiated at the standard rate of 20 mm/s. Although standard one-metre reduced rods were used, the average probing distance was chosen as half a metre so that the dissipation of excess pore pressure was frequently recorded. At several sites the first pass length was purposely decreased to 250 mm in order to gain dissipation data as close to the water table as possible. At no time did the pass length intentionally drop below 250 mm. An average of 15 dissipation tests were conducted during each probe, approximately 70 percent of which yielded reliable values for t_{50} (time to 50 percent dissipation of excess pore pressure). These values may be used to deduce information about the drainage, permeability and consolidation characteristics of the probed soil (Campanella and Robertson, 1988).

The piezocone data was recorded using the University of Canterbury CPTU data logging system. The data-logging computer read the four cone channels three times each second, on average. An output file was generated for each probe, containing the penetration and dissipation data. In addition to the cone resistance, sleeve friction, pore water pressure and inclinometer data recorded by computer, points of interest such as evidence of liquefaction were noted and site maps constructed.

3.3 ERROR SOURCES DURING CALIFORNIA TESTING

During February 1990, a number of CPTU soundings were conducted at the northern end of the South Island of New Zealand, near Blenheim. The purpose of this fieldwork was primarily to record data from the Wairau Pa site associated with historical liquefaction, but it also allowed all hardware and software components to be checked before the California visit. The cone was calibrated before departing for California, and two calibrations were performed in California to monitor its integrity - one before the first test early in May 1990, and a second late in June 1990 at the end of the field testing. The variation between the two sets of calibration factors came to less than half a percent, indicating that there were no significant changes in the cone strain-gauges or transducer during testing. Zero readings for the piezocone were stable, with only minor fluctuations of approximately one percent. There was, however, one erroneous pore pressure zero reading (at Test 21, the second test at the Scattini site), and this was abandoned during data reduction in favour of the average pore pressure zero value.

The depth recording device mounted on the drilling rig consistently measured short during probing in dense sands, due to complications with the rig lifting. This cumulative depth error was checked regularly, and consistently measured less than one percent. Typically, a probe of one metre in dense sand registered as 993 millimetres on the recording device. The error was

greatest during the final few metres of a penetration test, generally when the cone entered a dense sand deposit and the drilling rig began to lift off the ground. The raw depths have not been corrected for the small effect of this error.

An error was discovered in the dissipation times recorded during the California testing. The program timing device recorded significantly smaller dissipation times than the computer clock for dissipation tests longer than a few seconds. Fortunately, this software error was systematic, and there was sufficient redundant time information recorded to enable the data to be corrected. The erroneous values were discarded and replaced with the correct times.

3.4 PORE PRESSURE EFFECTS

Referring back to Figure 3.1, it is evident that the pore water pressure field surrounding the cone can influence the recorded values of cone resistance and sleeve friction, due to an imbalance of water pressure forces acting on the unequal end areas of the cone tip and sleeve respectively. Thus, as it is recorded, q_c corresponds neither to an effective stress nor a total stress. The corrections required to make allowance for the pore water pressure and determine total stresses from the raw measured data are presented below, and normalisation procedures are discussed.

3.4.1 Cone Resistance

The measured value of cone resistance q_c is converted to total resistance q_t by applying the following correction

$$q_t = q_c + (1-a)u \quad (3.1)$$

proposed by Baligh *et al.* (1981), and Campanella *et al.* (1982). In equation (3.1) the pore water pressure u is that measured between the cone tip and friction sleeve, and a represents the net area ratio. From Figure 3.1, it is apparent that this ratio should be given by

$$a = \frac{d^2}{D^2} \quad (3.2)$$

where d is the diameter of load cell support and D is the external cone diameter as shown in Figure 3.1. However, Robertson (1990) observes that this expression does not take into account friction forces which develop due to distortion of the O-ring water-soil seal, and recommends that in practice a be determined in a small calibration chamber. A value of $a = 0.75$ was provided by the manufacturer of the Fugro cone used for the field testing performed in California, and this value was verified by a simple laboratory experiment. Like most penetrometers, the Fugro cone has square-sectioned O-ring water-soil seals above and below

the friction sleeve. There was some uncertainty as to how the presence of the lower O-ring would influence the value of a . It was thought that its presence was possibly obscuring the annulus on which the back water pressure was presumed to act. A laboratory experiment was conducted to determine a , and establish whether the presence of the lower O-ring affected the cone resistance measured at high pore pressures. The lower O-ring was removed from the cone and the cone was de-aired. The portion of the cone below the middle of the friction sleeve was positioned vertically in a flooded calibration chamber. Chamber water pressure was raised to 0.5 MPa, and the expected value for cone resistance of 0.375 MPa was recorded. The procedure was repeated, this time with the square O-ring in position. The measured load on the cone tip was the same, indicating the presence of the square O-ring has no effect on the value of cone resistance measured (this implies the O-ring must have similar compressibility properties to water, with a Poisson's Ratio of approximately 0.5). The experiment verified the given value of $a = 0.75$.

In practice, the correction of q_c to q_t is only important in soft clays and silts, where high pore water pressures are generated during penetration and cone resistance is low. In these soils, raw values of q_c that are less than the pore pressure may be observed, apparently implying a negative effective cone resistance. While the correction to q_t is important for penetration testing in deep, submerged, soft marine sediments, it is negligible in cohesionless soils. Although its effect is difficult to detect, it has been applied to all of the field data collected in California for the purposes of standardising the data (refer Appendix A).

To remove the effect on q_c of increasing overburden pressure with depth, attempts have been made to normalise cone resistance data (Olsen and Malone, 1988; Wroth, 1988). These methods can be quite complicated to implement as they require different normalisation procedures for different types of soil. Wroth suggested the following method for normalising q_t measured in clays to Q_t

$$Q_t = \frac{q_t - \sigma_{vo}}{\sigma_{vo}'} \quad (3.3)$$

where σ_{vo} and σ_{vo}' are total and effective vertical stresses respectively (when testing in sands, these stresses are substituted for mean principal total and effective stresses respectively). To calculate these stresses, values for *in situ* densities are required for soil layers above and below the water table. Hence the value of normalisation is dependent upon the precision of these unit weights. Robertson (1990) indicates that, to be consistent, normalisation should also allow for changes in horizontal stress with depth. The complications involved in the determination of *in situ* horizontal stresses, combined with the approximate nature of the overburden stress calculations, considerably reduce the benefit of normalising cone resistance data. For this reason, the California cone resistance data has not been normalised.

3.4.2 Sleeve Friction

A similar pore water pressure correction to that described in Section 3.4.1 is necessary to convert the measured value of sleeve friction f_s to the total sleeve friction f_t , particularly if the friction sleeve has unequal end areas. The expression for f_t is given by Konrad (1987) as

$$f_t = f_s - (1 - \beta b)cu \quad (3.4)$$

where

$$b = \frac{A_{st}}{A_{sb}}; \quad c = \frac{A_{sb}}{A_s}; \quad \beta = \frac{u_s}{u}$$

A_{st} is the top end area of the sleeve and A_{sb} the bottom end area of the sleeve (refer Figure 3.1). A_s is the sleeve outside surface area (150 square centimetres for a standard cone), and u_s is the pore pressure measured at the top end of the friction sleeve.

The above correction was not applied to the California data since for the Fugro cone u_s is not measured. Typically, u_s is considerably less than pore pressures recorded behind the shoulder of the cone (Baligh *et al.*, 1980). Robertson (1990) observes that for the case of a cone with an equal end area friction sleeve, such as the Fugro cone, the correction is significantly less than the large corrections calculated by Konrad which in some cases exceed 30 percent of measured f_s . As with cone resistance, the correction of f_s to f_t is only important in soft soils where high pore water pressures are generated during penetration.

When presenting the results of a cone penetrometer test, sleeve friction data is usually omitted in favour of the derived friction ratio, $R_f (= f_s/q_c)$. For this reason, it is not common practice to normalise sleeve friction data, although suggestions have been made (Olsen and Malone, 1988). However, a method for normalising raw friction ratio R_f to F_R , has been suggested by Wroth (1988). Like raw friction ratio, F_R is expressed as a percentage, and is defined as

$$F_R = \frac{f_s}{q_t - \sigma_{vo}} \quad (3.5)$$

Once again, the merit of this normalisation depends on the accuracy of the overburden stress calculation. It has not been applied to the California data. R_f and f_s data are provided in Appendix A.

In addition to correcting the effects of pore pressure on measured sleeve friction where possible, it is necessary to lag the sleeve friction data with respect to cone resistance before calculating raw friction ratio, due to the physical separation of the friction sleeve and the cone tip. The author recommends the use of a standard value of 150 mm for lag between these two parameters when penetrating relatively stiff or interbedded soils of average resistance 10 MPa with a

standard 10 square centimetre cone. A lower value of approximately 120 mm would be more appropriate when probing in soft marine sediments. The basis for these figures is outlined in Chapter 7, in which sleeve friction is examined in detail.

3.4.3 Pore Water Pressure

Dynamic pore water pressures measured during penetration will be accurate if the pore water pressure transducer within the cone is calibrated accurately, and if complete saturation of the water pressure measuring system is maintained throughout testing. However, maintaining saturation is complicated and difficult to guarantee. Large negative values of pore pressure generated during probing may induce cavitation of the fluid in the transducer chamber and result in a temporary or permanent loss of saturation. Negative pore pressures were recorded in two thirds of the 32 fully saturated probes conducted in California. It is possible that a loss of saturation has affected the pore pressures recorded during Tests 12, 26 and 32.

Campanella and Robertson (1988) provide a brief history of suggested methods for normalising the measured pressure, u . It is generally accepted that B_q , defined as

$$B_q = \frac{u - u_0}{q_t - \sigma_{vo}} = \frac{\Delta u}{q_t - \sigma_{vo}} \quad (3.6)$$

by Senneset *et al.* (1982), Jones and Rust (1982), and Wroth (1984), is the most appropriate normalised pore water pressure parameter (here u_0 is hydrostatic pressure). Although the research presented in this report does not focus on pore water pressure aspects of piezocone response, B_q has been calculated for each CPTU probe conducted in California (refer Appendix A).

3.5 THE INFLUENCE OF SOIL LAYERING

Where possible, piezocone data should be corrected for the effects of pore water pressure acting on unequal tip and sleeve end areas, as discussed above. Such corrections are particularly important when probing in deep, soft, saturated soils. However, the scale of such errors is far outweighed by other systematic errors present in the data. These systematic errors are related to the response of the cone when it encounters layering in the soil column. We expect pore water pressure not to be affected by soil layering, since the value of u measured during penetration is directly related to the soil type in the immediate vicinity of the pore pressure filter (Robertson and Campanella, 1983). However, the parameters q_c and f_s , and therefore R_f , are strongly influenced by soil layering. These effects are discussed and quantified in Chapters 5, 6 and 7.

4

Performance of Liquefaction Prediction Models

4.1 INTRODUCTION

A primary motivation for investigation of the Loma Prieta liquefaction sites was to obtain data which could be used to test various liquefaction prediction models. The objective of such models is to identify sites which are susceptible to liquefaction in probable, future earthquakes, so that countermeasures can be taken to alleviate liquefaction damage. In this Chapter, the performance of five liquefaction prediction models is assessed using the Loma Prieta CPTU data.

4.2 LIQUEFACTION PREDICTION MODELS

Liquefaction prediction models may be classed as either deterministic or probabilistic. Deterministic models estimate the soil liquefaction potential at a site, for a given seismic event, by calculating a critical value of either SPT N or CPT q_c with depth. The soil is deemed likely to liquefy at depths where the measured blowcount N or cone resistance q_c is less than the critical value. By contrast, probabilistic liquefaction models estimate the probability of occurrence of liquefaction at a site for a given seismic event.

Several prediction models have been developed in recent years, ranging from purely empirical to highly analytical. Models may be categorised as either source models, which estimate site response to earthquake shaking using a combination of earthquake magnitude and an appropriate attenuation model, or site models, which use the maximum horizontal acceleration a_{\max} recorded

at a site to estimate site response. The more subjective measure of earthquake intensity may be employed as a predictor of site response, although its resolution is poor in comparison with magnitude and a_{\max} .

The estimated site response information for a given seismic event is then combined with various site parameters, such as depth to water table, mean grain size (D_{50}) and effective overburden stress, to calculate a critical value of N or q_c with depth for the site. Implicit in this calculation is a comparison between the characteristics of the source and site in question, and a catalogue of field data (N or q_c) collected from sites of liquefaction and non-liquefaction during historic earthquakes.

Traditionally, the SPT has been the *in situ* testing tool used to determine soil strength, thus many early liquefaction prediction models were expressed in terms of SPT blowcount. In order to use these early models alongside more recent prediction methods in which CPT cone resistance is used to measure soil strength, an expression relating N and q_c is required. This may be achieved by making use of the following approximate relationship

$$\frac{q_c}{N} = 4 \text{ bars} = 0.4 \text{ MPa} \quad (4.1)$$

This simple expression was first suggested by Meyerhof (1956), and is still widely used. However, a study conducted by Robertson and Campanella (1985) shows that the ratio of q_c to N is not constant but increases with mean grain size D_{50} , from a value of 1 for $D_{50} = 0.001$ mm to a value of 8 for $D_{50} = 10$ mm. In addition, Figure 4.1 shows the high

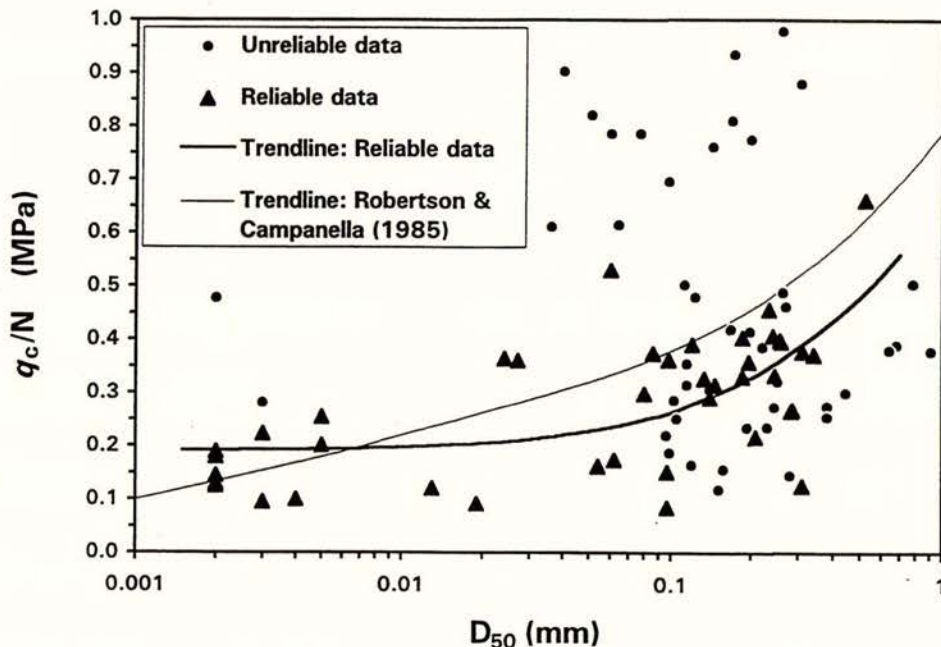


Figure 4.1 Relationship between q_c/N and D_{50} for Loma Prieta liquefaction sites

level of scatter in the q_c/N correlation results for the Loma Prieta data. From a total of 88 possible data points (refer Appendix A), only 42 were considered reliable. The 46 unreliable data points were considered questionable, primarily because of the effects of layering on the measured value of q_c at the same depth as the adjacent SPT. The way in which soil layering affects measured cone resistance will be discussed in detail in the following Chapters. The average q_c/N ratio for the reliable data set was calculated to be 0.4 MPa. Although the trendline for the reliable data points shown in Figure 4.1 underestimates the trendline predicted by Robertson and Campanella (1985), the curves exhibit the same overall behaviour.

Although some D_{50} values were recorded during the California work, for most of the CPTU records reliable, detailed mean-grain-size information is unavailable and therefore the average conversion value of $q_c/N = 0.4$ MPa has been chosen for this study. Unfortunately, this approximation may introduce large uncertainties into the three prediction methods that require the conversion of N to q_c .

Five liquefaction prediction models have been chosen for investigation using the Loma Prieta CPTU data, including two models based on cyclic stress ratio, two energy based methods, and one purely empirical model. Each of the five models is outlined below.

4.2.1 Davis and Berrill

Davis and Berrill (1982) developed an energy-based model for estimating site liquefaction potential. Their model is based on the hypothesis of Nemat-Nasser and Shokoh (1979) that pore pressure increase at a site is directly related to the amount of seismic energy dissipated in the soil. Geometric attenuation of ground shaking is incorporated into their model. The model empirically relates the SPT N value (corrected to an overburden pressure of 100 kPa) with the site pore pressure increase through the following formula

$$\Delta u = \frac{450 \cdot 10^{1.5M}}{r^2 \bar{N}^2 \sqrt{\sigma_0'}} \quad (4.2)$$

Here Δu is site pore pressure increase (kPa), M earthquake magnitude, r epicentral distance (metres), \bar{N} corrected SPT N value, and σ_0' initial effective overburden stress (kPa). Peck *et al.* (1974) give the following relation for calculating \bar{N} from N

$$\bar{N} = 0.77 \log_{10} \left(\frac{2000}{\sigma_0'} \right) N \quad (4.3)$$

Alternative procedures exist for converting N to \bar{N} , as discussed by Liao and Whitman (1986). The relationship given in equation (4.3) is favoured in this instance since it was used in the

original development of the Davis and Berrill model. Generally, the upper limit for C_N is taken as 2, where $\bar{N} = C_N N$.

By definition, the condition of liquefaction is deemed to occur when $\Delta u = \sigma_0'$. A critical value for N is obtained, therefore, by substituting this expression into equation (4.2) and reversing the correction of equation (4.3). Critical N may be converted to q_c using equation (4.1). The final expression for calculating a critical value of q_c (MPa) from the Davis and Berrill model is given by

$$(q_c)_{\text{critical}} = \frac{0.4}{0.77} \frac{\sqrt{450 \cdot 10^{1.5M}}}{r^2 (\sigma_0')^{1.5}} \left[\log_{10} \left(\frac{2000}{\sigma_0'} \right) \right]^{-1} \quad (4.4)$$

where r is measured in metres and σ_0' in kPa. The prediction curve calculated from this model is labelled as "D&B" (refer Appendix A).

4.2.2 Seed *et al.*

Seed and Idriss (1971) originally proposed using the cyclic stress ratio ($\text{CSR} = \tau/\sigma_0'$) as a measure of earthquake intensity at a given site. The CSR has most recently been defined by Seed *et al.* (1985) as

$$\frac{\tau}{\sigma_0'} = 0.65 \frac{a_{\text{max}}}{g} \frac{\sigma_0}{\sigma_0'} \frac{r_d}{r_M} \quad (4.5)$$

where a_{max} is peak ground-surface acceleration at the site; σ_0 and σ_0' are total and effective overburden pressures respectively, at depth under consideration; r_M is a magnitude normalisation factor to convert CSR for a given magnitude M to CSR for an equivalent magnitude $M = 7.5$ earthquake; and r_d is a stress reduction factor allowing for flexible rather than rigid behaviour of the overlying soil, proposed by Iwasaki *et al.* (1978) as

$$r_d = (1 - 0.015z) \quad (4.6)$$

where z is depth below ground surface in metres. A magnitude normalisation factor of $r_{M=7.1} = 1.1$ was calculated by interpolation for this study, using the correction factors listed in Table 4 of Seed *et al.* (1985).

By examining the database of historical earthquakes, Seed (1979) and co-workers determined the level of CSR required to cause liquefaction as a function of earthquake magnitude and standard penetration resistance. The relationship between CSR and $(N_1)_{60}$ for a magnitude $M_s = 7.1$ earthquake at a site with low fines content (less than five per cent) is shown in Figure 4.2. The position of this curve has been estimated using the original and revised curves

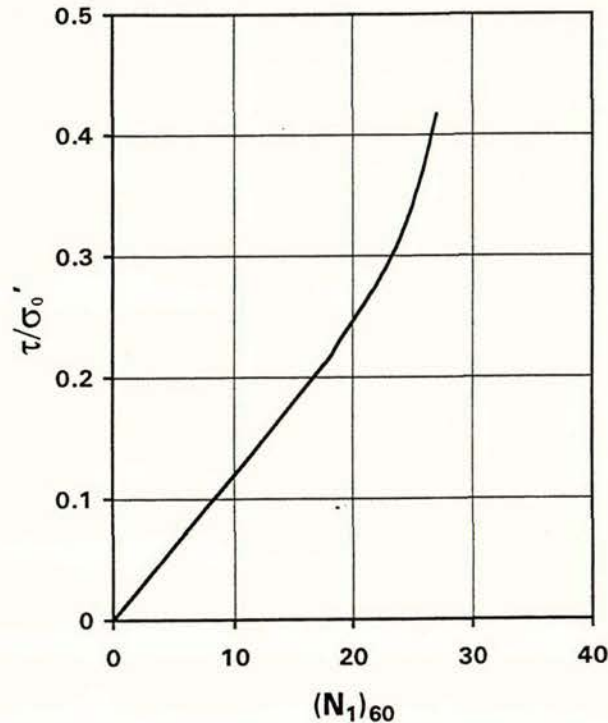


Figure 4.2 Estimated relationship between CSR causing liquefaction and corrected SPT N for magnitude $M_s = 7.1$ earthquake (fines content $\leq 5\%$)

of Seed (1979) and Seed *et al.* (1985), respectively. In addition to an overburden stress correction to 1 ton per square foot (approximately 100 kPa), the SPT N has been corrected to a hammer energy efficiency of 60 per cent. Kovacs *et al.* (1984) estimate the average energy efficiency of hammers used in the United States to be 55 per cent. Thus, it is possible that the curve in Figure 4.2 underestimates values for critical N_1 by approximately 10 per cent on the average. Although this could result in an unconservative calculation of critical cone resistance, no adjustments for energy efficiency have been made in this analysis. The hammer efficiency of the USGS SPT rig used in this investigation has been calculated to be 68 per cent (Douglas and Strutynsky, 1984).

Figure 4.2 shows that for SPT \bar{N} values of less than approximately 18, a linear relationship exists between \bar{N} and CSR such that $\tau/\sigma_0' = 0.01194(N_1)_{60}$. This compares favourably with an expression relating \bar{N} , M and CSR given by Davis and Berrill (1983). For values of \bar{N} between 18 and 27, the CSR is closely approximated by the fourth-order polynomial in $(N_1)_{60}$, given in equation (4.7)

$$\frac{\tau}{\sigma_0'} = A(N_1)_{60}^4 + B(N_1)_{60}^3 + C(N_1)_{60}^2 + D(N_1)_{60} + E \quad (4.7)$$

where the constants A through E are given by: $A = 1.452 \cdot 10^{-5}$; $B = -1.061 \cdot 10^{-3}$; $C = 0.02877$; $D = -0.3272$; and $E = 1.448$.

The CSR may be calculated with depth for a given site using equation (4.5); critical values for $(N_1)_{60}$ are obtained using the simple linear expression given above. If this linear expression returns a value for $(N_1)_{60}$ greater than 18, equation (4.7) can be solved numerically for the unique value of critical $(N_1)_{60}$ corresponding to the given CSR at depth z .

Liao and Whitman (1986) give the following relationship for correcting N to N_1 (or \bar{N}) which closely approximates Seed's correction curve for overburden pressure

$$\bar{N} = C_N N = \sqrt{\frac{100}{\sigma_0'}} N \quad (4.8)$$

where σ_0' is measured in kPa. Thus, a critical value of q_c (MPa) may be calculated from the liquefaction susceptibility analysis of Seed *et al.* using

$$(q_c)_{\text{critical}} = 0.4 \sqrt{\frac{\sigma_0'}{100}} (N_1)_{60} \quad (4.9)$$

Here σ_0' is measured in kPa, and critical $(N_1)_{60}$ is calculated at the same depth z (metres) either from the simple expression $\tau/\sigma_0' = 0.01194(N_1)_{60}$ for $(N_1)_{60} \leq 18$, or from equation (4.7) for $18 < (N_1)_{60} < 27$; the CSR at depth z is given by equation (4.5). The prediction curve calculated from this model is labelled as "SEED" (refer Appendix A).

4.2.3 Shibata and Teparaksa

A liquefaction prediction method similar to that proposed by Seed and co-workers has been developed by Shibata and Teparaksa (1988). Their method is based on a cyclic stress ratio which incorporates earthquake magnitude in the following way

$$\left(\frac{\tau}{\sigma_0'}\right)_{S\&T} = 0.1(M-1) \frac{a_{\text{max}}}{g} \frac{\sigma_0}{\sigma_0'} (1-0.015z) \quad (4.10)$$

Data from sites of liquefaction and non-liquefaction from five earthquakes were used to develop an expression relating critical normalised cone resistance $(q_{c1})_{\text{crit}}$ with CSR and median grain size D_{50} (mm)

$$(q_{c1})_{\text{crit}} = \frac{D_{50}}{0.25} \left[5 + 20 \left(\frac{\left(\frac{\tau}{\sigma_0'}\right)_{S\&T} - 0.1}{\left(\frac{\tau}{\sigma_0'}\right)_{S\&T} + 0.1} \right) \right] \quad (4.11)$$

Shibata and Teparaksa found that the critical cone resistance of fine-grained soils with $D_{50} < 0.25$ mm decreases as grain size decreases, whereas clean sands with $D_{50} \geq 0.25$ mm are independent of D_{50} . Thus, an upper bound of 0.25 mm exists for D_{50} in their model. It is obvious from equation (4.11) that the parameter D_{50} will have a strong influence on the calculation of critical cone resistance.

Raw cone resistance is normalised to a standard overburden pressure of 100 kPa by the following equation (σ_0' in kPa), proposed by Tokimatsu and Yoshimi (1983)

$$q_{c1} = q_c \left(\frac{170}{\sigma_0' + 70} \right) \quad (4.12)$$

Thus, the final expression for critical cone resistance q_c (MPa) using the Shibata and Teparaksa model is given by

$$(q_c)_{\text{critical}} = \frac{D_{50}}{0.25} \left(\frac{\sigma_0' + 70}{170} \right) \left[5 + 20 \left(\frac{0.1(M-1) \frac{a_{\text{max}}}{g} \frac{\sigma_0}{\sigma_0'} (1-0.015z) - 0.1}{0.1(M-1) \frac{a_{\text{max}}}{g} \frac{\sigma_0}{\sigma_0'} (1-0.015z) + 0.1} \right) \right] \quad (4.13)$$

where D_{50} is measured in mm, z in metres, and the stresses σ_0' (effective) and σ_0 (total) in kPa. The prediction curve calculated from this model is labelled as "S&T" (refer Appendix A).

4.2.4 Zhou

An empirical model based on liquefaction observed during the Tangshan, China, earthquake of 1976 has been developed by Zhou (1980). The model uses a discriminant analysis to separate 94 sites of liquefaction from 31 sites of non-liquefaction. The procedure developed was checked using data from the 1975 Haicheng earthquake.

Critical cone resistance q_c (kgf/cm²) at a given site is expressed as an empirical function of depth to water table H_w (metres), thickness of overlying cohesive layer H_0 (metres), and critical penetration resistance $q_{co}(I)$ (kgf/cm²) for a given design intensity I

$$(q_c)_{\text{critical}} = q_{co}(I) (1 - 0.065[H_w - 2])(1 - 0.05[H_0 - 2]) \quad (4.14)$$

The original formulation of the model, which incorporated epicentral distance in the calculation of q_{co} , was altered to produce a model consistent with the Chinese Building Code, which expresses design loads in terms of the intensity scale of China. Zhou replaced his original expression with a table of values for q_{co} depending on intensity, determined from average distances to the Tangshan isoseismals. These values are given in Table 4.1 below.

Intensity I	7	8	9	10
Critical Cone Resistance $q_{co}(I)$ (kgf/cm ²)	46.7	116.6	176.9	221.7

Table 4.1 Critical cone resistance as a function of intensity for Zhou's model

It is implicit in Zhou's paper that raw values of q_c are used. Making use of the conversion from kgf/cm² to MPa, the critical value of cone resistance q_c (MPa) from Zhou's model is given by

$$(q_c)_{\text{critical}} = 0.0981 q_{co}(I) (1 - 0.065 [H_w - 2]) (1 - 0.05 [H_0 - 2]) \quad (4.15)$$

where H_w and H_0 are both measured in metres. The prediction curve calculated from this model is labelled as "ZHOU" (refer Appendix A).

4.2.5 Liao, Veneziano and Whitman

Four statistical models based on binary regression have been developed by Liao *et al.* (1988) to express the probability of liquefaction at a given site as a function of earthquake load, and soil resistance as given by corrected-normalised SPT $(N_1)_{60}$. A catalogue comprising 278 cases of liquefaction and non-liquefaction during earthquakes was compiled to obtain the necessary results. Two of these four models employ the cyclic stress ratio as defined by Seed and Idriss (1971); the other two use explicit functions of earthquake magnitude and distance as loading parameters. One of these latter two models has been chosen for investigation in this study.

Liao and co-workers define the conditional probability of liquefaction P_L as

$$P_L = \frac{1}{1 + e^{-Q_L}} \quad (4.16)$$

Q_L , the logit transformation of P_L , is assumed to depend linearly on $X = [X_1, X_2, \dots, X_m]^T$, the vector of explanatory variables which includes ground motion and soil deposit characteristics. A linear logistic model results from this assumption, so that

$$Q_L = \beta_0 + \beta_1 X_1 + \dots + \beta_m X_m \quad (4.17)$$

where the parameters $\beta_0, \beta_1, \dots, \beta_m$ are estimated from the data. For the source model of interest, Liao *et al.* define $X = [\ln \Lambda_{EP}, (N_1)_{60}]^T$, where Λ_{EP} is an earthquake-load function similar to that proposed by Davis and Berrill (1982)

$$\Lambda_{EP} = \frac{10^{1.5M}}{(R_{EP})^2 (\sigma_0')^{1.5}} \quad (4.18)$$

Here M is earthquake magnitude, σ_0' is effective overburden stress (kgf/cm²) and R_{EP} epicentral distance (km). The resulting fitted logistic equation is given by

$$Q_L = -12.922 + 0.87213 \ln(\Lambda_{EP}) - 0.21056 (N_1)_{60} \quad (4.19)$$

The corrected SPT $(N_1)_{60}$ may be reduced to raw N by reversing the overburden stress correction procedure proposed by Liao and Whitman (1986) in equation (4.8). To determine a critical value of cone resistance from this analysis, the probability of liquefaction P_L must be set equal to 0.5, equivalent to setting $Q_L = 0$ in equation (4.19). By employing the conversion from N to q_c given by equation (4.1), the following expression for critical q_c (MPa) is obtained from the Liao, Whitman and Veneziano model

$$(q_c)_{\text{critical}} = \frac{0.4 \sqrt{\sigma_0'}}{2.1056} \left[0.87213 \ln \left(\frac{10^{1.5M}}{(R_{EP})^2 (0.0102 \sigma_0')^{1.5}} \right) - 12.922 \right] \quad (4.20)$$

where R_{EP} is measured in km and σ_0' in kPa. The prediction curve calculated from this model is labelled as "LV&W" (refer Appendix A).

4.3 MODEL PERFORMANCE

Critical cone resistances given in equations (4.4), (4.9), (4.13), (4.15) and (4.20) for the five liquefaction prediction models outlined above have been plotted over raw cone resistance q_c for each of the 35 tests (refer Appendix A). In addition, a classification bar labelled "R&C" has been included on each plot, indicating whether or not the (q_c, R_f) coordinate falls within the zone of liquefiable soils proposed in Figure 8 of Robertson and Campanella (1985). Hatched regions within the bar indicate soils which are not susceptible to liquefaction. As an example, the prediction curves for the five liquefaction models along with Robertson and Campanella's classification are shown for Tests 23 and 32 in Figure 4.3.

Table 4.2 shows the prediction results for each of the 35 probes. Each test has been classified as liquefied, non-liquefied or marginal, on the basis of field observations. As mentioned in

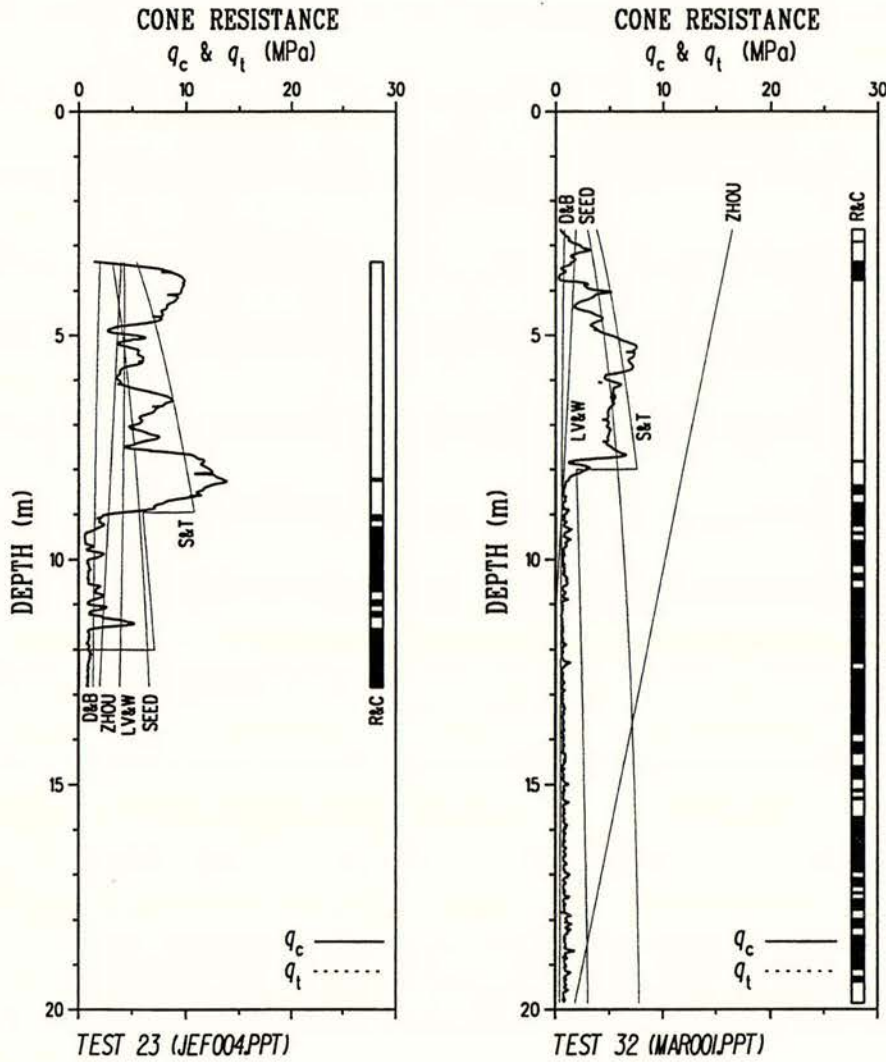


Figure 4.3 Critical cone resistance for five liquefaction prediction models and Robertson and Campanella’s classification (hatched areas non-liquefiable) (a) Test 23 (b) Test 32

Chapter 2, probes were conducted at each liquefaction site within and outside of the region of failure. The failure region was defined by the presence of either ejected sandy soils, or ground cracking and associated lateral spreading, or surface settlements, or a combination of these indicators. In some instances, probes were conducted at what appeared to be the edge of the failure region, in the transition zone separating obviously liquefied soils from seemingly non-liquefied soils. Probes conducted in regions of liquefaction are classified as "Y" in column three of Table 4.2, whereas probes in non-liquefied regions classify as "N", and those in the marginal transition zone classify as "M".

SITE	TEST No.	Liquefaction Observed	Liquefaction Predicted				
			D&B	SEED	S&T	ZHOU	LV&W
Moss Landing	1	N	M	M	Y	M	M
	2	N	M	M	Y	M	M
	3	Y	M	Y	Y	Y	Y
Pajaro Dunes	4	Y	M	Y	Y	M	Y
	5	N	N	M	M	N	M
Millers Farm	6	Y	Y	Y	Y	Y	Y
	7	N	M	Y	M	Y	Y
	8	N	M	Y	Y	Y	Y
	9	N	N	Y	Y	Y	Y
	10	Y	N	Y	Y	Y	Y
	11	Y	M	Y	Y	Y	Y
	13	Y	Y	Y	Y	Y	Y
14	M	M	Y	Y	Y	Y	
Airport Watsonville	12	N	Y	Y	Y	Y	Y
	15	Y	Y	Y	Y	Y	Y
	16	Y	Y	Y	Y	Y	Y
	17	M	Y	Y	Y	Y	Y
Jefferson	18	Y	Y	Y	Y	Y	Y
	19	Y	M	Y	Y	Y	Y
	22	M	N	Y	Y	Y	M
	23	N	N	Y	Y	M	Y
Scattini	20	Y	M	Y	Y	Y	Y
	21	N	Y	Y	Y	Y	Y
Sea Mist	24	Y	Y	Y	Y	Y	Y
	25	N	N	Y	N	M	M
Leonardini	26	Y	Y	Y	Y	Y	Y
	27	N	Y	Y	Y	Y	Y
Southern Pacific Railroad Bridge	28	M	M	Y	Y	Y	Y
	29	M	N	Y	Y	Y	Y
	30	N	Y	Y	Y	Y	Y
	31	M	Y	Y	Y	Y	Y
	34	Y	M	Y	Y	Y	Y
35	Y	M	Y	Y	Y	Y	
Marina	32	Y	N	Y	Y	Y	M
	33	M	M	Y	Y	Y	Y

Table 4.2 Summary of results for liquefaction prediction model performance
(Y = Yes, N = No, M = Marginal)

The predictions of each model for every probe are listed under the five columns labelled D&B, SEED, S&T, ZHOU and LV&W. At a given depth in the soil column below the water table, a model is ruled to have predicted liquefaction if the critical cone resistance exceeds the measured resistance *and* the soil at that depth classifies as liquefiable based on the R&C classification. Instances where liquefaction is clearly predicted are indicated by "Y" on Table 4.2, whereas instances of non-liquefaction are indicated by "N". For cases where the critical resistance exceeds the measured resistance by only a few per cent for a single, short section of the q_c record (less than 0.25 metres), the result is indicated as "M", provided the soil is deemed liquefiable by the R&C classification.

Using the results shown in Table 4.2, the accuracy of each prediction model may be assessed. To achieve this, it is useful to define the following simple scoring system

$$S = \frac{an_a + bn_b + cn_c}{35a} \quad (4.21)$$

where S is the resulting score, expressed as a percentage. Here n_a is the number of correct responses, comprising the following pairs of **observed/predicted** response: Y/Y, M/M, and N/N. Similarly, n_c is the number of incorrect responses, given by the combinations Y/N and N/Y. Lastly, n_b is the number of intermediate responses recorded by a given model, comprising the remaining possible combinations of Y/M, M/Y, M/N, and N/M. Note that $n_a + n_b + n_c = 35$. The parameters a , b and c are arbitrary "value" parameters. Naturally, correct responses are worth the most, and incorrect responses are worthless, so that $a > b > c = 0$. The performance of each model may be assessed by determining n_a and n_b from Table 4.2, and substituting various ratios of $b:a$ into equation (4.21). Table 4.3 shows

Ratio $b:a$	Score S (%)				
	D&B	SEED	S&T	ZHOU	LV&W
0	40.0	45.7	48.6	45.7	45.7
0.25	50.7	52.9	55.0	54.3	53.6
0.50	61.4	60.0	61.4	62.9	61.4
0.75	72.1	67.1	67.9	71.4	69.3
$n_a:n_b:n_c$	14:15:6	16:10:9	17:9:9	16:12:7	16:11:8

Table 4.3 Scores for prediction models for various ratios of $b:a$

the results of this analysis. If only correct responses are taken into account, then the S&T model scores highest at 48.6 per cent. Out of the 35 probes, the S&T model made 17 correct predictions, followed by the models of ZHOU, LV&W and SEED, each of which made 16 correct predictions. The D&B model made 14 correct predictions. However, the S&T model also made the greatest number of incorrect predictions along with the SEED model. As shown in the last row of Table 4.3, the S&T and SEED models made nine incorrect predictions out of 35, whereas the D&B model made only six.

It should be noted at this point that the data set used to test the models is small and biased. The 35 tests comprise 16 at which liquefaction occurred, 7 which were marginal, and 12 at which no evidence of liquefaction was found. Thus, a highly conservative model predicting liquefaction at every test would achieve a score of 45.7 per cent (16/35), whereas a highly unconservative model predicting no liquefaction at every test would score 34.3 per cent (12/35).

Let us now examine the effect of adding value to the intermediate prediction responses, those which are close to the observed response. When the $b:a$ ratio is increased to a value of 0.25, the S&T and D&B models still perform best and worst, scoring at 55.0 per cent and 50.7 per cent respectively. Increasing the $b:a$ ratio again to a value of 0.5 results in ZHOU and SEED performing best and worst, scoring at 62.9 per cent and 60.0 per cent respectively. A further increase in the $b:a$ ratio to a value of 0.75 results in the D&B model out-performing the other models, scoring 72.1 per cent. For $b:a = 0.75$, the models rank from best to worst as D&B, ZHOU, LV&W, S&T, SEED. Clearly, adding value to marginal predictions affects the relative performance of the models. However, it appears the models consistently score within a few per cent of each other for any $b:a$ ratio. Based on this scoring system, no single model clearly out-performs the others for this data set.

Another important factor in rating the performance of each model is the amount of variation in the predicted response. Table 4.4 below shows a comparison between the number of responses recorded of a given type against the number of responses observed of that type.

Response Type	Number Observed	Number Predicted				
		D&B	SEED	S&T	ZHOU	LV&W
Y	16	13	32	32	29	29
M	7	14	3	2	5	6
N	12	8	0	1	1	0

Table 4.4 Variation in model prediction response

As can be seen from Table 4.4, all of the models except the D&B model are highly conservative and show little variation in their response. The two models based on cyclic stress ratio, SEED and S&T, recorded a 91.4 per cent "Y" response; the SEED model did not register a "N" response. Similarly, the ZHOU and LV&W models recorded a 82.9 per cent "Y" response, with one and nil "N" responses respectively. In contrast, the D&B model recorded a 37.1 per cent "Y" response and a 22.9 per cent "N" response. This suggests the D&B model is more sensitive for this data set than the other more conservative models.

Although the SEED and S&T models scored 100 per cent for predicting liquefaction at the 16 tests which did liquefy, they both scored approximately 20 per cent for predicting no liquefaction at the 12 tests at which no liquefaction was observed (for $b:a = 0.75$). In contrast, the D&B model scored almost 80 per cent at the liquefied tests and approximately 60 per cent at the non-liquefied tests, almost twice the score of closest model, the ZHOU model.

The scoring system and variation analysis discussed above rely heavily on the accuracy of the site classification as "Y", "M" or "N". As discussed earlier, this categorisation is based on post-earthquake field observations. While the presence of sand boils is incontrovertible evidence of liquefaction, the converse, however, is not true. The absence of sand boils does not necessarily denote that liquefaction has not taken place. Thus, some uncertainty exists for tests which classify as "N".

As an example, consider the prediction results presented in Table 4.2 for the Leonardini site. The five models correctly predict liquefaction at Test 26. However, each model also predicts liquefaction at Test 27, the probe conducted outside the apparent zone of lateral spreading (refer Figure 2.9). By comparing the ejecta D_{50} (refer Appendix A) with the D_{50} of samples retrieved during SPT investigations, it appears the soil liquefied below the water table at 1.46 metres to a depth of 4 to 5 metres. By comparing the CPTU results for Tests 26 and 27, we find the soil conditions for the two tests appear to be almost identical between these depths (refer Appendix A). It is possible, therefore, that the soil at Test 27 did liquefy during the Loma Prieta event, only no evidence of this liquefaction migrated to the ground surface. If so, this would affect all of the attempts made above to estimate the relative performance of each prediction model. Although the absence of surface manifestations of liquefaction may not be a particularly reliable indicator of a non-liquefied site, there are, unfortunately, few other indicators available.

The above analysis indicates the S&T model performs best overall when considering correct responses only. If intermediate responses are assigned a relatively high level of value, then the D&B and ZHOU models out-perform the others. However, the difference in performance between the various models is less than 10 per cent, for all levels of value assigned to intermediate or close predictions. The D&B model appears to be the most sensitive, showing

the largest variation in response. Although the SEED and S&T models scored only slightly less than the D&B model for values of $b:a > 0.5$, these two models are conservative in their responses for this data set. Their conservative performance may be attributed in part to the strong influence of certain parameters. Factors affecting the performance of each model are discussed in the following section. Overall, the D&B model appears to have performed better than the other models for this data set, followed closely by the ZHOU model.

4.4 PARAMETER INFLUENCE AND SOURCES OF ERROR

The uncertainty inherent in the q_c/N correlation presented at the beginning of this Chapter will limit the accuracy of the D&B, SEED and LV&W critical q_c predictions. Figure 4.4 illustrates the amount of variation in critical cone resistance predicted by each of these models for values of q_c/N equal to 0.3 MPa and 0.5 MPa. The model of SEED is most drastically affected, followed in order by the models of LV&W and D&B. As discussed earlier, this ratio increases with increasing mean grain size D_{50} . Thus, the use of a constant, average value for this correlation at fluviually deposited sites is questionable.

There are several other factors which contribute to the uncertainty of the q_c/N ratio. Generally, sites with low N values ($N < 10$) are of interest for the assessment of liquefaction potential. Unfortunately, the reliability of low N values is questionable. Due to the discrete nature of the blowcount measurement, an error of one blowcount in a low N value will have a proportionally

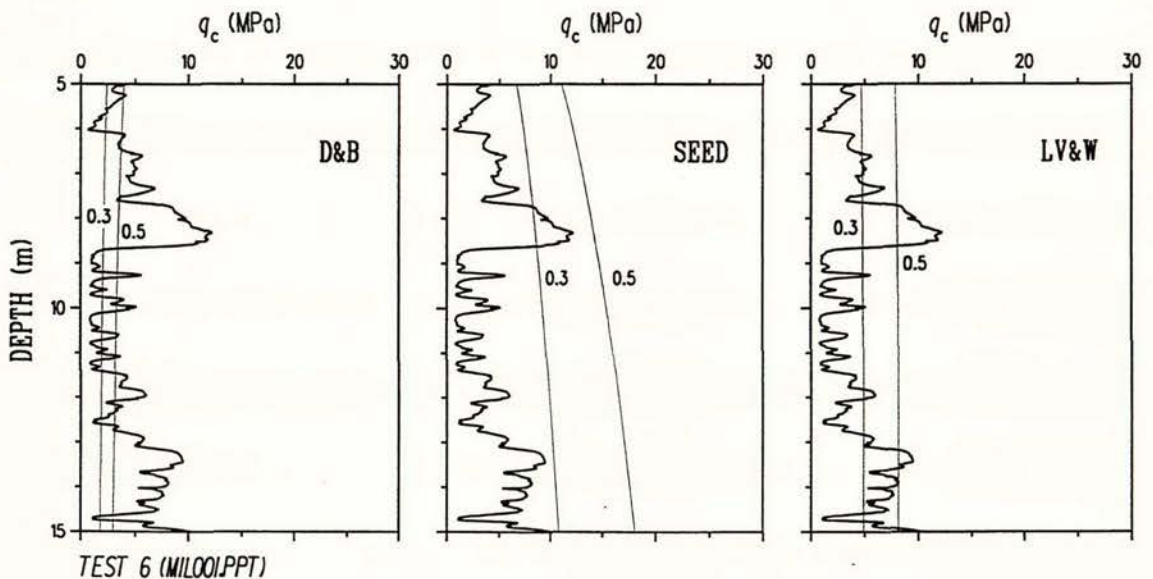


Figure 4.4 Influence of q_c/N ratio on predicted critical q_c for D&B, SEED and LV&W

greater effect on the calculated q_c/N ratio than an error in a high N value. In addition, if boiling occurs in the soil at the base of the hole during an SPT, the measured blowcount may be less than the true value of N for that material, resulting in an overestimation of the q_c/N ratio. Layering effects must also be taken into consideration for both the SPT and the CPT. Measured values of N and q_c tend to be underestimated in stiff layers wedged between softer materials (an effect more pronounced for the SPT since generally the sampler is of greater diameter than the CPT cone). The q_c/N ratio calculated in such situations is unreliable. Finally, it is not uncommon for adjacent CPTU probes conducted at fluvial sites to record quite different responses in q_c . Thus, although an SPT and CPTU may be performed at the same site, the q_c/N ratios calculated with depth may vary markedly if the tests are repeated within only 1.5 metres of the original holes (for example, refer Tests 1 and 2, Appendix A). The significant influence of this uncertain correlation on the calculation of critical cone resistance, as shown in Figure 4.4, indicates that it should be used with caution. As the catalogue of CPTU liquefaction case history data increases, it may be possible to recast some of the above liquefaction methods in terms of cone resistance, and avoid using the q_c/N correlation.

Four of the five models in their final form as presented in this study employ earthquake magnitude to determine liquefaction potential. In general, the calculation of magnitude for recent historical earthquakes is reasonably accurate. However, a possible source of confusion exists regarding what type of magnitude to use, as several types exist. The D&B, S&T and LV&W models all specify Surface Wave Magnitude M_S , thus a value of $M_S = 7.1$ has been used in this study. However, when using the above models to calculate critical cone resistance for large earthquakes it may be more appropriate to use the recently developed Moment Magnitude M_W , due to the saturation of the M_S scale at around $M_S = 7.5$.

A fundamental difference between the cyclic stress ratio models, SEED and S&T, and the other three models, is that the stress ratio models are two-step models. Under normal predictive circumstances, independent estimation of peak ground acceleration is required before the SEED and S&T models may be evaluated. This is usually accomplished by employing an appropriate attenuation relationship. However, this introduces a further empirical step to the prediction procedure, with additional uncertainties. Because of the unfortunate absence of strong ground motion accelerographs in the Monterey Bay region at the time of the Loma Prieta earthquake, an attenuation relationship was required to estimate the maximum horizontal ground accelerations for the southern nine sites. The deduced values are recorded in Table 2.1 of Chapter 2. It is probable that these values over-estimate the true ground accelerations for the Miller's Farm and SPR Bridge sites by approximately 30 per cent, based on the single measured value of $a_{max} = 0.390g$ recorded nearby at Watsonville (Benuska, 1990). Figure 4.5 shows the effect on the SEED and S&T models of reducing the site acceleration at the Miller's Farm site from the attenuation derived value of 0.528g to a value of 0.390g. Clearly the larger value of acceleration, if incorrect, is causing both models to predict conservative values of critical cone

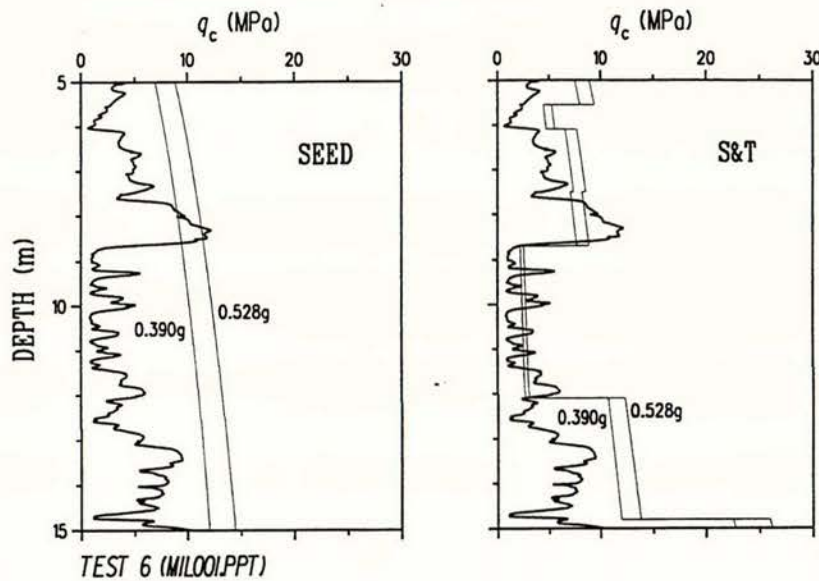


Figure 4.5 Influence of a_{\max} on predicted critical q_c for SEED and S&T

resistance, particularly the SEED model. The estimated accelerations for the remaining southern sites appear to be reasonable; however, no allowance is made in the attenuation model for site amplification effects which may have contributed to the liquefaction of these sites.

With the exception of the ZHOU model, all of the models require the calculation of the vertical stress distribution of the soil at the site. Unit weights of 18.9 and 20.4 kN/m^3 (120 and 130 lb/ft^3) have been assumed above and below the water table respectively (M.J. Bennett, USGS Menlo Park, California, personal communication). The water table depths, recorded on each test result plot in Appendix A, were measured at each site six months after the Loma Prieta event, and therefore may not be representative of the water table depth at the time of the earthquake due to seasonal variations. In spite of these assumptions, the effects of errors in the overburden stress calculations are small in comparison to the effects of the uncertainty in the parameters discussed thus far.

Although unable to cope with the site amplification and directivity effects which contributed to liquefaction at the distant Marina site, the D&B model is simple to use and has been found to perform well at large distances (Liao *et al.*, 1988). However, because few close sites ($r < 20000$ metres) were used in the development of the model, its predictive capability is compromised for near-source sites. Some uncertainty also exists regarding the most appropriate definition of the distance term, since the use of epicentral distance is clearly a serious

shortcoming at near-source sites. The D&B model consistently predicted a lower average value of critical resistance than all the others. The model unconservatively predicted no liquefaction at two tests at which liquefaction was observed, and marginal liquefaction at seven tests, all of which liquefied.

Like the D&B model, the LV&W model had difficulty predicting liquefaction at the Marina District site, 98 km from the epicentre. In fact, for this test the LV&W critical cone resistance reduced from a value of approximately 2 MPa immediately below the water table, to a value of zero at depth 11.425 metres for Test 32 (refer Figure 4.3(b)). Out of 35 probes, this was the only instance of a model predicting a finite depth range for liquefaction at a site.

A potential strength of the S&T model is the inclusion of the mean grain size variable D_{50} , up to a value of 0.25 mm. However, it has a very strong influence as can be seen by the large jumps in the predicted critical resistance in Figure 4.3. The model calculates a reduced value of critical resistance for fine soils. The rationale for decreased liquefaction susceptibility for soils of fine grain size is probably based on the expectation that the presence of cohesive fines will increase the resistance of soil to liquefaction. However, it is possible that an increase in fines may aid the liquefaction process by lowering the permeability of the soil, thereby reducing drainage. In addition, the relationship is unlikely to be linearly proportional, as the penetration pore pressures recorded in California indicate that materials with D_{50} less than about 0.090 mm were strongly dilatant, whereas those with D_{50} greater than about 0.120 mm were well drained. On average, only six D_{50} values were obtained at each test from samples taken from adjacent boreholes. Thus, estimation of D_{50} posed a problem for many critical soil layers, particularly at fluvial sites with highly variable soil profiles such as the Airport Watsonville site. In many cases, values were taken from adjacent layers with similar q_c and R_f values; often clearly variable strata were assumed to have a constant D_{50} equal to the average of nearby values. For tests where no immediate D_{50} data was available, estimates were made based on the grain size profile of adjacent tests. Although the S&T model is CPT based, the inclusion of D_{50} requires drilling and sampling at the site, thus negating much of the advantage of the CPT. It may be possible to infer D_{50} from CPTU measurements, or reformulate the model directly in terms of a critical q_c value for a given friction ratio.

In employing the ZHOU model, the Chinese intensity scale and the Modified Mercalli scale are assumed to be similar. Zhou (1980) states that intensities of 7, 8 and 9 correspond to accelerations of 0.1, 0.2 and 0.4g respectively. These are identical to the intensity-acceleration relations of the Soviet MSK scale, which corresponds closely to the Modified Mercalli scale. Some uncertainty exists in the correct application of the ZHOU model. It is formulated for the simple stratigraphy of a cohesive layer of thickness H_0 overlying a sand layer that may be susceptible to liquefaction. The problem of applying the model to sites with more complex stratigraphy is not addressed by Zhou. The presence of a cohesive material will undoubtedly

influence drainage conditions and the formation of sand boils. However, it is likely that the principal effect of the variable H_0 is to measure overburden pressure. Thus, to produce a continuous plot of critical cone resistance, H_0 was set equal to depth, z . This approach is supported by the similarity between Zhou's B_2 coefficient (the term depending on H_0) and the overburden pressure term of the D&B model. The ZHOU model is purely empirical, and therefore suffers less from model rigidity than does the D&B model, especially in its distance term. The use of intensity neatly solves the problem of measuring distance from a finite source. However, the large jumps evident in critical cone resistance across isoseismals gives away much of this advantage. The critical resistance predicted by the ZHOU model in Figure 4.3(a) for the $I = 7$ Jefferson site is markedly less than that predicted in Figure 4.3(b) for the $I = 9$ Marina District site. Thus, an obvious improvement would be to admit the use of a continuous intensity measure. The ZHOU model correctly predicts a decrease in liquefaction potential as the depth to water table increases. However, this effect is far outweighed by the discrete nature of the intensity measurement.

The ejecta D_{50} values for all sites ranged from about 0.05 to 0.6 mm, with an average of approximately 0.2 mm. Maps locating the tests relative to the positions and D_{50} values for sampled sand boils are provided in Appendix A. When compared with the soil stratigraphy deduced from SPT sampling and CPTU results, the above values suggest that at tests where liquefaction occurred, it developed either in the layer in which the water table was located, or in the layer immediately below the layer of the water table. This agrees with the findings of Florin and Ivanov (1961) who noted that, given uniform density, liquefaction begins at the top of a layer and propagates downwards. Two assumptions inherent in the comparison of ejecta and sample D_{50} values are (i) the origin of the ejecta is the liquefied material and (ii) there has been negligible contamination or entrainment of other materials during its passage to the ground surface. Generally, the ejected material could be traced back to a matching soil stratum within 4 metres below the water table. The ejecta D_{50} values suggest that liquefaction during the Loma Prieta event was shallow, and that no material below a depth of 10 metres liquefied. This is supported to some extent by the observation that the amounts of lateral spreading in the Loma Prieta earthquake were much less than those observed in the 1906 San Francisco earthquake, suggesting many sites just liquefied and no more.

A noticeable difference between the five models is the way in which critical cone resistance varies with depth. For the SEED and S&T models, critical q_c increases with depth; for the LV&W model, critical q_c initially increases slightly before slowly decreasing (although the behaviour of this model is sensitive to epicentral distance R_{EP}); for the D&B and ZHOU models critical q_c decreases with depth. Note that a model predicting a constant value for critical resistance by default predicts a decrease in liquefaction susceptibility with depth, due to the trend for cone resistance to increase with depth as average soil density increases. Even in cases where soil density remains constant with depth, the increase in pore pressure required to cause

deep liquefaction becomes prohibitive due to high overburden pressures. Thus, only the prediction models of D&B, ZHOU and LV&T reflect the natural tendency for soil liquefaction susceptibility to decrease with depth.

The behaviour of the SEED and S&T models contradicts both the field evidence of shallow liquefaction from this data set, and the experimental observations of Florin and Ivanov (1961). In addition, the trend of increasing critical q_c with depth appears counter-intuitive due to the inhibiting effects of increasing overburden stress. The SEED model in particular is governed by quite rigid assumptions regarding the way in which overburden stress and soil strength are included in the calculation of liquefaction susceptibility. To illustrate the variation with depth of liquefaction susceptibility as predicted by the SEED model, let us briefly examine the behaviour of the Cyclic Stress Ratio. Referring back to the depth dependent terms in equation (4.5), we see that the CSR is directly proportional to σ_0 and r_d , and is inversely proportional to σ_0' . If in reality liquefaction susceptibility decreases with depth, then, for a site with constant \bar{N} , the CSR should record a maximum value at the water table and decrease with greater depth. As shown in Figure 4.6, this is true for the SEED model if the water table is located at depth $z = 0$. However, if the water table is below the ground surface, then from Figure 4.6 we see that the maximum CSR occurs some distance below the water table, which

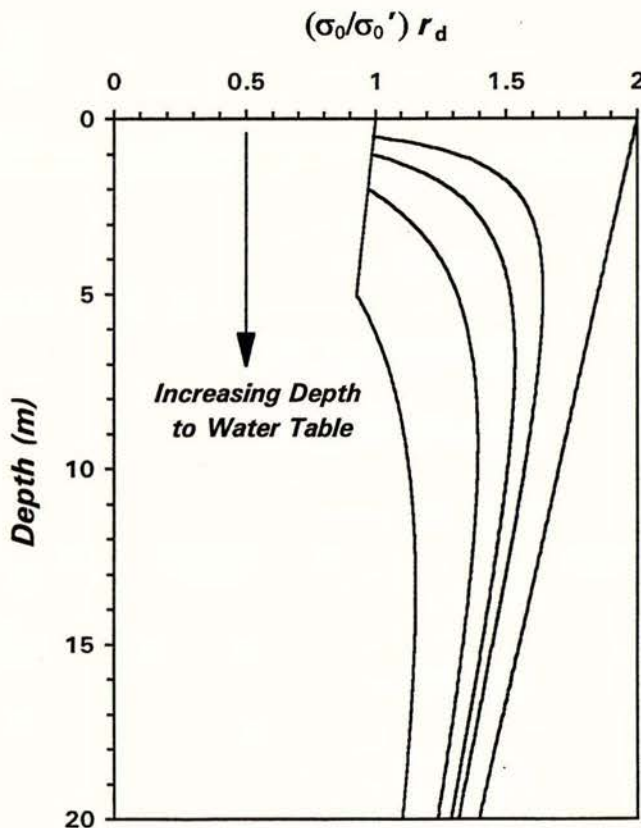


Figure 4.6 Behaviour of CSR depth-dependent terms with depth; water table located at 0, 0.5, 1, 2 and 5 metres (California unit weights assumed)

suggests that liquefaction would not initiate at the top of a uniform layer but at some considerable depth. For example, from Figure 4.6 we see that if the water table is located at a depth of one metre, the CSR function peaks at a depth of approximately seven metres, implying these deeper soils are more susceptible to liquefaction than the soils just below the water table. The inevitable conclusion is that if the CSR is used with no modifying factors, the SEED and S&T models will not predict decreasing liquefaction susceptibility with depth. This contradicts field and experimental observations, and the behaviour of the other models. Finally, the CSR may not be the most suitable parameter for liquefaction prediction analyses. For instance, Dobry *et al.* (1982) regard cyclic shear strain as the fundamental parameter controlling pore pressure increase during seismic loading as opposed to CSR.

4.5 SUMMARY

It is difficult to conclude from this short comparative study that one model is markedly superior to the others. Each has its strengths and weaknesses, which become apparent as one attempts to apply them. It appears the D&B model was the most sensitive, and in terms of prediction it performed the best. However, it was also the most unconservative model, and performed only marginally better than the purely empirical ZHOU model. The ZHOU and S&T models are particularly sensitive to the intensity I and mean grain size D_{50} parameters respectively. The performance of the SEED and S&T models was limited in part by their dependence on the empirical calculation of ground accelerations, which resulted in the prediction of highly conservative critical resistance values at some sites. In addition, the rigid form of both the SEED and S&T models causes these models to predict greater liquefaction susceptibility with depth; such behaviour contradicts experimental and field observations.

There is an obvious need for the development of a model which makes full use of all data retrieved from the CPTU. Such a model would avoid the uncertain q_c/N correlation and the need for drilling and sampling to determine D_{50} values. A preliminary attempt has been made to better exploit CPTU data by applying Pattern Recognition Theory to the problem of determining liquefaction potential (Dou and Berrill, 1993).

The California CPTU data set has been useful for assessing the relative performance of the five liquefaction prediction models. In the process, limitations of each model for predicting a reliable value of critical cone resistance have become apparent. The performance of each model has been assessed assuming the measured q_c is accurate. In many cases, however, measured q_c values are not reliable due to the influence of soil layering on cone resistance. These effects are discussed and quantified using simple elastic analyses in the following Chapters.

5

Interpretation of Cone Resistance: the Two Layer Case

5.1 INTRODUCTION

In spite of the continuous nature of the test, the CPT does not precisely define soil stratigraphy. Many researchers have recognised the influence of soil layering on cone resistance (Sanglerat, 1972; Meigh, 1987; Campanella and Robertson, 1988). However, surprisingly little has been done to quantify this layering effect, which far outweighs the pore water pressure effects discussed in Chapter 3. The effect was observed in early calibration chamber test results (Treadwell, 1975), and in more recent tests on layered soil samples in calibration chambers (Foray and Pautre, 1988; Canou, 1989). In addition, there were instances in the California field-test results where sharp interfaces between soil layers, observed in SPT samples, were recorded as gradual changes in cone resistance at the same depth in the soil column at the same site. The above observations indicate that the cone resistance senses an interface between soils of different stiffnesses several cone diameters ahead and behind the interface. As the cone approaches a stiffer layer, for example, it will sense the presence of this layer some distance before actual penetration of the stiffer soil occurs. Also, after the cone enters the stiffer layer, its response will continue to sense the softer soil above, and this will result in a lower resistance for some distance in the stiffer layer. In such cases, the perceived penetration resistance misrepresents the true resistance of the soils in the vicinity of the interface, particularly if the stiffness change across the interface is large.

It is helpful, therefore, to have an analytical model capable of predicting how cone resistance is affected by layering of soils with different stiffnesses. The model should be able to simulate the behaviour of q_c as the cone approaches and passes through soil layer interfaces. Numerical

methods have been employed with some success to model cone penetration in a two-layer soil system (van den Burg *et al.*, 1994). Unfortunately, such methods have a very high computational demand, and the results are strongly dependent on the material properties assigned to the layers. In this Chapter, an elastic analysis is presented to model the effects of soil layering on cone resistance in a two-layer soil system. The model is based on the classical elasticity solution of Plevako. Elasticity may appear to be an extremely poor model for a penetration problem in which large plastic strains must occur near the cone tip. However, it is not the actual penetration process that will be modeled, but the effect on the cone resistance of a nearby layer of soil. This suggests that an elastic analysis may prove to be useful since the layering effect at a distance from the cone tip must be essentially elastic in nature. The analysis produces results which compare favourably with calibration chamber test results.

5.2 POINT LOADS IN ELASTIC SPACES

Calibration chamber test results indicate that as a cone approaches a distinct interface between soils of different stiffness, q_c departs from its steady-state value some distance from the interface and does not reach a new steady-state value until the cone is some distance into the second material. This implies that cone resistance is influenced by the stiffness of the soil outside the zone of plastic deformation, and that the contribution of the elastic stress field to the development of q_c is significant. Moreover, the cone penetrometer is used primarily for *in situ* investigation of fine-grained soils, and penetration will be essentially undrained in these soils if they are fully saturated, provided the probe is not conducted slowly. In this undrained state the soil will behave very nearly as an incompressible elastic medium. Thus, in spite of the simple idealisation, solutions based on linear elastic models for cone resistance response in layered soils should capture at least part of the observed characteristics of q_c behaviour, particularly changes in q_c as interfaces are approached.

5.2.1 Classical Elasticity Solutions

At the present time, there exist very few exact closed-form solutions to the problem of determining displacement due to a point load acting within an unbounded, isotropic elastic space. Kausel and Seale (1987) present a chronological account of these solutions, which is summarised below.

In 1848, Lord Kelvin presented the first exact closed-form solution for the problem of a point force acting inside an infinite elastic body. This was followed by Boussinesq's solution, in 1878, for the action of a point force on the surface of an elastic half-space. In 1882, Cerruti solved the problem of a half-space loaded with a tangential surface point load. Mindlin, in 1936, provided solutions to the cases of vertical and horizontal point loads acting within an

elastic half-space. If the depth of the point load is taken as zero, his solutions reduce to those of Boussinesq and Cerruti respectively.

Plevako's solution (1969) for the displacement due to a point load in a two-layered infinite elastic medium is an exact solution which, under special conditions, can reduce to either Kelvin's or Boussinesq's solution. Plevako's solution, like the solutions of Rongved (1955) and Dundurs and Hetényi (1965) to similar problems, are closely related to Mindlin's solution. Other solutions, such as those of Burmister (1945) for surface displacements of layered half-spaces, are not closed-form and must be evaluated numerically.

5.2.2 Simulating the Elastic Effects of Layering

Plevako's solution provides a means for simulating the elastic effects of layering on cone resistance for the simple case of a two-layer soil system. No exact closed-form solutions are available for stresses and displacements in an elastic medium comprising three or more layers, thus approximate solutions must be developed to solve this problem. Before examining a multi-layered approximate solution, it is worthwhile determining the response of the exact solution for the two layer case, and assessing its performance against calibration chamber data. The performance of the exact solution will show that it is worthwhile developing a multilayered approximate solution.

Consider two linearly elastic, incompressible half-spaces in bonded contact as shown in Figure 5.1. The CPT will be represented by a disc-shaped region of radius a which supports a uniform applied stress p_0 as shown in the figure. For simplicity, the case of uniform loading on the disc will be considered, rather than uniform displacement of the disc. The radius of the cone is taken as a , and δ denotes the vertical deflection at the centre of the loaded region.

The exact solution to this problem may be obtained by integrating the point-load solution of Plevako given in Appendix B. The assumption of incompressibility is based on the expectation that the effects at a distance which are being modeled here will result primarily from undrained soil deformations. There is no difficulty in modifying the analysis to encompass compressible elastic materials, but this seems an unnecessary complication in view of the approximate nature of the idealisation and the likelihood of undrained deformation being predominant.

The general method of modelling the effect of layering on cone resistance response involves two steps: firstly, extending a solution for the displacement due to a vertical point load in an elastic space, to a uniformly distributed load on a circular area of the same radius as the cone; secondly, solving the resulting expression for the stress required to displace the centre of the circular disc a unit amount at incremented depths in the layered, linear elastic material. For clarity of presentation, the resulting stress versus depth plots are made dimensionless.

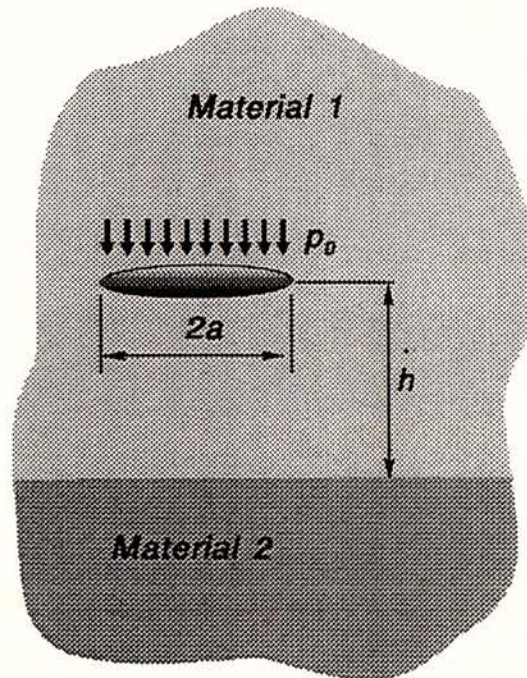


Figure 5.1 Representation of CPT by circular uniform load

5.3 THE PLEVAKO SOLUTION

Plevako (1969) published a solution to the problem of calculating the displacements due to the action of a point force, P , within a pair of perfectly bonded half-spaces with different elastic constants E_1 , ν_1 and E_2 , ν_2 . He considered the two cases of when the line of action of the force is parallel to the interface between the half-spaces, and when it is perpendicular. It is possible to develop the latter of these cases by the general method described above, to determine the elastic response of cone resistance as the cone approaches an interface separating two soils.

5.3.1 Mathematical Development

Details of the integration of the Plevako Solution for a point load to give displacements due to a loaded disc parallel to the interface between two soil layers can be found in Appendix B. An overview is presented here, along with the main results. Figure 5.2(a) illustrates the case of interest from the problem Plevako solved. The modified configuration of a loaded disc is shown in Figure 5.2(b). The original solution was integrated twice in order to determine the vertical displacement, δ , of a horizontal disc of radius a , due to an applied stress p_0 acting on this disc (where $P = p_0 \pi a^2$).

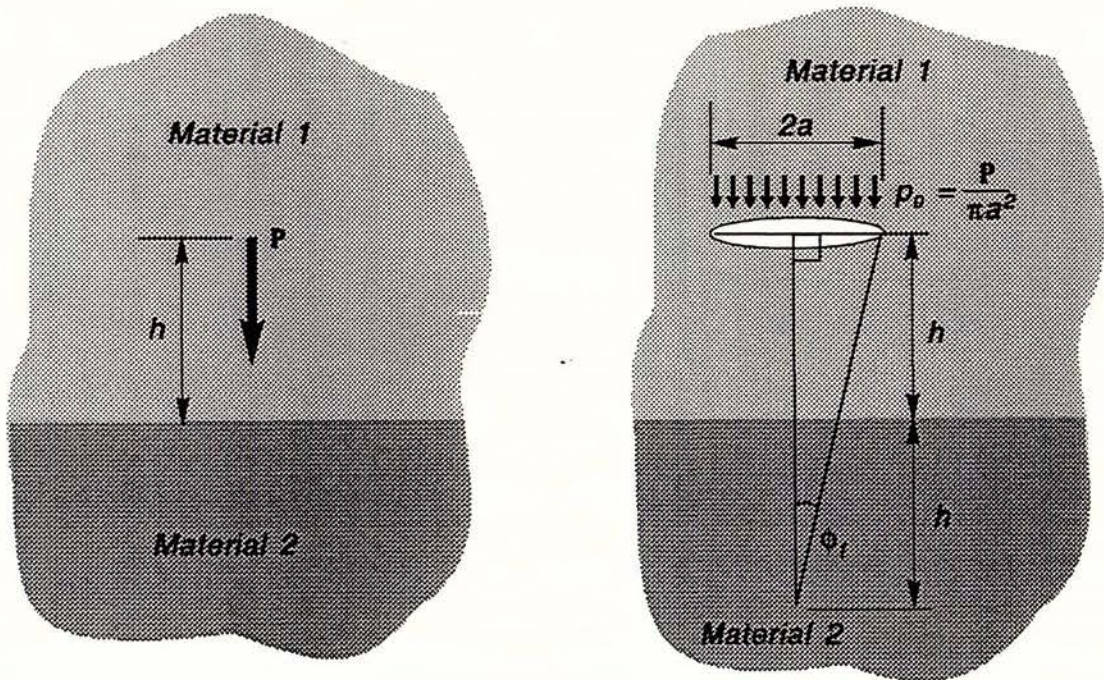


Figure 5.2 Method of analysis: (a) Plevako's problem of a vertical point force inside a pair of cohering half-spaces; (b) extension of (a) to represent a cone approaching the interface between materials 1 and 2

The displacement in material 1 is given in equation (5.1) as

$$\delta_1 = \frac{P_0 a}{4G_1} \left(1 - \frac{h}{a} \left[2(\alpha - 1)(\sec \phi_1 - 1) - \beta(\cos^3 \phi_1 + \cos \phi_1 - 2) \right] \right) \quad (5.1)$$

where h is the vertical distance between the disc and the interface, G_1 is the shear modulus of layer 1, and ϕ_1 is the angle shown in Figure 5.2(b), defined as the Principal Value of

$$\phi_1 = \tan^{-1} \left(\frac{a}{2h} \right) \quad (5.2)$$

Equation (5.1) holds for the special case of incompressibility, when $\nu_1 = \nu_2 = 0.5$. The dimensionless constants α and β of this equation are functions of the elastic properties of the two materials (refer Appendix B). When $\nu = 0.5$ they reduce to

$$\alpha = \frac{2k}{k+1} \quad \beta = \frac{k-1}{k+1} \quad \text{where } k = \frac{G_2}{G_1} = \frac{E_2}{E_1} \quad (5.3)$$

Here k is the stiffness ratio. The limiting cases for δ_1 from equation (5.1) are correctly predicted as follows (refer Appendix B)

$$\begin{aligned} \text{for } h \rightarrow \infty, \quad \delta_1 &\rightarrow \frac{p_0 a}{4G_1} \\ \text{for } h \rightarrow 0, \quad \delta_1 &\rightarrow \frac{p_0 a}{2(G_1 + G_2)} \end{aligned}$$

It is useful to simplify equation (5.1) further by noting that $\beta = (\alpha - 1)$, and to non-dimensionalise the solution by placing it in the following form

$$\frac{p_0 a}{G_1 \delta_1} = \frac{4}{1 + \frac{h\beta}{a} [\cos^3 \phi_1 + \cos \phi_1 - 2 \sec \phi_1]} \quad (5.4)$$

The left hand side of equation (5.4) may be defined as dimensionless cone resistance, η

$$\eta = \frac{p_0 a}{G_1 \delta} \quad (5.5)$$

Note that η is directly proportional to p_0 , the stress applied to the disc to cause a constant displacement of δ . Equation (5.5) is still in terms of G_1 , so that all η values are scaled relative to the stiffness of material 1. However, the subscript has been dropped from the displacement term since we have set $\delta_1 = \delta_2 = \delta$. Thus, the equation also holds for the when the disc is inside the second layer.

The exact solution given in equation (5.4) is easily extended into material 2 by reversing the roles of the two layers, and changing the sign of the applied stress. It is necessary to factor η values in material 2 by the dimensionless stiffness ratio k , to maintain compatibility with equation (5.5).

Now the dimensionless penetration resistance η may be plotted as a function of position for the situation where the cone moves downward through material 1, crosses the interface, and continues into material 2. Results are shown in Figure 5.3(a) for the case where $k = 2$, and in Figure 5.3(b) for the case where $k = 10$. The interface is located at a dimensionless depth zero, and (h/a) is measured positive upward.

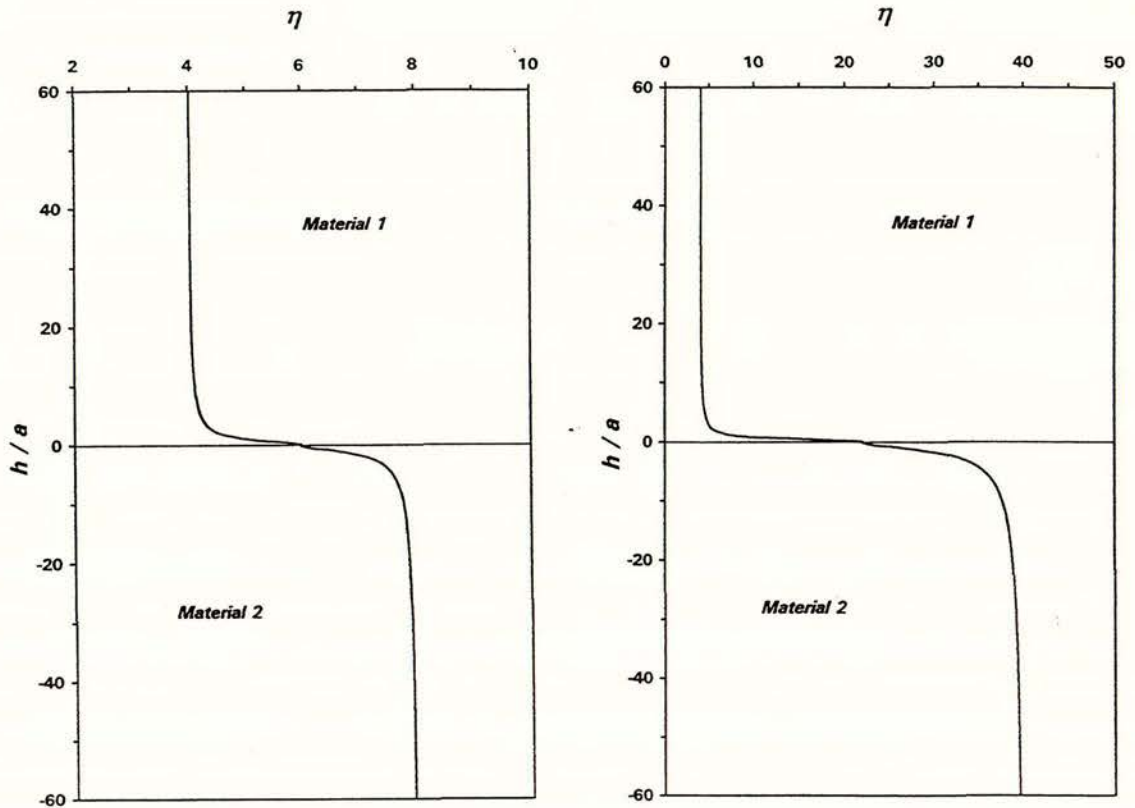


Figure 5.3 Plevako solution dimensionless response: (a) $k = 2$; (b) $k = 10$

Note the behaviour of η at points distant from the interface, and approaching the interface

$$\text{for } h/a \rightarrow \infty, \quad \eta \rightarrow 4$$

$$\text{for } h/a \rightarrow 0, \quad \eta \rightarrow 2(1+k)$$

$$\text{for } h/a \rightarrow -\infty, \quad \eta \rightarrow 4k$$

5.3.2 Features of the Plevako Solution

From Figure 5.3, it is evident that the solution based on Plevako's analysis exhibits several features that are characteristic of cone resistance response when a penetrometer approaches an interface between two soils. As the disc approaches the interface the resistance changes, even though the disc is still within material 1. The disc senses the presence of a layer of different stiffness ahead; in both cases the stiffer layer ahead causes an increase in resistance before the disc encounters material 2. The value of η recorded at the interface is the average of the fully-developed values of η in materials 1 and 2. As the disc moves into the stiffer soil, it gradually tends to develop full resistance. The higher the stiffness ratio, the greater the distance of

penetration required from the interface to develop a steady-state value of resistance in material 2, the stiffer soil. If material 1 is very soft compared with material 2, the disc will sense its presence even after a comparatively large distance of penetration into material 2.

Consider for a moment the case where $k = 2$, as shown in Figure 5.3(a). The elastic solution predicts the same response in each layer, regardless of whether the direction of displacement is from the soft to the stiff material, or from the stiff to the soft material. Because of the linearity of the elastic model, the solution exhibits the exact inverse of the characteristics described above for the case of $k = 0.5$.

The amount the solution deviates from the value of steady-state resistance in each layer appears to be entirely a function of the stiffness ratio k , the cone radius a , and h , the distance of the disc from the interface. It is useful to quantify this deviation of the solution away from the value of fully-developed dimensionless cone resistance. This is achieved by defining the proportion of full development from one layer to another as Δ , expressed as a percentage

$$\Delta = \frac{\eta - \eta_1}{\eta_2 - \eta_1} \quad (5.6)$$

Here η_i is the steady-state value of η that would be registered in a homogeneous deposit of material i . Using Δ , it is now possible to examine the development of cone resistance in more detail. Figure 5.4 shows the behaviour of Δ against dimensionless depth for the several different values of k . It is evident from this figure that the deviation of cone resistance away from the steady-state value is more pronounced when the cone is embedded in a material which is stiffer than an adjoining layer. This implies the perceived or measured resistance in very soft materials will be relatively accurate. Considering the case of $k = 10$ illustrated in Figure 5.4, we see that when the disc is in material 1, Δ exceeds 10 per cent only when the disc is within two cone radii of the interface. The perceived resistance in the stiffer material, however, is underestimated for quite some distance into the material. When the disc is in material 2, Δ exceeds 10 per cent when the disc reaches within six cone radii of the interface. Thus, layers which are more stiff than those that surround them will require a greater distance of penetration before reaching a steady-state value of resistance.

It is important to recognise the effect that the relative stiffness of the layers has on the scaling of the results. This is best achieved by way of an example. If layer 2 is four times as stiff as layer 1, then k is set equal to 4, and η ranges from 4 to 16 when going from layer 1 to layer 2. However, if layer 1 is four times as stiff as layer 2, then k is set equal to 0.25, and η ranges from 4 to 1 when going from layer 1 to layer 2. This can be generalised for the simple two-layer case: if k is greater than one then $\eta \in \{4, \infty\}$; if k is less than one then $\eta \in \{0, 4\}$. Note that k cannot be negative; also, the case of $k = 1$ implies that there is only one material

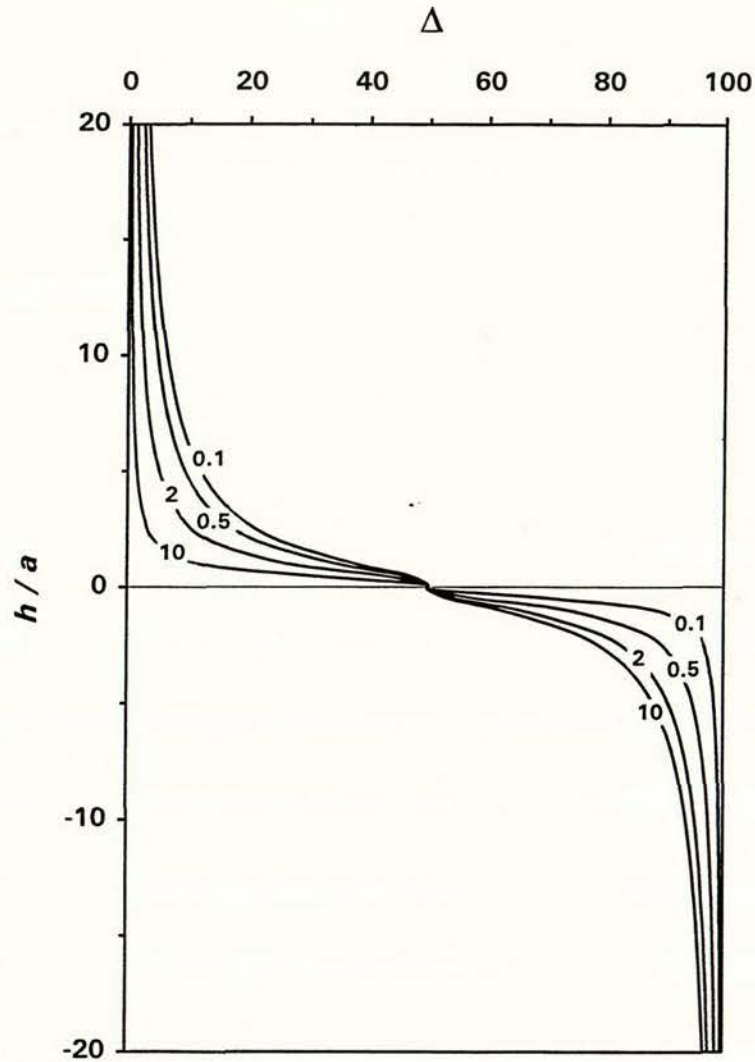


Figure 5.4 Percentage of steady-state resistance achieved in two-layer soil system for values of $k = 0.1, 0.5, 2, 10$

present. The above example suggests that more appropriate scaling will be achieved if the shear modulus of the reference layer, G_1 , is less than G_2 , since there will be a stretching of scale as the difference between layer stiffnesses increases rather than a compression of scale. For the purpose of standardising procedure, layer 1 has been chosen as the reference layer. Thus, it is important to be aware that though curves may appear to be well matched when η is less than 4, there may be a significant difference between experimental and analytical results in this region.

5.3.3 Application to Two-Layer Soil Systems

In what follows, it is intended that η will be used to model actual penetration resistance recorded during calibration chamber testing as a function of depth. In this regard, there is no

suggestion that the elastic analysis given here accounts in any way for the immediate effects of penetration and plastic deformation which occur near the tip of a penetrating cone. The analysis is intended solely to model the effects of layering sensed by the cone in its own vicinity. To accomplish this, the right-hand side of equation (5.4) will be evaluated as in the above example, this time using values of cone radius a and stiffness ratio k which correspond to a specific calibration chamber test. We may represent the stiffness ratio as the ratio of the average middle-third resistance of layer 2 to layer 1. This is reasonable since a strong correlation exists between G (specifically the small-strain shear modulus G_0) and q_c (Baldi *et al.*, 1988). The remaining variable ϕ_1 on the right-hand side of equation (5.4) is easily determined as a function of the position of the disc, h . This yields the required analytical response.

To determine the experimental response, actual values of cone resistance will be made dimensionless so that they agree with the value of η when there is no layering in the near vicinity. Referring to the individual terms on the right hand side of equation (5.5), p_0 and a are assumed to correspond to the measured penetration resistance q_c and the cone radius, respectively. The quantity $G_1 \delta$ must then be set equal to a constant reference value. This is chosen so that η in the reference layer (material 1) tends to 4 at large distances from the material 1-material 2 interface, thus

$$G_1 \delta = \frac{1}{4} \bar{q}_c a \quad (5.7)$$

Here \bar{q}_c is the average middle-third resistance measured in layer 1. In effect, plotting $4 q_c \sqrt{\bar{q}_c}$ gives the required experimental curve. In one sense this calibrates the model to the actual data. In another sense it completely avoids the problems associated with the actual penetration process and allows us to concentrate our attention on the elastic effects of layering.

5.4 COMPARISON WITH CALIBRATION CHAMBER TEST DATA

A number of calibration chamber experiments have been carried out using layered soil profiles by Canou (1989) at CERMES, Paris, and Foray and Pautre (1988) and co-workers at the IMG, Grenoble, France. The CERMES tests employed a mini-cone of diameter 11.3 mm, the calibration chamber having dimensions of 180 mm diameter and 400 mm depth. Hostun RF, a fine silica sand with $D_{50} = 0.35$ mm (Flavigny *et al.*, 1990), was used in the chamber tests. The tests conducted at the IMG, Grenoble, used a Parez cone of 45 mm diameter in a chamber measuring 1.20 metres in diameter and 1.50 metres in depth; the sand used was from Kilkenny Park, New Zealand, with $D_{50} = 0.27$ mm (Foray and Pautre, 1988).

Figures 5.5(a) and 5.5(b) show two sets of dimensionless mini-cone resistance data (solid lines) and corresponding theoretical resistance curves η for situations in which material 2 is stiffer

(Figure 5.5(a)) and in which material 2 is softer (Figure 5.5(b)). In both cases the actual mini-cone resistance is made dimensionless in such a way that its average value in the upper layer away from the interface is equal to 4. The corresponding average resistance in the lower layer is 28 in Figure 5.5(a) and 2.17 in Figure 5.5(b). Vertical dimensions are shown measured from the upper soil surface in the chamber and made dimensionless by dividing by a . The theoretical dashed lines on the two figures were obtained using equation (5.4) with k set equal to 7 ($k = 28/4$) in Figure 5.5(a) and set equal to 0.544 ($k = 2.17/4$) in Figure 5.5(b). In both instances the experimental and theoretical curves bear a reasonable likeness, particularly in the case of Figure 5.5(a).

As is expected, the model does not capture all aspects of observed cone resistance behaviour. Real soils are rarely homogeneous, and cone resistance records reflect this by the amount of variation in the fully developed q_c within a layer. In addition, the results of the model are independent of penetration direction, whereas, for the cone, plastic deformation of the soil is controlled by the direction of penetration. The yielding of the soil, which the model does not take into account, will affect the value of resistance recorded at an interface, and it is unlikely that a precise average of the steady-state q_c in layers 1 and 2 will be recorded at the interface.

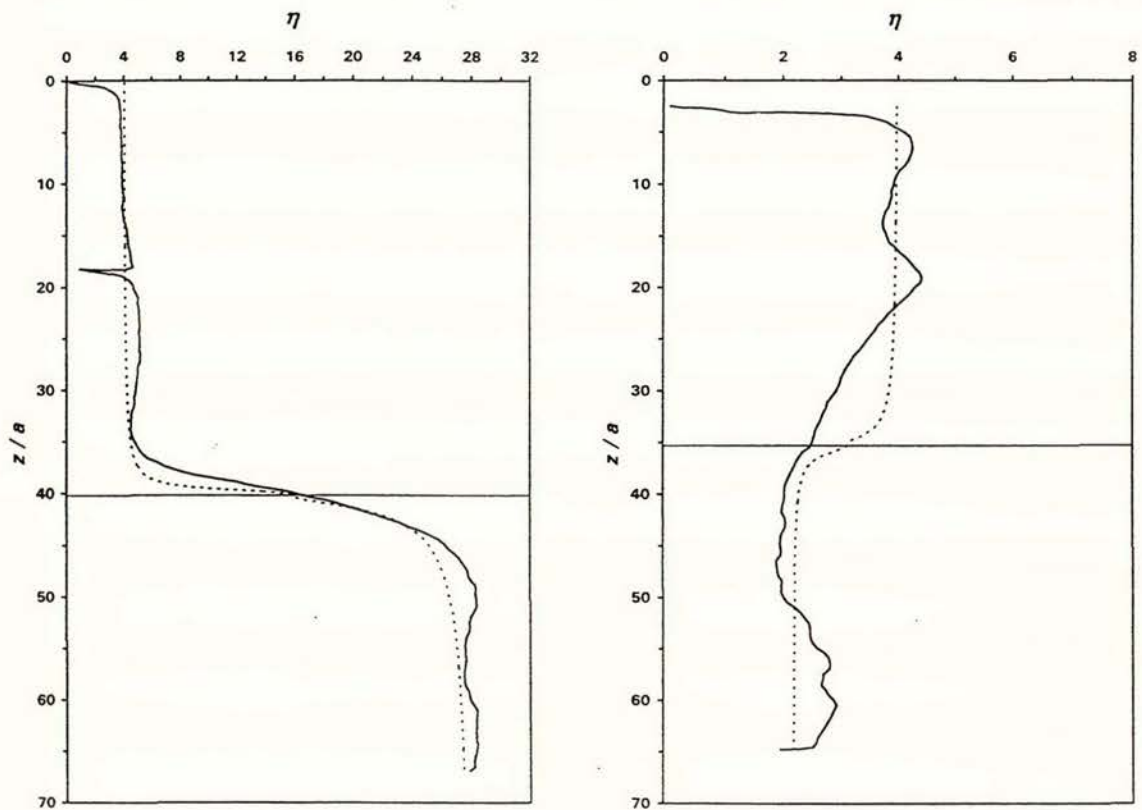


Figure 5.5 Comparison of Plevako solution with calibration chamber test results: (a) soft layer above stiff (Kilkenney Park sand); (b) stiff layer above soft (Hostun RF sand)

The behaviour of the solution very close to the interface is unusual. The solution predicts a constant value of η within approximately $0.25a$ either side of the interface, resulting in a small step in the η function where layers 1 and 2 meet. To determine the reason for this step, the expression for η given in the right hand side of equation (5.4) was differentiated twice with respect to h for given values of a and k . The resulting slope (η') and curvature (η'') functions verified that the step in the η function at the interface is predicted, and that it is not a result of calculation accuracy limitations. In fact, several points of inflexion exist in the η curve. Two of these points are located a distance of approximately $0.25a$ either side of the interface, the separation between them decreasing with increasing stiffness ratio k . The small step does not detract from the overall ability of the model to simulate the effects of soil layering on q_c .

5.5 TOWARDS A MORE GENERAL MODEL

The modified Plevako solution appears to be a useful tool for simulating the effects of layering on cone resistance in two-layered soil systems. It exhibits several characteristics that are typical of q_c behaviour when the cone approaches and passes through an interface between soils of different stiffnesses. The theoretical dimensionless resistance curves show good agreement with the calibration chamber test data, which suggests there is merit in using the above approach to investigate the effect of layering on cone resistance. However, the Plevako solution is restricted to prediction of q_c in two-layer soil systems, and it is not possible to extend this solution further to examine cases of three or more layers. Strictly speaking, the above calibration chamber tests are examples of three-layer soil systems if the effect of the rigid base of the chamber is taken into account. Thus, an approximate model must be developed which is able to simulate cone resistance in multilayered soil systems.

6

Interpretation of Cone Resistance: the Multilayer Case

6.1 INTRODUCTION

The subject of this Chapter is the development of a model which is able to quantify the influence of multiple soil layering on cone resistance. Since it is not possible to extend the exact Plevako solution presented in the previous Chapter to represent cases of three or more layers, it is necessary to develop an approximate solution.

An attempt was made to solve this problem, using Kelvin's solution and the principle of superposition to model a multilayered soil. However, the behaviour of this solution was found to be grossly inaccurate at and approaching interfaces, when compared with experimental results from calibration chamber tests and with the exact Plevako solution. The solution, when approaching an interface, tended towards the steady-state value for cone resistance of the approaching layer, rather than to an average value for resistance of the two layers.

The problem was solved by the development of a model, based on the superposition of integrated Boussinesq solutions. The results of this model are in good agreement with both calibration chamber and field testing data, and help explain the evolution of cone resistance during penetration testing in a multilayered soil system. The model is able to predict the percentage of steady-state cone resistance that will be achieved in a layer, given information about the thickness and stiffness of the layers comprising the soil column. There may be potential application of this method to the interpretation of calibration chamber tests as well as to the interpretation of actual field CPT data.

6.2 DEVELOPMENT OF APPROXIMATE SOLUTION

The model described below is an approximate solution to the problem of modelling the effects of layering on cone resistance in a multilayered soil. It is based on the Boussinesq solution for the displacement due to a point load on and normal to the surface of an elastic halfspace. Superposition of the solution is used to represent multiple layering. An overview of the mathematical development of the model is presented here, along with the main results. A detailed development of the solution can be found in Appendix B.

6.2.1 The Solution for Two Layers

As in the previous chapter, consider two linearly elastic, incompressible half-spaces in bonded contact as shown in Figure 6.1(a). Again, the CPT will be represented by a disc-shaped region of radius a which supports a uniform applied stress p_0 as shown in the figure; a is taken to be the radius of the cone and δ denotes the vertical deflection at the centre of the loaded region.

The first step in the analysis is to decompose the layered infinite space in Figure 6.1(a) into two elastic half-spaces as shown in Figure 6.1(b). Each half-space supports a uniform stress, p_0' or p_0'' , over the disc-shaped region of radius a . The upper half-space is homogeneous, while the lower half-space is layered. For the upper half-space, Boussinesq's point-load solution may be easily integrated over the disc-shaped region to give the displacement δ' at the centre of the disc. For an incompressible material the result is as follows

$$\delta' = \frac{p_0' a}{2G_1} \quad (6.1)$$

Here G_1 denotes the elastic shear modulus of material 1. For the lower, layered half-space, an approximation can be used, based on Boussinesq's solution in which the relative displacements in the two layers are combined. The displacement δ'' at the centre of the loaded region is given by

$$\delta'' = \frac{p_0'' a}{2G_1} - \frac{p_0'' a^2}{2G_1 \sqrt{a^2 + h^2}} + \frac{p_0'' a^2}{2G_2 \sqrt{a^2 + h^2}} \quad (6.2)$$

The three terms on the right-hand side of this equation represent (i) the surface displacement of a homogeneous half-space composed of material 1, (ii) the displacement at depth h beneath the centre of the loaded disc in a homogeneous half-space composed of material 1, and (iii) the displacement at depth h beneath the centre of the loaded disc in a homogeneous half-space composed of material 2. The difference between terms (i) and (ii) represents the relative shortening in the layer of thickness h . Term (iii) represents the displacement of a half-space

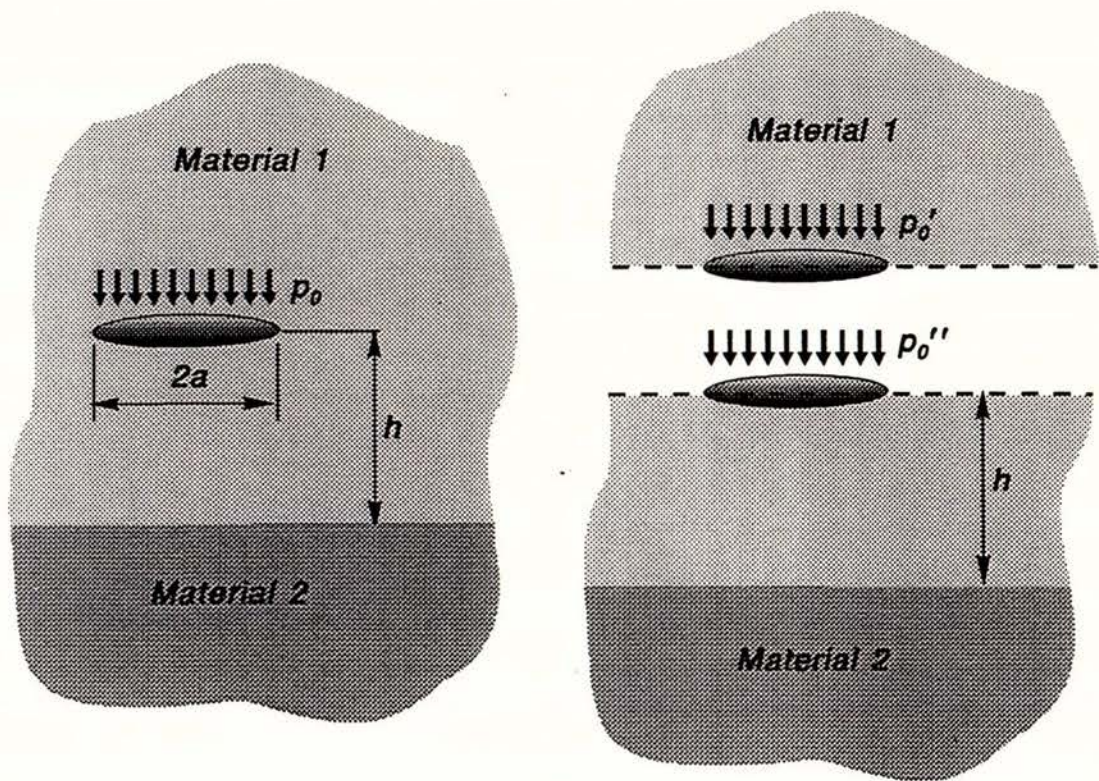


Figure 6.1 Method of analysis: (a) representation of CPT by circular uniform load; (b) decomposition of (a) into two half-space problems

of material 2 below the depth h . Equation (6.2) is a well-known approximation for the surface displacement of a layered half-space, and although not exact, it will give a good approximate value for the displacement. It compares favourably with exact solutions based on Burmister's analysis (Poulos, 1967).

It is possible to combine the two half-space solutions in Figure 6.1(b) to represent the infinite space problem in Figure 6.1(a). This is accomplished by setting $\delta' = \delta'' = \delta$ and by setting $p_0' + p_0'' = p_0$. These two conditions can be used together with equations (6.1) and (6.2) to obtain

$$\delta = \frac{p_0 a}{2G_1} \left(\frac{1 - \lambda_1}{2 - \lambda_1} \right) \quad (6.3)$$

where

$$\lambda_1 = \left(1 - \frac{G_1}{G_2} \right) \frac{a}{\sqrt{a^2 + h^2}}$$

In effect, the two half-spaces are being joined on the horizontal plane passing through the loaded region. This approach can be motivated by the fact that, for an incompressible material, Kelvin's solution for a point load in an infinite space gives exactly the same stresses and displacements in the half-space above or below the load point as does Boussinesq's solution for a half-space with a point load equal to half that used in Kelvin's problem. Note that the solution becomes exact in the limiting cases (refer Appendix B)

$$\text{for } h \rightarrow \infty, \quad \delta \rightarrow \frac{p_0 a}{4G_1}$$

$$\text{for } h \rightarrow 0, \quad \delta \rightarrow \frac{p_0 a}{2(G_1 + G_2)}$$

6.2.2 Extending the Solution to Several Layers

It is an easy matter to generalize this analysis to multilayered situations. For example, consider the three layer case shown in Figure 6.2. Following the same method of analysis, equation (6.1) is unchanged while equation (6.2) is replaced by

$$\delta'' = \frac{p_0'' a}{2G_1} \left[1 - \left(1 - \frac{G_1}{G_2}\right) \frac{a}{\sqrt{a^2 + h_1^2}} - \frac{G_1}{G_2} \left(1 - \frac{G_2}{G_3}\right) \frac{a}{\sqrt{a^2 + h_2^2}} \right] \quad (6.4)$$

Then the conditions of compatibility of displacements ($\delta' = \delta'' = \delta$) and equilibrium ($p_0' + p_0'' = p_0$) lead to

$$\delta = \frac{p_0 a}{2G_1} \left[\frac{1 - \lambda_1 - \frac{G_1}{G_2} \lambda_2}{2 - \lambda_1 - \frac{G_1}{G_2} \lambda_2} \right] \quad (6.5)$$

where

$$\lambda_j = \left(1 - \frac{G_j}{G_{j+1}}\right) \frac{a}{\sqrt{a^2 + h_j^2}} \quad (6.6)$$

Further layers are easily incorporated if need be, and layering in the upper half-space may be treated by the same approach. In this way the displacement δ at any point in a multilayered

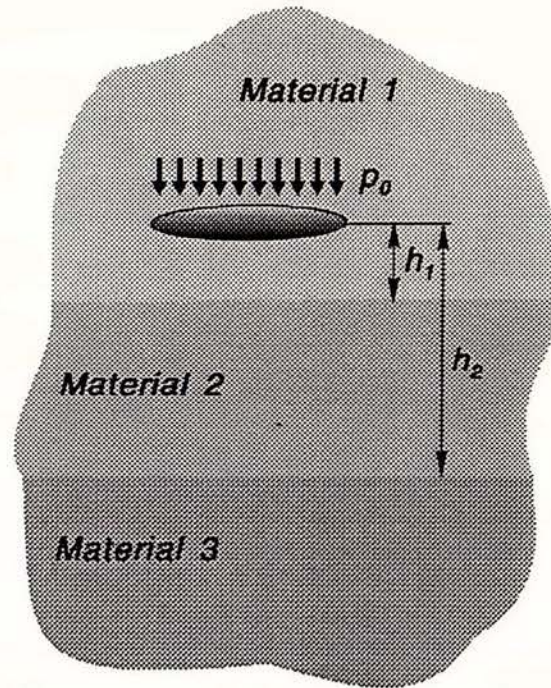


Figure 6.2 Problem with multiple layers

infinite space may be estimated. It is necessary to define a more general dimensionless stiffness ratio for the multilayer case

$$k_i = \frac{G_{i+1}}{G_1} \quad i = 0, 1, 2, \dots, N \quad (6.7)$$

Here N is the number of interfaces, so $(N + 1)$ is the number of layers; note that $k_0 = 1$. Finally, recall the dimensionless penetration resistance, defined in the previous chapter as

$$\eta = \frac{P_0 a}{G_1 \delta} \quad (6.8)$$

Thus, for any number of layers, the dimensionless stiffness ratio η may be defined by a functional relationship of the form

$$\eta = F(\lambda_1, \lambda_2, \lambda_3, \dots, k_1, k_2, k_3, \dots) \quad (6.9)$$

The exact form of F depends on the number of layers involved and the position at which the load is applied. For example, in the simple single-interface geometry of Figure 6.1(a), the expression for η for load points above the interface is

$$\eta = 2 \left(\frac{2 - \lambda_1}{1 - \lambda_1} \right) \quad (6.10)$$

while for load points below the interface, the solution is as follows

$$\eta = 2k_1 \left(\frac{2 + k_1\lambda_1}{1 + k_1\lambda_1} \right) \quad (6.11)$$

Note that when $h = 0$ equation (6.6) shows that

$$\lambda_1 = 1 - \frac{1}{k_1}$$

and equations (6.10) and (6.11) give the same result for η . For more complex layering, equations (6.10) and (6.11) must be replaced by more complex expressions. It is convenient to redefine λ_j given in equation (6.6) as $\lambda'_j = \lambda_j / k_{j-1}$, thus

$$\lambda'_j = \left(\frac{1}{k_{j-1}} - \frac{1}{k_j} \right) / \sqrt{1 + \left(\frac{h_j}{a} \right)^2} \quad j = 1, 2, 3, \dots, N \quad (6.12)$$

where h_j is the vertical distance between the disc and interface j . The general form for η is then given by

$$\eta_i = 2 k_{i-1} \left(\frac{2 + A_i - B_i}{(1 + A_i)(1 - B_i)} \right) \quad i = 1, 2, 3, \dots, (N+1) \quad (6.13)$$

where

$$A_1 = 0, \quad A_i = k_{i-1} \sum_{j=1}^{j=i-1} \lambda'_j \quad i = 2, 3, 4, \dots, (N+1)$$

$$B_{N+1} = 0, \quad B_i = k_{i-1} \sum_{j=i}^{j=N} \lambda'_j \quad i = 1, 2, 3, \dots, N$$

The term A_i predicts the influence that layers of different stiffnesses above the disc will have on the dimensionless resistance η , and the term B_i represents the effect of layering below the

disc. The calculation is primarily controlled by two dimensionless quantities: the stiffness ratio k_i , and the position of the disc (h_j / a), which is incorporated within λ_j' in equation (6.12).

6.2.3 Comparison with Plevako Solution

The approximate solution for the two layer case given in equations (6.10) and (6.11) may now be compared with the exact solution of Plevako. A comparison for the case where $k_1 = 2$ is shown in Figure 6.3. The approximate solution clearly gives results close to the exact solution, although the discrepancy between the two solutions is greater in the stiffer material. This discrepancy increases slightly with increasing stiffness ratio. Note that the approximate solution becomes exact in the limiting cases where $h \rightarrow \pm \infty$ or $h \rightarrow 0$. The limiting cases for η are the same as in the previous chapter, so that η tends to a value of 4 in material 1, and $4k_1$ in material 2. In fact, this result can be generalised for the multilayer case: η will tend to a value of 4 in material 1, and $4k_i$ in material i .

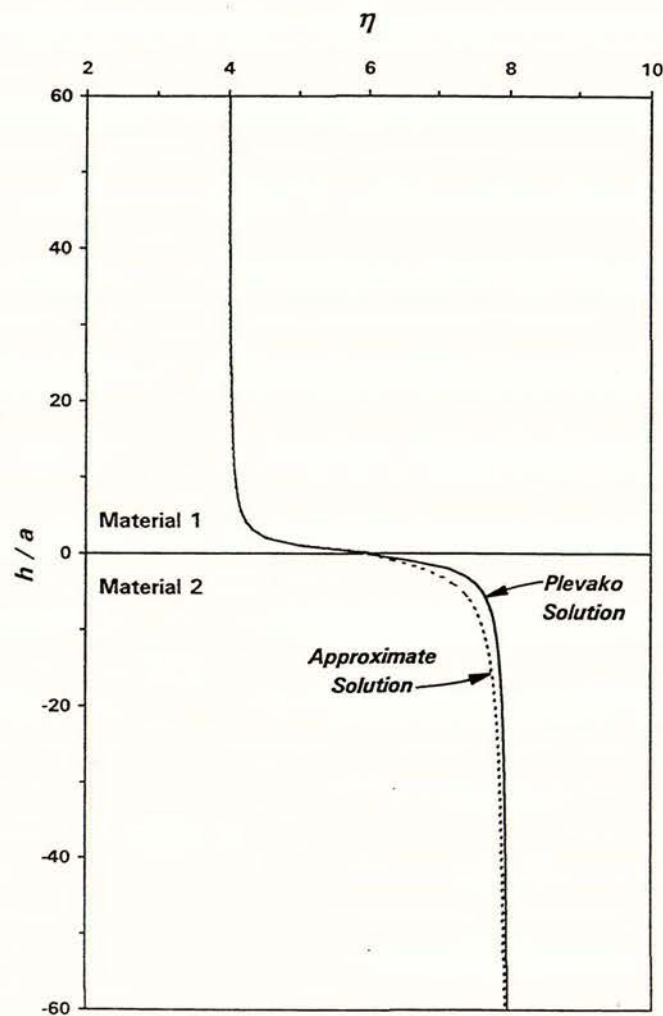


Figure 6.3 Comparison of exact Plevako and approximate solutions for $k_1 = 2$

6.3 COMPARISON WITH EXPERIMENTAL DATA

It is now possible to examine the performance of the approximate solution using calibration chamber data. Figures 6.4(a) and 6.4(b) show the same two sets of dimensionless mini-cone resistance data (solid lines) as Figures 5.5(a) and 5.5(b) of the previous chapter. Figure 6.4(a) represents the situation where material 2 is stiffer than material 1 ($k_1 = 7$), and Figure 6.4(b) represents the situation where material 2 is softer ($k_1 = 0.544$). The theoretical dashed curves in this instance, however, are derived from the approximate solution, rather than Plevako's exact solution. Again, in both instances the experimental and theoretical curves bear a reasonable likeness.

Note on both figures that the theoretical line bends toward greater values of η at dimensionless depths nearing 70 (the soil free surface is at dimensionless depth $z/a = 0$). This occurs because it is now possible to include the effect of the presence of the base of the calibration chamber in the theoretical calculations. This point is discussed further below.

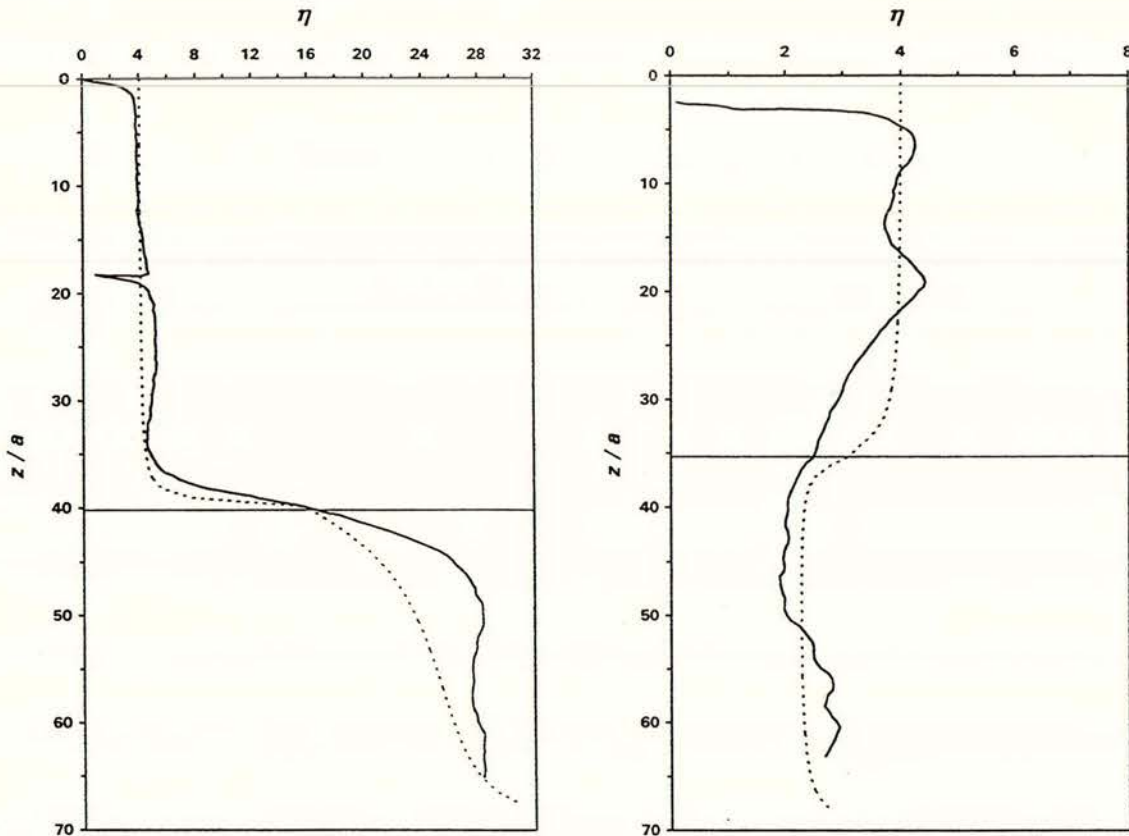


Figure 6.4 Comparison of approximate solution with calibration chamber results: (a) soft layer above stiff (Kilkenney Park sand); (b) stiff layer above soft (Hostun RF sand)

Figures 6.5(a) and 6.5(b) show results from a third experiment involving a soft layer over a stiffer layer. The experimental data (solid lines) in both figures are the same, but the theoretical results (dashed lines) are different. In Figure 6.5(a) calculations were performed without attempting to represent the chamber base. In Figure 6.5(b) the base was included in the theoretical calculation by introducing a near-rigid layer at dimensionless depth 70.9. Figure 6.5(b) appears to model the experimental data remarkably well, and the effect of the chamber base is seen to extend a significant distance upward into the sample.

Figure 6.6 shows a final experimental plot in which three soil layers were involved: a soft layer sandwiched between two stiffer layers. The stiffness ratios used to model these results were $k_1 = 0.34$ and $k_2 = 2.51$. The rigid base layer has been incorporated into the calculations. Once again, the theoretical penetration resistance appears to adequately model the layer effects observed in the experiment.

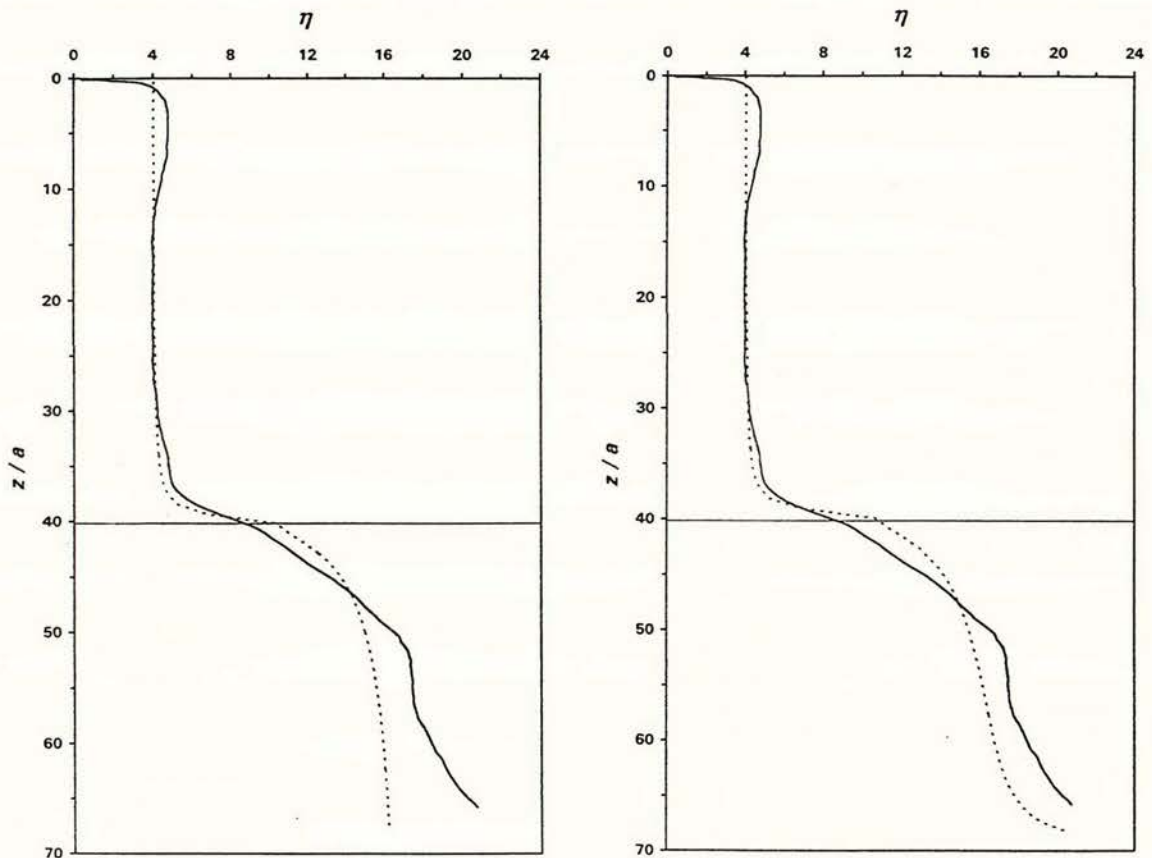


Figure 6.5 Comparison of theory with calibration chamber results. Theoretical response: (a) without chamber base; (b) with chamber base

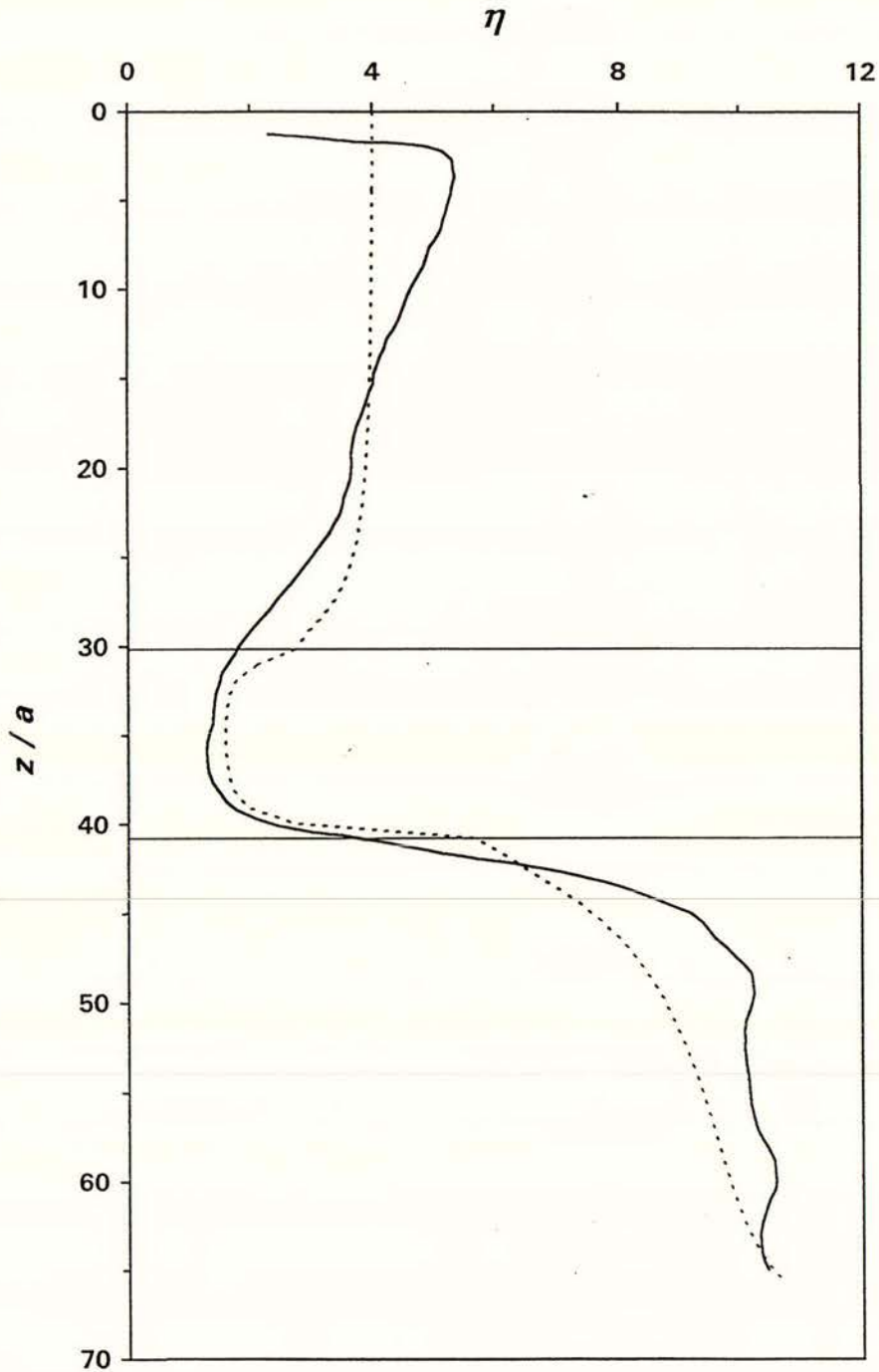


Figure 6.6 Comparison of theory with calibration chamber results: three-layer example

Clearly, the above theoretical results do not agree exactly with the experimental data. Nevertheless, there is a remarkable degree of correlation in most cases, despite the noisiness evident in the experimental traces. The approximate model may now be used to examine cone resistance response in layered soils of various configurations. The special case of symmetric layering is examined below.

6.4 SOLUTION RESPONSE FOR SYMMETRIC LAYERING

An obvious use for this analysis appears to be in the interpretation of cone resistance data where thin soil layers are involved. As an example, consider the symmetric situation depicted in Figure 6.7. A layer of material 2 of thickness H is sandwiched between two deposits of material 1. The origin is located at the mid-height of the layer. Theoretical penetration resistance plots for two cases where material 2 is stiffer than material 1 are shown in Figures 6.8(a) and 6.8(b). Figure 6.8(a) shows results for a stiffness ratio $k_1 = 2$ while Figure 6.8(b) corresponds to $k_1 = 10$. The six dimensionless curves generated for each figure correspond to the theoretical penetration resistance of a standard cone with radius 17.84 mm (projected area = 10 cm²) penetrating material 2 layers with thickness H equal to 0.1, 0.25, 0.5, 1, 2 and 5 metres. It is obvious from this figure that thin layers will not yield a perceived penetration resistance nearly so great as the actual value, and this effect is more pronounced for the higher stiffness ratio $k_1 = 10$ than for the lower ratio $k_1 = 2$.

The situation in which the thin layer is softer than the surrounding material is illustrated in Figures 6.9(a) and 6.9(b). Figure 6.9(a) corresponds to a stiffness ratio k_1 of 0.5 while Figure 6.9(b) shows the case where k_1 is 0.1. In this case, the perceived resistance is not so drastically affected as in the case where the thin layer is the stiffer material. This seems reasonable since a soft layer would be expected to isolate the penetrating cone from materials it has yet to encounter, while a stiff layer will not have this effect.

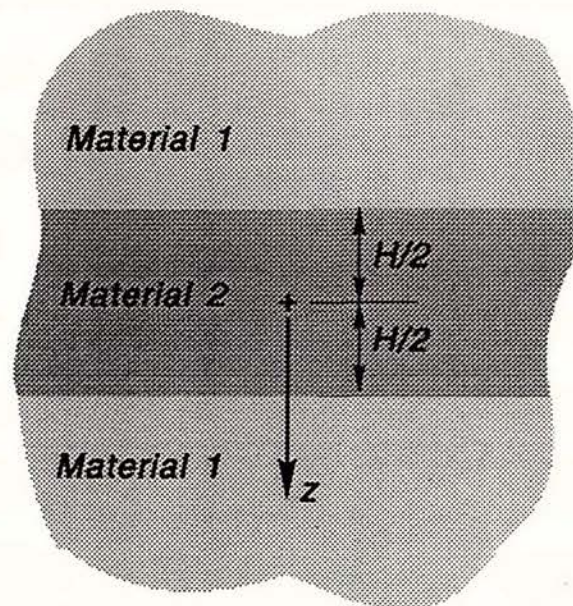


Figure 6.7 Symmetric case of thin layer sandwiched between thicker deposits of another soil

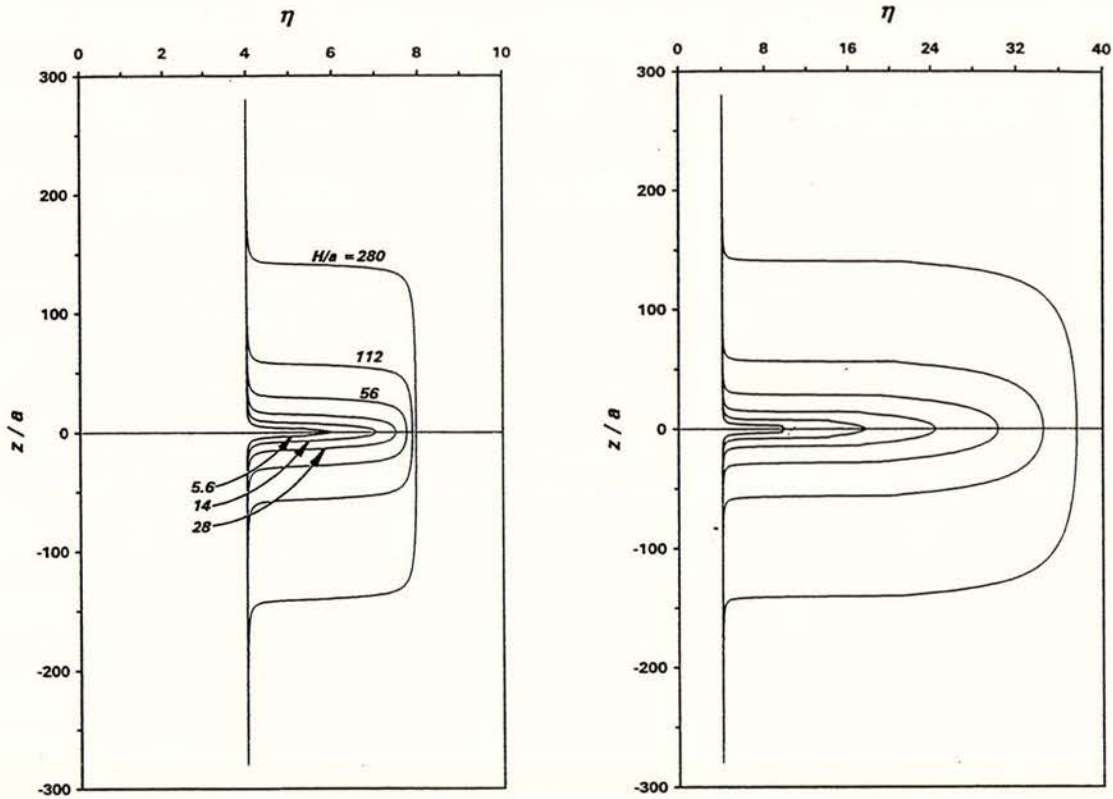


Figure 6.8 Theoretical results for penetration of a thin layer: (a) $k_1 = 2$
 (b) $k_1 = 10$ (layer thicknesses same as for Figure 6.8(a))

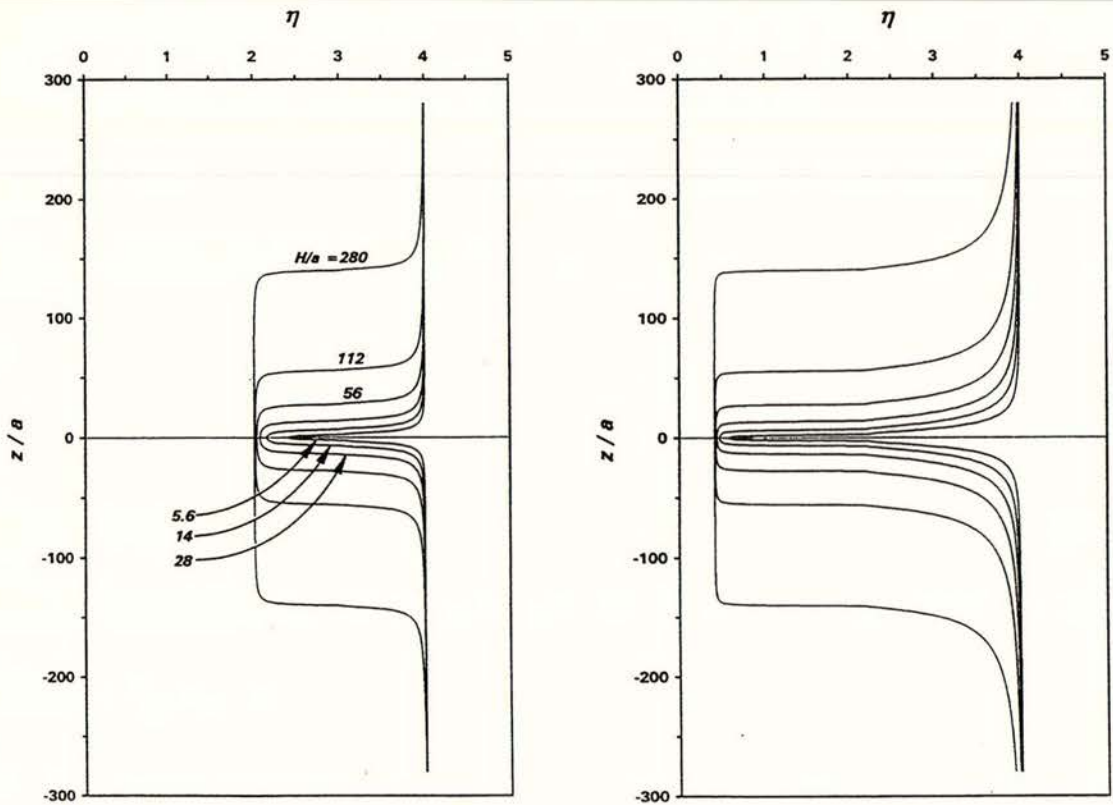


Figure 6.9 Theoretical results for penetration of a thin layer: (a) $k_1 = 0.5$
 (b) $k_1 = 0.1$ (layer thicknesses same as for Figure 6.9(a))

Predictably, the elastic solution gives a symmetric response for cases of symmetric layering, as seen in Figures 6.7 and 6.8. The above results closely represent the expected cone resistance response in most symmetrically configured soil systems (it is unlikely that the response will ever be purely symmetric, due to the effects of plastic deformation and yielding of the soil). However, research by Houlsby and colleagues at Oxford has shown that in instances where the interbedded layer is cemented, the resistance to penetration is governed by quite different mechanisms of failure (Evans, 1987). In such cases, asymmetric resistance curves are both expected and observed.

The effect layer thickness may have on the evolution of cone resistance can be assessed by examining the proportion of steady state cone resistance achieved at $z = 0$ (the layer mid-height) for the symmetric case detailed in Figure 6.7. The parameter Δ , introduced in the previous chapter, is redefined in equation (6.14). Here η_1 and η_2 are the steady state values of cone resistance which would be achieved in homogeneous deposits of materials 1 and 2 respectively, and η_0 is the perceived value of resistance found at the mid-height of layer 2 (where $z/a = 0$). If layer 2 is very thick, then η_0 will approach η_2 and Δ will approach 100 per cent. For less thick layers, Δ will be appropriately smaller.

$$\Delta = \frac{\eta_0 - \eta_1}{\eta_2 - \eta_1} = \frac{\eta_0 - 4}{4(k_1 - 1)} \quad (6.14)$$

The analysis outlined above may be used to find the value of η_0 for the situation depicted in Figure 6.7. This gives

$$\eta_0 = \frac{4k_1}{1 - \left(\frac{1 - k_1}{\sqrt{1 + \frac{H^2}{4a^2}}} \right)} \quad (6.15)$$

Using this result in equation (6.14) and rearranging leads to

$$\frac{H}{a} = 2 \sqrt{\left(1 + \frac{k_1 \Delta}{1 - \Delta} \right)^2 - 1} \quad (6.16)$$

This equation gives the dimensionless thickness H/a required to achieve a certain percentage Δ for any given value of stiffness ratio k_1 . Equation (6.16) is illustrated graphically in Figure 6.10(a) and 6.10(b) for several values of Δ . Figure 6.10(a) corresponds to values of k_1 greater than 1. Referring to Figure 6.10(a), note that the lines of constant Δ are near linear. As a general rule, doubling the stiffness ratio k_1 implies H/a must also be doubled to maintain a particular value of Δ , in the case where the layer is stiffer than the surrounding soil.

The results shown in Figure 6.10(a) imply a greater thickness is required than that previously thought, to develop full cone resistance in a layer. Meigh (1987) suggests that to reach full cone resistance in a sand layer bounded by soft clay layers, the layer should be at least 0.7 metres thick. For a standard cone, this value corresponds to a dimensionless layer thickness of $H/a = 40$. It is evident from Figure 6.10(a) that, for this dimensionless thickness, only values of $k_1 \leq 2.25$ will ensure Δ reaches at least 90 per cent. When $k_1 = 5$, a value perhaps more representative of the scenario outlined by Meigh, Figure 6.10(a) returns a value for Δ of approximately 65 per cent; to achieve $\Delta = 90$ per cent for this stiffness ratio, the layer thickness must be increased to $H/a = 90$, equivalent to a thickness of approximately 1.6 metres for a standard cone.

Figure 6.10(b) presents the case where the layer is softer than the surrounding material and here, at first glance, the results appear counter-intuitive. As the layer stiffness becomes smaller in relation to the surrounding soil, the thickness H required for a specified Δ becomes smaller, the opposite to what might initially be expected. This occurs because of the isolating nature of a soft layer, mentioned earlier. When the cone is in the soft material it is much more difficult for it to sense the surrounding soil, and this effect is exaggerated for smaller stiffness ratios. Thus for a stiffness ratio of $k_1 = 0.5$, a layer thickness of nearly $12a$ is required to reach a Δ

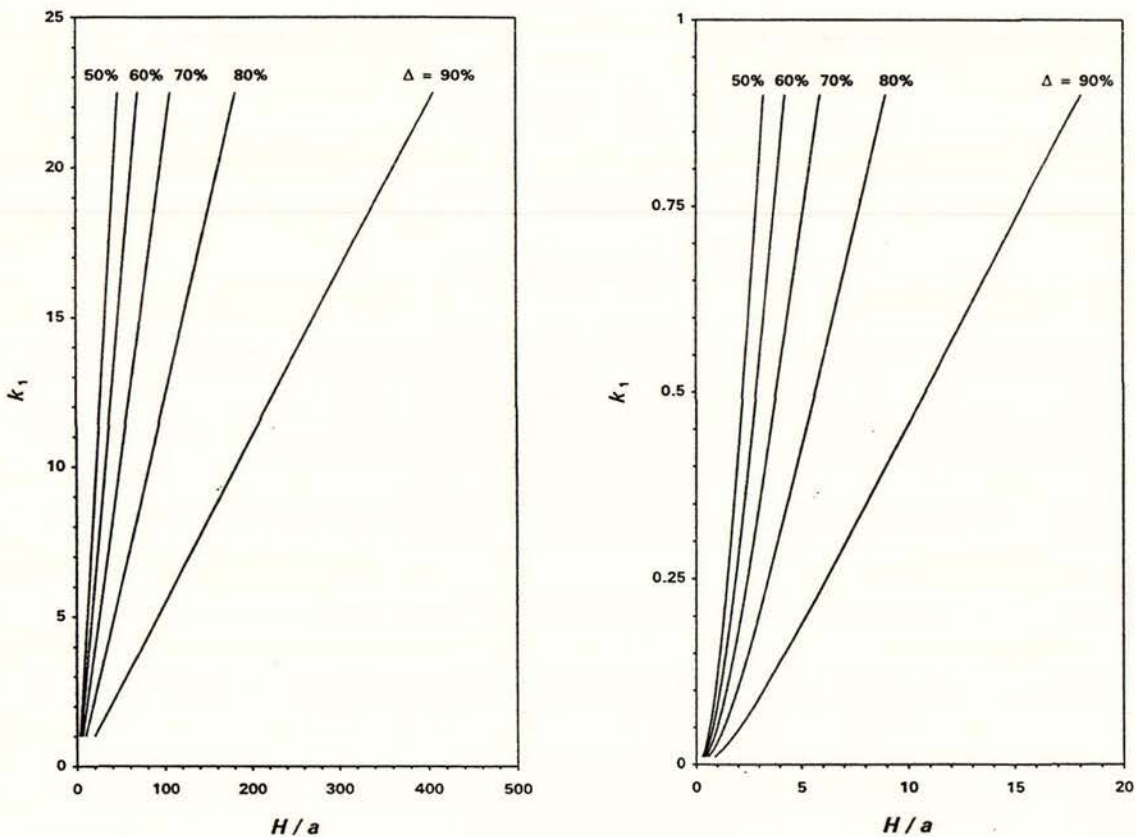


Figure 6.10 Dimensionless layer thickness required to achieve a specified value of Δ for given stiffness ratio: (a) $k_1 > 1$; (b) $k_1 < 1$

of 90 per cent, while for a ratio ten times smaller of $k_1 = 0.05$, a thickness of only $2a$ is needed. A very soft layer will generally yield a perceived penetration resistance close to its genuine value even when the layer thickness is quite small.

6.5 APPLICATION OF SOLUTION TO CPTU RECORDS

The above analysis has clear implications for interpretation of cone resistance records. The resistance of a thin soil layer that is stiffer than the surrounding soil may be underestimated, possibly resulting in a soil type or soil strength misclassification of the layer. Instances of these misclassifications are presented below.

6.5.1 Soil Type Misclassification

As an example of how this analysis might be applied, consider the following actual field record. Figure 6.11 shows a section of the cone resistance record from Test 26, the first of the two probes conducted at the Leonardini site near the Salinas River mouth (refer Figure 2.9). Focusing attention on the segment between 8.5 metres and 10 metres depth, there appears to

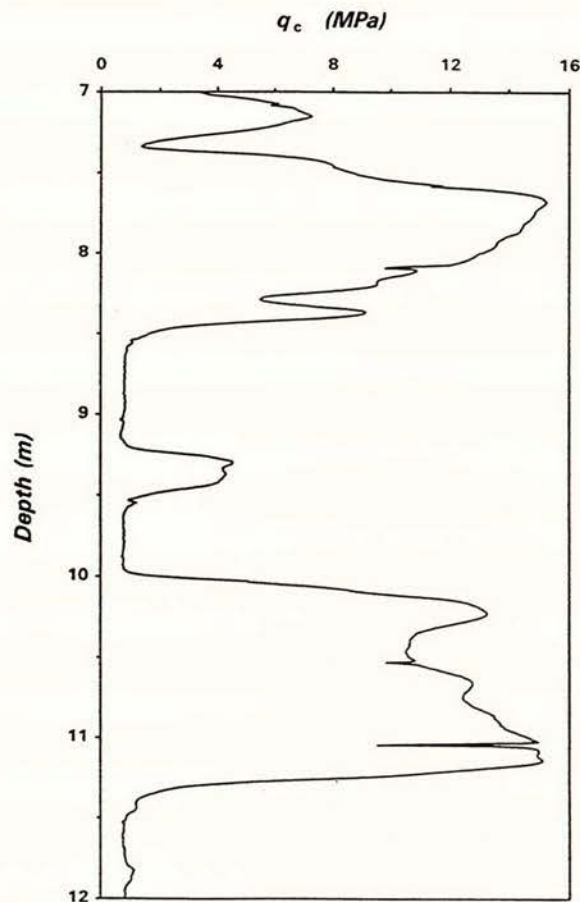


Figure 6.11 Measured penetration resistance at Leonardini (Test 26)

be a thin layer of stiff soil embedded between two softer layers. An attempt will be made to model this segment of the record. The cone had a standard radius a of 17.84 mm. The raw value of \bar{q}_c recorded in the soft soil was, on average, 0.8 MPa. To convert this into dimensionless form such that $\eta = 4$ in the soft material, equation (6.8) was used; $G_1\delta$ was calculated as

$$G_1\delta = \frac{1}{4} \times 0.80 \times 17.84 = 3.58 \text{ MPa}\cdot\text{mm}$$

The positions of the two interfaces at top and bottom of the stiff layer were determined from the pore pressure record obtained simultaneously with the penetration record. Clear cut jumps in pore pressure occurred both at the top and bottom of the layer.

Based purely on the perceived values of q_c in the soft soil and in the layer, a value of $k_1 = 5.4$ was initially used to calculate the theoretical response. That calculation produced a theoretical curve which severely underestimated the resistance in the layer as shown in Figure 6.12. Referring back to Figure 6.11, it is plausible to suspect that the thin layer material could be the same as that found above 8.5 metres or below 10 metres, but that its perceived resistance is diminished due to its small layer thickness. The soils above 8.5 metres and below 10 metres both have mean penetration resistance approximately 15 times that found in the soft material. This suggests resetting k_1 to 15 and recalculating the theoretical response. When this is done the theoretical curve agrees with the field record much more closely as shown in Figure 6.12.

The unavoidable conclusion is that the thin layer at depth 9.4 metres is in fact identical to the soils found above 8.5 metres and below 10 metres. Clearly this conclusion would not be reached based on the raw data shown in Figure 6.11. According to the classification chart proposed by Robertson (1990), the thin layer is misclassified as a silty sand, while the soils above 8.5 metres and below 10 metres classify as clean sands.

One final point can be made concerning Figure 6.12. In the figure, the location of the top of the layer appears to be slightly higher than the field resistance curve would suggest. This may be due to the fact that the standard procedure of referring all depths to the location of the cone tip has been followed. It may be that the experimental result should be compared with the analytical solution at the depth where the entire projected area of the cone is embedded, rather than at the tip. If allowance was made for this fact, the upper interface would be shifted downwards approximately $2a$, and the analytical solution would fit the experimental data even more closely. Of course, the lower interface would also shift downward by the same amount, and this might cause the theoretical data to fit somewhat less well at the base of the layer. It should be noted however that, at a dimensionless depth of $z/a = 534$, the field penetration was

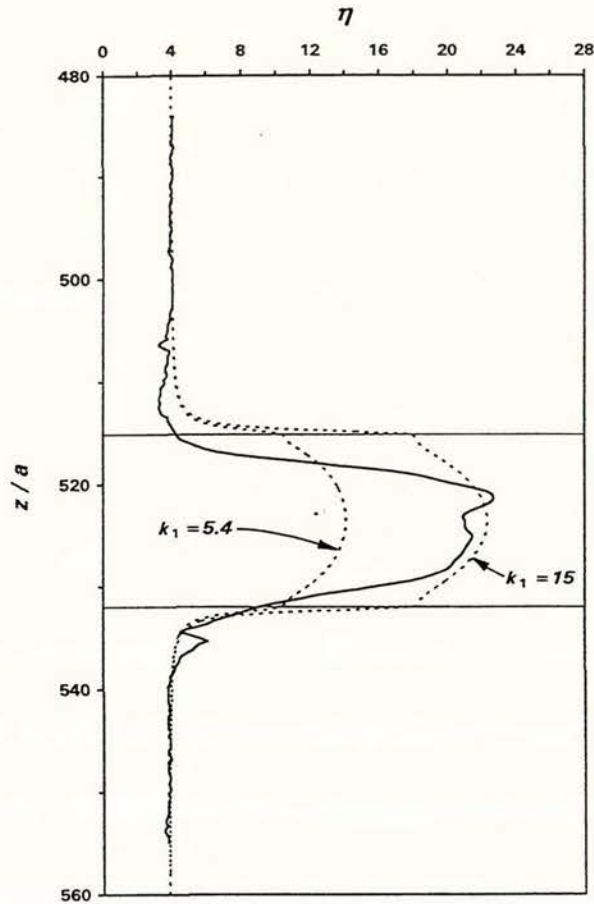


Figure 6.12 Enlargement from Figure 6.11 showing comparisons with theoretical response for $k_1 = 5.4$ and $k_1 = 15$

halted for a brief time in order that a new drill rod be added to the string. This would have resulted in an unload/reload situation at the cone tip, and possibly distorted the experimental results near the base of the layer.

6.5.2 Soil Strength Misclassification

As a second example, consider how this correction for layering effects might alter the results of liquefaction potential analyses which utilise CPTU records. Figure 6.13 shows part of the CPTU record from Test 6, one of the eight probes conducted at the Miller's Farm site alongside the Pajaro River (refer Figure 2.6). Raw cone resistance, friction ratio and pore water pressure have been plotted, along with lines of critical q_c evaluated using the five liquefaction prediction models described in Chapter 4. It is evident from Figure 6.13 that all of the models predict that the soil between depths 5.75 metres and 6 metres is likely to have liquefied during the Loma Prieta earthquake. However, three of the models also predict liquefaction of a thin, stiff layer at a depth of 9.25 metres. The segment of the record between 9 metres and 9.5 metres will be modeled in the same manner as in the previous example.

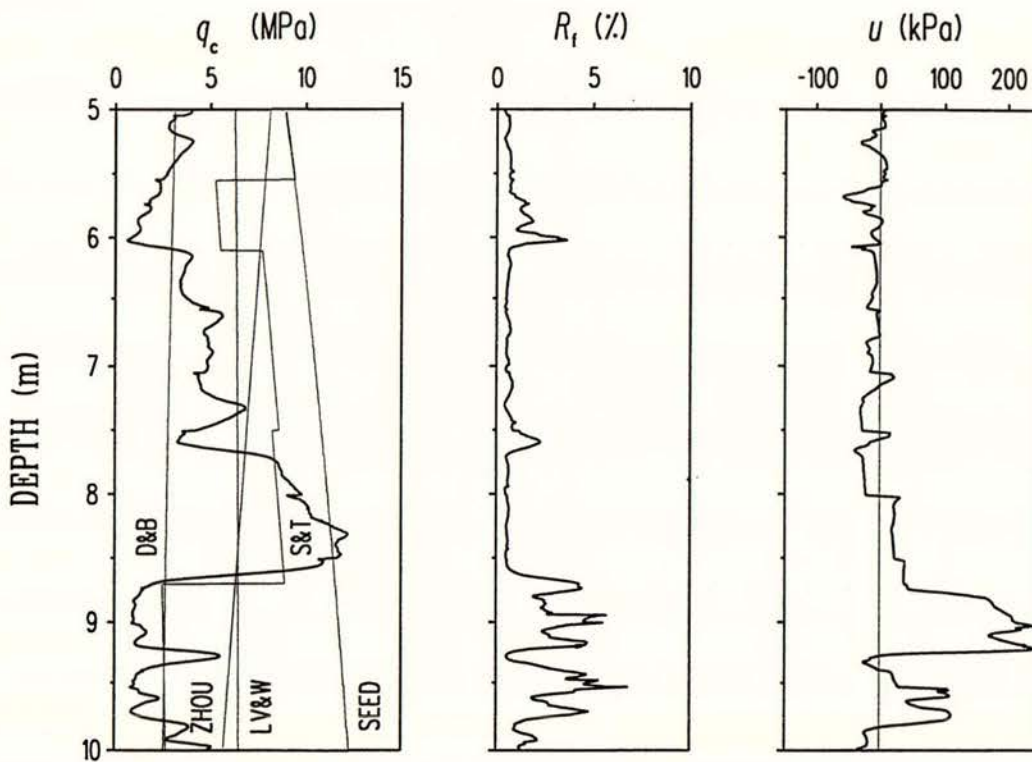


Figure 6.13 Section of CPTU record from Miller's Farm (Test 6). Critical q_c lines have been included from five liquefaction potential analyses.

The CPTU was conducted using the same standard 10 cm^2 cone. Once again, equation (6.8) is used to convert the raw q_c values to dimensionless cone resistance, scaled so that $\eta = 4$ in the soil above the thin stiff layer by setting $G_1\delta$ equal to $6.37 \text{ MPa}\cdot\text{mm}$. The pore water pressure record was used to determine the position of the upper and lower layer interfaces. Depths were referred to the shoulder of the cone rather than to the tip. The theoretical solution was calculated using an initial value of $k_1 = 3.9$, chosen on the basis of the perceived values of q_c in the soft soil and in the thin, stiff layer. As in the previous example, this calculation severely underestimates the resistance in the layer as shown in Figure 6.14.

A second value of $k_1 = 8.4$ was then chosen, on the supposition that the thin layer might be of the same material as the stiff layer between 8 metres and 8.5 metres. This assumption is supported to some extent by the similarity between the R_f and u records in this region and in the layer. The theoretical curve is shown in Figure 6.14. Although it matches the field record more closely, the resistance is still underestimated, and a better estimate could be obtained by further trial and error. Nevertheless, it is reasonable to conclude that the thin layer soil is at least as stiff as the material between 8 metres and 8.5 metres, and that it is therefore unlikely to be susceptible to liquefaction.

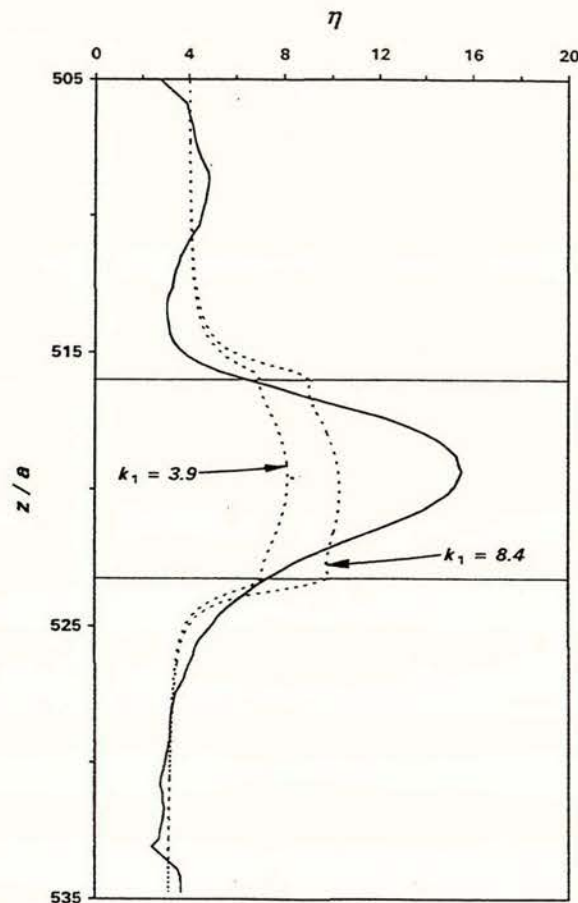


Figure 6.14 Enlargement from Figure 6.13 showing comparisons with theoretical response for two stiffness ratios

It is important to note that in the context of the elastic analysis presented here, the layer of material between 8 metres and 8.5 metres should also be considered as "thin". It is probable that the perceived resistance of this layer, shown in Figure 6.13 to be approximately 11 MPa, is less than the resistance that would be recorded in a thick layer of this material at the same density. It is, therefore, still possible that the material of this layer and the thin layer at 9.25 metres is the same.

6.6 RAMIFICATIONS OF MODEL

The above examples of misclassification demonstrate that cone resistance values recorded during field testing may be misleading if layer thickness and relative stiffness are not taken into account. Care must be taken when using soil classification charts based on CPTU parameters to avoid this error. Similarly, when assessing the liquefaction potential of a layer of soil by its resistance to penetration, allowance must be made for the effect of layer thickness and relative stiffness. As shown, it is possible that a thin layer might be classified as susceptible to

liquefaction based on perceived cone data, whereas, in fact, it is sufficiently dense to be not liquefiable.

Misclassifying a layer as liquefiable when in reality it is not liquefiable appears to be a conservative error from considerations of safety. However, it is unconservative from considerations of time and finance required to treat the supposedly liquefiable soil. More importantly, a serious problem is raised by this analysis concerning the "average" layer thickness of data sets used in calibrating liquefaction models. A large number of calibration data from thin layers would have the effect of making a model unconservative when applied to thicker layers. For example, consider the case of a thin layer with a measured resistance of $q_c = 4$ MPa and a true resistance of 10 MPa, recorded at a site which failed to liquefy during a given earthquake. At first glance, it would appear that any material registering a resistance of at least 4 MPa would not be susceptible to liquefaction in a similar, future seismic event. If this incorrect information is used to calibrate liquefaction models, the model may yield an unconservative estimate of critical cone resistance.

6.7 SUMMARY

In this Chapter, a simple elastic analysis has been presented to explain how cone penetration resistance may be affected by the presence of nearby layers of soil with different stiffness characteristics. The approximate analysis is based on the superposition of integrated Boussinesq solutions. It is suggested that the penetration resistance may sense nearby layers elastically, and comparisons with experimental data obtained in calibration chamber experiments and in the field support this. The analysis has clear implications concerning the interpretation of cone data for soil classification, particularly where strength or liquefaction potential of thin layers happens to be under consideration. The simple elastic analysis presented here allows a more reliable and realistic interpretation of any cone penetration data.

Referring to the examples given in Section 6.5, correction of the second CPTU profile was more difficult than the first. This makes apparent the need for a general inversion procedure for cone resistance recorded in multilayered soils with arbitrary layer thickness and stiffness. A potential solution to this problem is investigated in Chapter 8. Chapter 7 focuses on interpretation and resolution of sleeve friction and cone resistance.

7

Resolution of Sleeve Friction and Cone Resistance

7.1 INTRODUCTION

Sleeve friction response is essentially an interface phenomenon. The sleeve friction measured by a penetrating cone is primarily due to a combination of peripheral shear and an increase in normal (radial) stress due to the displacement of soil during penetration, both of which are localised effects. Thus, in contrast to cone resistance which is strongly influenced by the properties of the soil ahead and behind the cone tip, friction measurements yield information principally about the properties of the remoulded soil in direct contact with the sleeve.

Like cone resistance, sleeve friction recorded during penetration testing is influenced by soil layering. However, the localised nature of the measurement allows the effects of soil layering to be more easily understood for the case of sleeve friction than cone resistance. In this Chapter, the nature of the sleeve friction function is discussed, and a comparison is made between q_c and f_s resolution in light of the approximate solution presented in Chapter 6. In addition, results are presented from a statistical analysis performed on the California CPTU data to determine lag between q_c and f_s .

7.2 SLEEVE FRICTION RESPONSE TO SOIL LAYERING

Boulon (1991) has conducted extensive research at the IMG, France, on the behaviour of interfaces between granular soils and structures, with particular emphasis on the prediction of

lateral friction on piles. The results of this research are useful for developing an understanding of sleeve friction during cone penetration testing.

Pile tests in pluviated sand samples have shown that during pile penetration, large shear displacements are localised in a very thin zone of about ten times the mean grain diameter, close to the pile shaft. This zone is referred to as the interface layer. The properties of the soil comprising the thin interface layer, and the level of applied normal or radial stress, determine the amount of friction developed. The soil mass beyond the interface layer of a penetrating pile contributes very little to the measured skin friction. This result can be directly related to sleeve friction measured during cone penetration testing.

Because sleeve friction depends solely on local soil properties, the response of f_s as the cone encounters an interface between two soils is more easily understood than the response of q_c . In such a situation, measured values of f_s should be directly proportional to the length of sleeve in contact with each material. Thus, when passing through an interface from one soil to another, we expect a ramp-like response in the f_s function. Sleeve friction will remain constant while the sleeve is within a homogenous soil layer, so that there is no change in the f_s function as the cone approaches a boundary between two different soils. However, as soon as the sleeve encounters the new material, its response will begin to change from the steady-state friction resistance of material 1 to the steady-state friction resistance of material 2. The linear, ramp-like transition is complete as soon as the entire sleeve has entered material 2. This idealised response does not take into account the small, but real effect of increasing horizontal stress with depth, or any change in position of the interface due to remoulding of the soil during penetration.

The above response is observed in field records, and an example is given later in this Chapter. Due to the systematic, linearly proportional nature of sleeve friction response, it should be possible to deconvolve sleeve friction data to remove the ramp-like features which occur across soil layer interfaces.

7.3 RESOLUTION OF SLEEVE FRICTION AND CONE RESISTANCE

In Chapter 6, the approximate solution developed to simulate the elastic effects of layering on cone resistance was applied to symmetric cases of soil layering, illustrating how the perceived resistance of an isolated thin layer may be incorrect and may lead to misclassification of the soil. The problem of soil misclassification, however, is not limited to symmetric cases of soil layering. In this Section, the resolution of sleeve friction is compared against that of cone resistance, for cases of asymmetric layering.

7.3.1 Cone Resistance Behaviour for Asymmetric Layering

Consider the asymmetric three layer case where $1 < k_1 < k_2$, so that the layers increase in stiffness with depth. Figure 7.1(a) shows the specific case where $k_1 = 2$ and $k_2 = 3$. Each layer is of dimensionless thickness $50a$, where a is cone radius. The fully developed values for η of 4, 8 and 12 in layers 1, 2 and 3 respectively are clearly visible in the figure, along with the transition at each interface. The transition zones at each interface reduce the distance of steady-state cone resistance registered in layer 2 from $50a$ to approximately $35a$.

If the overall thickness of the intermediate layer is reduced, however, the distance over which it displays a steady-state value of resistance also reduces. At some critical value of thickness the intermediate layer will not be detected by the cone as a distinct layer, as it will appear to merge with materials 1 and 3. Instead of correctly indicating the presence of a distinct intermediate layer, the cone resistance record will infer that the boundary between materials 1 and 3 is graded. This effect is modeled in Figure 7.1(b). This figure illustrates the same situation as Figure 7.1(a), only the thickness of the intermediate layer has been decreased to $7a$, and as a result the layer is not clearly defined. This analysis shows it is possible that sections

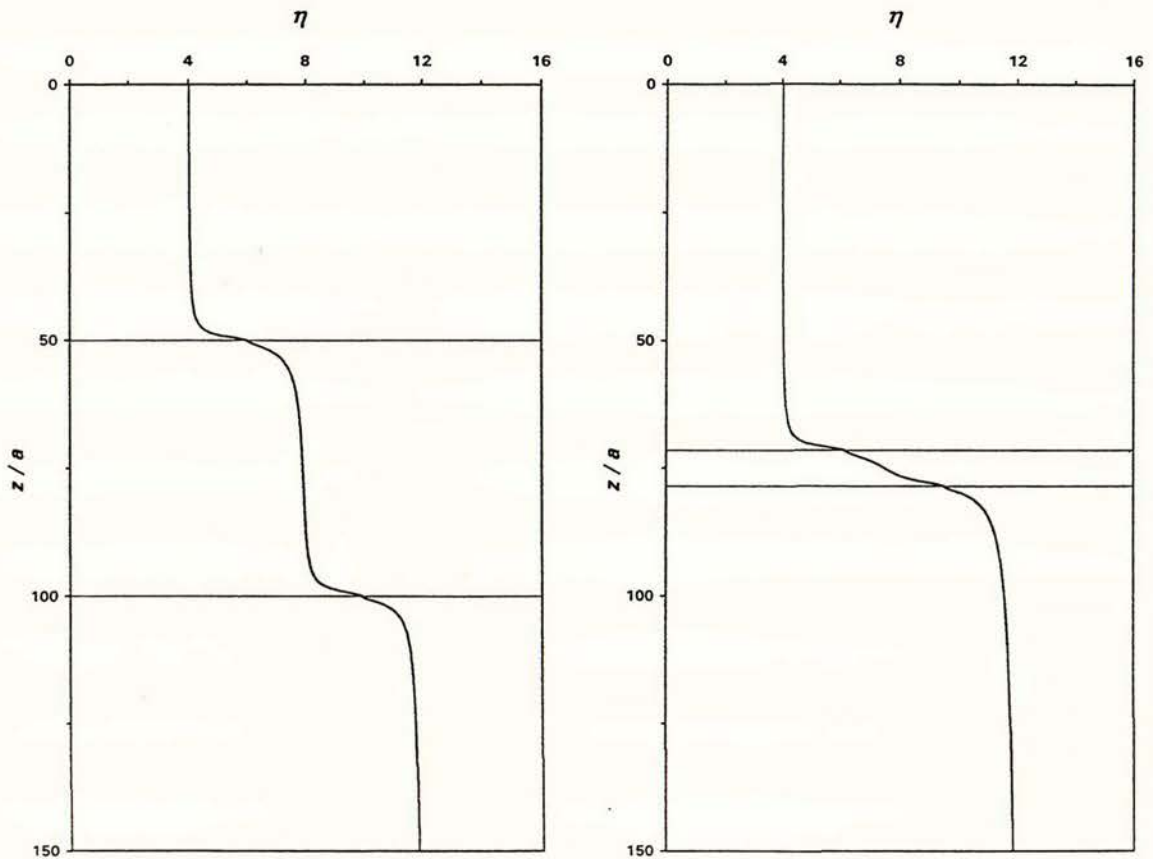


Figure 7.1 Effect of reducing intermediate layer thickness for asymmetric case:

(a) $H/a = 50a$; (b) $H/a = 7a$

of cone resistance records which show gradual changes in resistance with depth may in fact be misrepresenting distinct soil layering. Clearly, it is more difficult to correct cone resistance records for this asymmetric layering effect than for the symmetric layering effect described in the previous Chapter. However, referring to Figure 7.1(b) for a moment, note there are slope inflexions in the η function within material 2. It may be that such inflexions will aid in the detection of an interbedded layer of intermediate stiffness in field records.

The layer thickness of $7a$ given in the above example at which the intermediate layer merged with the surrounding materials is specific to the values of stiffness ratios used. For example, if $k_1 = 5$ and $k_2 = 10$ then the critical layer thickness at which the intermediate layer is hidden increases from $7a$ to approximately $10a$. This is consistent with results from the symmetric case analysis of the previous Chapter: as k_1 increases, the required thickness of the intermediate layer to achieve a certain percentage of steady-state resistance also increases. However, the relationship in this instance is more complicated, and cannot be easily generalised because of the additional variable, k_2 .

There are obvious ramifications of the above analysis regarding the relative resolution of q_c and f_s . A standard 10 square centimetre cone generally has a friction sleeve of area 150 square centimetres. This corresponds to a sleeve length of 13.4 cm, or $7.5a$. The resolution of sleeve friction, therefore, should not exceed $7.5a$. In fact, sleeve friction resolution can be improved to substantially less than $7.5a$ if the soil is homogeneous and the layer interfaces well defined, by deconvolving the friction record as suggested earlier. In contrast, the elastic analysis of Chapter 6 suggests the resolution of cone resistance in layered soils is highly variable and frequently exceeds $7.5a$ if there is a large difference between layer stiffnesses. In spite of greater resolution, however, sleeve friction conveys less meaningful information about soil strength than cone resistance.

7.3.2 Analysis of CPTU Data for Test 19

Instances of the above behaviour are observed in CPTU records. Figure 7.2 shows a section of CPTU record from the second test at the Jefferson site, Test 19. Cone resistance between 2.6 metres and 3.8 metres is shown in Figure 7.2(a), while Figure 7.2(b) shows the raw sleeve friction record (not lagged). At first glance, the cone resistance record suggests there are two soil layers present, an upper layer with average resistance of approximately 2 MPa, and a lower layer with average resistance of approximately 7.5 MPa. Between the two layers there appears to be a smooth, well graded transition zone. However, the raw sleeve friction shown in Figure 7.2(b) suggests that three distinct soil layers are present. Three steady-state plateaux are visible in the f_s function, with resistance increasing from approximately 14 kPa to 23 kPa, and again from 23 kPa to 35 kPa. Linear, ramp-like transitions are visible between the plateaux.

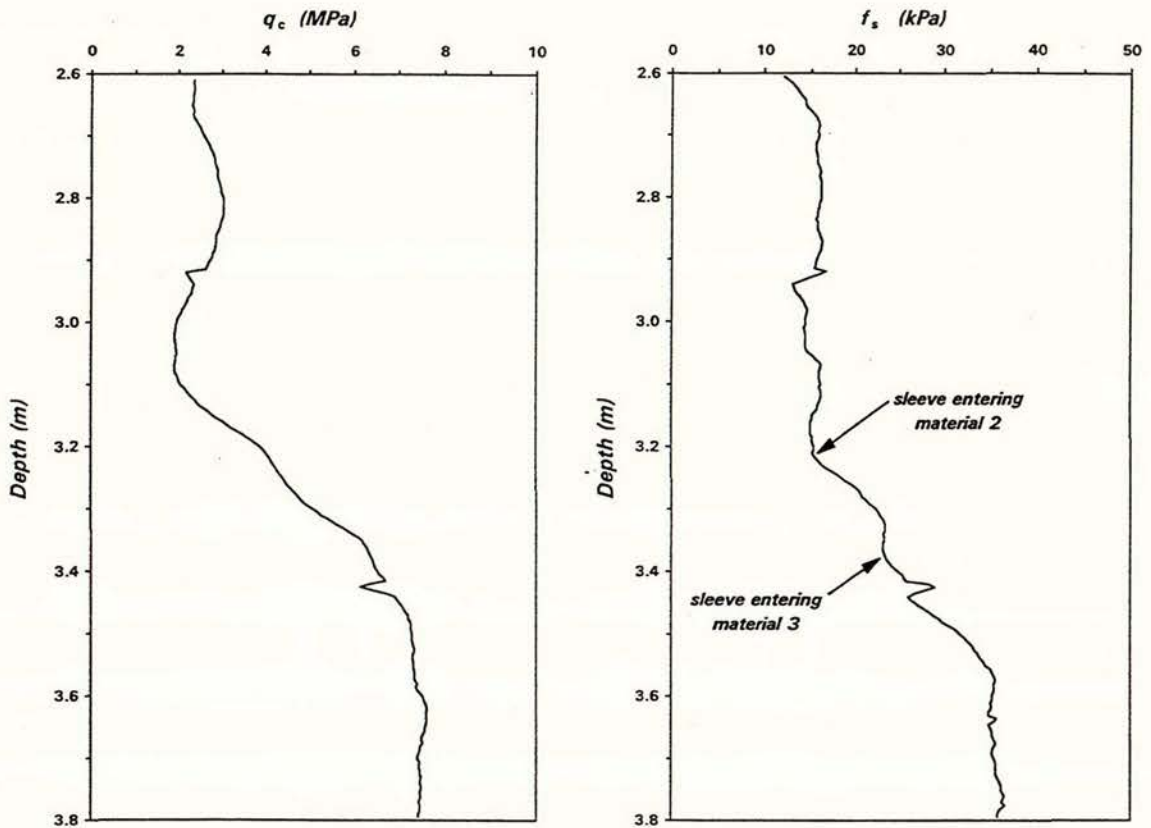


Figure 7.2 Section of CPTU record for Test 19 at Jefferson:
 (a) cone resistance; (b) raw sleeve friction (not lagged)

Furthermore, the first transition occurs over a depth of approximately 130 mm, the length of the sleeve. The second transition, however, occurs over a slightly greater depth; this point is discussed further below. Before employing the approximate solution to model this asymmetric layering case, it is necessary to establish accurately the positions of the two layer interfaces.

From the raw sleeve friction data, we see the sleeve encountered the first interface when the cone tip was at a depth of 3.200 metres. Since the tip and the leading edge of the sleeve are physically separated by a distance of approximately 50 mm or $3a$, we can conclude that the position of the first interface is at depth 3.150 metres. The raw sleeve friction data clearly yields the thickness of the intermediate layer (the distance from the start of the first ramp to the start of the second ramp) as 180 mm, approximately $10a$. Hence, the position of the interface between materials 2 and 3 is at depth 3.330 metres. Note that in Figure 7.2(b), the midpoint of the first ramp occurs at a depth of 3.265 metres. This yields a value for lag between q_c and f_s of approximately 115 mm. The following section will show that 115 mm is a reasonable value for lag in soils with average $q_c = 4$ MPa.

It is now possible to apply the approximate solution to this record, and assess how the cone resistance will be affected by the asymmetric layering. Having determined the positions of the two layer interfaces, all that remains is to estimate the stiffness ratios. Once again, these are estimated as the ratio of the average middle-third resistance in each layer, to the average middle-third resistance in layer one. This yields a value for k_1 of 2.04 and a value for k_2 of 3.51. The measured cone resistance is made dimensionless by multiplying q_c by the cone radius, 17.84 mm, and dividing by the factor $G_1 \delta$, which is calculated to be 9.41 MPa·mm.

Figure 7.3 shows there is good agreement between the dimensionless penetration resistance and the corresponding theoretical solution. The approximate solution predicts the intermediate layer will not develop steady-state resistance, and will be concealed in the transition from material 1 to material 3. In this case, therefore, the resolution of f_s exceeds that of q_c . It is also evident from Figure 7.3 that the curvature of the elastic solution matches the curvature of the measured cone resistance in the intermediate layer. Points of slope inflexion in the dimensionless resistance curve in material 2 are matched at the same depths by slope inflexions in the approximate solution, although the inflexions in the dimensionless resistance curve are slightly

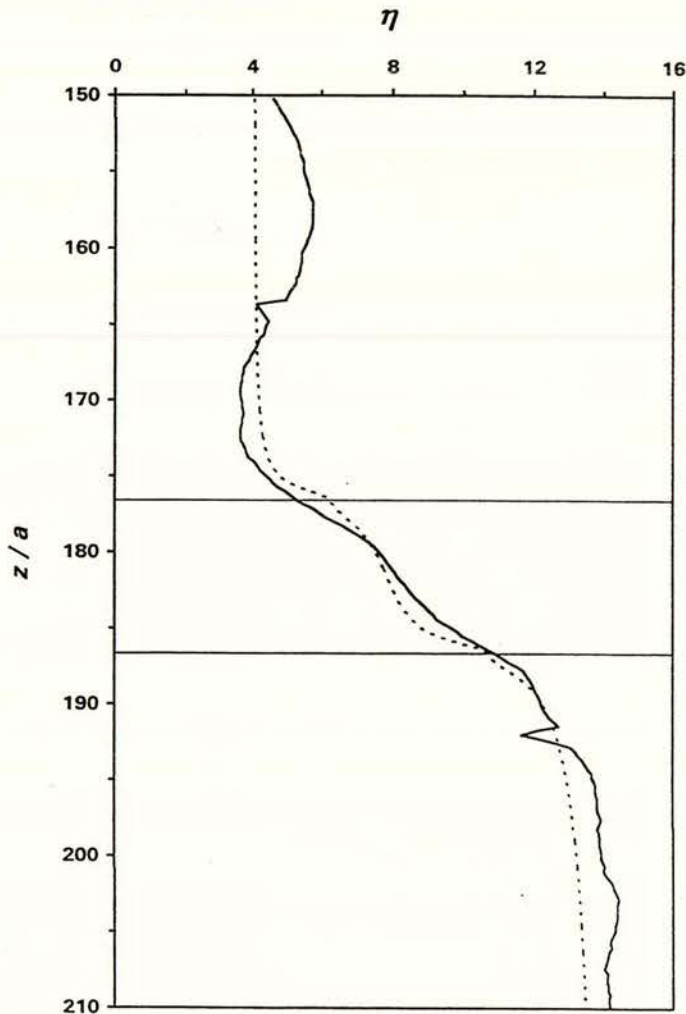


Figure 7.3 Comparison between field data and approximate solution

less exaggerated than those in the approximate solution. It is possible that plastic yielding of the soil as it flows around the cone has the effect of smoothing the actual resistance data. There is no guarantee that the observed inflexions in the measured resistance are directly related to the elastic effects of soil layering. Nevertheless, such inflexions observed in cone data recorded in asymmetrically layered soils may indicate the presence of a concealed layer of intermediate stiffness.

Referring back to Figure 7.2(b) for a moment, we see that the linear, ramp-like transition into material 3 is not as short or smooth as the transition into material 2. This is, in part, due to a pause in the penetration at a depth of 3.425 metres while a new rod was added to the string. In addition, it is possible that there is some grading of soil within material 3, close to the interface. A small zone of increasing stiffness within material 3 would have the effect of extending the length of the sleeve friction transition zone. This would also explain why the approximate solution slightly underestimates the measured resistance in material 3. Inhomogeneities within material 3 should be more easily located if the raw sleeve friction data were deconvolved to remove the ramp-like features at soil layer interfaces, although systematic deconvolution has not been attempted in the course of this study.

7.4 THE QUESTION OF LAG

In addition to the pore water pressure effects discussed in Chapter 3, and the layering effects considered in this Chapter and in Chapters 5 and 6, there is a further possible source of misinterpretation of CPTU data. Data is relayed electronically from each channel of the cone in the ground to the logging computer, at set time intervals. During each of the probes conducted in California, the computer scanned the four cone channels and recorded the depth of the cone tip at approximately 0.3 second intervals. Because of the necessary physical separation of the cone sensing elements, however, each element of the data set collected references a different depth in the soil column. Thus, although q_c , u , and f_s readings are returned simultaneously, these readings are not associated with the same depth. For this reason it is necessary to choose a point of reference for depth measurement, and lag the data with respect to this point.

It is standard practice to measure depth with respect to the apex of the cone, assign q_c and u to this depth, and lag the f_s record accordingly. However, due to the elastic effects of layering it is unclear what point in the soil column a measured value of q_c refers to. It may be more accurate to use the mid-point of the friction sleeve or the mid-point of the pore-pressure filter as a reference point, and lag the cone resistance record, since both f_s and u are more localised measurements. Alternatively, it could be argued that depth measurement should be assigned to the cone shoulder rather than the tip, since the entire 10 square centimetre projected area of

the cone is first encountered by the soil at the shoulder. In addition, if the shoulder of the cone is used as a reference point, it would not be necessary to lag the pore water pressure record since the separation between the shoulder and filter mid-point is generally of the order of $a/2$ or less. If the cone shoulder is chosen as the depth reference point, it is still necessary to calculate the lag between q_c and f_s .

There is surprisingly little available information in penetration testing literature describing how to calculate the lag between q_c and f_s . Robertson (1982) suggests using a lag value of 100 mm for a standard cone, but cautions that this value may be an underestimate of the true lag in heavily interbedded or relatively stiff soils. The CPT International Reference Test Procedure states: "*Care shall be taken to calculate the friction ratio and/or the friction index for measurements of cone resistance and local side friction resistance at the same depth*" (De Beer *et al.*, 1988), without describing how to effect this. It is important to determine the true lag between q_c and f_s for the correct presentation of data, but more importantly because an incorrect lag value could introduce substantial errors into the calculation of raw friction ratio R_f or normalised friction ratio F_R , possibly leading to misclassification of the soil.

The problem of determining a value for lag between q_c and f_s is complicated by the fact that the relationship between cone resistance and sleeve friction is not simply one of negative correlation, since f_s is sensitive to soil density and fines content. Thus, f_s is likely to increase after q_c when the cone enters a dense sand layer, even though the sand may classify as clean. Figure 7.4 shows a portion of a CPTU record from Test 20, the first test at the Scattini site, which illustrates this.

A statistical cross-correlation analysis of q_c and f_s was performed on the Loma Prieta data set. The objective of the analysis was to investigate the variation in lag τ with soil stiffness, and to assess whether a single value of lag is representative of all soil types for the Fugro piezocone.

Bendat and Piersol (1986) give the formulation of the direct cross-correlation function that formed the basis of the analysis. Upon substitution of appropriate parameters, the unbiased estimate of the cross-correlation function at lag number $r = 0, 1, 2, \dots, m$ with $m < N$ is defined as

$$R_{q_c f_s}(r\Delta z) = \frac{1}{N-r} \sum_{n=1}^{N-r} q_{c_n} f_{s_{n+r}} \quad (7.1)$$

Here, N is the number of data points in a given field record, and r the lag number. Note that the depth increment Δz is used in place of the time increment Δt present in the original formulation. They are interchangeable if the rate of penetration is constant, since a constant increment in one corresponds to a constant increment in the other.

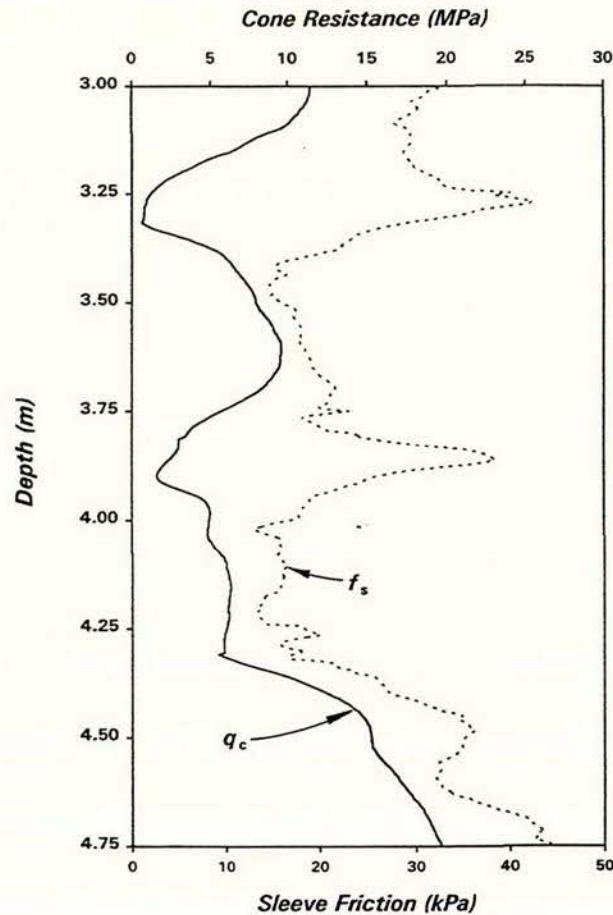


Figure 7.4 Section of CPTU record showing strong positive and negative correlation between q_c and f_s (lagged) for Test 20

Following a standard procedure, equation (7.1) was normalised to have values between positive and negative one, which defined the following cross-correlation coefficient function

$$\rho_{q_c f_s}(r\Delta z) = \frac{R_{q_c f_s}(r\Delta z)}{\sqrt{R_{q_c q_c}(0)}\sqrt{R_{f_s f_s}(0)}} \quad r = 0, 1, 2, \dots, m \quad (7.2)$$

Computer code based on linear interpolation was generated to standardise the data files to a depth scale incrementing in multiples of $\Delta z = 5$ mm, and to calculate the cross-correlation coefficient function. A simple relationship was used to calculate τ in millimetres, namely $\tau = r\Delta z = 5r$.

The 35 California CPTU records were examined in their entirety, to determine the average value of τ corresponding to the maximum ρ for each test. An example of the resulting cross-correlation coefficient function for the second test at Airport Watsonville (Test 15) is shown in Figure 7.5, for the range $0 < \tau < 600$ mm. A peak value of $\rho = 0.862$ is evident in the

function at lag $\tau = 145$ mm. Of the 35 Loma Prieta records analysed, 19 others had similar distinct peaks. The average value of the normalised cross-correlation coefficient for these 20 sites was $\rho = 0.877$, at an average lag of $\tau = 164$ mm. The response of the remaining sites was more difficult to interpret, as the coefficient function peaked continuously over a large lag range for some records.

The high degree of correlation between the q_c and f_s data indicates that these parameters are measuring similar characteristics of the soil mass during penetration. This confirms the observation made earlier regarding positive and negative correlation between sleeve friction and cone resistance. On examining f_s records, it is apparent that sleeve friction behaviour is similar to cone resistance behaviour in all materials except very fine soils. Strong positive correlation between q_c and f_s exists in probes conducted in dense sands, whereas strong negative correlation exists only in sections of probes when cone resistance is less than approximately 2 MPa.

Following this general analysis, sections of each record that exhibited either strong positive or negative correlation between q_c and f_s were examined individually, to assess the dependence of lag τ on soil stiffness. The results of this analysis are illustrated in Figure 7.6, which shows

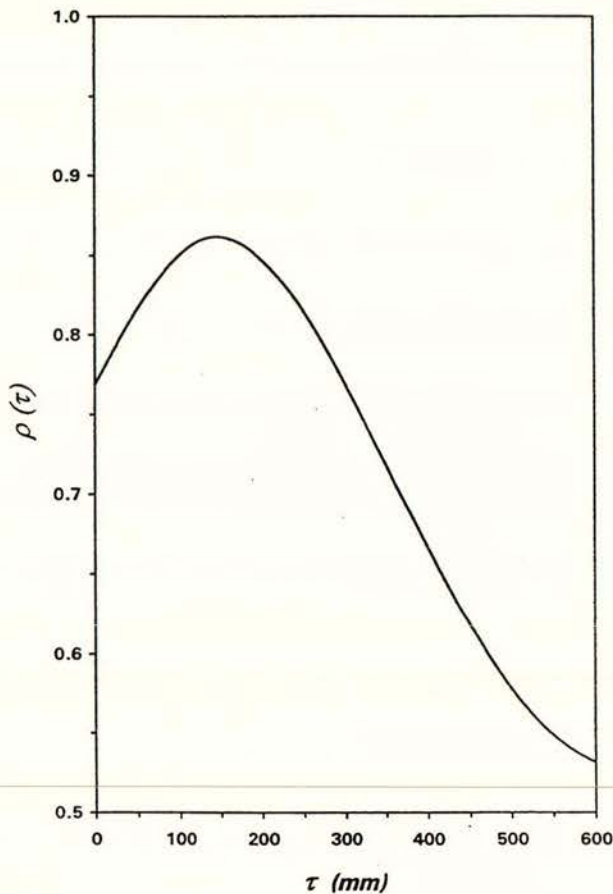


Figure 7.5 Normalised cross-correlation function (q_c versus f_s) for Test 15

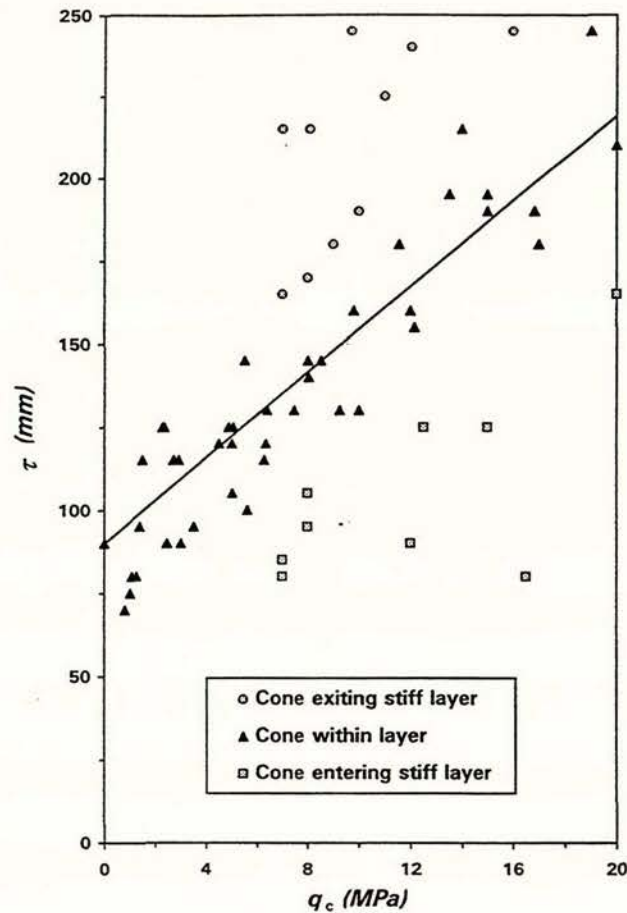


Figure 7.6 Dependence of lag τ on soil stiffness

three sets of data points, comprising a total of 62 short sections of record taken from the 35 California CPTU results. A trendline has been plotted through the central set of points. Each point in this data set corresponds to a value of lag calculated within a relatively homogeneous soil layer which exhibited either strong positive or negative correlation between q_c and f_s . Although there is some scatter of the results, a linear trendline matches the data well.

It is evident from the Figure that as soil stiffness increases, lag between q_c and f_s increases from a value of $\tau = 90$ mm at $q_c = 0$ MPa to a value of about $\tau = 210$ mm at $q_c = 20$ MPa. On the basis of this linear relationship, the expected value of lag for soils of $q_c = 4$ MPa is $\tau = 114$ mm, a result which agrees with the example given earlier in this Chapter.

The value of $\tau = 90$ mm at $q_c = 0$ MPa is significant, as it represents the physical distance between the mid-point of the sleeve and the shoulder of the cone. This is the theoretical minimum possible value for lag, representing the case of zero soil stiffness. The point of action for cone resistance will extend further ahead of the shoulder as soil stiffness increases, due to the displacement and flow of soil out and away from the cone face. However, values of lag less than 90 mm may be calculated in some situations. This apparent contradiction is due to the

cross-correlation function underestimating the lag between q_c and f_s when the cone passes from a soft to a stiff soil.

Under these circumstances, the elastic solution predicts quite different curvature of the q_c function either side of the interface, with the cone requiring a greater distance of penetration into the stiffer material to reach steady-state resistance. Because of this asymmetric curvature of the q_c function, the lag at which the highest degree of correlation occurs between q_c and f_s will not match the two curves at the interface. Instead, the f_s record will be best correlated with the q_c record below the interface, some distance into the stiffer material, resulting in an underestimation of the lag. The effect is exaggerated with increasing stiffness ratio. This situation is represented by the lower set of data points in Figure 7.6. The value of q_c reported for each of these points is that of the stiff layer, which controls the cone response. The converse of this scenario is also true. The cross-correlation function overestimates the lag between q_c and f_s when the cone passes from a stiff to a soft soil. Instances of this response are represented in Figure 7.6 by the upper set of data points. Once again the measured q_c refers to that of the stiff layer, which controls the cone response.

It is evident from the general analysis above, and the more specific analysis summarised in Figure 7.6, that a value for lag of $\tau \leq 120$ mm is reasonable when correcting probes conducted in soft clays or marine sediments with average $q_c \leq 4.5$ MPa. For stiffer materials, appropriately larger values for lag should be adopted. In particular, for sandy or silty soils with interbedded sand layers of average resistance $q_c = 10$ MPa, a value for lag of $\tau = 150$ mm is suggested. These values are transferable only for cones which have the same tip area, and the same sleeve area and position as the standard Fugro cone used during the California testing. A value of $\tau = 150$ mm has been used in the calculation of friction ratio R_f for all of the Loma Prieta CPTU records presented in Appendix A.

In the next Chapter, a method for inverting a cone resistance record is investigated, to determine the positions of layer interfaces within the record and corresponding stiffness ratios. The method employs the approximate solution developed in Chapter 6 within a Genetic Algorithm. Before moving on however, it is worth noting in passing that a cross-correlation analysis was performed on q_c and raw u records to determine if pore water pressure should be lagged with respect to cone resistance. The results of this analysis indicated that although the cross-correlation function occasionally peaked at a lag of less than approximately 40 mm, the degree of correlation between the two parameters was extremely low (ρ failed to exceed 0.1). There is, therefore, insufficient evidence to support lagging the u record with respect to the q_c record. However, the low degree of correlation between q_c and u confirms that these two parameters are independent or orthogonal, and represent different aspects of the soil mass response to penetration.

8

Optimisation of Approximate Solution by Genetic Algorithm

8.1 INTRODUCTION

It is possible to invert a cone resistance record to extract soil stiffness and layer thickness information, by making use of the approximate solution developed in Chapter 6. As seen in the examples of the previous chapters, the elastic effects of layering cause measured cone resistance to misrepresent true soil layer stiffnesses and thicknesses. Values for layer stiffness ratios and thicknesses, estimated by inversion, should yield a more accurate representation of the true soil profile than that indicated by the perceived penetration resistance. Soil stiffness information obtained through inversion may be useful in deformation analyses and settlement calculations. In addition, because it is possible to estimate the relative density of a soil from its stiffness, inversion could provide information on the state of strength of the soil which may also be useful in the assessment of liquefaction potential.

Thus far, the approximate solution has only been used to model simple, symmetric sections of field q_c records involving three layers. To calculate the response of the approximate solution under these circumstances, the stiffness ratio k_1 and the positions of the two soil layer interfaces were estimated from the CPTU data. Unfortunately, the reliability of such estimates is compromised to some extent because of the way in which CPTU data is affected by soil layering. These estimates of soil layer thickness and stiffness ratio may be improved by trial and error. However, it is preferable that an automated, iterative process be employed to determine the set of layer thicknesses and stiffness ratios which gives the best fit between the approximate solution and a cone resistance record. The Genetic Algorithm (GA) is a comparatively recently developed optimisation technique which is both powerful and flexible.

In this Chapter, an attempt is made to invert cone resistance records, using a Genetic Algorithm to optimise the approximate solution developed in Chapter 6.

8.2 THE GENETIC ALGORITHM

A Genetic Algorithm (GA) is a powerful, iterative search or optimisation procedure, modeled on the mechanics of evolutionary biology and genetics. Like other optimisation procedures, the object of a GA is to test the fit of a candidate solution for a given problem, generate an improved candidate solution, and repeat the process until an acceptable solution is found. The simplicity of GA structure renders it highly flexible, in that it can be applied to a wide variety of problems. Recently, GAs have been successfully applied to problems of optimisation (Schaffer *et al.*, 1989), pattern recognition (Ankenbrandt *et al.*, 1990) and inversion (Sen and Stoffa, 1992).

GAs were initially developed by Holland (1975), who used elementary concepts from the theory of evolution to develop solutions to problems involving numerical computation. In spite of the simplicity of the algorithms, GAs are powerful and robust, striking a good balance between effectiveness and efficiency. As a result, GAs are characterised by rapid convergence to a global optimum within a search space. The text by Goldberg (1989) provides a comprehensive review of GA mechanics, which is summarised below.

An outline of the genetic algorithm is presented in Figure 8.1. The overall structure of a GA is simple, as is evident from the Figure. The first step in the algorithm involves the random generation of a population of individuals, each of which represents a candidate solution for the problem being solved. Next, the merit of each individual is assessed. The "best" individuals,

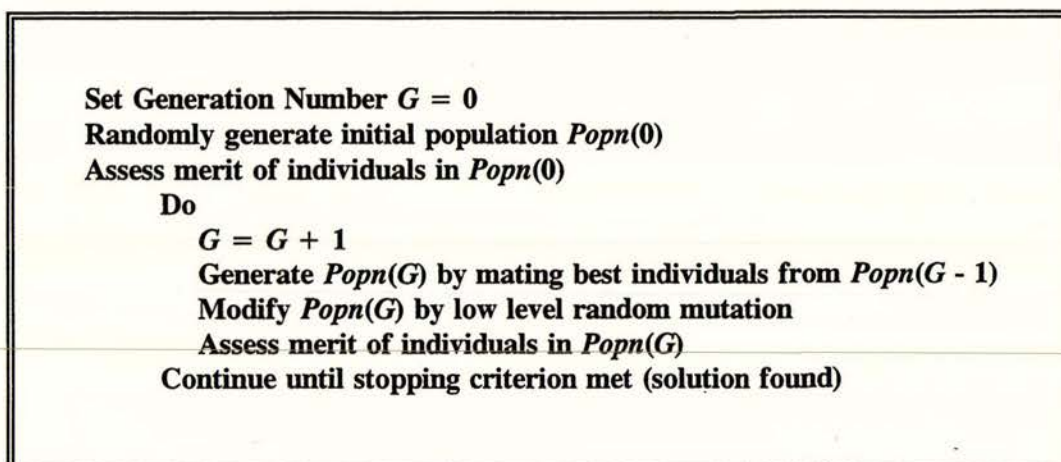


Figure 8.1 Fundamental GA structure

those who have the highest level of fitness, are selected to breed from, generating a new population of individuals for the next generation. Individual merit is reassessed and, once again, the best individuals are selected to breed from. This process of selection and breeding continues until a solution is found, which occurs when the stopping criterion is met. The stopping criterion for the algorithm is flexible. A GA can terminate either when all the individuals are the same, or after a specified number of generations, or after a set amount of time has elapsed, or once the error between the solution (as represented by the best individual) and the actual data being modeled has fallen below a preset limiting value.

According to Goldberg (1989), GAs differ from classical gradient search techniques and conventional search and optimisation procedures in four ways. Firstly, they work with a coding of the parameter set, rather than the parameters themselves. Secondly, they search from a population of points, rather than a single point. Because GAs use a large database of points simultaneously, they are able to search large spaces quickly. Thirdly, GAs operate without specific knowledge of the problem being solved. A GA only interacts with the problem itself during the stage where a figure of merit is assigned to each individual. At this stage, a fitness function or objective function links the GA with the problem domain. Fourthly, GAs use probabilistic rather than deterministic transition rules since they employ randomised operators. This contributes to GA robustness. However, although GAs are randomised, they are not random search algorithms. Research has shown that the ability of a GA to solve non-linear optimisation problems is far superior to the Monte Carlo "random walk" technique (Gallagher *et al.*, 1991). In contrast to Monte Carlo methods, information gathered by a GA from current search points is used to direct the following step in the search.

To employ a GA to solve a specific problem with a defined candidate solution, it is helpful to represent the problem in equivalent biological terms. Each parameter within a candidate solution is termed a chromosome, and is represented as a string of characters from a selected alphabet. In general, the binary alphabet $\{0,1\}$ is favoured for ease of representation and computation. The characters comprising a chromosome are the genes, and the position of a gene on a chromosome is its locus. The value assigned to a gene is known as an allele. Using binary coding, there are two possible alleles that a gene can assume, 0 or 1.

Generally, a candidate solution consisting of n parameters is represented as an individual organism with n chromosomes. Several organisms comprise a population, and successive populations are called generations. Every generation is one iteration of the overall algorithm. In some instances, however, it may be preferable to allow each chromosome to represent an individual organism. For such cases, a candidate solution consisting of n parameters is represented as a family of n individual organisms, with several families comprising a population.

The three main genetic recombination operators employed in a GA are reproduction, crossover and mutation. A fitness function assigns a figure of merit to each organism or family of organisms. Natural selection is then used to determine which strings are selected to breed and which strings continue on to the next generation intact. Rules are established governing how often any individual may breed. After selecting which strings to breed, crossover takes place. Two strings are randomly selected from the mating pool and undergo crossover at a random site or locus, by swapping the sub-strings beyond the crossover site. Following breeding some of the offspring will undergo a mutation, where the value of a randomly selected gene is altered to a different allele. While selective breeding takes advantage of positive characteristics in individuals within the current generation, mutation offers an opportunity for new genetic material to be introduced into a population.

To demonstrate the above operations, consider the example illustrated in Figure 8.2 which shows a single generation of a GA with a population of four individuals. The object of this GA is to search the integer set $[0, 255]$ for the target integer value 130. To achieve this, the fitness function determines the absolute value of the difference between an individual and the target, and uses this information to rank the individuals from "best" to "worst", the best being the individual closest to the target. The two highest ranked individuals are then selected to breed twice, undergoing crossover at two random sites, and half of the offspring experience a single mutation, producing a new population for the next generation. Note the average population fitness improves from a value of 61.25 for generation 1 to a value of 47.5 for generation 2, illustrating convergence. The example demonstrates the simple, randomised mechanics of a GA. The problem could be further randomised by selecting two pairs to breed from the best three individuals, rather than breeding from the best two individuals twice. In addition, to avoid loss of information, the best individual in a population could be carried over into the next generation intact.

Additional refinements to the basic GA outlined in Figure 8.1 are possible. Low-level operators may be added, such as dominance, inversion, duplication, deletion, and restriction of mating (Goldberg, 1989). Hybrid optimisation schemes are also possible, which employ a GA globally then use a local search method. Such schemes capitalise on the ability of a GA to sort out interesting areas of a search space quickly, and avoid the problem of non-guaranteed convergence with a GA. For some problems, more rapidly converging optimisation procedures will exist. In general, however, these more rapid methods tend to be less flexible than GAs and are limited in their application, whereas GAs are universal.

8.2.1 Implicit Parallelism

Implicit parallelism is recognised as the driving mechanism of a GA (Grefenstette and Baker, 1989). In every generation, highly fit strings will have certain patterns or schemata which have

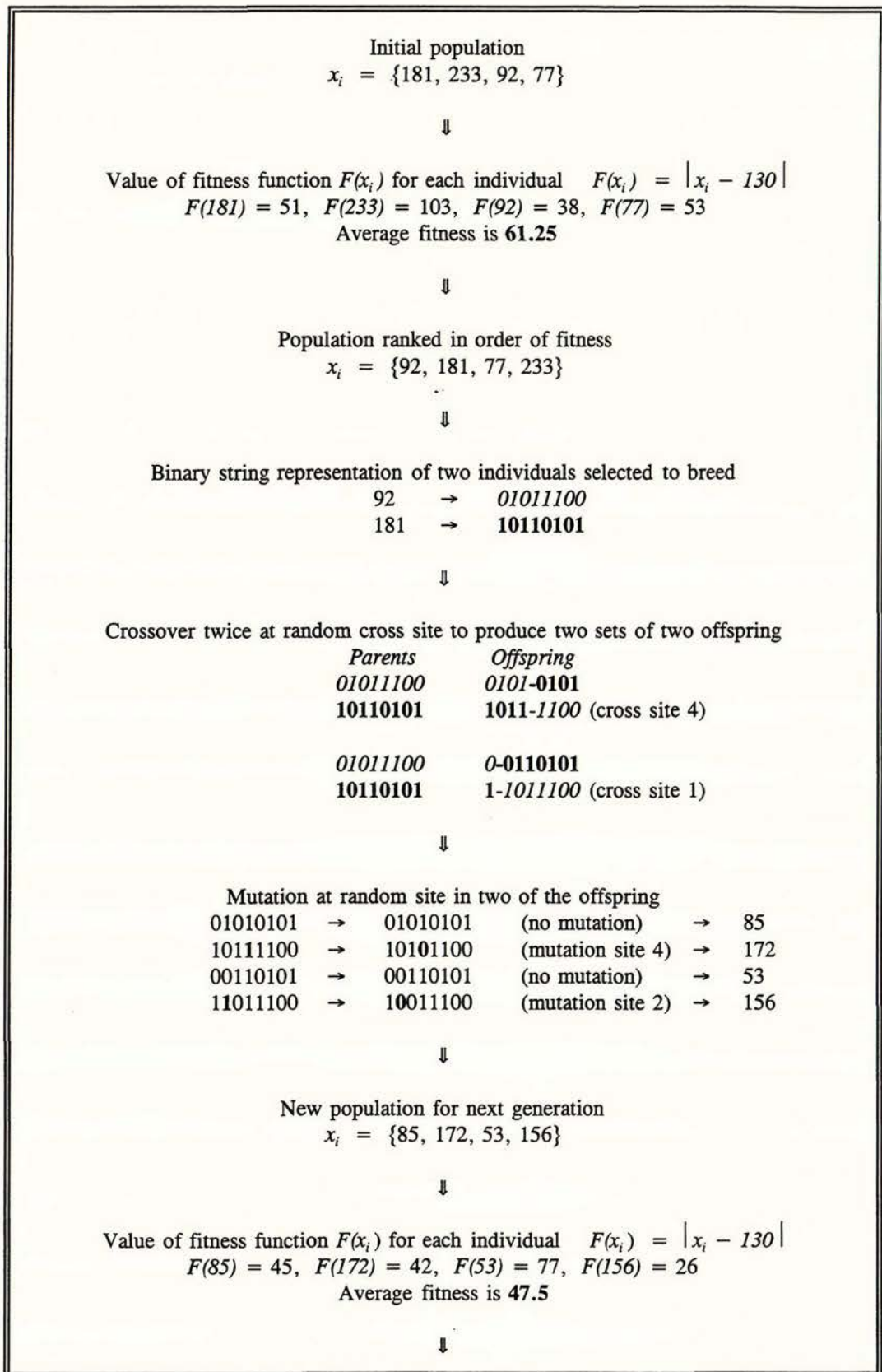


Figure 8.2 Illustration of genetic recombination operators for a simple GA

a high probability of being successfully propagated to the next generation during crossover, if they have a short defining length. For example, the strings *11001* and *10100* both contain the schemata *1★★★★*, *★★★0★* and *1★★0★* (the symbol "★" stands for "don't care"). The order of a schema is the number of non-★ characters it contains, and its length is the distance from the first to the last non-★ gene. Hence the schema *1★★0★* has a length of three and is of order two. During crossover the last of these three schemata is more likely to be disrupted than the first or second.

As several strings are explicitly processed during each generation, many more schemata are implicitly processed, and this gives a GA the large processing "leverage" or power referred to as implicit parallelism. The Schema Theorem, the fundamental theorem of GAs developed by Holland (1975), states that more fit schemata will appear with exponentially greater frequency in successive generations. Thus, although n structures are processed in each generation, approximately n^3 schemata are processed.

The effect of a GA is equivalent to an extensive search of hyperplanes within a given search space, without directly testing all the hyperplane values. To illustrate this concept, consider a GA employing strings of length three. Schemata of order three represent points in the search space, whereas schemata of order two represent lines, and schemata of order one represent planes. Generalising this result to strings of greater length, it is apparent that each schema represents a hyperplane in the search space. Thus, GAs search the solution space for improved performance, explicitly processing populations of strings, but implicitly processing schemata denoting hyperplanes.

Each individual organism or family of organisms represents a point in search space, an intersection of hyperplanes. This information sheds new light on the role of each of the three major genetic recombination operators. Selection designates hyperplanes of interest within the search space, culling regions of poor fit in the process. Breeding provides new points for further testing within hyperplanes already represented in the population. Mutation, however, introduces representatives of new hyperplanes into the population, ensuring connectedness of the search space. By using the three operators outlined above, GAs balance the need to explore new points within the search space and to exploit information discovered thus far.

8.2.2 Factors Affecting GA Performance

Users benefit from GA flexibility, since for any problem there exist many coding options. However, flexibility comes at a cost. Before coding a specific problem, there is no way of knowing the parameter settings that will give rise to the fastest rate of convergence to a global optimum. This must either be determined by trial and error, or by some optimisation

technique. Research has been conducted, however, to determine the parameters which strongly influence GA performance (Grefenstette and Baker, 1989; Goldberg, 1989b).

Because GAs essentially process populations of strings, population size and string length will affect GA performance. The number of generations, and whether there is overlap between generations are also factors which will affect GA convergence. Other important variables include how the fitness function is defined, how the mating process is established, and whether multiple crossover is allowed. In addition, performance is affected by the method of generation of the initial population, the choice of values for mutation and crossover probabilities, and whether these values remain constant during the GA.

Typically, GAs with randomly generated initial populations converge more slowly than those where the initial population is a "first guess". Large populations ensure better ultimate convergence since a larger pool of diverse schema exists. However, the initial performance of large populations can be quite poor due to large inertia. Smaller populations which can change more rapidly often perform better at the start. Optimum population size varies with respect to organism length, and with the rate of mutation. Often organism length is less flexible than population size. Good GA performance requires a moderate population size of around 30 to 50 individuals, but a population comprising 10 or less individuals may perform well if the mutation rate is comparatively high.

A greater number of generations tends to correlate positively with better convergence, since more candidate solutions have been examined. This is especially the case for GAs in which generation overlap exists. Carrying-over a "champion" individual intact to the next generation prevents loss of information gained thus far in the search. GAs with no generation overlap have no insurance against losing valuable schema.

In general, better GA performance is likely if the crossover and mutation operators are assigned high and low values of occurrence probability respectively. The crossover operator facilitates the recombination of highly fit schema, and therefore should be assigned a probability of occurrence value in excess of 0.9. By contrast, the mutation operator provides an opportunity for new genetic material to enter the population.

According to Goldberg (1989), the mutation rate should be approximately equal to the inverse of population size, equivalent to a probability of occurrence of 0.03 or less. A high mutation rate may result in a random search. Alternatively, a low mutation rate may result in convergence to a wrong solution, a local rather than a global optimum. The exception to this is the case of small population size mentioned earlier, which may perform best with a mutation rate of 0.3 or higher.

8.3 GA APPLICATION TO CONE RESISTANCE MODELLING

Let us now turn our attention to the specific case of employing a GA to optimise the approximate solution of Chapter 6 for a typical field CPT profile. As mentioned earlier, GAs are very flexible, thus many options are available for coding this problem. A universal GA was coded, capable of partially or completely inverting a section of cone resistance record. Before applying the GA to sections of real cone resistance records, trials were conducted to establish reliable breeding rules and recombination operator probability levels for the GA, and to assess GA convergence for this optimisation problem. The trials were conducted on a 1.5 metre long, artificial, symmetric resistance record generated by the approximate solution. Before discussing the results of the trials, or the results of tests performed on sections of actual q_c records, a description of the approximate solution in a GA framework is given below.

8.3.1 The Approximate Solution in a GA Framework

The task of defining a candidate solution is a relatively simple one for the case of optimising the approximate solution presented in Chapter 6. To effect full inversion of a section of cone resistance record, two parameters are required to model each soil layer, a layer thickness and a stiffness ratio. Here layer i of n has a thickness of h_i and a stiffness ratio of k_{i-1} , consistent with the notation of previous chapters. The stiffness ratio of the uppermost soil layer is known to be $k_0 = 1$, by definition. Thus, $(2n - 1)$ parameters are required to simulate the elastic effects of layering on a section of cone resistance record with n layers.

Each of the $\{k_{i-1}, h_i\}$ sets with $(2n - 1)$ elements represents one candidate solution. However, for the special case of partial inversion when layer thicknesses are known, a q_c record with n layers may be represented by a candidate solution comprising the set of stiffness ratios $\{k_{i-1}\}$, having $(n - 1)$ members. Adopting the biological terminology introduced earlier, each k and h value represents a chromosome made up of a string of binary characters. A pair of chromosomes (k_{i-1}, h_i) comprise an individual organism. An equivalent formulation is given by combining the k and h strings for one layer to form one long string or chromosome $(k_{i-1} h_i)$, representing a single organism for that layer. Combining the individual organisms yields a family, representing one candidate solution, and in each population there are several families. The reason for choosing this more detailed representation of a candidate solution as a family of individuals is discussed further below.

The approximate solution corresponding to a given candidate solution may be generated by making use of equations (6.7), (6.12) and (6.13). To simulate measured cone resistance, q_c is converted to dimensionless resistance η using equation (6.8); $G_1 \delta$ is calculated as outlined in Chapter 6. The goodness of fit of each candidate solution, or each family of organisms, is tested using a fitness or objective function. For a given depth while in layer i of n , the fitness

function determines the normalised root-mean-square deviation between the analytical solution and the real η data derived from the cone resistance record being modeled. The root-mean-square error is normalised by multiplying by the factor $\bar{q}_c / 4$, where \bar{q}_c is the average middle-third resistance of layer 1. This is necessary, since the error in the η domain is dependent on the choice of layer 1 resistance in the q_c domain. Normalisation, therefore, allows for meaningful comparison of results from optimisations performed on different cone records. Note that the fitness function outlined above is not unique, as several alternatives exist for calculating the fitness of a candidate solution. This particular function was chosen as a starting point for simplicity.

By calculating the goodness of fit for an entire candidate solution, essentially we are treating each candidate solution as an individual organism, represented by either $(2n - 1)$ chromosomes or a single large chromosome made up of $(2n - 1)$ sub-strings. For large families of more than five individuals, however, it is advisable to assess the goodness of fit of each layer. Although this increases the computational effort required to process each generation, it allows the algorithm to detect isolated layers of poor fit, which may negatively bias the overall performance of a candidate solution. This problem makes it necessary to represent a candidate solution as a family of individual organisms, rather than simply representing each candidate solution as an individual.

With the candidate solution and fitness function defined, an initial population of candidate solutions may be randomly generated to model a section of a cone resistance record, then the fitness of each individual organism (layer) within a family and of the family as a whole may be assessed. This information is used to rank the families in order of fitness. From this point, the genetic recombination operators of selection, breeding and mutation are engaged to create a new population for the next generation.

8.3.2 Preliminary Results from an Artificial Record

The first test of the GA was to fully invert an artificial 1.5 metre cone record. The approximate solution was used to generate the symmetric record, which comprised three soil layers of equal thickness $h = 0.5$ m, and a stiffness ratio of $k_1 = 5$. An initial population of eight candidate solutions was randomly chosen, each of the form $\{h_1, k_1, h_2, k_2, h_3\}$. Because of the small number of layers involved, the fitness function tested only the fit of the entire candidate solution, and neglected to test the fit of each individual layer.

The best four solutions were selected to breed seven new individuals. Rules were established to ensure that four different breeding pairs were chosen from the six combinations possible. Before breeding, each k and h value was converted to a binary string. With the crossover probability set at 1, all breeding pairs underwent a single crossover at a random site. Offspring

were subjected to a single mutation on occasions when the mutation criterion was met. Layer thicknesses were normalised when necessary, to ensure the overall depth of the three layers remained constant. The new population comprised the seven offspring and the best solution from the previous generation, which was carried over intact. The algorithm terminated when the fitness function returned a normalised error value less than the limiting value of $\epsilon = 0.0625$ MPa (equivalent to $\Delta\eta = 0.25$).

A range of different mutation probabilities were investigated using the same randomly generated initial population. The optimum mutation rate for this small population size was found to be 0.3. A total of 100 runs were conducted at this mutation rate. Based on the geometric mean of the resulting skew-symmetric distribution, approximately 150 generations were required on average for convergence. For lower and higher mutation rates of 0.2 and 0.5, the approximate average number of generations required for convergence was 180 and 650 respectively. As expected, the global rate of convergence is adversely affected by low or high values of mutation probability since, in the case of the former, no new genetic material is introduced into the population, and in the latter case, information gained from previous generations is often lost and the search approaches a random walk.

Figure 8.3 shows typical convergence of the GA for the mutation probability of 0.3. The stepwise convergence of the algorithm is obvious from the Figure, with the larger steps attributed to positive mutations. The best candidate solution from the randomly generated initial population, and the best solution from the population after 157 generations are presented in Table 8.1. The candidate solution to which the algorithm converged, with a normalised error of $\epsilon = 0.044$ MPa, compares very favourably with the actual solution presented in Table 8.1.

The above analysis was repeated for a larger population size of 30 candidate solutions. The optimum mutation rate for this larger population size was found to be 0.15. For this mutation rate, the algorithm converged on average after approximately 38 generations. Convergence worsened, as expected, for lower and higher mutation rates of 0.05 and 0.25. The approximate average number of generations required for convergence for these rates was 150 and 74 respectively.

The average number of generations required for GA convergence decreases with increasing population size as expected, since for larger populations a greater area of the search space is explored during each generation. However, as the population size increases, the computational effort required to process each generation also increases. Thus, although the algorithm may converge in fewer generations for larger populations, this does not guarantee a saving in computational effort.

	Best candidate solution from randomly generated initial population	Best candidate solution after 157 generations	Actual Solution
ϵ (MPa)	1.080	0.044	0
h_1 (mm)	232.5	500.2	500
k_1	7	4.88	5
h_2 (mm)	730	498.8	500
k_2	0.11	0.99	1
h_3 (mm)	537.5	501.0	500

Table 8.1 Candidate solutions for GA trial on artificial cone resistance record; mutation rate 0.3 (convergence history shown in Figure 8.3)

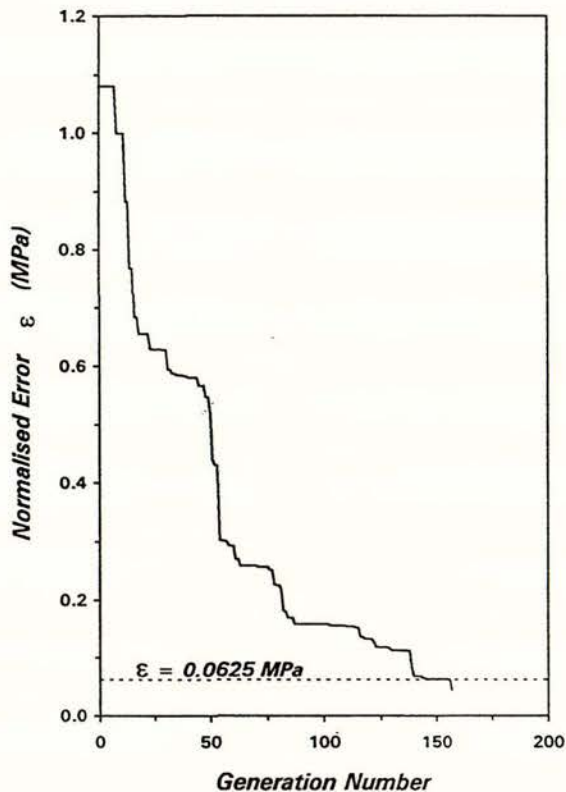


Figure 8.3 GA convergence history for artificial, symmetric layering case; mutation rate 0.3

8.3.3 Results from GA Application to Field q_c Records

The above investigation verified the ability of the coded GA to fully invert a symmetric section of an artificial cone resistance record, and provided information about the relationship between population size and mutation rate. Following this investigation, an attempt was made to fully invert multilayered sections of the California q_c data.

As discussed earlier, for cases involving five or more layers, treating a candidate solution as an individual may hinder convergence of the GA. A candidate solution may be assigned a poor fitness value even if the approximate solution closely matches the real data in all layers except one. To overcome this problem, the resolution of the fitness function was increased. For the multilayered tests, each layer was treated as an individual organism and assigned a fitness value, along with the candidate solution as a whole. Note that because of the connectedness of the approximate solution, the fitness of a given layer is not controlled solely by the thickness and stiffness ratio of that layer. Adjoining layer thicknesses and stiffness ratios will strongly influence the value of η recorded in a given layer. There is some merit in this approach, however, as it may enable the algorithm to discard spurious values of layer stiffness ratio.

Several trials were conducted on various multilayered sections of q_c records, using different combinations of population size and mutation rate. However, the global rate of convergence was slow, and the approximate solutions calculated from the best candidate solution after several thousand generations closely matched only short sections of the real resistance records. For these reasons, methods of partial inversion were investigated.

The first of these involved dividing the real resistance record into very thin layers of equal thickness, and determining the corresponding stiffness ratio profile. This method, however, suffered greatly from the problem of non-uniqueness of solution. As with many optimisation techniques, different candidate solutions may yield quite similar error values. We know from the results of previous chapters that values for resistance may be greatly underestimated for very thin, stiff layers. Because of this, the normalised error for stiff layers less than approximately $5a$ thick was found to be similar for several different values of stiffness ratio. In addition to the problem of non-uniqueness, the large number of layers involved markedly increased the amount of processing effort required.

A second method of partial inversion was attempted. This involved deducing layer thicknesses using the CPTU record, and borelog information where available, then inverting the resistance record for the stiffness ratios alone. This method of partial inversion was reasonably successful, in spite of the difficulties involved with accurately estimating interface positions from the CPTU records. Often more layers exist than that apparently indicated by a cone resistance record, as

demonstrated by the example of Chapter 7. Presented below are two examples of partial inversion of multilayered sections of real q_c records, based on this method.

The first example involves the same section of q_c record from Test 6 as that presented in the final example of Chapter 6, in which a thin layer was misclassified as liquefiable according to three of five liquefaction prediction models. A 13-layer section of the resistance record from 7.1 metres to 9.7 metres was modeled by the GA. The positions of the 12 interfaces were estimated from the CPTU data. An initial population of 30 candidate solutions, each comprising a set of 12 stiffness ratios $\{k_1, k_2, k_3, \dots, k_{10}, k_{11}, k_{12}\}$, was randomly generated.

Candidate solutions were ranked on their overall performance, and individual layers were also ranked on their performance. A new population of 28 candidate solutions was formed by breeding 14 times from a pool comprising the seven best performing candidate solutions, and seven sets of the best performing individual layers. This effectively increased the breeding pool, since offspring could be formed either by breeding from two different candidate solutions, or by breeding from parts of several different candidate solutions. The best overall candidate solution, and the best performing set of individual stiffness ratios, were carried over to the next generation intact.

After some investigation of initial convergence of the algorithm, the mutation operator probability was set equal to 0.3, reducing to 0.25 when the normalised error dropped below $\epsilon = 3$ MPa. Although these probabilities seem high for a population of 30 individuals, the GA appeared to converge consistently using these rates. The higher value for mutation rate of 0.3 was engaged at the start of the search to accelerate the sampling of information from all areas of the search space.

Several runs were conducted with the GA, all of which converged, but at varying rates. The convergence history for one of the trials is shown in Figure 8.4. The normalised error of the best candidate solution from the randomly generated starting population was $\epsilon = 5.03$ MPa. After 1110 generations, the normalised error of the best candidate solution had reduced to a value of $\epsilon = 0.79$ MPa. Comparisons between the approximate solution and the measured dimensionless resistance for these two candidate solutions are shown as insets on Figure 8.4. The curves on the lower of the two insets are quite closely matched, indicating good GA performance. However, the inset also shows that the stiffness ratios of layers 8 and 9 need to be interchanged, and that slight adjustment of some interface positions is required. Following these adjustments, the GA converged on a solution with normalised error $\epsilon = 0.64$ MPa within a few generations. The corresponding approximate solution shows good agreement with the measured dimensionless penetration resistance, as seen in Figure 8.5(a). Figure 8.5(b) illustrates the values of stiffness ratio to which the GA converged, along with the positions of the layer interfaces.

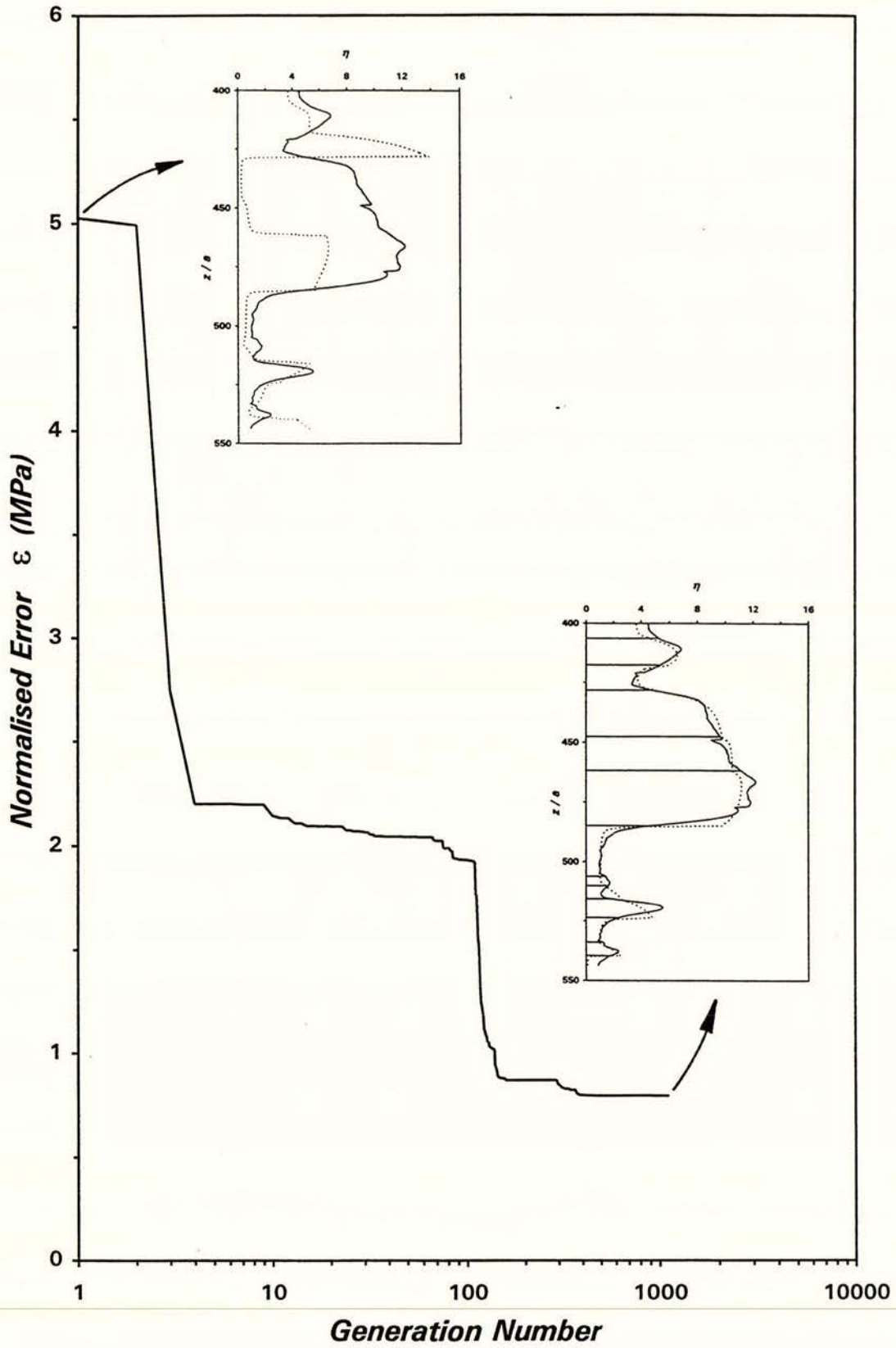


Figure 8.4 GA convergence history for partial inversion of 13-layer section of Test 6

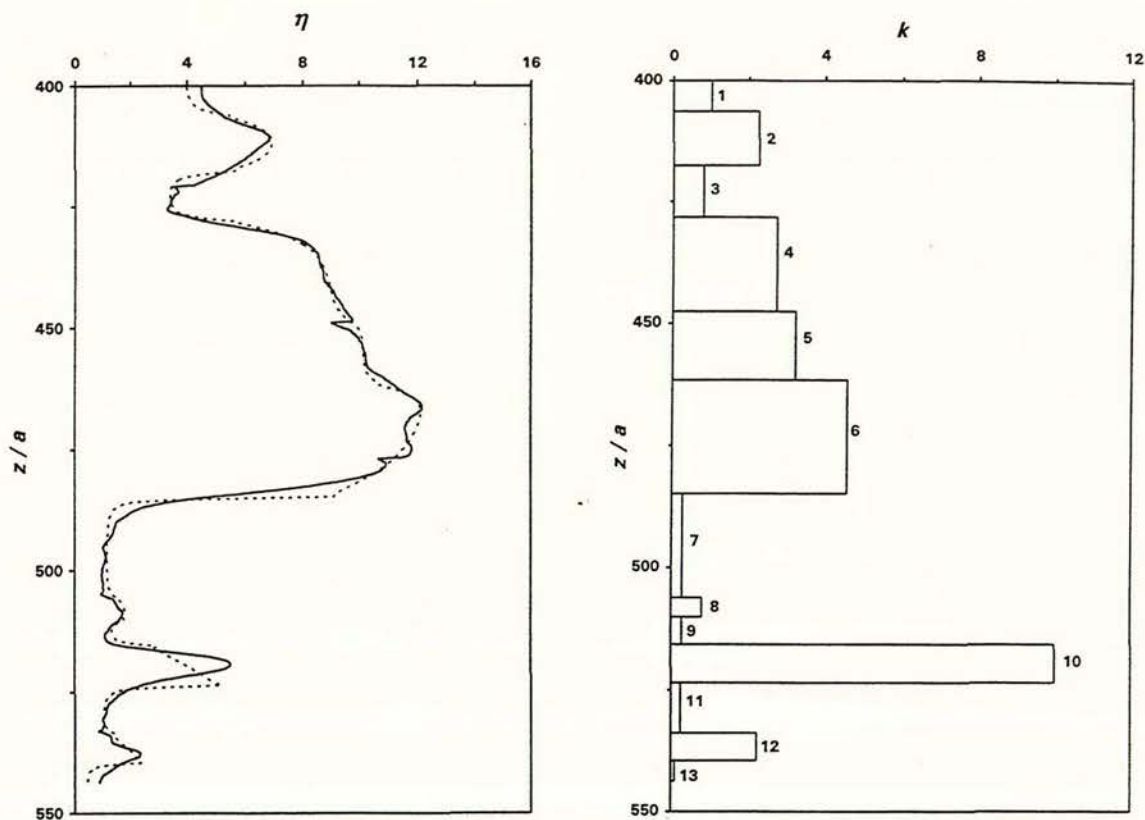


Figure 8.5 (a) Comparison between theoretical and measured resistance for 13-layer section of Test 6; (b) Corresponding stiffness ratio profile

It is evident from Figure 8.5(b) that layer 10, the thin layer at dimensionless depth $z/a = 520$, is in fact quite stiff, and would most certainly not be susceptible to liquefaction. In addition, it is interesting to note the behaviour of both the approximate solution and the measured resistance in layers 4, 5 and 6. According to Figure 8.5(b), these layers are asymmetrically arranged, similar to the examples presented and discussed in Chapter 7. The expected changes of curvature, due to the elastic effects of layering, are visible in Figure 8.5(a) in both curves with more pronounced curvature in the approximate solution. Clearly the middle layer of the three, layer 5, is too thin to evidence a steady-state value of resistance, despite having a thickness of $14a$.

The convergence history of the second, more complicated example of partial inversion is shown in Figure 8.6. A 3.8 metre long section of the Test 15 (Airport Watsonville site) cone resistance record was inverted for stiffness ratios. This was a more difficult inversion problem than the above example, since the record was divided into 24 layers between 4.9 metres and 8.7 metres, and the range of stiffness ratios was greater. Nevertheless, the GA was able to optimise the solution from an initial normalised error value of $\epsilon = 6.65$ MPa to a value of $\epsilon = 0.85$ MPa after 7898 generations. The initial population containing only eight candidate

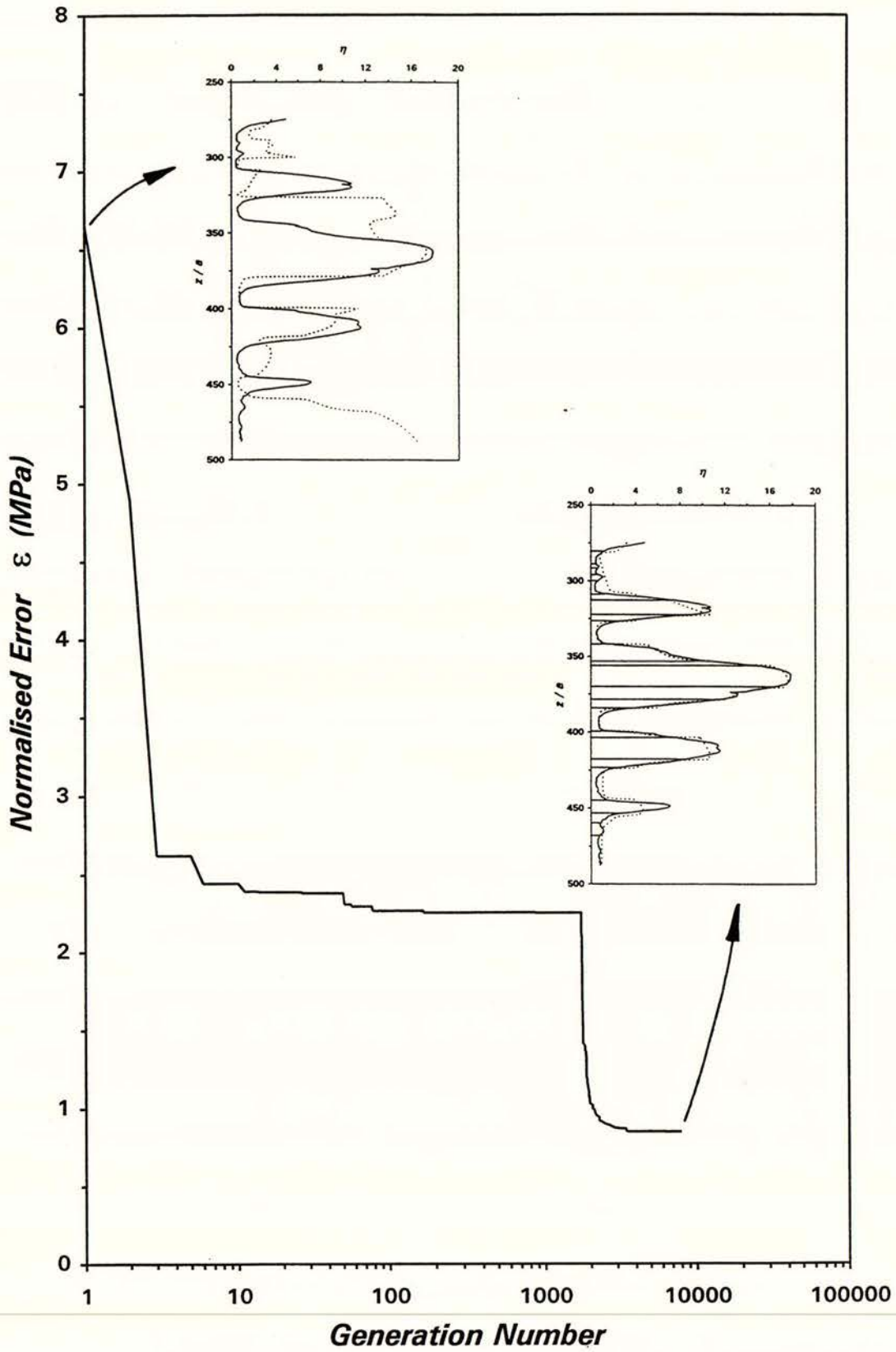


Figure 8.6 GA convergence history for partial inversion of 24-layer section of Test 15

solutions was randomly generated. Each candidate solution comprised the set of 23 stiffness ratios $\{k_1, k_2, k_3, \dots, k_{21}, k_{22}, k_{23}\}$. After some investigation of initial convergence, the mutation operator probability was set at 0.3. The mutation rate was reduced once the normalised error dropped below $\epsilon = 3$ MPa, by setting it equal to $(\epsilon / 10)$ each time the error ϵ decreased. This formulation increased the stability of the small population as the algorithm converged to a solution. Candidate solutions were ranked on their overall performance, and individual layers were also ranked on their performance. A new population of six candidate solutions was formed by breeding three times from a pool comprising the four best performing candidate solutions, and four sets of the best performing individual layers. The best overall candidate solution, and the best performing set of individual stiffness ratios were, carried over to the next generation intact, as in the first example.

Comparisons between the approximate solution and the measured dimensionless resistance for the best candidate solutions of generations 1 and 7898 are shown as insets on Figure 8.6. After making some slight adjustments to some of the interface positions, the GA converged on a slightly improved solution with normalised error $\epsilon = 0.80$ MPa within a few generations. The corresponding approximate solution shows good agreement with the measured dimensionless penetration resistance, as seen in Figure 8.7(a); values for stiffness ratio of this solution and the positions of layer interfaces are illustrated in Figure 8.7(b).

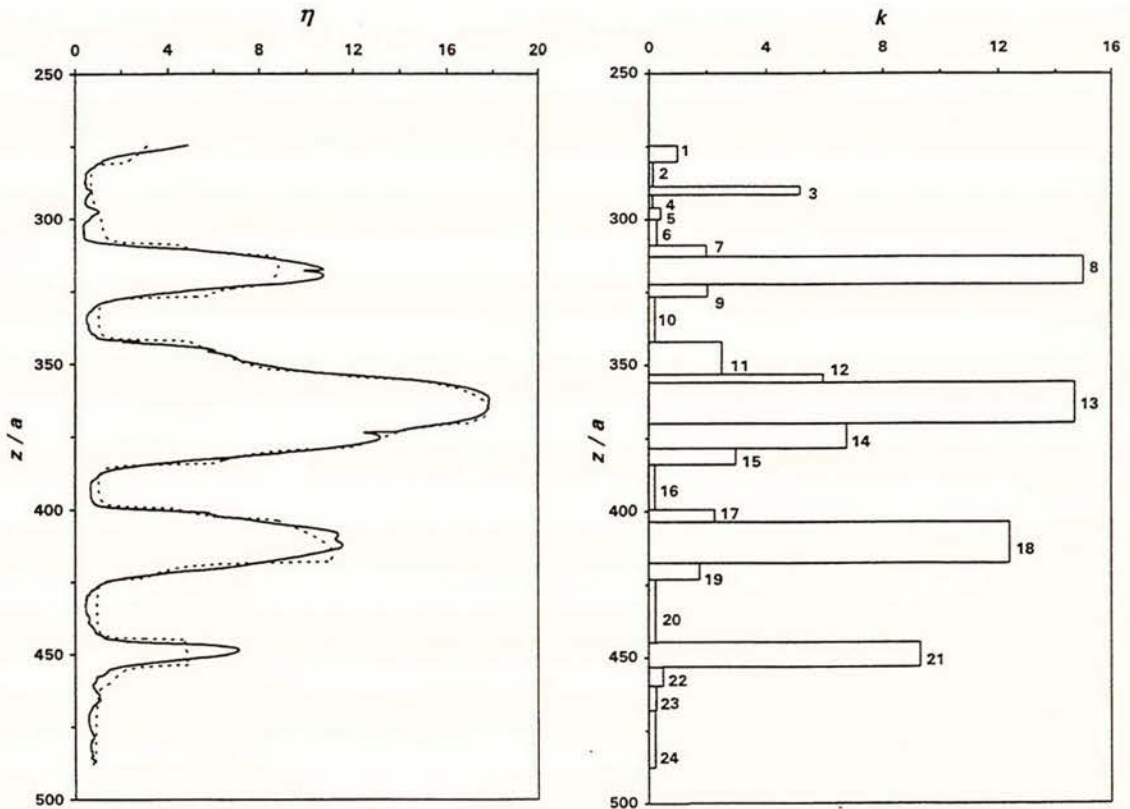


Figure 8.7 (a) Comparison between theoretical and measured resistance for 24-layer section of Test 15; (b) Corresponding stiffness ratio profile

Comparing Figure 8.7(a) with Figure 8.7(b), it is evident that the measured penetration resistance somewhat misrepresents the actual stiffness profile. Looking at this section of the q_c record, there appear to be four distinct stiff layers, and the second of these registers the greatest resistance to penetration. However, from the stiffness ratio profile we see that the first layer is at least as stiff as the second, and is most probably as strong. Again note the asymmetric layering of layers 11, 12 and 13, and layers 13, 14 and 15. The changes of curvature in the approximate solution match the dimensionless resistance curve particularly well in layers 12 and 14. However, also note from Figure 8.7(a) that the approximate solution does not correctly predict the measured cone resistance behaviour at the maximum resistance recorded in thin layers. It appears the limits of the approximate elastic solution have been reached. To improve the prediction, the effects of plastic yielding of the soil on cone resistance may need to be incorporated into the model, and provision made for inhomogeneities or variation in soil properties within layers.

8.4 SUMMARY

The above examples demonstrate that the GA is a useful tool for this optimisation problem. It may be used to fully invert a short section of cone resistance record for estimates of layer thicknesses and stiffness ratios, or partially invert longer sections of cone resistance records for estimates of stiffness ratios only. Partial inversion, using predetermined estimates of layer thicknesses, is favoured for longer records due to slow convergence of the algorithm for full inversion of highly variable q_c records. Trials are necessary to assess the performance of the algorithm for different breeding rules and objective functions, and to determine the optimum combination of population size and mutation rate.

In general, the algorithm performs well, although uniqueness of the final solution is not guaranteed. The limits of the elastic model may have been reached, as in the second example not all features of measured cone resistance behaviour are well modeled by the approximate solution. To capture more aspects of cone resistance behaviour, the effects of plasticity could be incorporated into the approximate solution, and allowance made for variation in soil properties within a layer.

9

Conclusions and Future Research

Liquefaction of natural dune and river sand deposits in the Monterey Bay region of California contributed greatly to damage resulting from the $M_s = 7.1$ Loma Prieta earthquake of 17 October, 1989. Directivity effects, combined with site amplification of ground motion in artificial fills, contributed to the unusual occurrence of liquefaction almost 100 km from the source. Clearly, accurate assessment of site liquefaction potential is necessary to minimize liquefaction damage in future seismic events.

The Loma Prieta earthquake represented an important opportunity to expand the catalogue of well-documented case histories detailing seismic liquefaction of level ground sites. Following the earthquake, CPTU and SPT were conducted at ten sites of liquefaction as part of a joint research venture between the Department of Civil Engineering at the University of Canterbury, New Zealand, and the Western Region Headquarters of the United States Geological Survey. Nine of these sites were in the Monterey Bay region of central California; the tenth site was at the Marina District of San Francisco. Data relating to each test are recorded in Appendix A.

The CPTU appears to be a more accurate and reliable site investigation tool than the traditional SPT for identifying soils susceptible to liquefaction. However, piezocone data is still affected by random errors, and systematic errors that stem from standard cone design. Depth measurements should be referenced to the cone shoulder rather than the cone tip, since the entire 10 square centimetre projected area of a standard cone is first encountered by the soil at the shoulder. Reliability of measured pore water pressure u is highly dependent on thorough de-airing of the cone before testing, and maintaining saturation during probing. Raw cone resistance q_c requires correction to total resistance q_t for pore water pressure effects. This correction, though barely noticeable for the sites tested in California, is particularly important in soft clays or silts. The merit of CPTU q_c data normalisation is debatable, due to uncertainty in the calculation of the normalising vertical stress.

Sleeve friction f_s should be lagged with respect to cone resistance q_c to yield accurate values for friction ratio R_f . A statistical cross-correlation analysis of the Loma Prieta CPTU data suggests that, when probing in soft clays or silts with average resistance less than approximately 4.5 MPa, a value of 120 mm is appropriate for lag τ between q_c and f_s for a standard Fugro cone. The lag should increase to a value of 150 mm when probing in stiffer, interbedded sandy soils, with average resistance of approximately 10 MPa. The parameters q_c and f_s generally show strong positive correlation in all soils except those with average resistance less than approximately 2 MPa. The high average degree of correlation between q_c and f_s implies these parameters are measuring similar characteristics of the soil mass during penetration. In contrast, pore pressure u correlates poorly with q_c , indicating that these parameters are orthogonal and measure different aspects of the soil mass response to penetration. Lag and pore water pressure effects are secondary, however, to the influence of soil layering on measured sleeve friction and cone resistance in particular. Pore pressures measured during probing appear to be sensitive only to the soil in contact with the pore water filter, whereas q_c is affected by stiffness changes in the soil several cone diameters ahead and behind the cone shoulder.

The performance of five liquefaction prediction models has been assessed using the CPTU and SPT data collected from the ten Loma Prieta liquefaction test sites. The models chosen for this study included two which are energy-based (D&B and LV&W), two which are based on cyclic stress ratio (SEED and S&T), and one which is purely empirical (ZHOU). To determine a value for critical cone resistance with depth for the D&B, SEED and LV&W models, the widely-used expression of $q_c/N = 0.4$ MPa was adopted. This ratio, however, varies with mean grain size, and is inherently uncertain. This relationship should be used with caution, particularly when assessing the liquefaction potential of highly variable fluvial sites. As the catalogue of CPTU liquefaction case histories increases, it may be possible to recast some of the earlier, SPT N-based methods in terms of q_c to avoid the use of this uncertain relationship.

At each of the 35 cone tests, a model was ruled to have predicted liquefaction at any depth below the water table where the calculated critical cone resistance exceeded the measured resistance *and* the soil at that depth classified as liquefiable based on the Robertson and Campanella (1985) classification. Although the S&T model scored the most correct answers, the D&B model scored the highest number of combined correct and marginal predictions, and the least incorrect answers. The D&B model appears to be the most sensitive for this data set, exhibiting the most variation in response. However, the D&B model is also the most unconservative of the five models, and only marginally out-performs the purely empirical ZHOU model. The D&B model consistently predicts a lower average value of critical cone resistance than all the other models. Like the LV&W model, the predictive capability of the D&B model is compromised at near-source sites (epicentral distance less than approximately 20 km), due to the definition of the distance term as epicentral distance. The ZHOU model avoids the distance definition problem by employing earthquake intensity rather than magnitude

as a measure of site response. However, the performance of the ZHOU model could be improved by exchanging the discrete intensity scale for a continuous counterpart. The responses of the SEED and S&T models are highly conservative for this data set, in part due to their reliance on the estimation of ground acceleration from an attenuation relationship. This extra empirical step in the calculation of critical cone resistance introduces additional uncertainties. The S&T model is strongly influenced by the mean grain size variable D_{50} . To some extent, the inclusion of D_{50} negates the advantages of conducting CPT over SPT. It may be possible to estimate grain size information from CPT records, or reformulate the S&T model in terms of a critical q_c value for a given friction ratio.

The absence of surface manifestations of liquefaction may not be a particularly reliable indicator of a non-liquefied site, though few other indicators are available. Based on the comparison of ejecta D_{50} values, and D_{50} values from samples collected from nearby SPT, liquefaction appears to have been shallow for the Loma Prieta event. The evidence suggests that liquefaction developed either in the layer in which the water table was located, or in the layer immediately below the layer of the water table. This conclusion is based on the assumptions that the origin of the ejecta is the liquefied material, and that there has been negligible contamination or entrainment of other materials during its passage to the ground surface. Deeper layers may have liquefied, only no evidence of this liquefaction migrated to the ground surface.

Based on the simple scoring system proposed, the five liquefaction prediction models score very closely to each other, regardless of the value assigned to marginal or close predictions. This is due, in part, to the small size and biased nature of the data set. No single model clearly outperformed all the others. The D&B, ZHOU and LV&W models infer that liquefaction susceptibility decreases with depth. If the CSR is used with no modifying factors, the SEED and S&T models do not predict decreasing liquefaction susceptibility with depth. This contradicts field and experimental observations, and the behaviour of the other models. The results of this analysis suggest that it is unwise to rely on the prediction of only one model when investigating the liquefaction potential of a site for a design earthquake. Clearly, refinements can be made to each of the models assessed in this report. In addition, there is an obvious need for the development of a model which fully utilises CPTU data for liquefaction prediction.

The performance of a liquefaction prediction model relies in part on the accuracy of the measured cone resistance. However, due to the influence of soil layering on cone resistance, raw values of q_c are not always reliable. In particular, interpretation of piezocone data is not a straightforward task in heavily interbedded soils. Thus, in spite of the continuous nature of the test, raw cone resistance profiles do not necessarily represent the true stratification of the soil.

Although evident in both early and recent calibration chamber tests and also in field test results, few serious attempts have been made to quantify the effects of soil layering on the development of cone resistance. As part of this study, a simple model has been developed to investigate layering effects on a loaded disc in a two-layer, incompressible, elastic medium. The model is based on the exact solution of Plevako to the problem of calculating the displacements due to a point load acting perpendicular to the interface between two perfectly bonded elastic materials. The elastic analysis presented is not intended to account for the immediate effects of penetration and deformation which occur near the tip of a penetrating cone. It is solely intended to model the effects of layering sensed by the cone in its own vicinity. The assumption of incompressibility is based on the expectation that the effects at a distance which are being modeled will result primarily from undrained soil deformations. The model predicts the behaviour of dimensionless cone resistance η as the idealised cone approaches and passes through a soil layer interface. A greater distance of penetration is predicted in stiffer materials to achieve steady-state resistance than softer materials. This implies the perceived resistance in very soft materials will be relatively accurate. The theoretical dimensionless resistance curves from this simple elastic model show good agreement with calibration chamber test data. However, since it is not possible to extend this exact solution to more complex layering cases, an approximate solution has been developed.

The approximate solution for layering effects on cone resistance is based on the superposition of integrated Boussinesq solutions. In each layer of a section of q_c record being modeled, the dimensionless resistance η is defined as a function of stiffness ratios k_i and geometry parameters λ_j' (refer Chapter 6). The solution compares well with the modified Plevako solution for the two layer case, and is exact in the limiting cases. It also compares favourably with calibration chamber data and field CPTU data. However, the elastic solution response is symmetric for symmetric layering cases, an obvious simplification of actual cone resistance response.

The elastic model verifies that the resistance of a thin stiff layer embedded in a softer material is underestimated, and that this effect is amplified with increasing stiffness ratio. As a general rule, doubling the stiffness ratio implies layer thickness must also be doubled to maintain a given percentage of steady-state resistance. The results of this analysis suggest that greater values of layer thickness are required to achieve steady-state resistance in stiffer materials than previously thought. For a soft layer embedded in a stiffer material, layering effects are relatively small, and the perceived resistance in the soft material will closely approximate the true resistance. This is because the softer material isolates the penetrating cone from surrounding materials. Examples have demonstrated how a thin stiff layer can be misclassified, with regard to soil type and soil strength. Care must be taken when using soil classification charts based on CPTU parameters to avoid such a soil type misclassification. Based on perceived resistance alone, thin stiff layers may be conservatively misclassified as liquefiable. However, if such information is used in the calibration of liquefaction prediction models, it may

cause the model to predict an unconservative value for critical cone resistance. Overall, the approximate solution is able to quantify the development of cone resistance in a multilayered soil system, and thus it is a useful tool for interpreting calibration chamber tests and field tests at sites with highly variable stratigraphy. The solution allows for more reliable and realistic interpretation of any cone resistance data.

Laboratory testing and field test data indicate that sleeve friction is essentially an interface phenomenon. Thus, the resolution of f_s is directly related to friction sleeve length. An example has demonstrated that, under the conditions of asymmetric layering, the resolution of f_s may exceed that of q_c . This is because layers of intermediate stiffness, relative to surrounding layers, may be obscured in a q_c record even if they are of greater thickness than the length of the sleeve. Inflexions in measured q_c curves match those in traces generated by the approximate solution for asymmetric layering cases, suggesting that the contribution of the elastic stress field around a penetrating cone to the development of cone resistance is significant. Further calibration chamber testing is necessary to investigate this observation. It may be possible to deconvolve f_s data to remove ramp-like features at soil layer interfaces. This would allow for increased precision in determining interface positions, and the detection of grading or inhomogeneities within a soil layer.

The approximate solution may be employed to invert cone resistance records. Values for layer stiffness ratios and thicknesses, estimated by inversion, should yield a more accurate representation of the true soil profile than that indicated by the perceived penetration resistance. Information gained through inversion may be useful in deformation analyses, settlement calculations and the assessment of liquefaction potential. An attempt has been made to optimise the approximate solution using a Genetic Algorithm. A GA is a powerful, robust, iterative method of optimisation, modeled on mechanics of evolutionary biology and genetics. GAs search solution space for improved performance, explicitly processing populations of strings, but implicitly processing schemata denoting hyperplanes. Unlike Monte Carlo techniques, GAs are randomised, but not random, search algorithms. A GA has been successfully employed to fully invert a simple, short artificial cone record generated by the approximate solution. Following some experimentation with parameter settings, sections of two field records from two Loma Prieta liquefaction sites have been partially inverted using a GA. Partial inversion for stiffness ratios using predetermined estimates of layer thicknesses is favoured for longer records, due to slow GA convergence for full inversion of highly variable q_c records. For both field records, the resulting stiffness ratio profile indicated that the perceived resistance of several relatively thin, stiff layers underestimated their true resistance. Although the application of a GA to this optimisation problem has been quite successful, the uniqueness of the final solution is not guaranteed. In addition, it appears the limits of the elastic model have been reached. The performance of the approximate solution may be improved by incorporating plasticity effects into the model, and allowing for variation in soil properties within a layer.

References

- Ankenbrandt, C.A., B.P. Buckles and F.E. Petry (1990), "Scene recognition using genetic algorithms with semantic nets", *Pattern Recognition Letters*, Vol. 11, pp. 285-293
- Baldi, G., D. Bruzzi, S. Superbo, M. Battaglio and M. Jamiolkowski (1988), "Seismic cone in Po River sand", *Proceedings, First International Symposium on Penetration Testing, ISOPT-1*, Balkema, J. De Ruyter (Ed.), Vol. 2, pp. 643-650
- Baligh, M.M., V. Vivatrat and C.C. Ladd (1980), "Cone penetration in soil profiling", *J. Geotech. Eng. Div.*, ASCE, Vol. 106, No. GT4, pp. 447-461
- Baligh, M.M., A.D. Azzouz, A.Z.E. Wissa, R.T. Martin and M.H. Morrison (1981), "The piezocone penetrometer", *Symposium on Cone Penetrometer Testing and Experience*, Geotech. Eng. Div., ASCE, St Louis, pp.247-263
- Bendat, J.S. and A.G. Piersol (1986), *Random Data: Analysis and Measurement Procedures*, Second Edition, Revised and Expanded, John Wiley and Sons Inc., New York, 566pp.
- Bennett, M.J. (1990), "Ground deformation and liquefaction of soil in the Marina District", Chapter D, *Effects of the Loma Prieta Earthquake on the Marina District, San Francisco, California*, USGS Open-File Report 90-253
- Benuska, L. (Tech. Ed.) (1990), "Loma Prieta earthquake reconnaissance report", *Earthquake Spectra*, Supplement to Vol. 6, May 1990, El Cerrito, California, 448pp.
- Boatwright, J., L.C. Seekins, T.E. Fumal, H.-P. Liu and C.S. Mueller (1991), "Ground motion amplification in the Marina District", *Bull. Seis. Soc. Amer.*, Vol. 81, No. 5, pp. 1980-1997
- Boore, D.M., W.B. Joyner and T.E. Fumal (1993), *Estimation of Response Spectra and Peak Accelerations from Western North American Earthquakes: an Interim Report*, USGS Open-File Report 93-509
- Boulon, M. (1991), "Le comportement d'interface sol-structure: aspects expérimentaux et numériques", *Rev. Franç. Géotech.*, No. 54, pp. 27-37
- Burmister, D.M. (1945), "The general theory of stresses and displacements in layered systems", *J. Appl. Phys.*, Vol. 16, No. 2, pp. 89-94, No. 3, pp. 126-127, No. 5, pp. 296-302
- Campanella, R.G., D. Gillespie and P.K. Robertson (1982), "Pore pressures during cone penetration testing", *Proceedings, Second European Symposium on Penetration Testing, ESOPT-II*, Amsterdam, Vol. 2, pp. 507-512
- Campanella, R.G. and P.K. Robertson (1988), "Current status of the piezocone test", *Proceedings, First International Symposium on Penetration Testing, ISOPT-1*, Balkema, J. De Ruyter (Ed.), Vol. 1, pp. 93-116
- Canou, J. (1989), *Piezocône et liquéfaction des sables: rapport de synthèse des travaux réalisés au CERMES (1986-1988)*, Research Report, CERMES/ENPC, Paris, 176 pp.

- Davis, R.O. and J.B. Berrill (1982), "Energy dissipation and seismic liquefaction in sands", *Earthquake Engineering and Structural Dynamics*, Vol. 10, pp. 59-68
- Davis, R.O. and J.B. Berrill (1983), "Comparison of a liquefaction theory with field observations", Technical Note, *Géotechnique*, Vol. 33, No. 4, pp. 455-460
- De Beer, E.E., E. Goelen, W.J. Heynen and K. Jousra (1988), "Cone penetration test (CPT): international reference test procedure", *Proceedings, First International Symposium on Penetration Testing*, ISOPT-1, Balkema, J. De Ruiter (Ed.), Vol.1, pp. 27-51
- Dobry, R., R.S. Ladd, F.Y. Yokel and R.M. Chung (1982), "Prediction of pore water pressure buildup and liquefaction of sands during earthquakes by the cyclic strain method", *Building Science Series 138*, National Bureau of Standards, US Dept of Commerce, US Government Printing Office, Washington, DC
- Dou Yiqiang and J.B. Berrill (1993), "A pattern recognition approach to evaluation of soil liquefaction potential using piezocone data", *Soil Dyn. Earthq. Eng.*, Vol. 12, pp. 91-101
- Douglas, B.J. and A.I. Strutynsky (1984), *Cone Penetrometer Test, Pore Pressure Measurement and SPT Hammer Energy Calibration for Liquefaction Hazard Assessment*, Earth Technology Corporation, Long Beach, California, USGS contract no. 14-08-001-19105, project no. 83-101
- Dundurs, J. and H. Hetényi (1965), "Transmission of force between two semi-infinite solids", *J. Appl. Mech.*, ASME, pp. 671-674
- Evans, K.M. (1987), *A Model Study of the End Bearing Capacity of Piles in Layered Calcareous Soils*, Doctoral Thesis, University of Oxford
- Flavigny, E., J. Desrues and B. Palayer (1990), "Note technique: le sable d'Hostun 'RF' ", *Revue Française de Géotechnique*, No. 53, pp. 67-70
- Florin, V.A. (1959), *Fundamentals of Soil Mechanics*, Vol. I, Leningrad
- Florin, V.A. and P.L. Ivanov (1961), "Liquefaction of saturated sandy soils", *Proceedings, Fifth International Conference on Soil Mechanics and Foundation Engineering*, Paris, Vol. 1, pp. 107-111
- Foray, P. and J.-L. Pautre (1988), *Piézocone et liquéfaction des sables: synthèse des essais sur sites en Nouvelle-Zélande et des essais en chambre de calibration à l'IMG*, Research Report, IMG, Grenoble, 70 pp.
- Gallagher, K., M. Sambridge and G. Drijkoningen (1991), "Genetic algorithms: an evolution from Monte Carlo methods for strongly non-linear geophysical optimization problems", *Geophysical Research Letters*, Vol. 18, No. 12, pp. 2177-2180
- Goldberg, D.E. (1989), *Genetic Algorithms in Search, Optimization and Machine Learning*, Addison-Wesley, Reading, MA, USA, 412pp.

- Goldberg, D.E. (1989b), "Sizing populations for serial and parallel genetic algorithms", *Proceedings, Third International Conference on Genetic Algorithms*, Morgan Kaufmann, San Mateo, California, pp. 70-79.
- Grefenstette, J.J. and J.E. Baker (1989), "How genetic algorithms work: a critical look at implicit parallelism", *Proceedings, Third International Conference on Genetic Algorithms*, Morgan Kaufmann, San Mateo, California, pp. 20-27
- Hanks, T.C. and A.G. Brady (1991), "The Loma Prieta earthquake, ground motion, and damage in Oakland, Treasure Island, and San Francisco", *Bull. Seis. Soc. Amer.*, Vol. 81, No. 5, pp. 2019-2047
- Holland, J.H. (1975), *Adaptation in Natural and Artificial Systems*, University of Michigan Press, Ann Arbor, MI, USA (reprinted by MIT Press, Cambridge, MA, USA, 1992, 211pp.)
- Ishihara, K. (1993), "Liquefaction and flow failures during earthquakes", *Géotechnique*, Vol. 43, No. 3, pp. 351-415
- Iwasaki, T., F. Tatsuoka, K. Tokida and S. Yasuda (1978), "A practical method for assessing soil liquefaction potential based on case studies at various sites in Japan", *Proceedings, Second International Conference on Microzonation for Safer Construction Research and Application*, Vol. 2, pp. 885-896
- Jones, G.A. and E.A. Rust (1982), "Piezometer penetration testing CUPT", *Proceedings, Second European Symposium on Penetration Testing*, ESOPT-II, Amsterdam, Vol. 2, pp. 607-613
- Kausel, E. and S.H. Seale (1987), "Static loads in layered halfspaces", *J. Appl. Mech.*, Vol. 54, pp. 403-408
- Konrad, J.M. (1987), "Piezo-friction-cone penetrometer testing in soft clays", *Can Geotech. J.*, Vol. 24, pp. 645-652
- Konrad, J.M. and K.T. Law (1987), "Undrained shear strength from piezocone tests", *Can. Geotech. J.*, Vol. 24, pp. 392-405
- Kovacs, W.D., F.Y. Yokel, L.A. Salomone and R.D. Holtz (1984), "Liquefaction potential and the international SPT", *Proceedings, Eighth World Conference on Earthquake Engineering*, San Francisco, CA, Vol. 3, pp. 263-268
- Liao, S.S.C. and R.V. Whitman (1986), "Overburden correction factors for SPT in sand", *J. Geotech. Eng. Div.*, ASCE, Vol. 112, No. 3, pp. 373-377
- Liao, S.S.C., D. Veneziano and R.V. Whitman (1988), "Regression models for evaluating liquefaction probability", *J. Geotech. Eng. Div.*, ASCE, Vol. 114, No. 4, pp. 389-411
- Meigh, A.C. (1987), *Cone Penetration Testing: Methods and Interpretation*, CIRIA ground engineering report: in-situ testing, Butterworths, London, 141pp.
- Meyerhof, G.G. (1956), "Penetration tests and bearing capacity of cohesionless soils", *Proceedings, J. Soil Mech. Found. Div.*, ASCE, Vol. 82, No. SM1, pp. 1-19

- National Research Council (1985), *Liquefaction of Soils during Earthquakes*, Committee on Earthquake Engineering, Commission on Engineering and Technical Systems, Washington D.C., National Academy Press (Report No. CETS-EE-001), 240pp.
- Nemat-Nasser, S. and A. Shokoh (1979), "A unified approach to densification and liquefaction of cohesionless sand in cyclic shearing", *Can. Geotech. J.*, Vol. 16, pp. 659-678
- Olsen, R.S. and P.G. Malone (1988), "Soil classification and site characterisation using the cone penetrometer test", *Proceedings, First International Symposium on Penetration Testing*, ISOPT-1, Balkema, J. De Ruiter (Ed.), Vol. 2, pp. 887-893
- Peck, R.B., W.E. Hanson and T.H. Thornburn (1974), *Foundation Engineering*, Second Edition, John Wiley and Sons, Inc., New York, 515pp.
- Plafker, G. and Galloway, J.P. (Eds) (1989), *Lessons learned from the Loma Prieta, California, earthquake of October 17, 1989*, USGS Circular 1045, 48pp.
- Plevako, V.P. (1969), "A point force inside a pair of cohering half-spaces", *Soil Mech. Found. Eng.* (Translated from *Osnovaniya Fundamenty i Mekhanika Gruntov*), No. 3, pp. 9-11
- Poulos, H.G. (1967), "Stresses and displacements in an elastic layer underlain by a rough rigid base", *Géotechnique*, Vol. 17, pp. 378-410
- Robertson, P.K. (1982), *In-situ Testing of Soil with emphasis on its Application to Liquefaction Assessment*, PhD Thesis, University of British Columbia, 395pp.
- Robertson, P.K. and R.G. Campanella (1983), "Interpretation of cone penetration tests. Part I: Sand", *Can. Geotech. J.*, Vol. 20, pp. 718-733
- Robertson, P.K. and R.G. Campanella (1985), "Liquefaction potential of sands using the CPT", *J. Geotech. Eng. Div.*, ASCE, Vol. 111, No. 3, pp. 384-403
- Robertson, P.K. (1990), "Soil classification using the cone penetration test", *Can. Geotech. J.*, Vol. 27, pp. 151-158
- Rongved, L. (1955), "Force interior to one of two joined semi-infinite solids", *Proceedings, Second Midwestern Conference on Solid Mechanics*, pp. 1-13
- Sanglerat, G. (1972), *The Penetrometer and Soil Exploration: Interpretation of Penetration Diagrams - Theory and Practice*, Developments in Geotechnical Engineering, Vol. 1, Elsevier, Amsterdam, 464 pp.
- Schaffer, J.D., R.A. Caruana, L.J. Eshelman and R. Das (1989), "A study of control parameters affecting online performance of genetic algorithms for function optimization", *Proceedings, Third International Conference on Genetic Algorithms*, Fairfax, VA, pp. 51-60
- Seed, H.B. and I.M. Idriss (1971), "Simplified procedure for evaluating soil liquefaction potential", *Proceedings, J. Soil Mech. Found. Div.*, ASCE, Vol. 97, No. SM9, pp. 1249-1273

- Seed, H.B. (1979), "Soil liquefaction and cyclic mobility evaluation for level ground during earthquakes", *J. Geotech. Eng. Div.*, ASCE, Vol. 105, No. GT2, pp. 210-255
- Seed, H.B., K. Tokimatsu, L.F. Harder and R.M. Chung (1985), "Influence of SPT procedures in soil liquefaction resistance evaluations", *J. Geotech. Eng. Div.*, ASCE, Vol. 111, No. 12, pp. 1425-1445
- Sen, M.K. and P.L. Stoffa (1992), "Rapid sampling of model space using genetic algorithms: examples from seismic waveform inversion", *Geophys. J. Int.*, Vol. 108, pp. 281-292
- Senneset, K., N. Janbu and G. Svano (1982), "Strength and deformation parameters from cone penetration tests", *Proceedings, Second European Symposium on Penetration Testing, ESOPT-II, Amsterdam*, Vol. 2, pp. 863-870
- Shephard, R.B., P.R. Wood, J.B. Berrill, N.R. Gillon, P.J. North, A.K. Perry and D.P. Bent (1990), "The Loma Prieta, California, earthquake of October 17, 1989, Report of the NZNSEE Reconnaissance Team", *Bull. New Zealand National Soc. Earthquake Eng.*, Vol. 23, No. 1, pp. 1-78
- Shibata, T. and W. Teparaksa (1988), "Evaluation of liquefaction potentials of soils using cone penetration tests", *Soils and Foundations*, Vol. 28, No. 2, pp. 49-60
- Smits, F.P. (1982), "Penetration pore pressure measured with piezometer cones", *Proceedings, Second European Symposium on Penetration Testing, ESOPT-II, Amsterdam*, Vol. 2, pp. 871-876
- Tokimatsu, K. and Y. Yoshimi (1983), "Empirical correlation of soil liquefaction based on SPT N-value and fines content", *Soils and Foundations*, Vol. 23, No. 4, pp. 56-74
- Treadwell, D.D. (1975), *The Influence of Gravity, Prestress, Compressibility, and Layering on Soil Resistance to Static Penetration*, PhD dissertation, Graduate division of the University of California, Berkeley, 210 pp.
- van den Burg, P., J.A.M. Teunissen and J. Huetink (1994), "Cone penetration in layered media, an ALE finite element formulation", *Proceedings, Eighth International Conference on Computer Methods and Advances in Geomechanics*, Vol. 3, pp. 1957-1962, Siriwardane and Zaman (Eds.), Balkema, Rotterdam
- Wroth, C.P. (1984), "The interpretation of in situ soil tests", Rankine Lecture, *Géotechnique*, Vol. 34, No. 4, pp. 449-489
- Wroth, C.P. (1988), "Penetration testing - a more rigorous approach to interpretation", *Proceedings, First International Symposium on Penetration Testing, ISOPT-1, Balkema, J. De Ruiter (Ed.)*, Vol. 1, pp. 303-311
- Zhou, S.G. (1980), "Evaluation of the liquefaction of sands by static cone penetration test", *Proceedings, Seventh World Conference on Earthquake Engineering, Istanbul, Turkey*, Vol. 3, pp. 156-162

Appendix A

This Appendix may be divided into three sections. The first section contains CPTU data from ten sites of liquefaction associated with the Loma Prieta earthquake. A record of q_c and q_t , R_f , u , B_q and f_s is displayed for each of the 35 probes conducted in California. Note the q_c and q_t curves are almost identical in every case. The positions of pauses for rod changes and/or dissipation tests are also shown, and values for t_{50} are given where available. Pore water pressure related information has not been displayed for the three tests where the cone was not de-aired, Tests 1, 29 and 34. For the 32 CPTU probes, no information on soil stratigraphy is available above the water table; these probes commenced below the water table to maintain saturation of the cone. Maps showing the location of each Test can be found in Chapter 2.

For sites at which both CPT/CPTU and SPT were performed, the SPT raw N is given, along with the D_{50} of the retrieved sample. This SPT N information has been used in the q_c/N ratio calculation. In some instances no D_{50} information is available as the sample was lost during the raising of the split-spoon to the ground surface (these cases are denoted as [LS] = "Lost Sample" on the plots). Bennett (1990) presents D_{50} values for ejecta and samples recovered at the Marina District.

Lines of critical cone resistance from the five liquefaction prediction models discussed in Chapter 4 have been plotted over the raw cone resistance curve. The classification of Robertson and Campanella (1985) has been plotted in the rectangular box positioned within the cone resistance box. Hatching indicates the soil is non-liquefiable according to their classification. Table 4.2 of Chapter 4 provides information on whether or not liquefaction was observed at each Test.

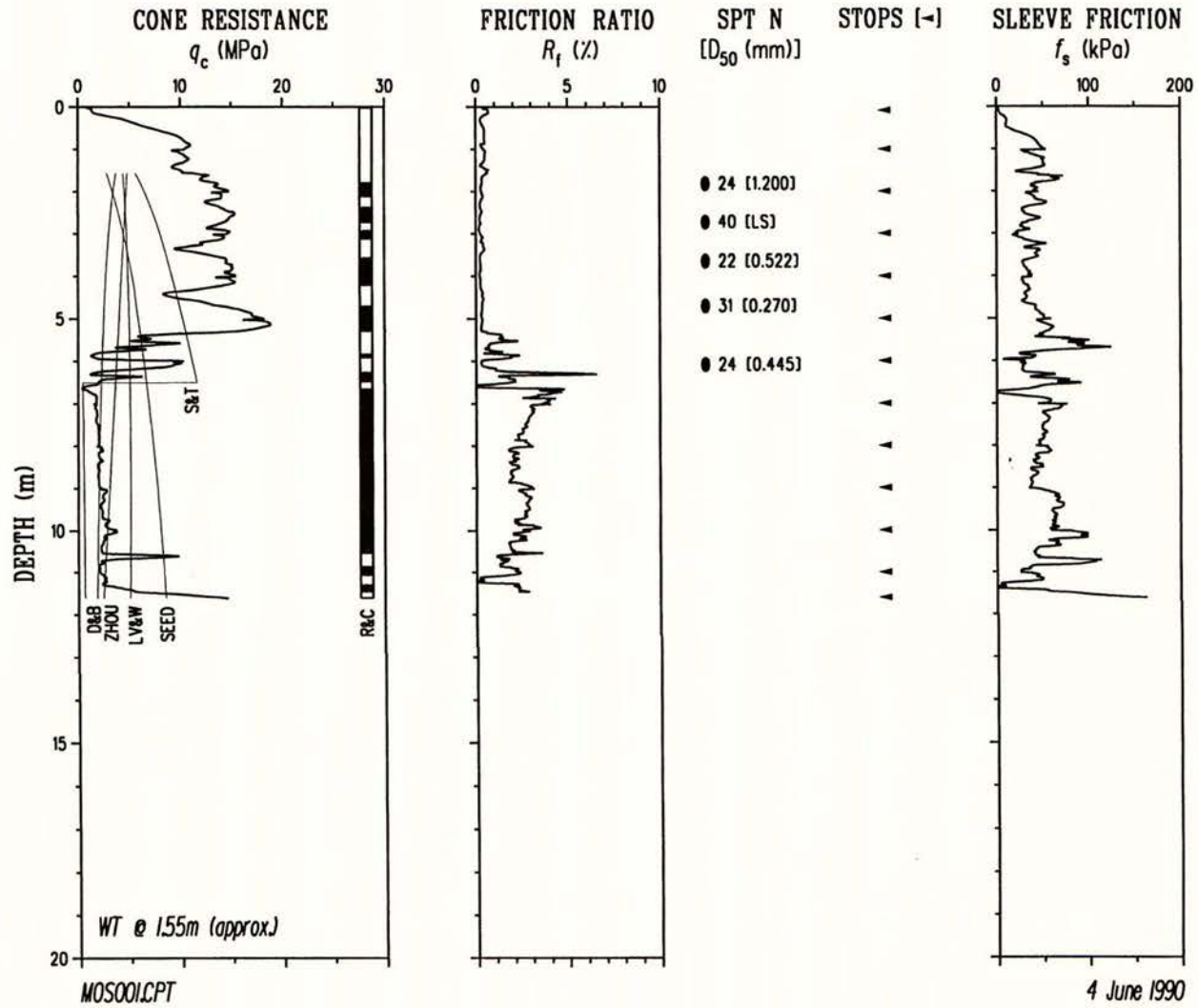
The water table (WT) depth provided on the plots is that recorded at the time of testing, approximately seven months after the earthquake. These values have been used in the calculation of total and effective overburden stresses, which are required in the calculation of B_q and q_t . Unit weights of 18.9 kN/m^3 and 20.4 kN/m^3 have been assumed above and below the water table respectively. Finally, all CPT/CPTU data was obtained using a 50 kN Fugro piezocone, with 10 cm^2 projected tip area and 150 cm^2 sleeve surface area. Reduced rods were used during each test. The test procedure adopted is outlined in Chapter 3.

Tabulated SPT results are given in the second section of this Appendix for 20 of the 35 cone penetration tests. These include the SPT N data and D_{50} values shown on the CPTU result plots along with additional D_{50} values, C_u information ($C_u = D_{60}/D_{10}$), the Unified Soil Classification (USC) for the sample, a brief soil description and $(N_1)_{60}$, corrected SPT N. To calculate $(N_1)_{60}$, raw N values were increased by 13.3 per cent to make allowance for the relatively high

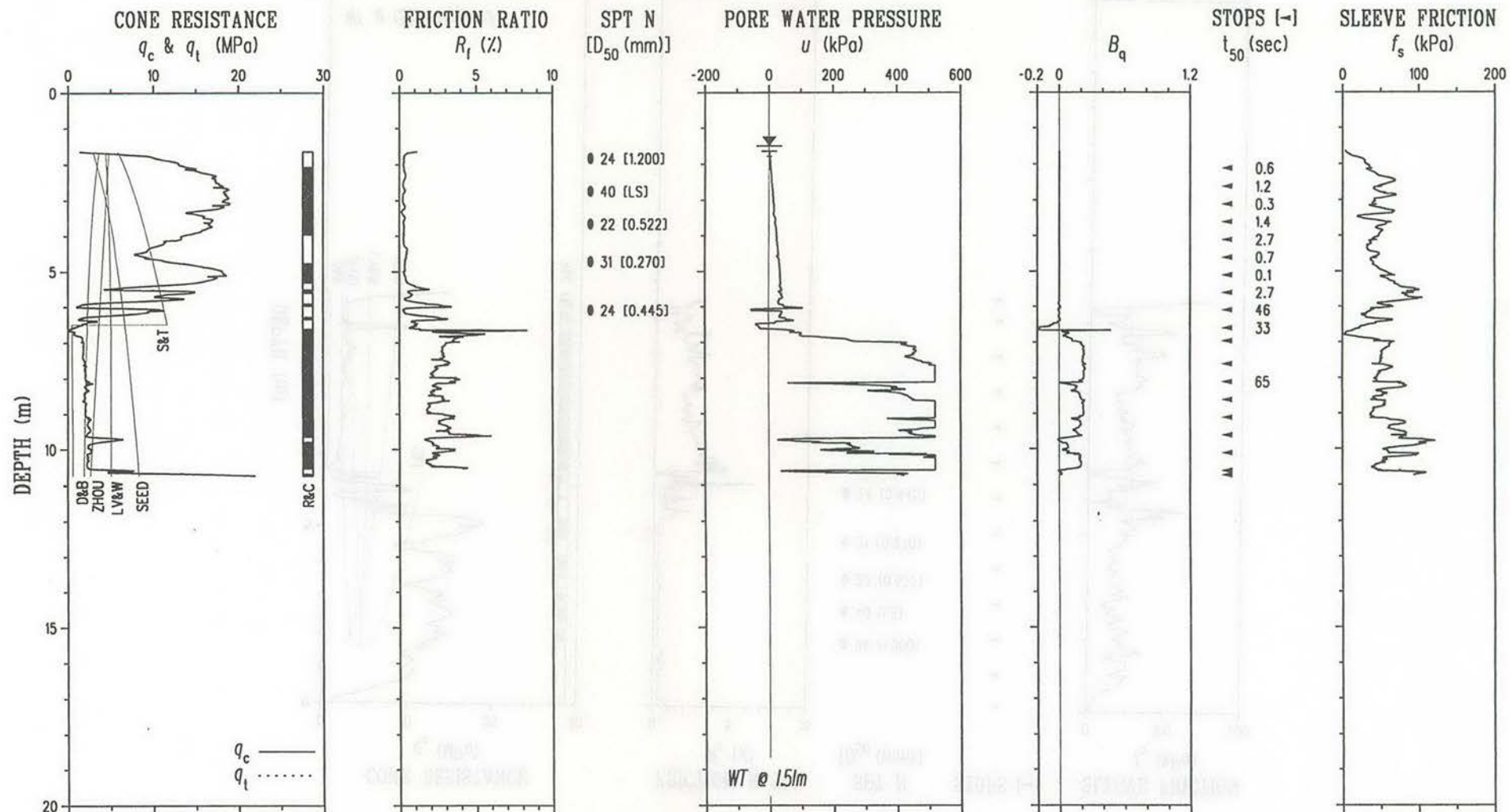
efficiency of 68 per cent for the USGS SPT rig used (Douglas and Strutytsky, 1984), and the overburden correction factor of Liao and Whitman (1986) was applied to adjust the N values to a standard overburden pressure of 100 kPa. The upper bound for the overburden correction factor C_N was set equal to 2. Water table values are given here also, along with University of Canterbury and USGS site labels (the USGS labels are in square brackets). For example, Test 4, the first test at the Pajaro Dunes site, is labelled as "PAJ001" by the University of Canterbury, and as "PAJ44" by the USGS.

In the third section of this Appendix, the distribution of sampled sand boils is plotted relative to the CPTU probes conducted for the nine southern sites near Monterey Bay. Each sand boil is tagged with a value of D_{50} determined from grain size distribution analyses performed on the ejecta. The coordinate system used for all of these plots is the California State Coordinate System. All of the southern sites lie in Zone 4 of this coordinate system which is visible on all USGS maps; the Marina District is located in Zone 3.

TEST 1 - MOSS LANDING



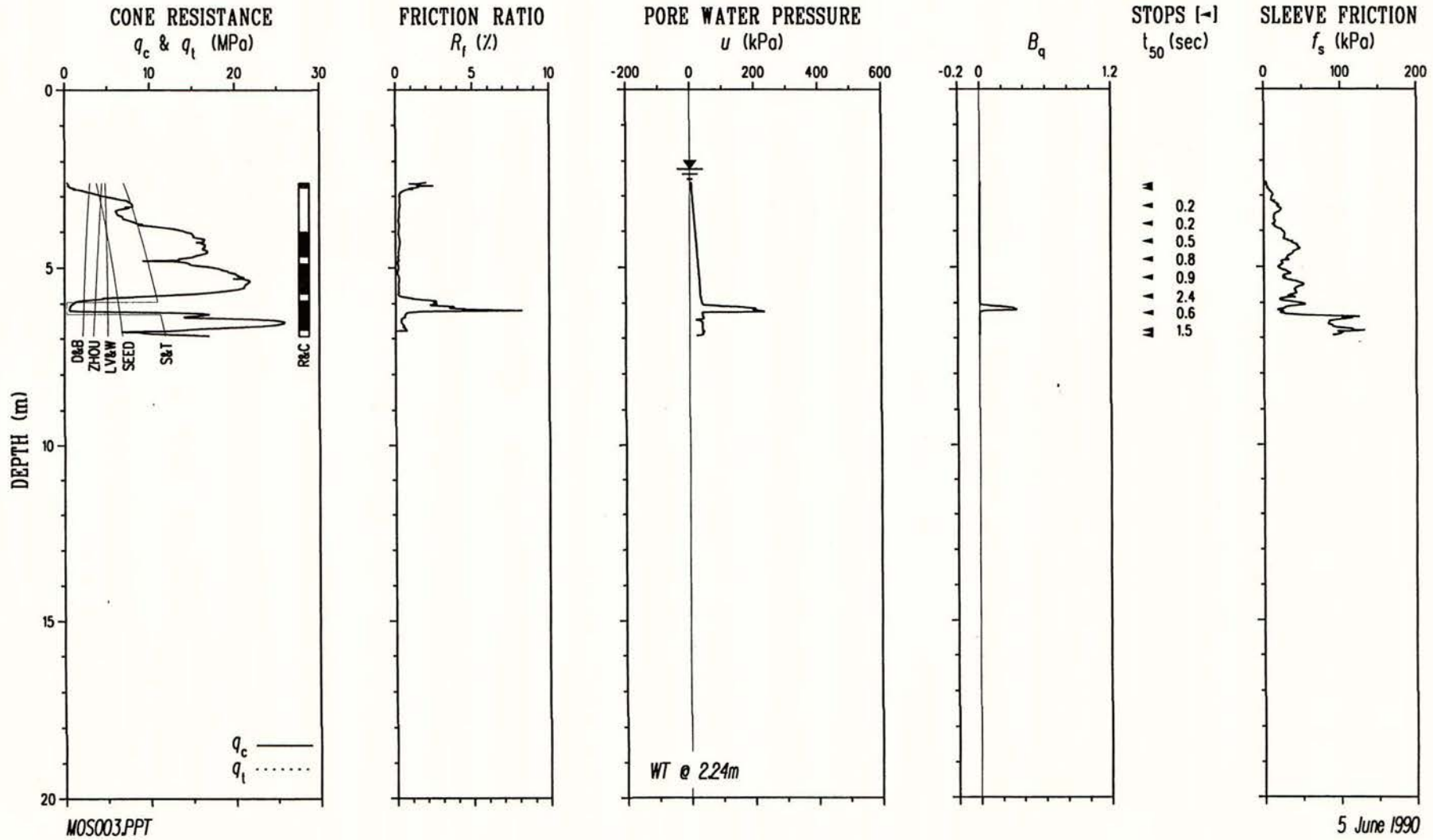
TEST 2 - MOSS LANDING



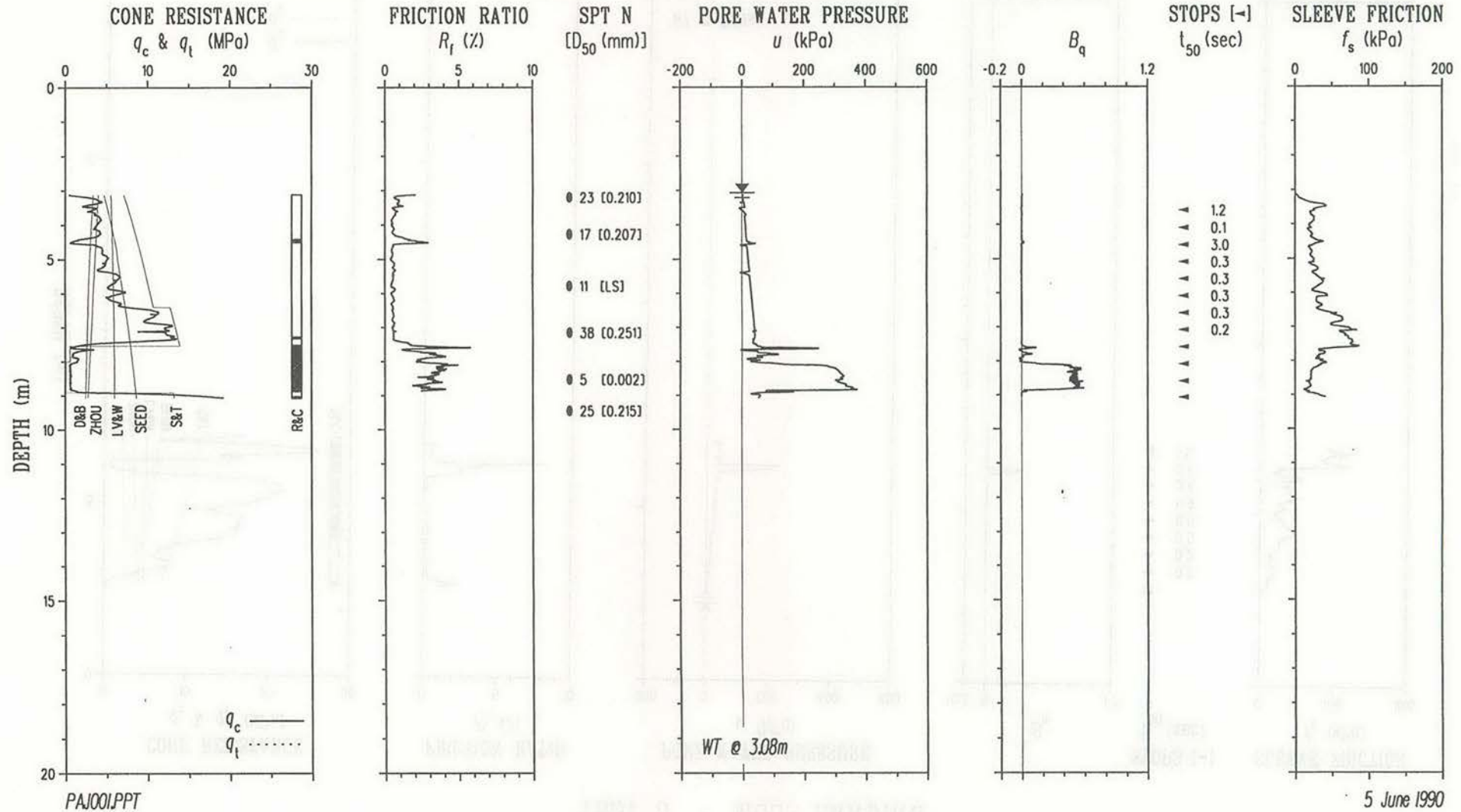
MOS002.PPT

4 June 1990

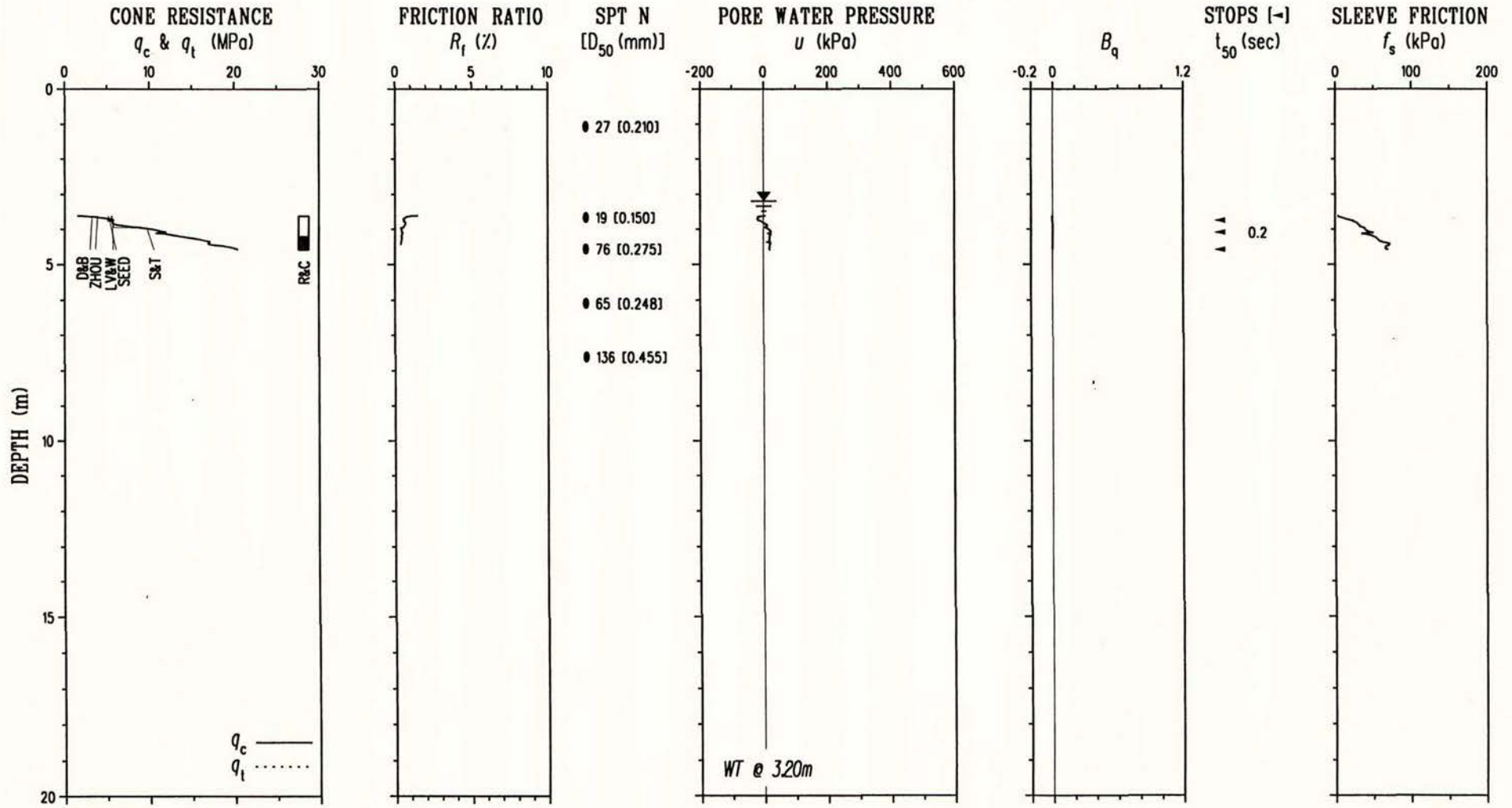
TEST 3 - MOSS LANDING



TEST 4 - PAJARO DUNES



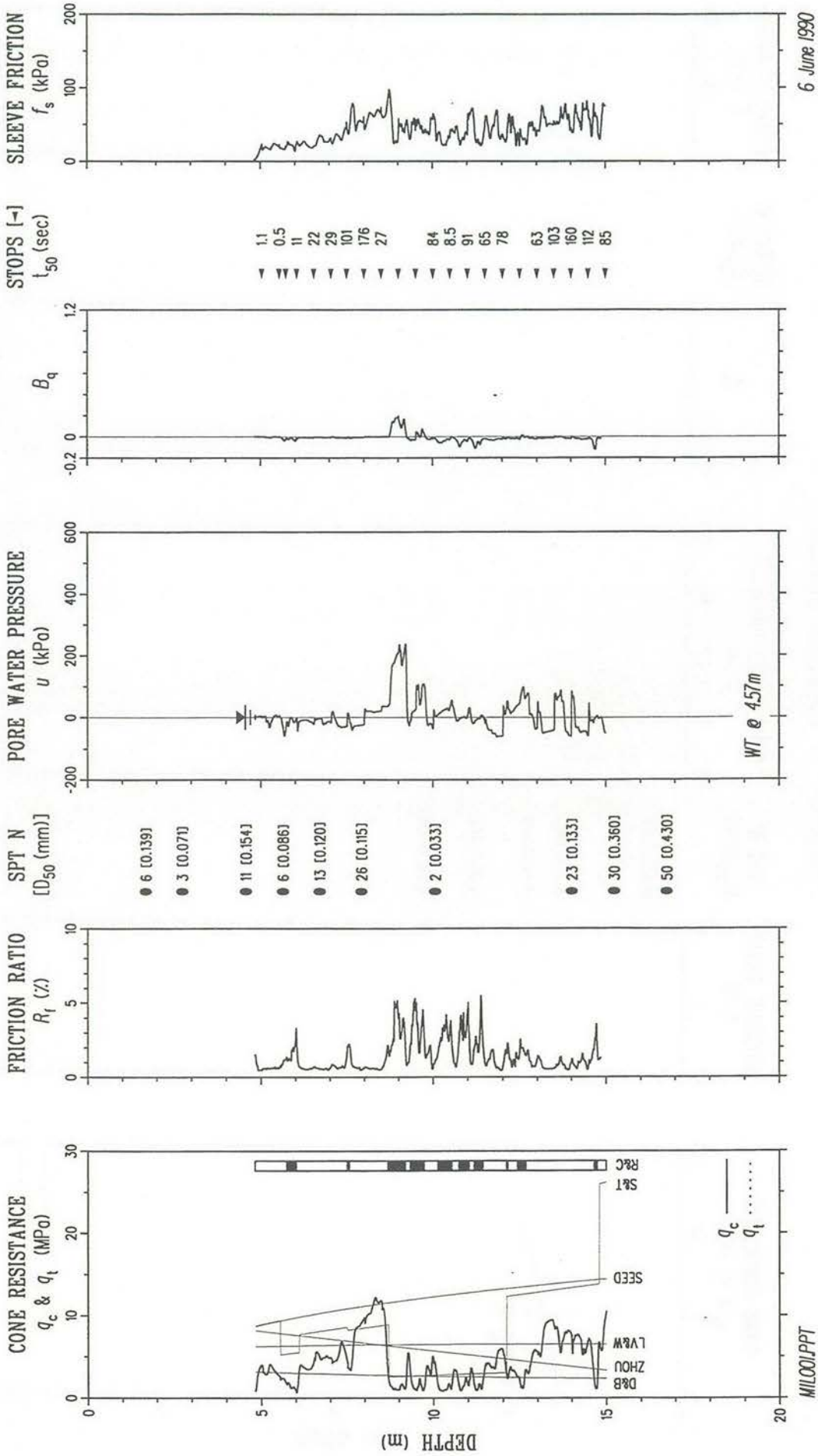
TEST 5 - PAJARO DUNES



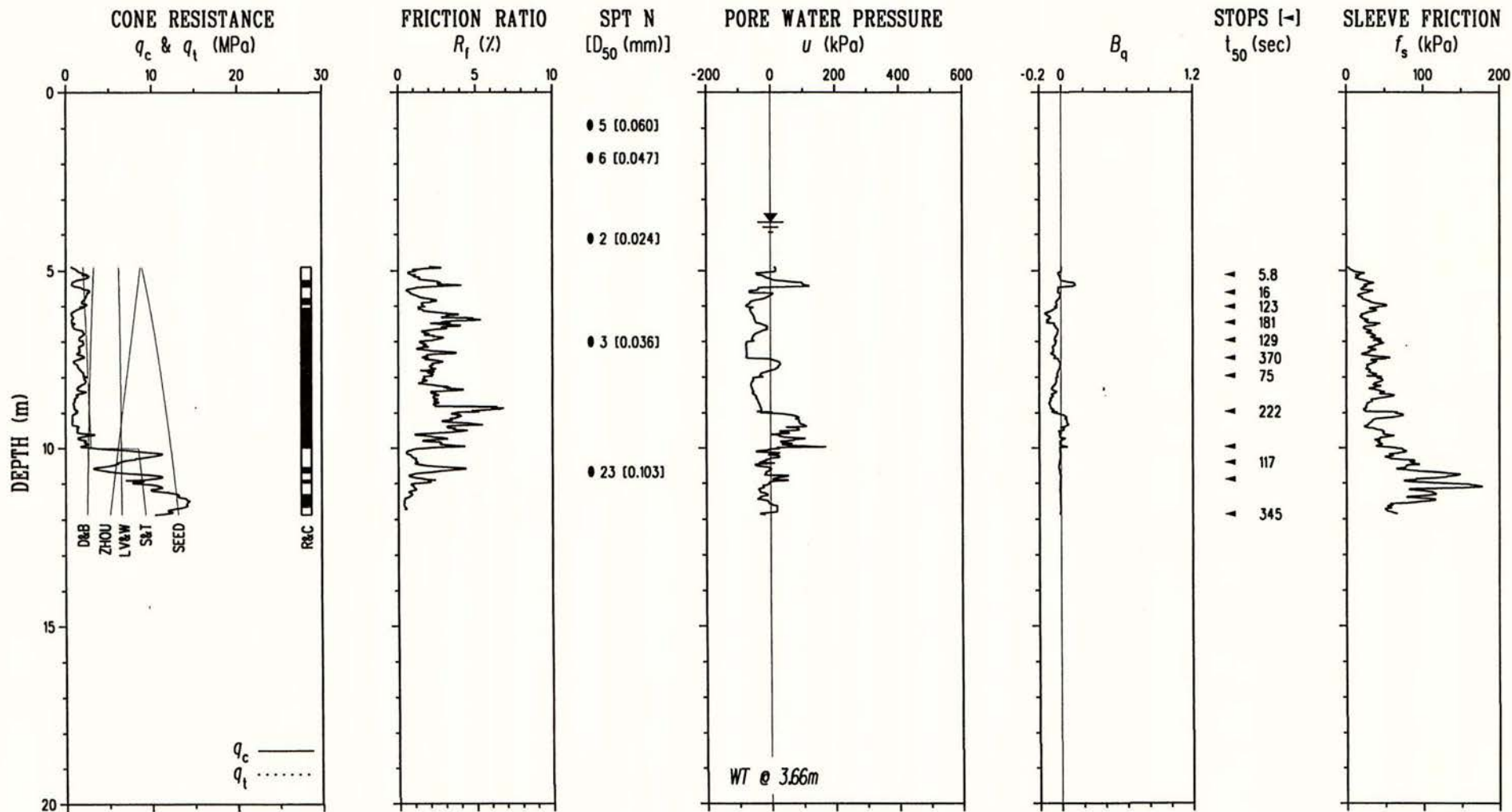
PAJ002.PPT

5 June 1990

TEST 6 - MILLERS FARM



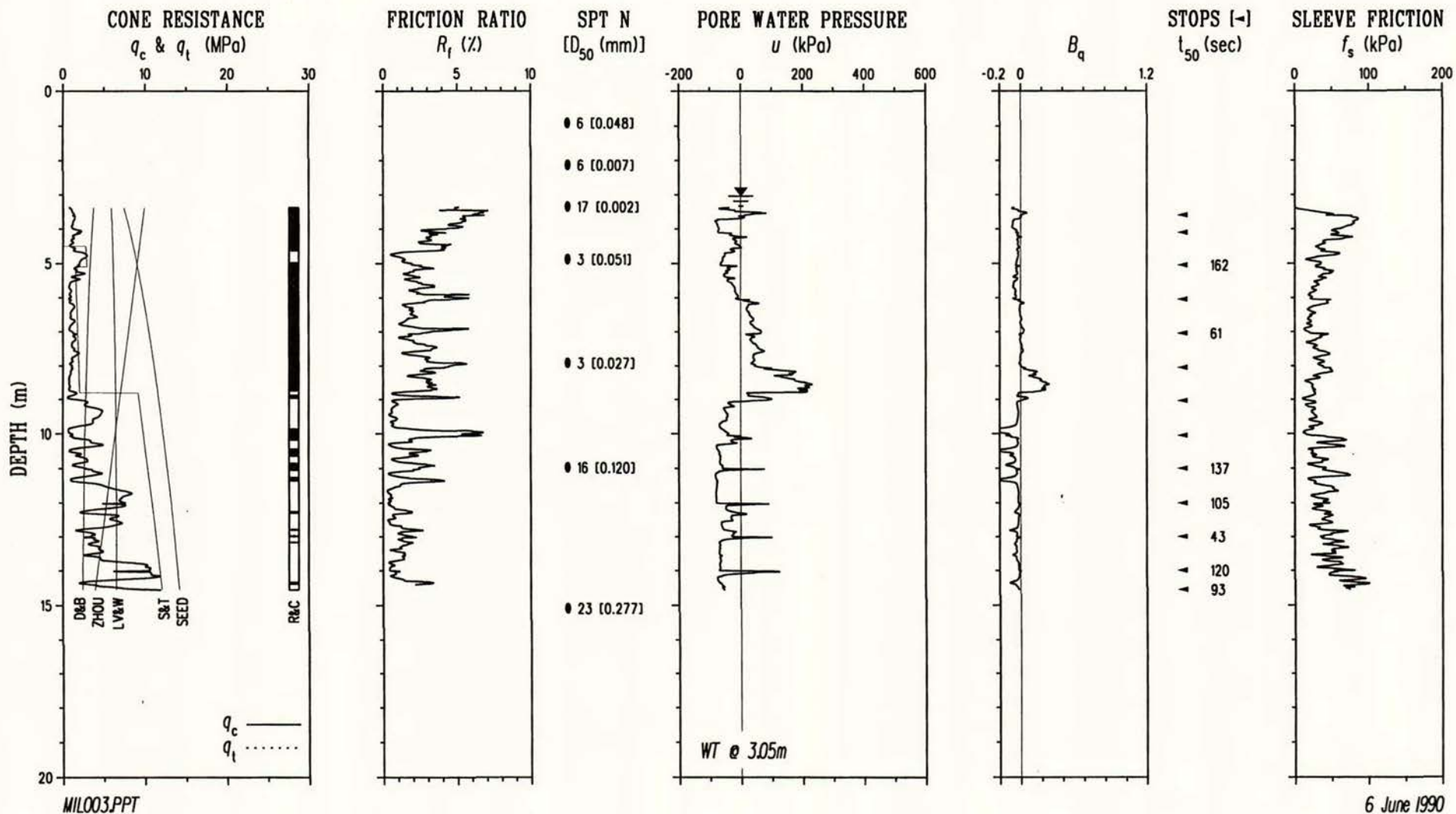
TEST 7 - MILLERS FARM



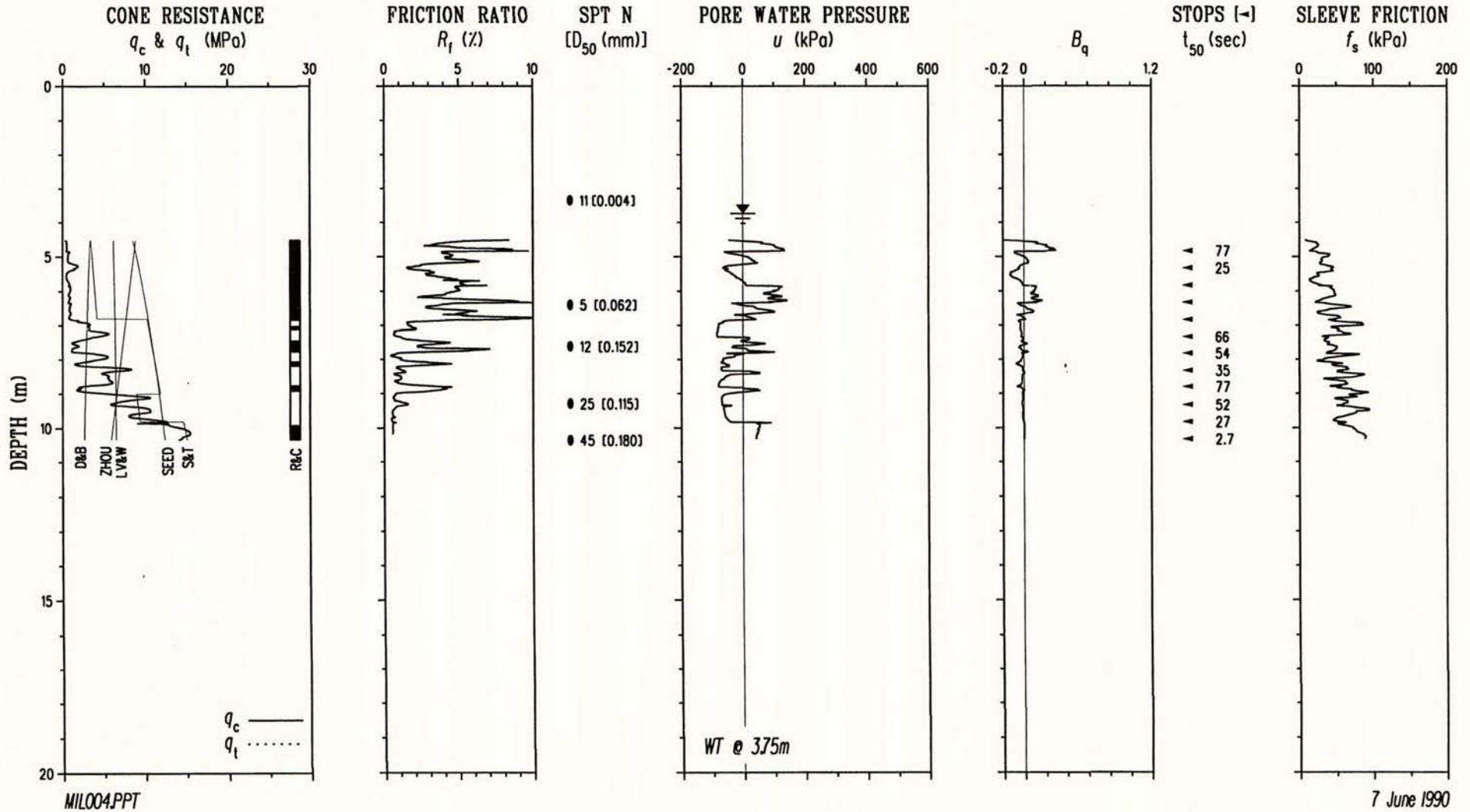
MIL002.PPT

6 June 1990

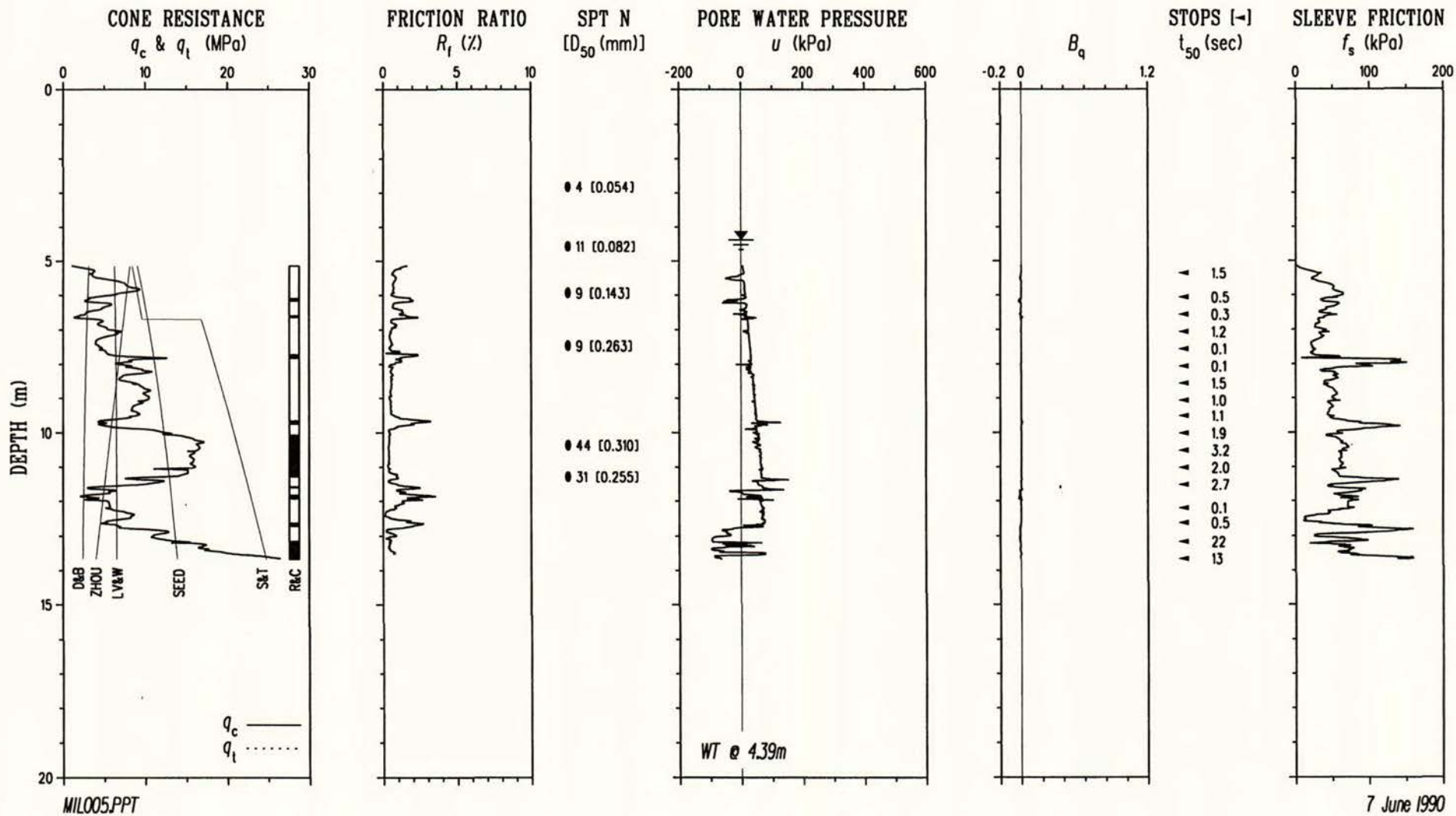
TEST 8 - MILLERS FARM



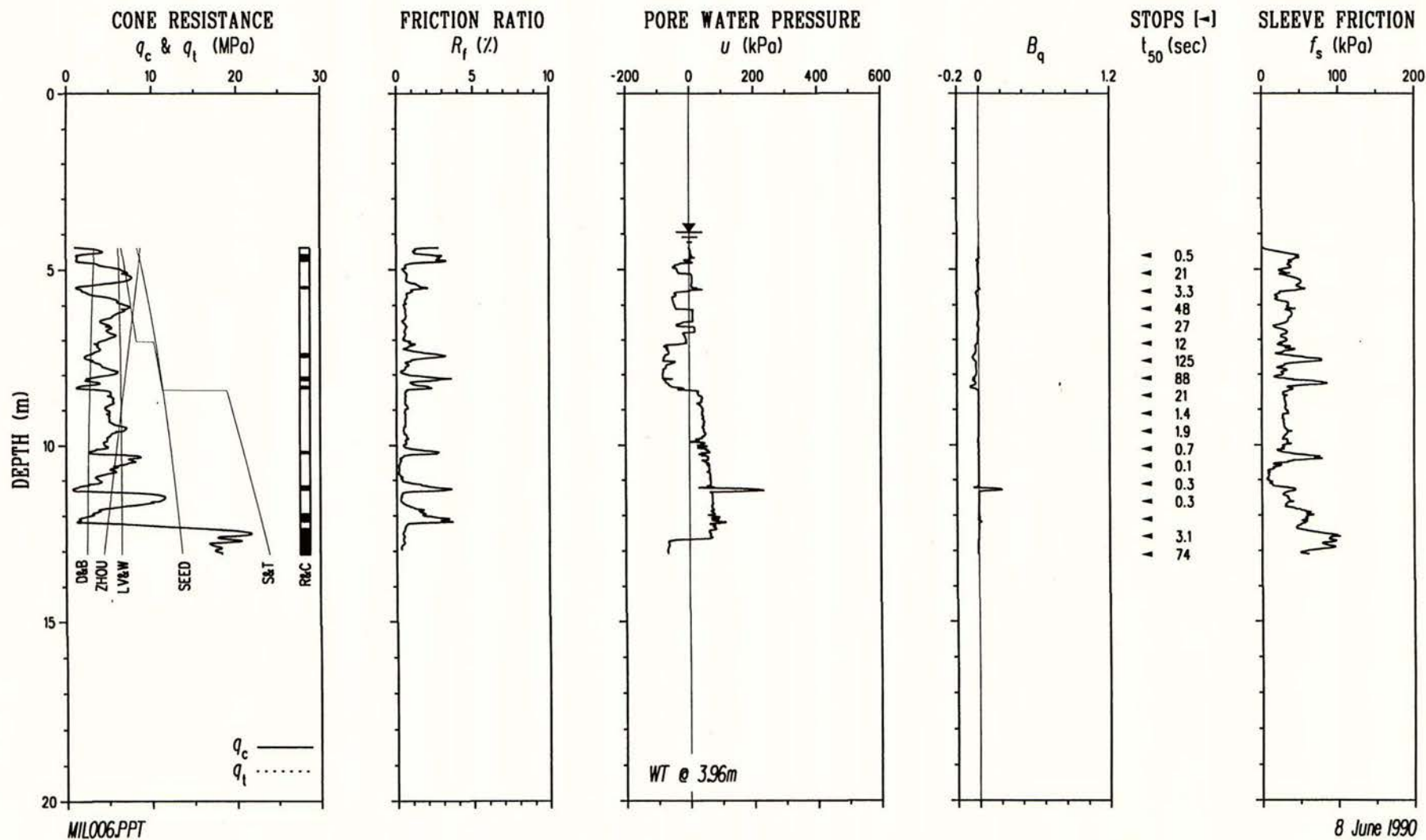
TEST 9 - MILLERS FARM



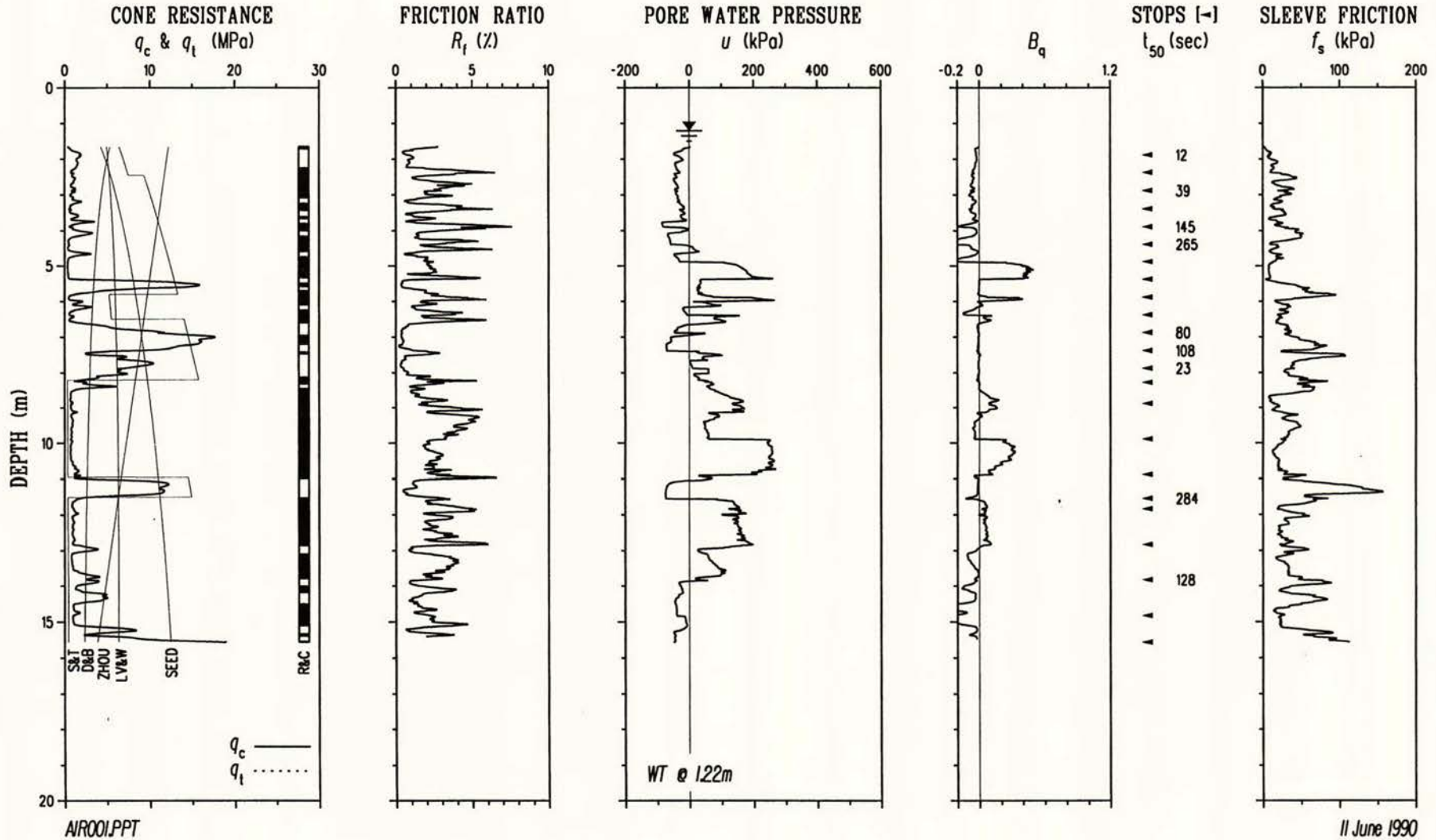
TEST 10 - MILLERS FARM



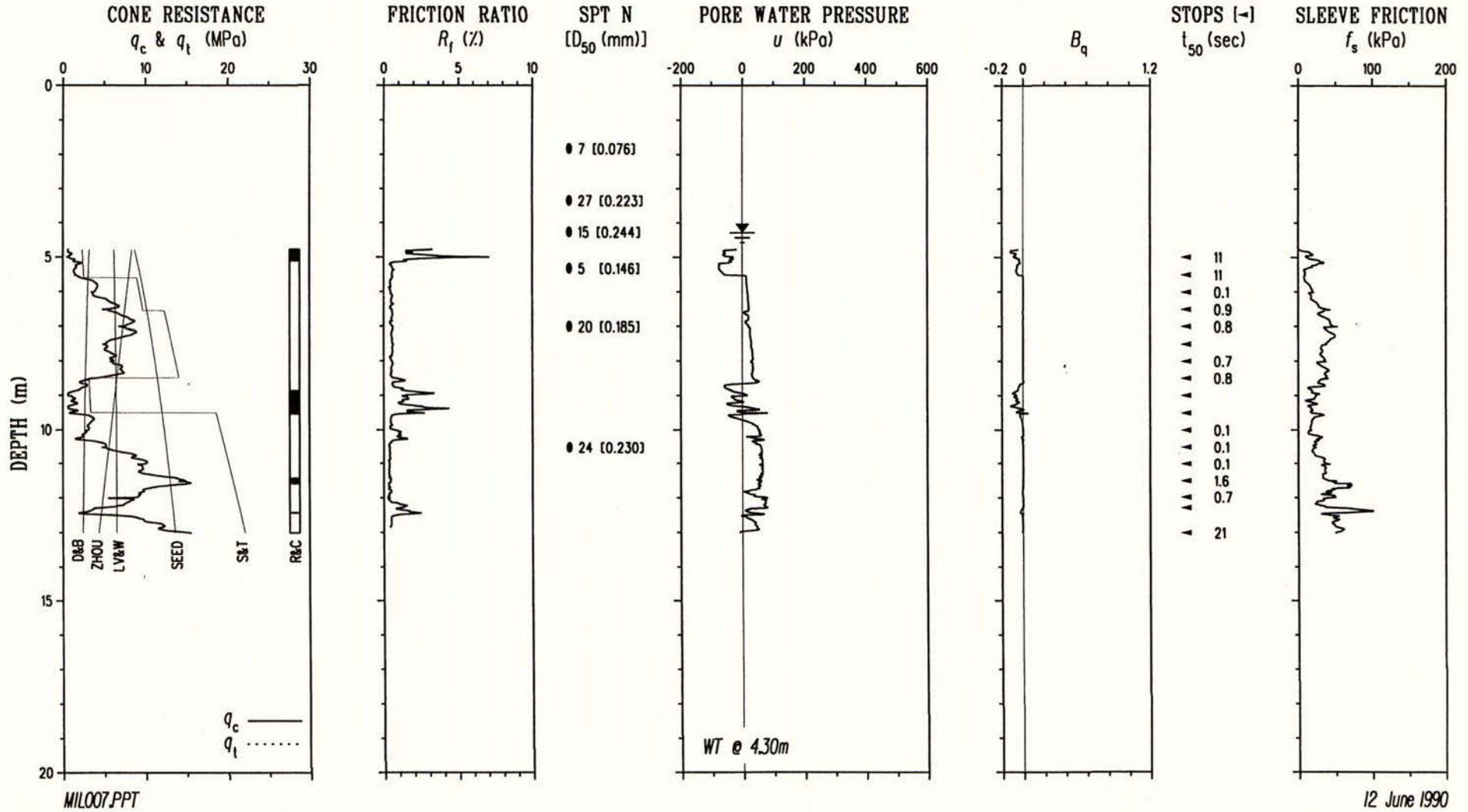
TEST 11 - MILLERS FARM



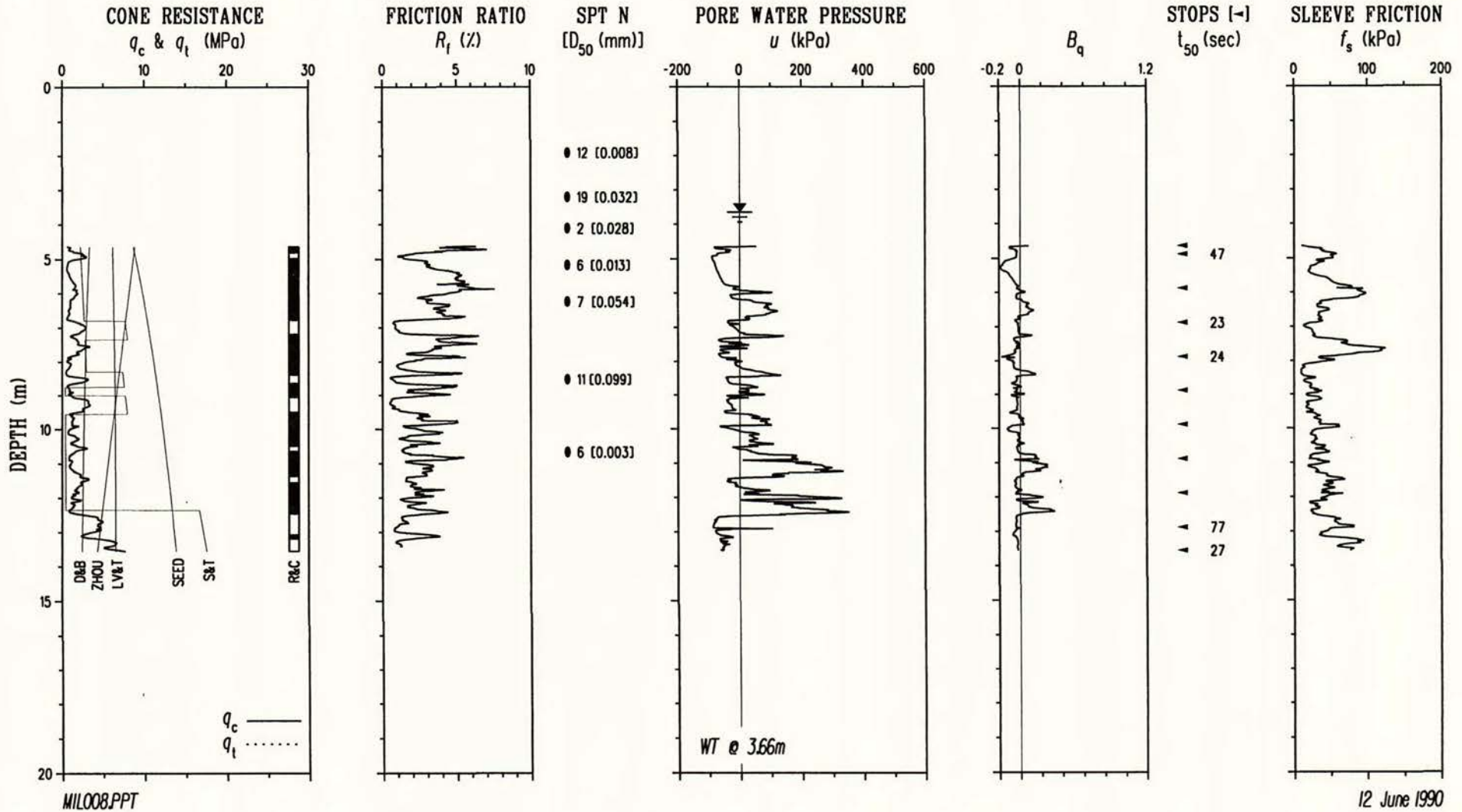
TEST 12 - AIRPORT WATSONVILLE



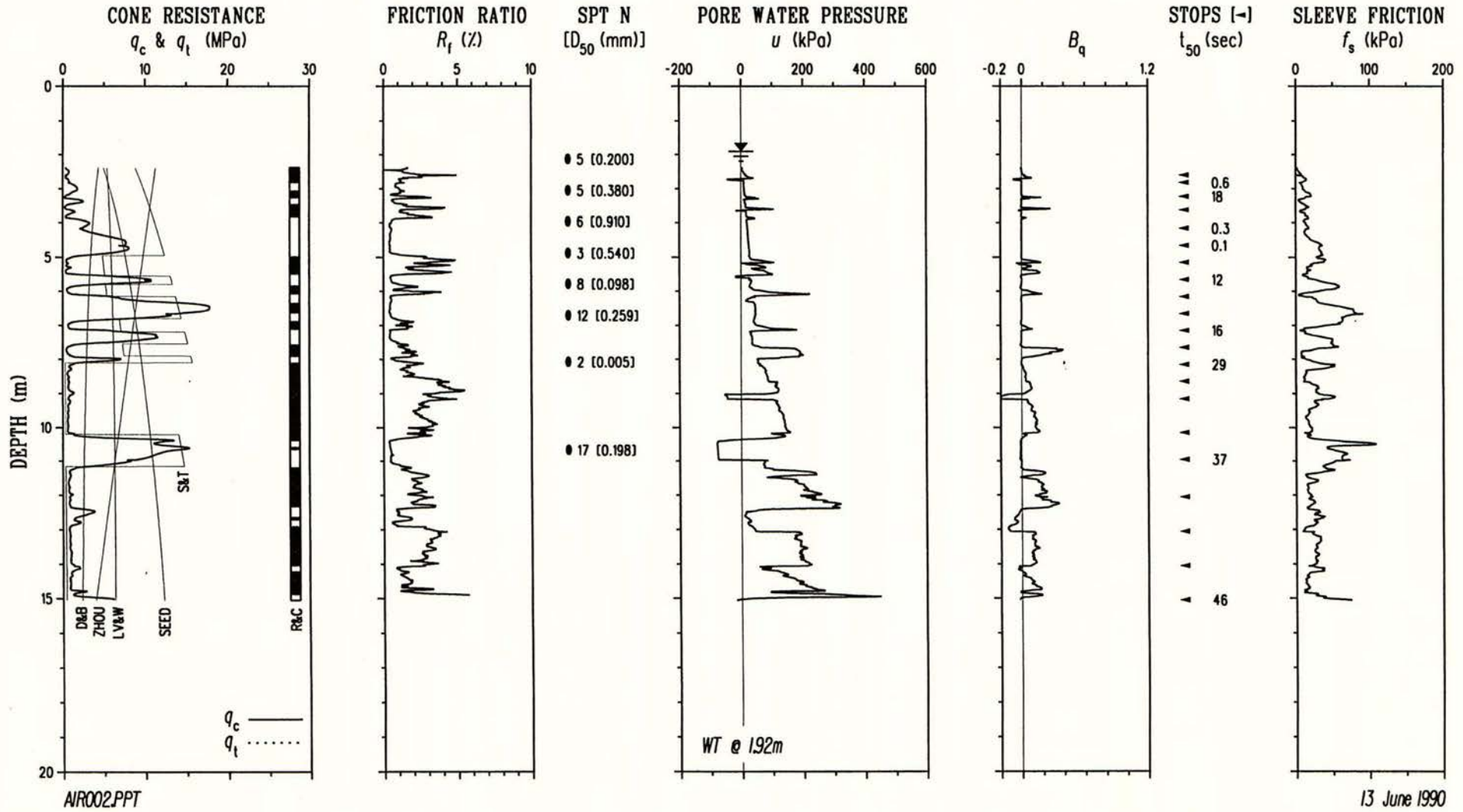
TEST 13 - MILLERS FARM



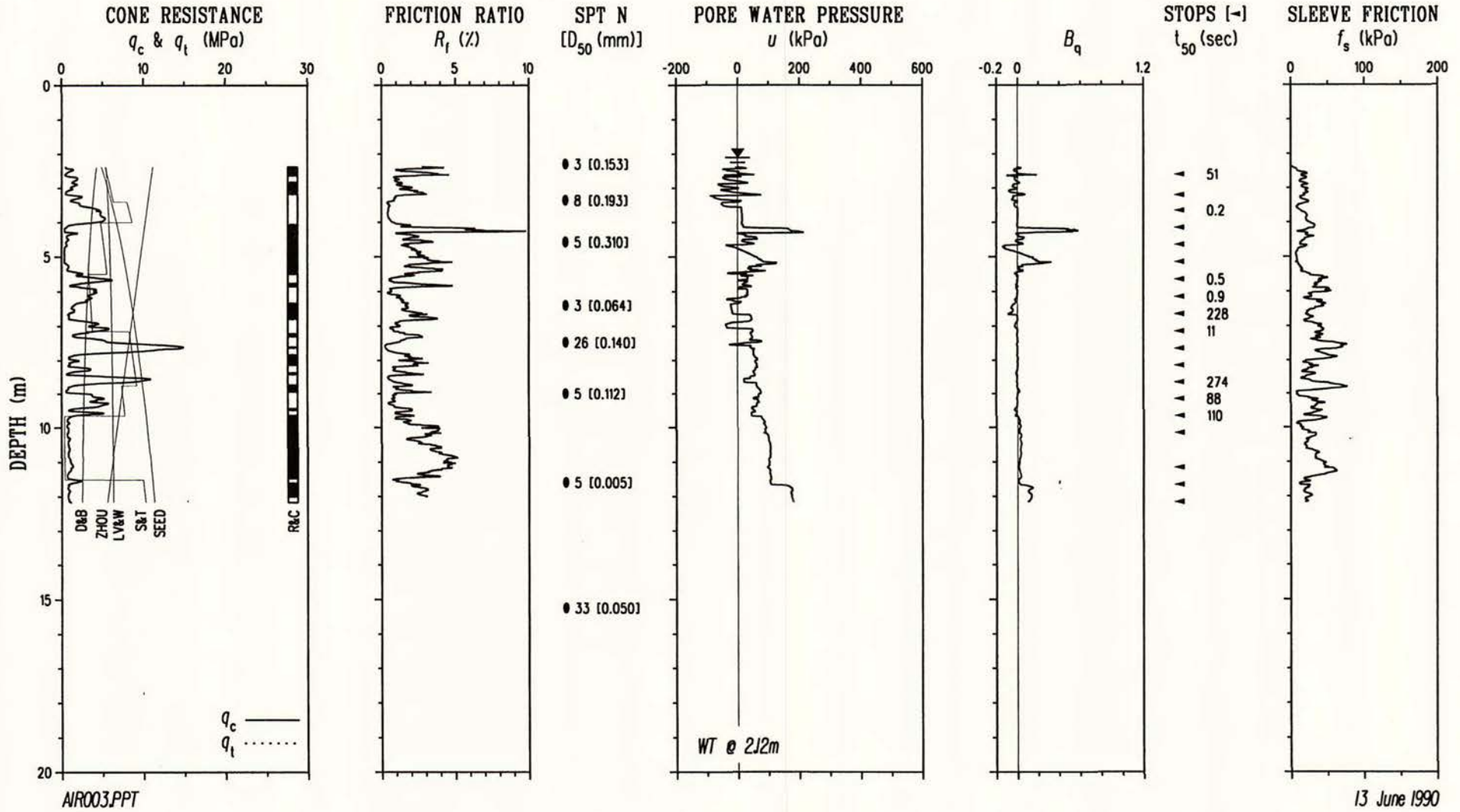
TEST 14 - MILLERS FARM



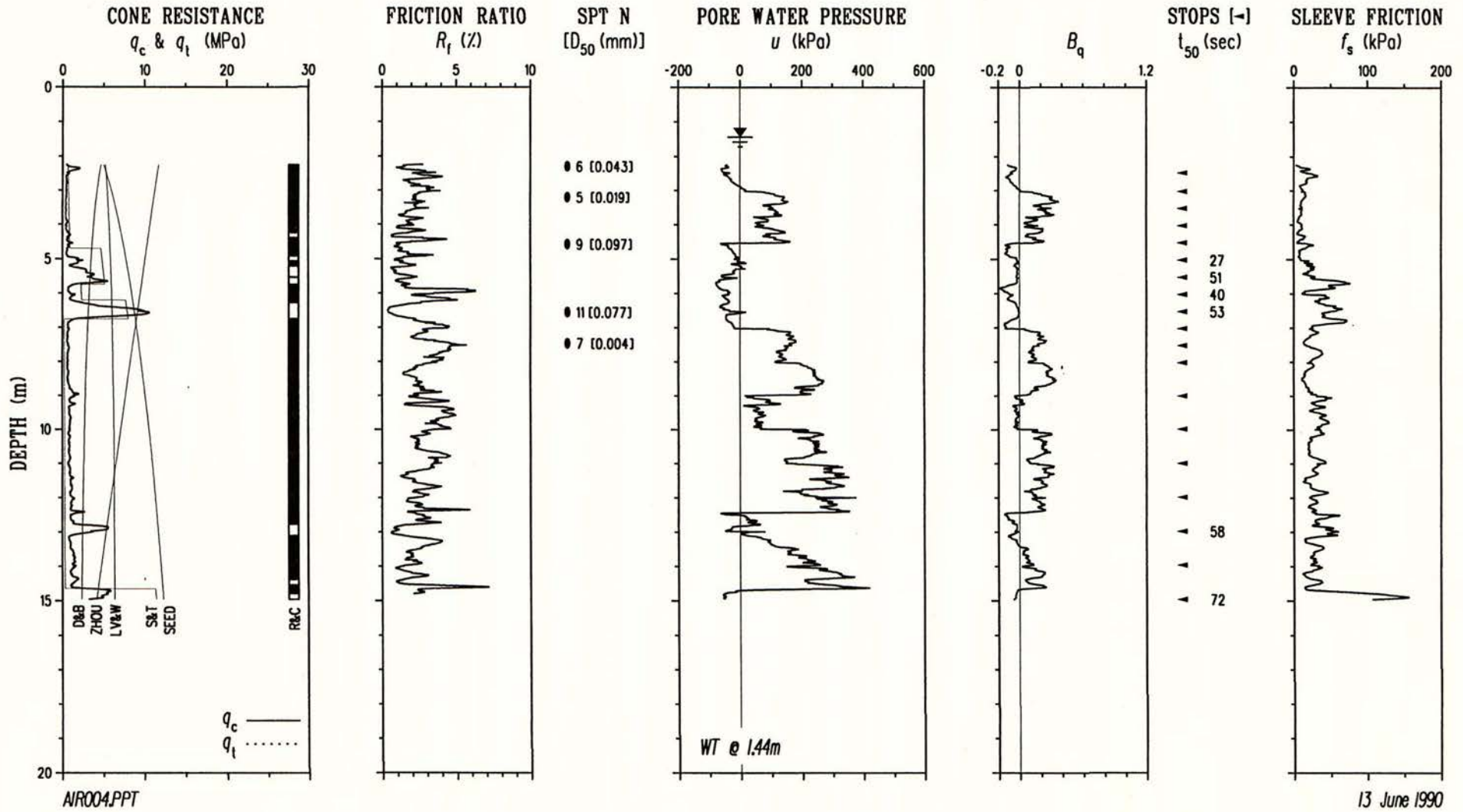
TEST 15 - AIRPORT WATSONVILLE



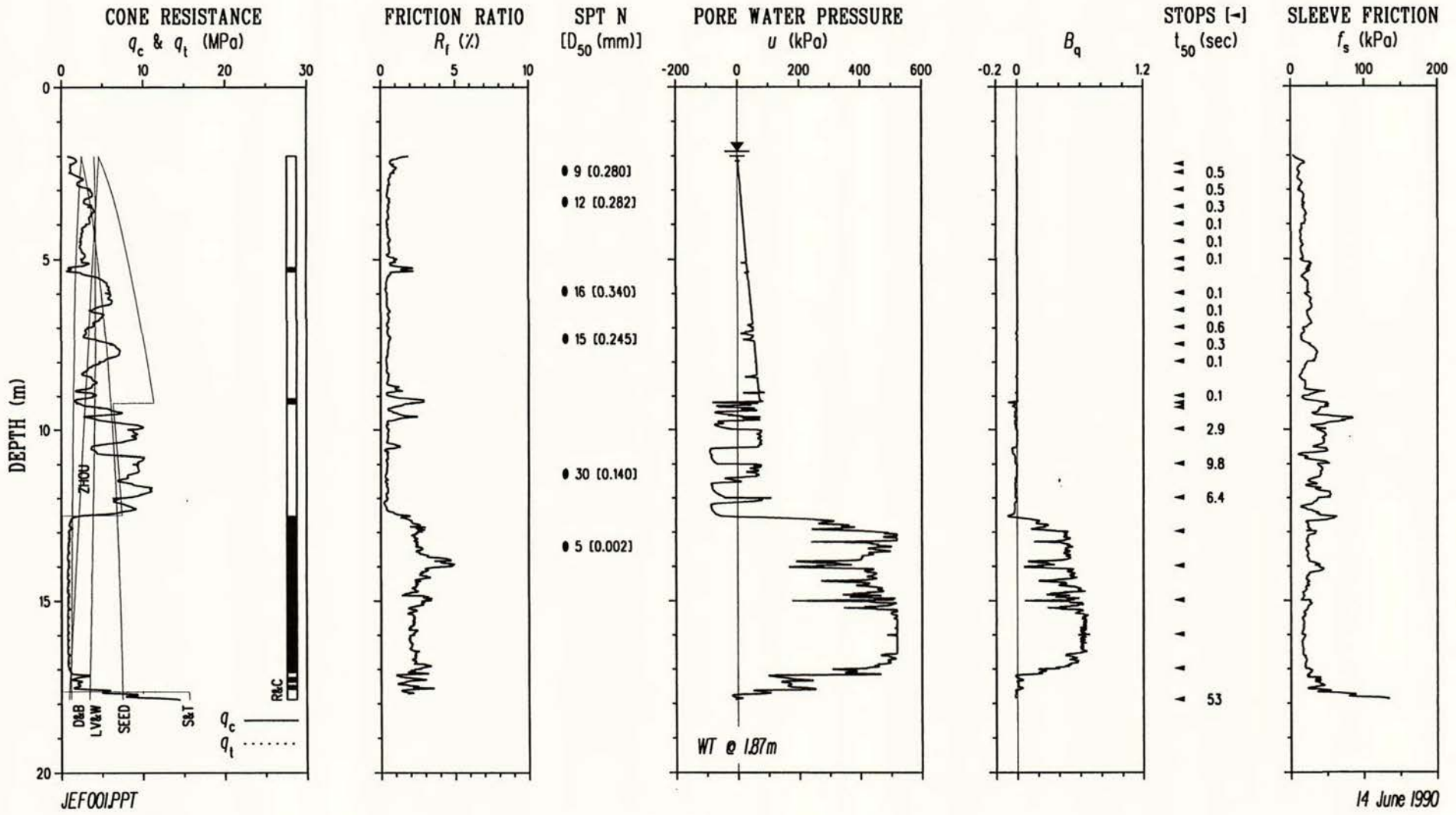
TEST 16 - AIRPORT WATSONVILLE



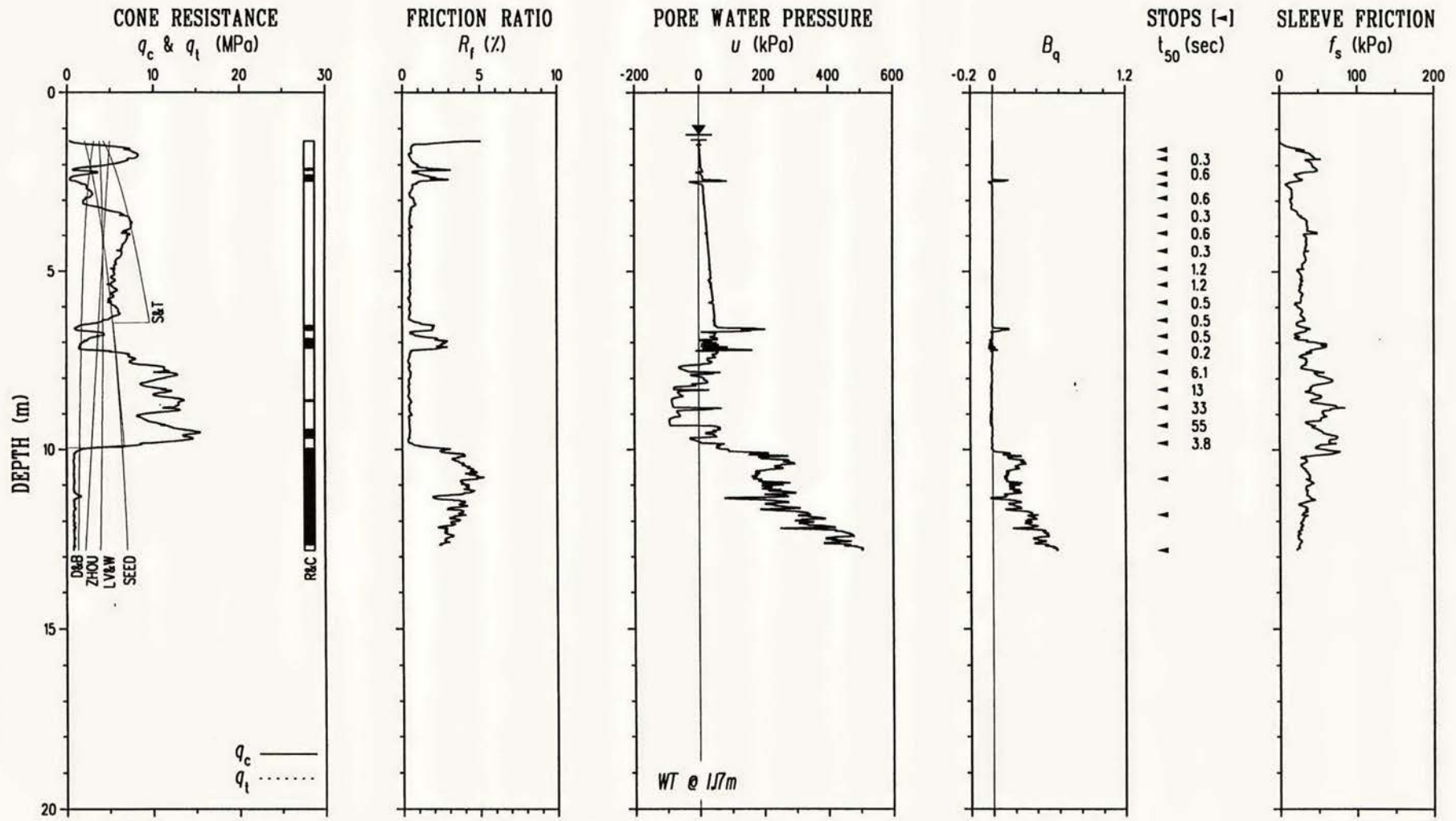
TEST 17 - AIRPORT WATSONVILLE



TEST 18 - JEFFERSON



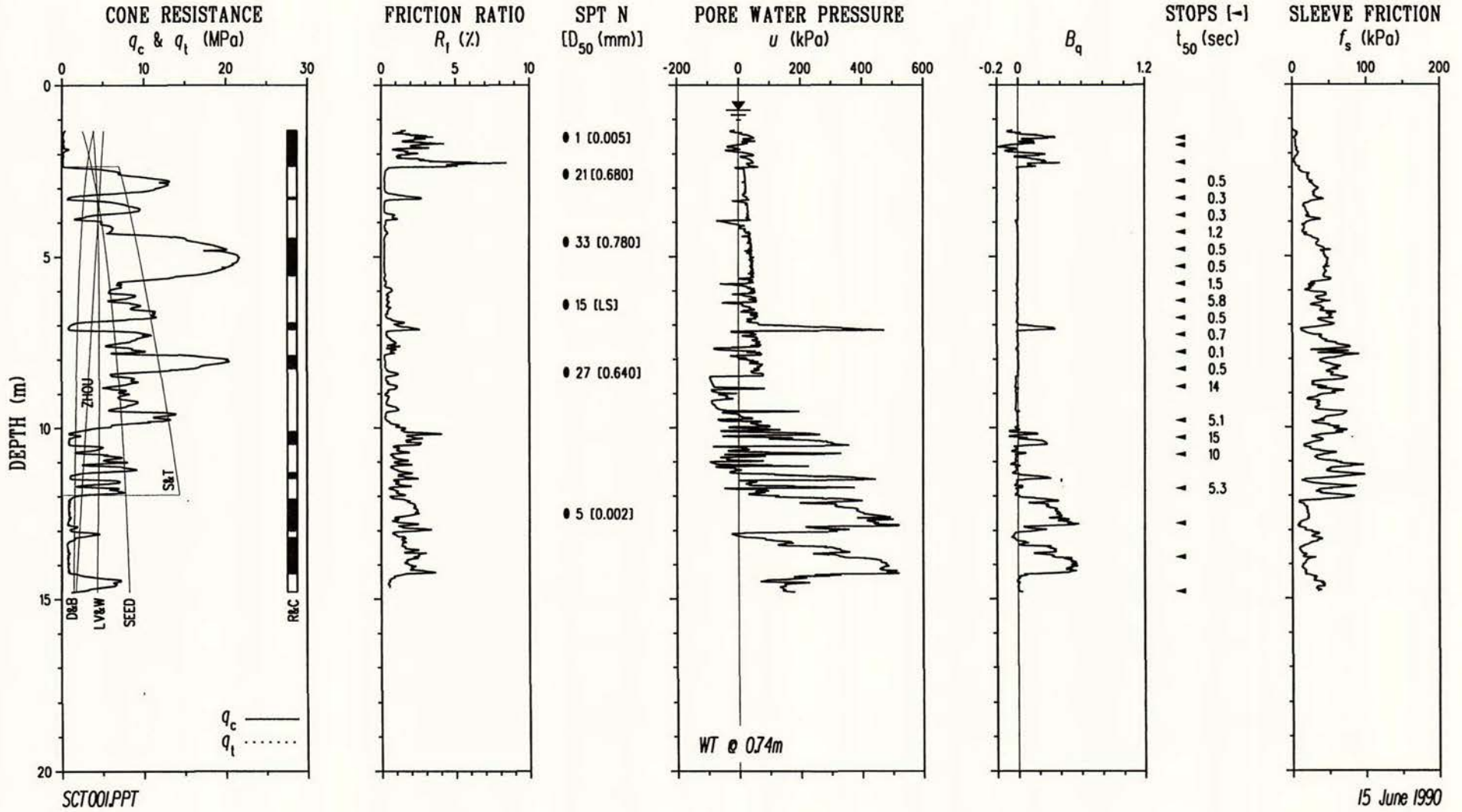
TEST 19 - JEFFERSON



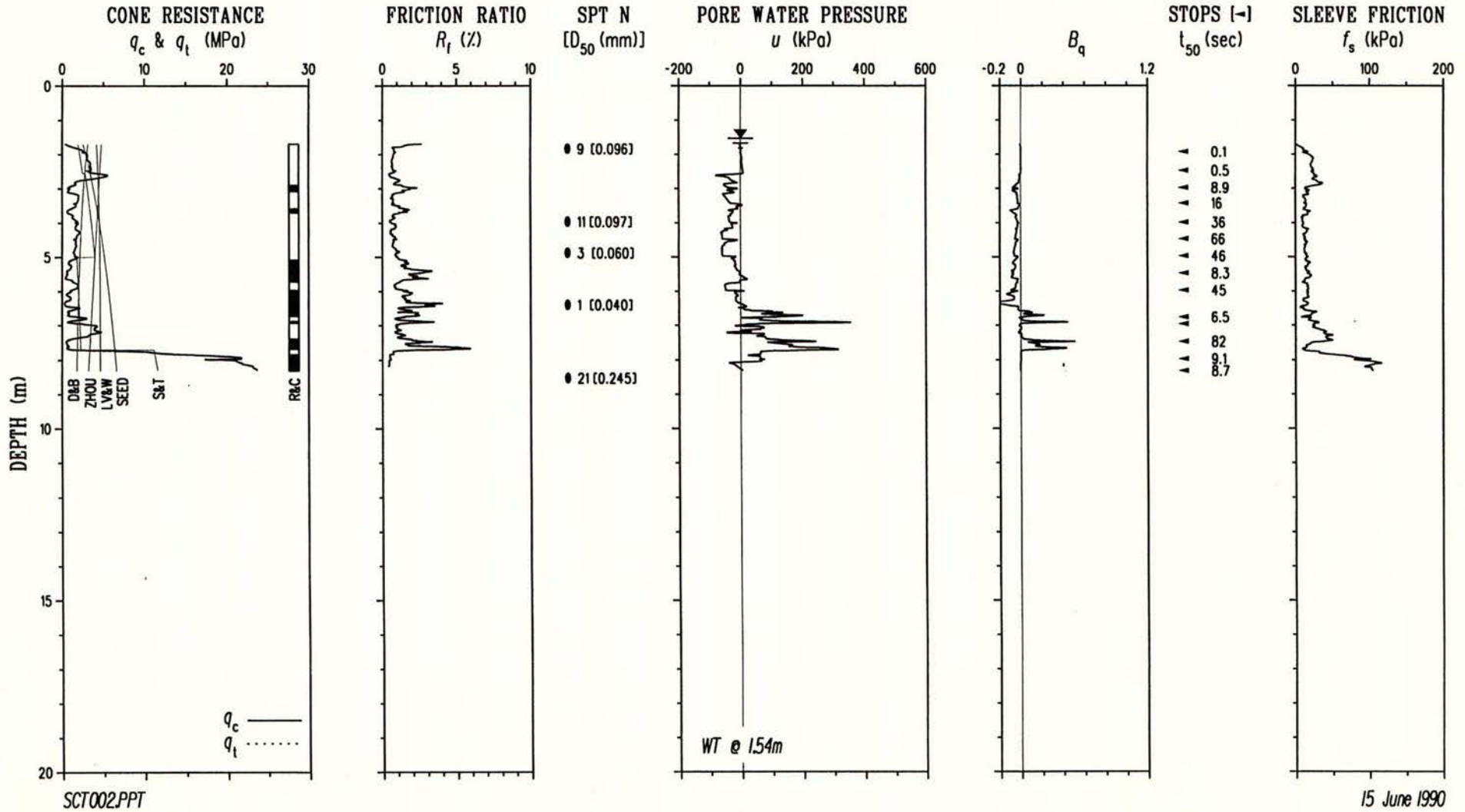
JEF002.PPT

14 June 1990

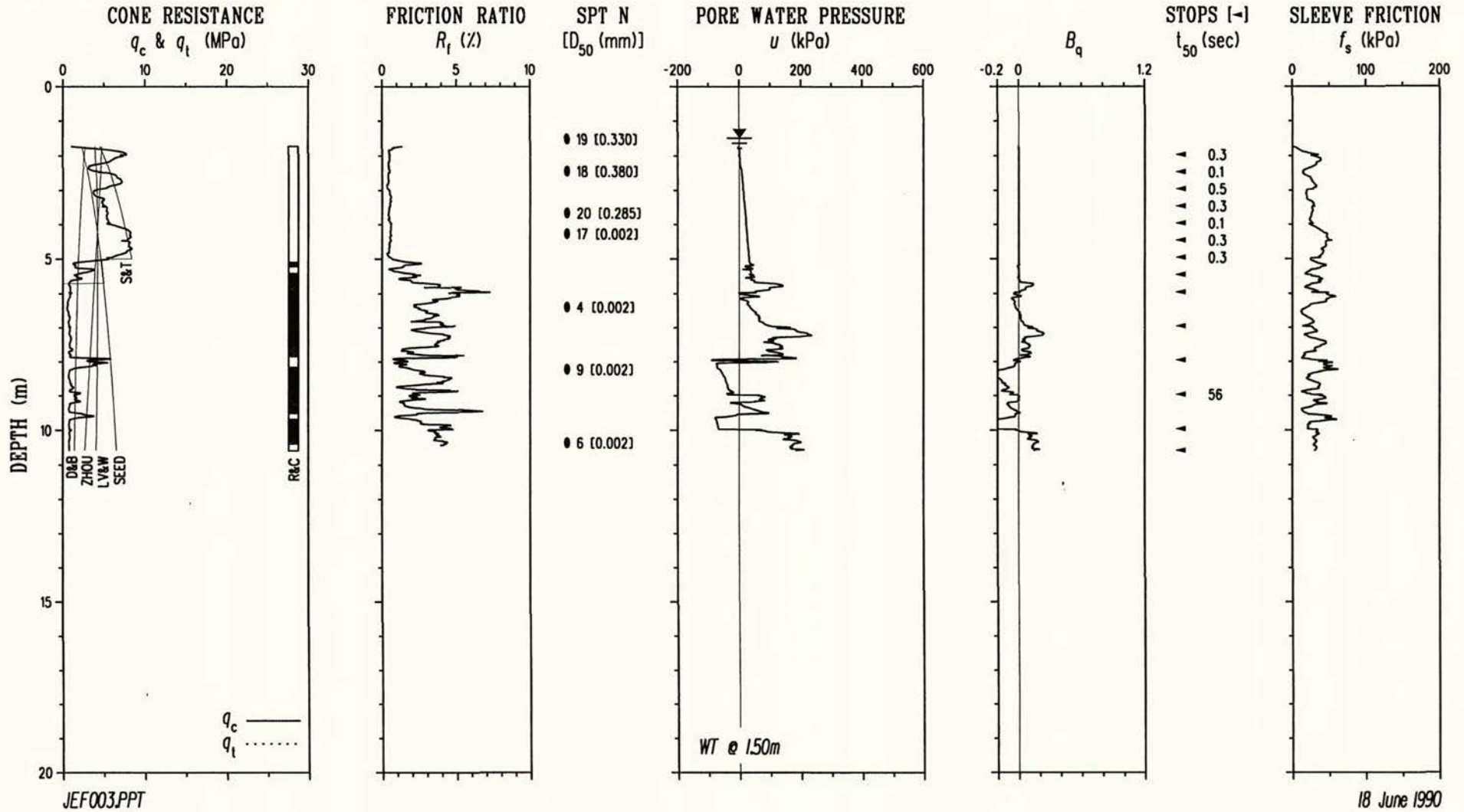
TEST 20 - SCATTINI



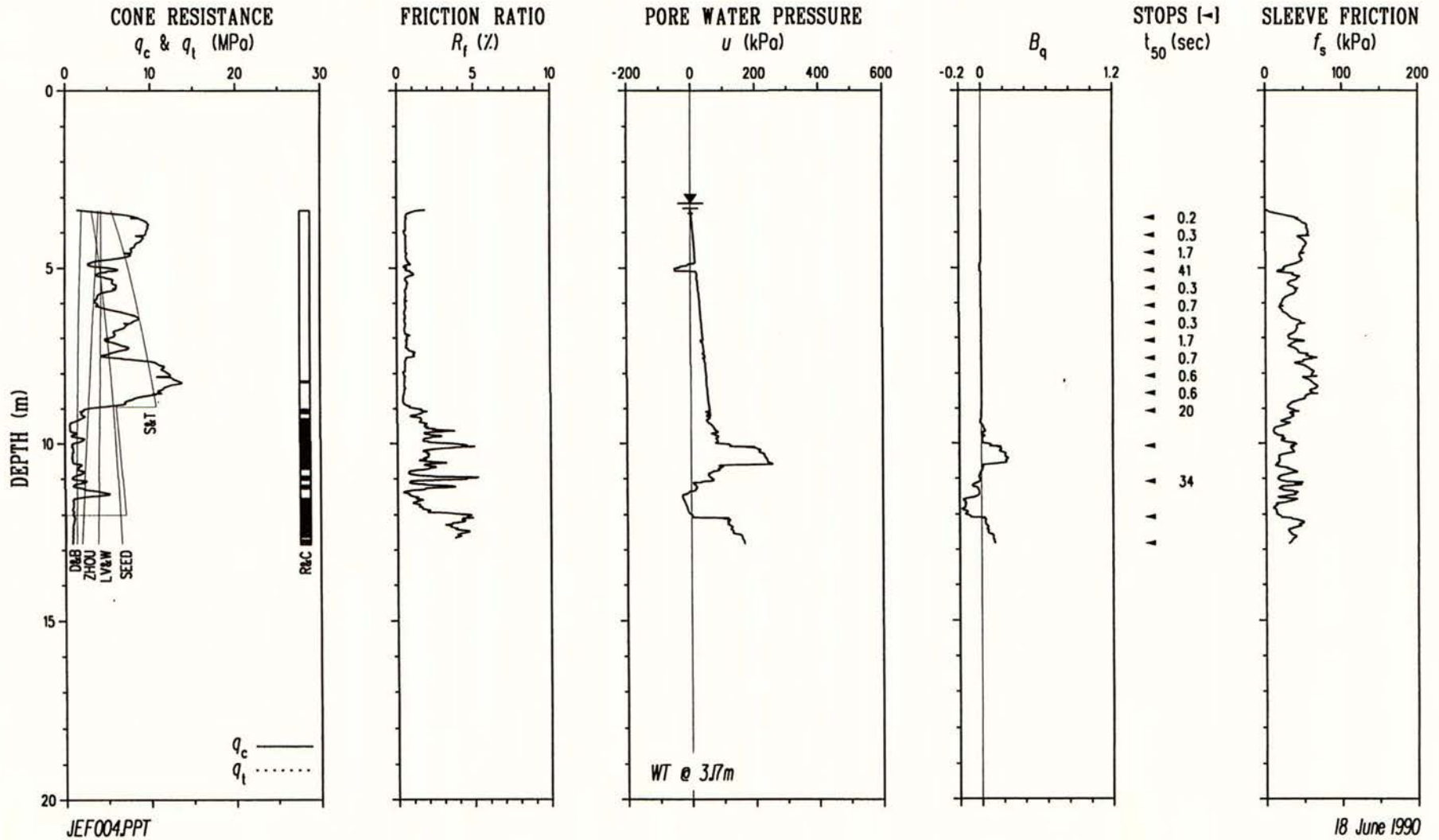
TEST 21 - SCATTINI



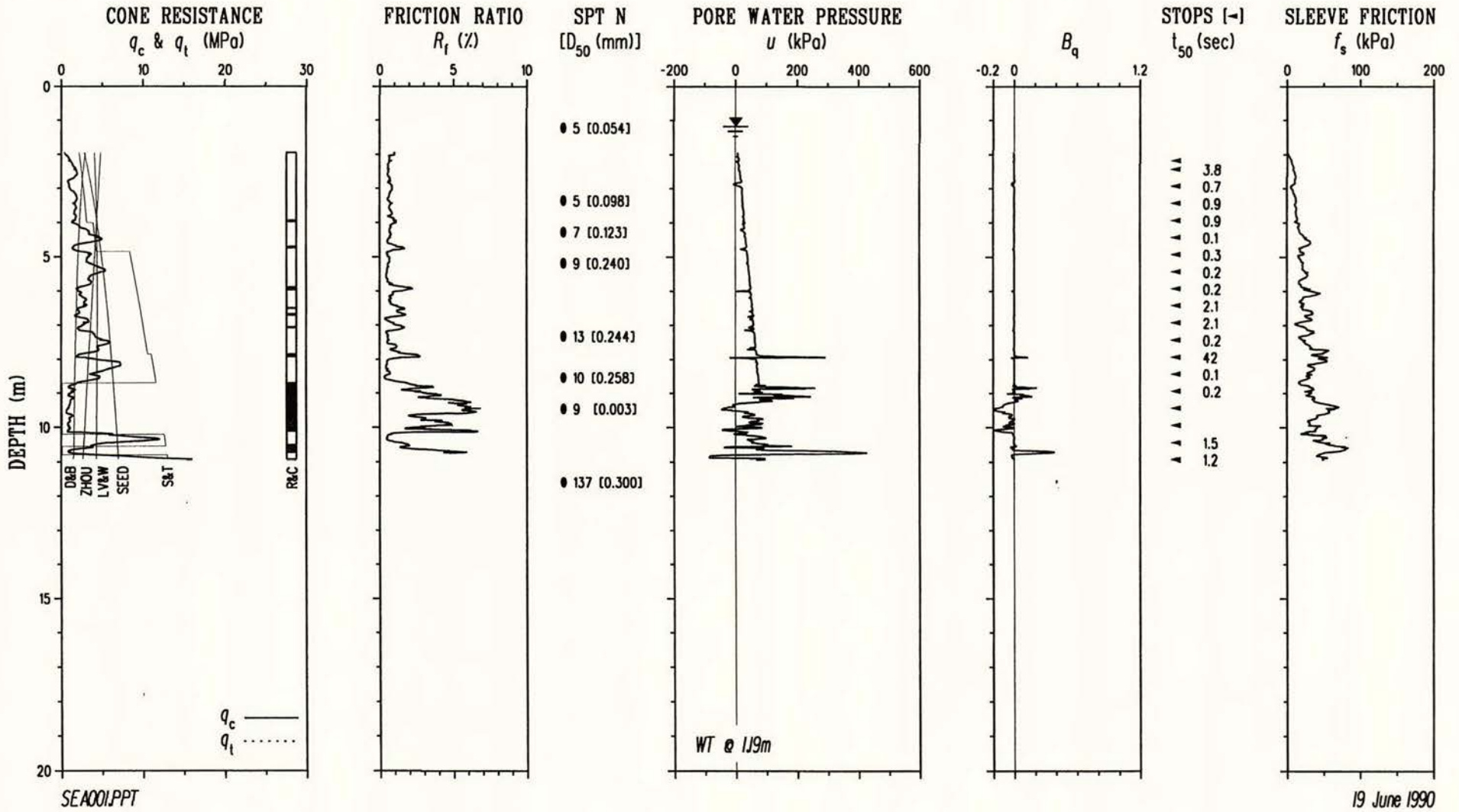
TEST 22 - JEFFERSON



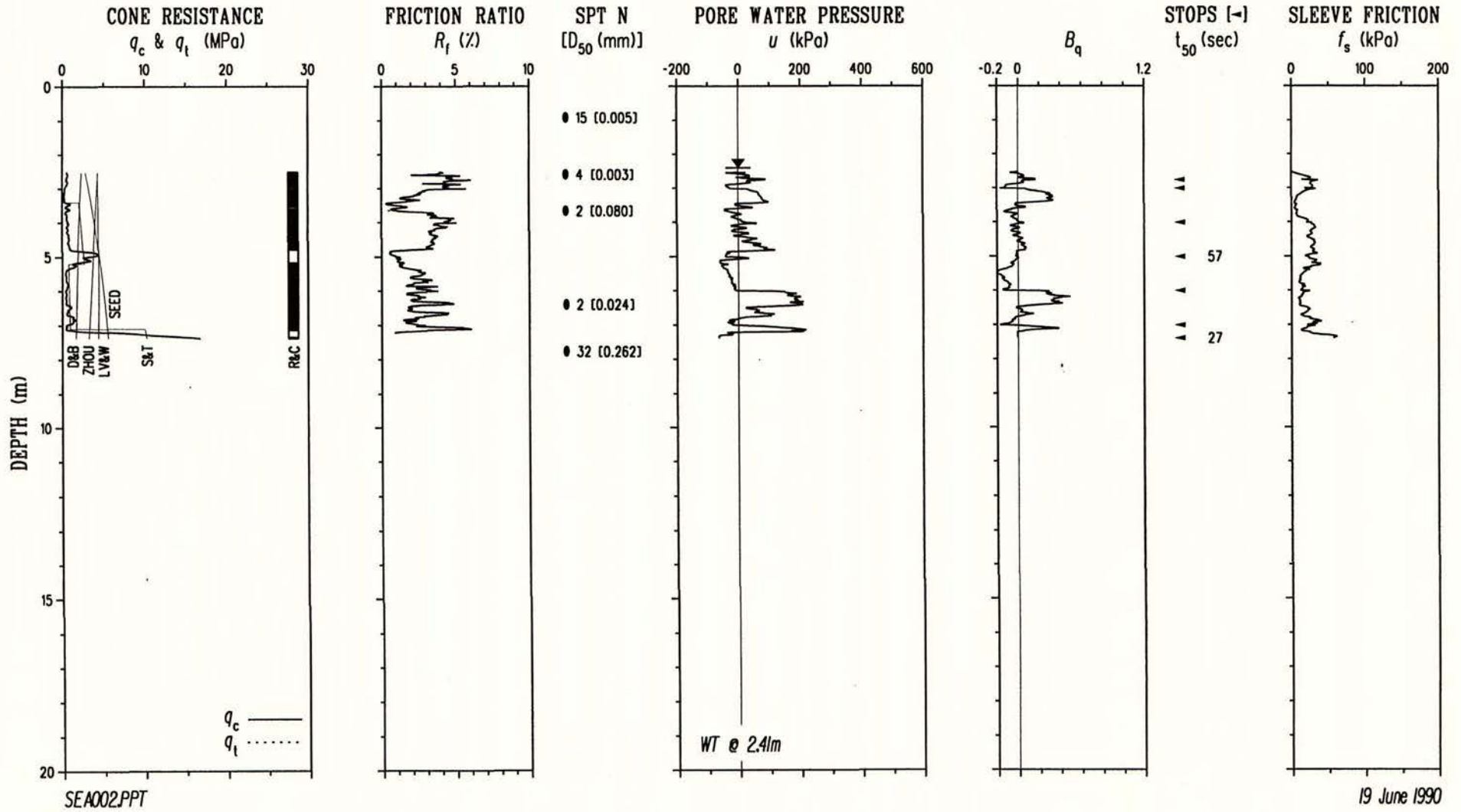
TEST 23 - JEFFERSON



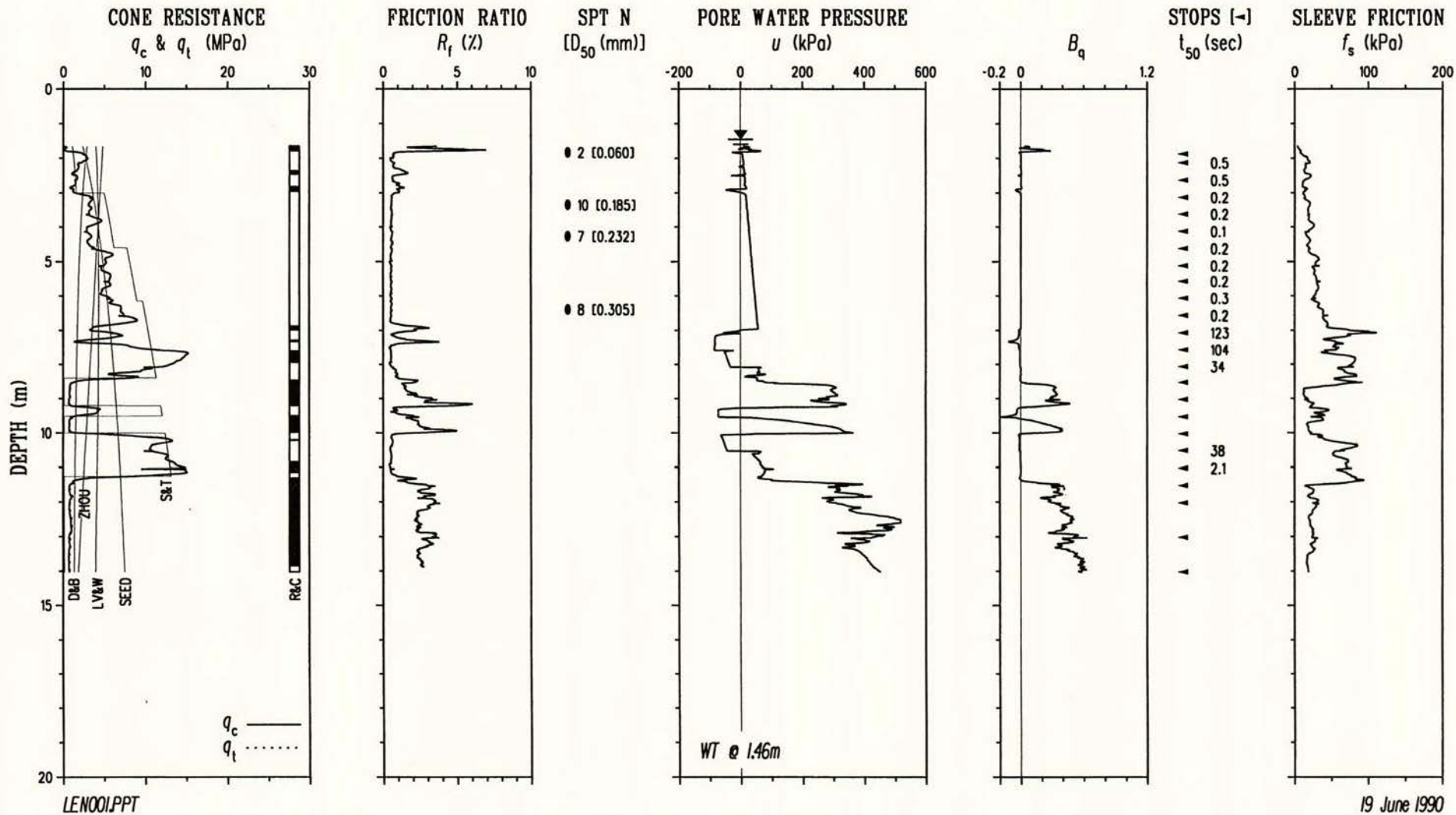
TEST 24 - SEA MIST



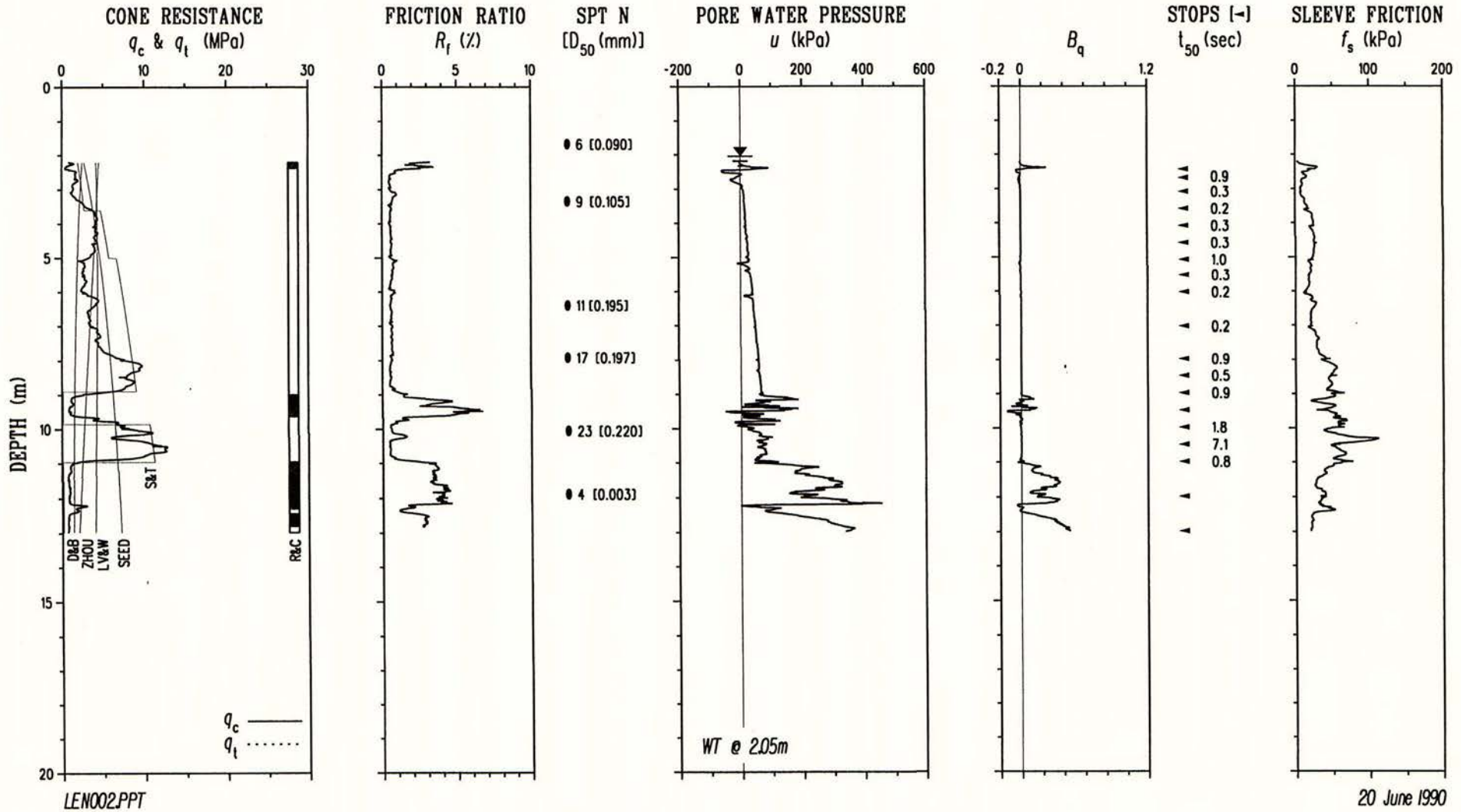
TEST 25 - SEA MIST



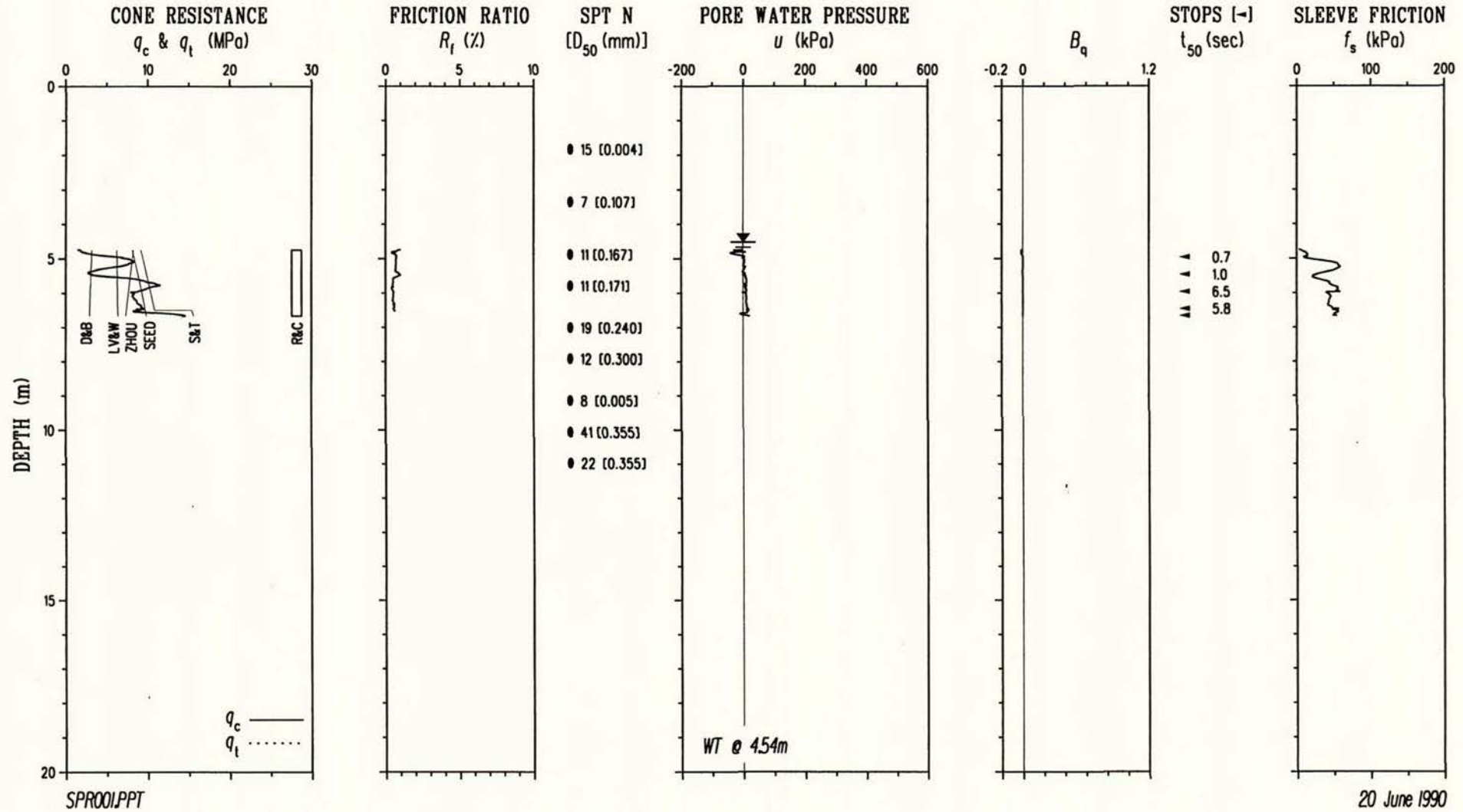
TEST 26 - LEONARDINI



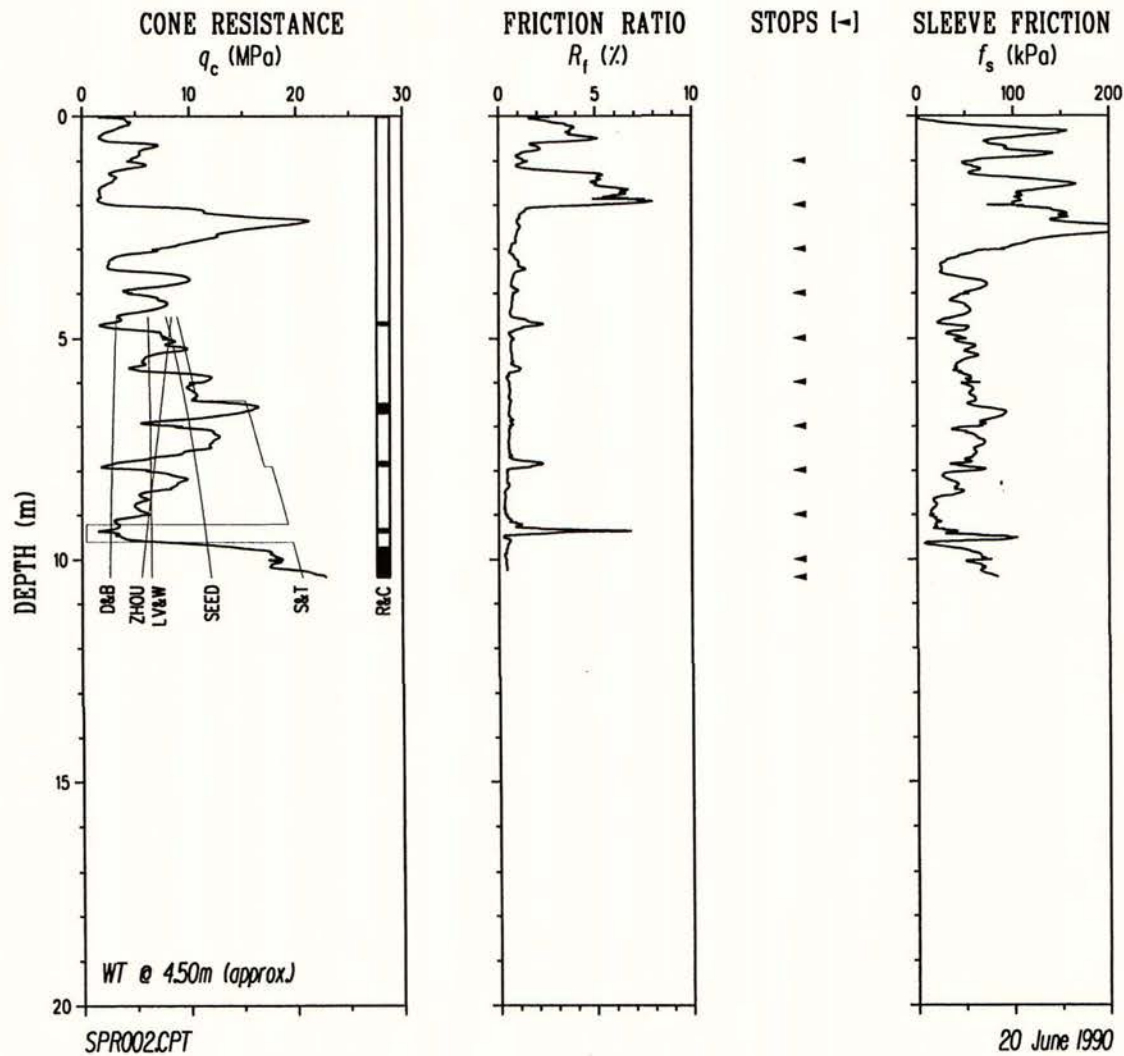
TEST 27 - LEONARDINI



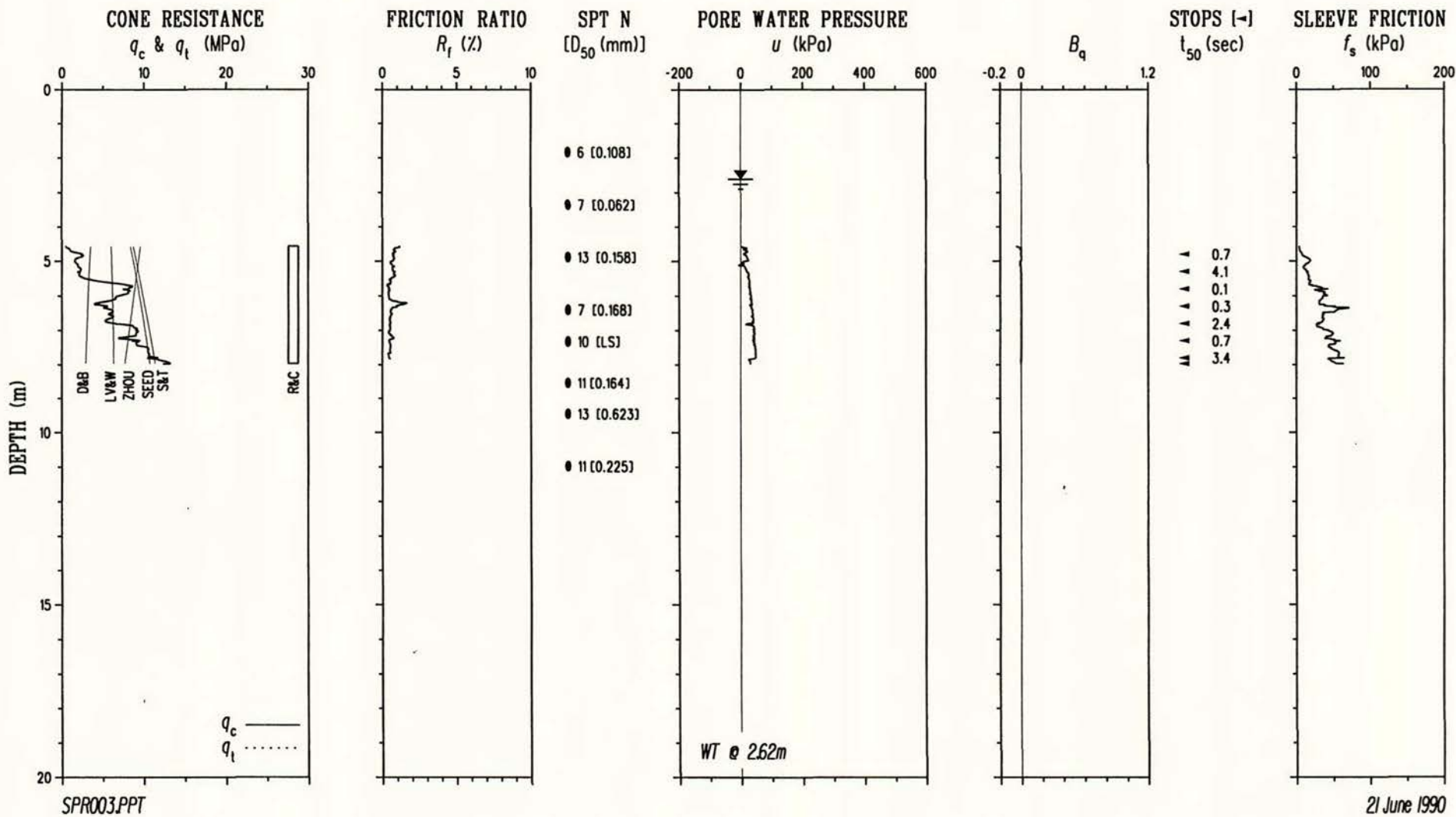
TEST 28 - SPR BRIDGE



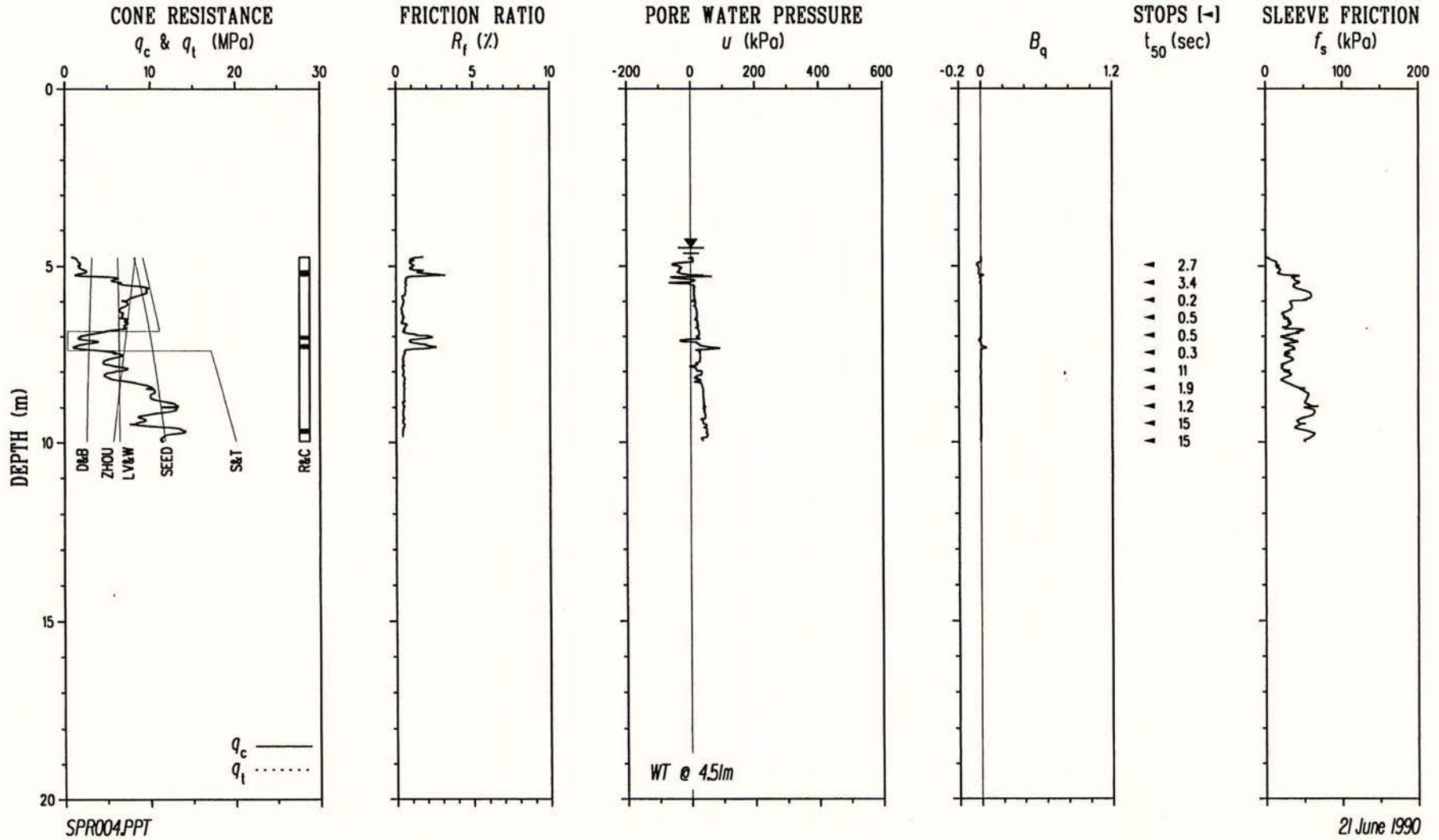
TEST 29 - SPR BRIDGE



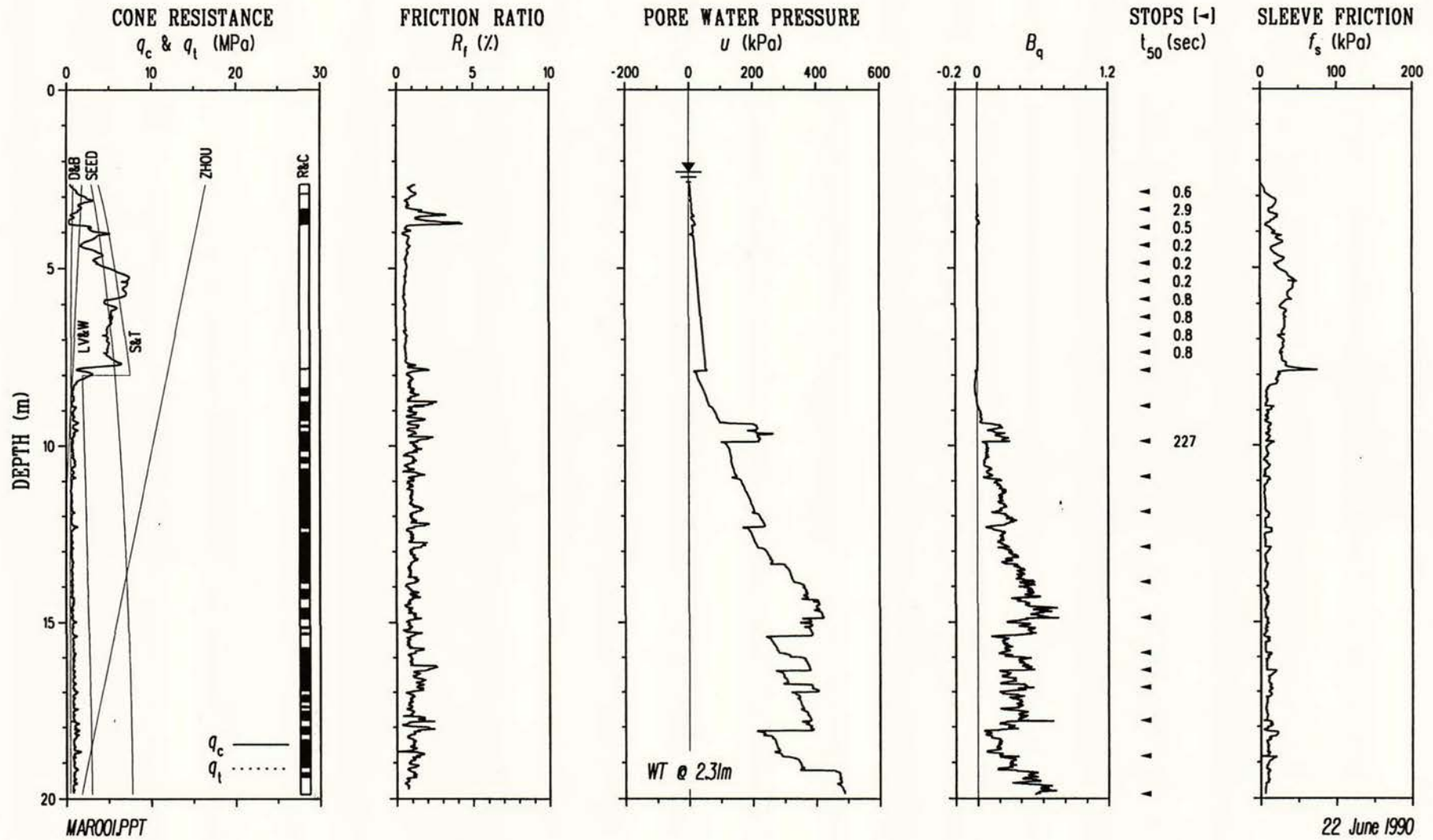
TEST 30 - SPR BRIDGE



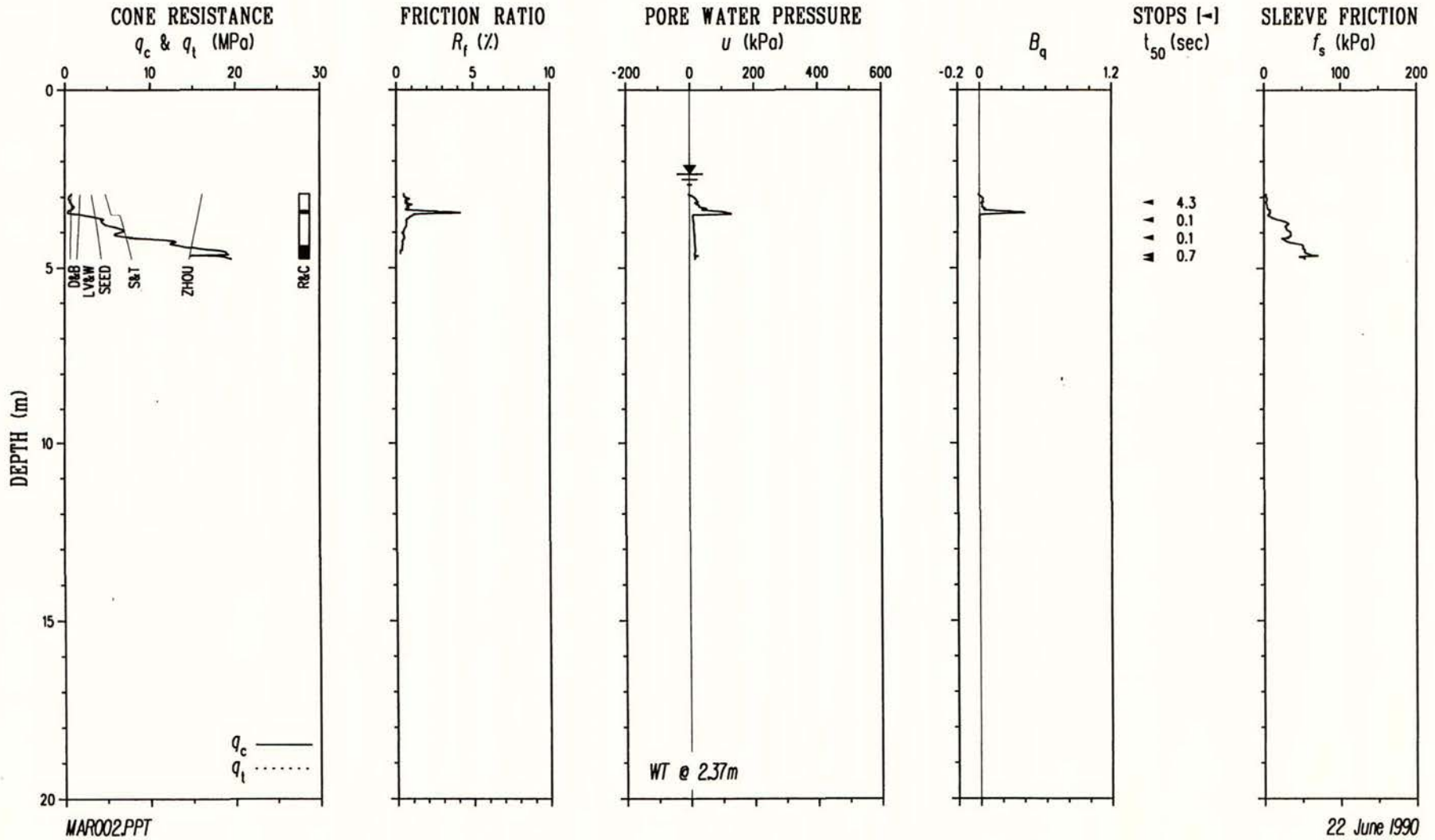
TEST 31 - SPR BRIDGE



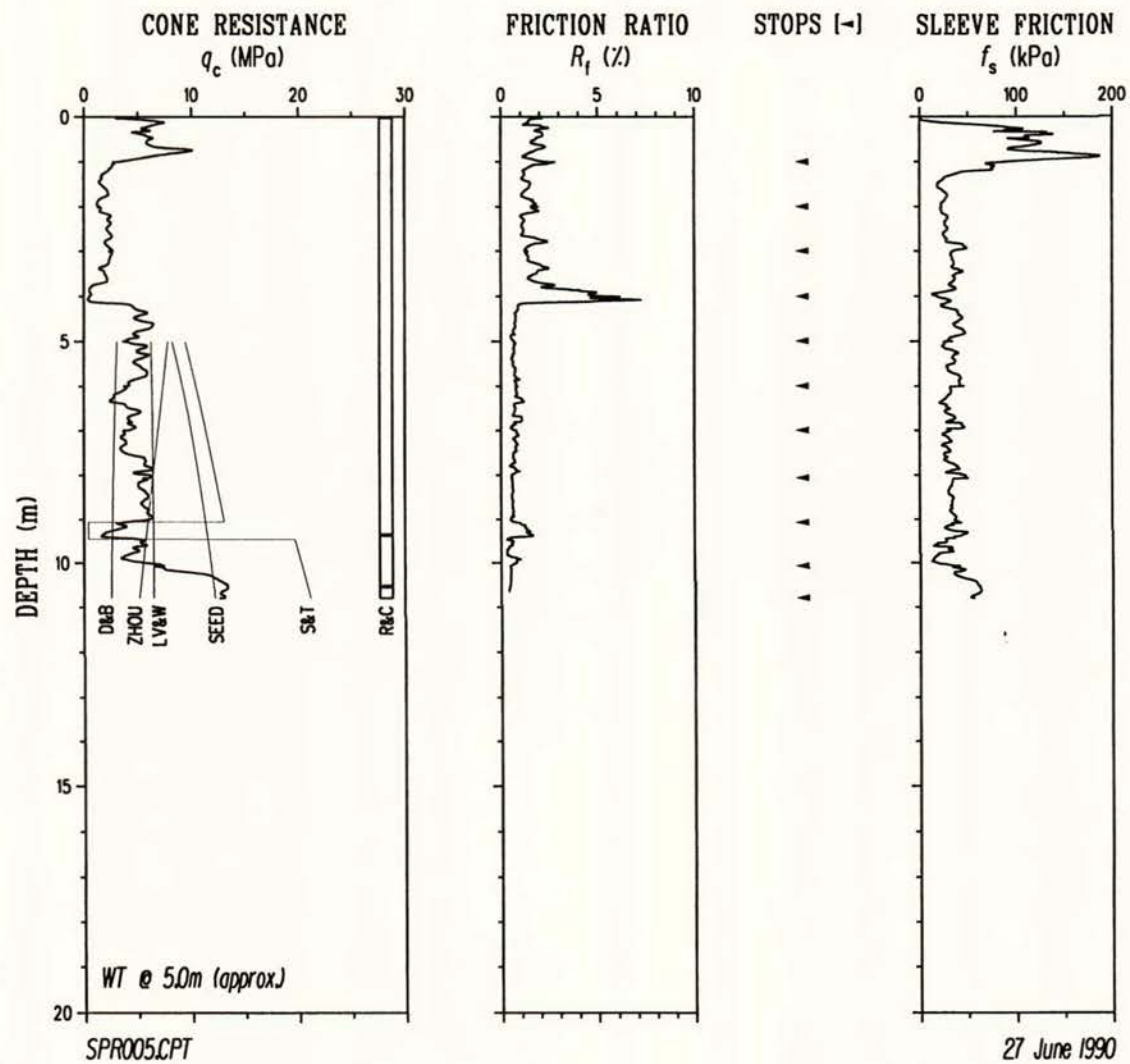
TEST 32 - MARINA DISTRICT



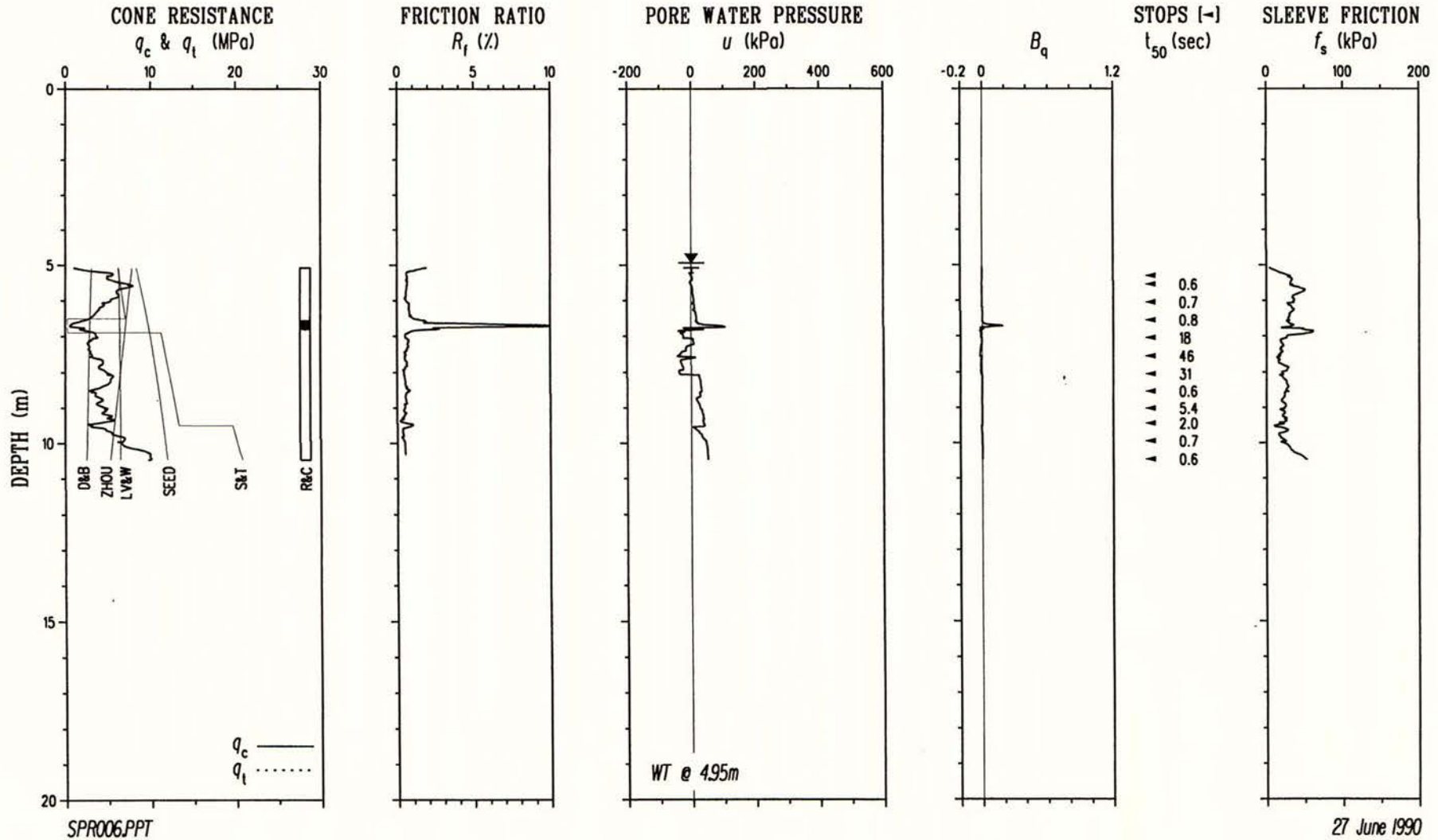
TEST 33 - MARINA DISTRICT



TEST 34 - SPR BRIDGE



TEST 35 - SPR BRIDGE



LOMA PRIETA SPT N and D₅₀ DATA

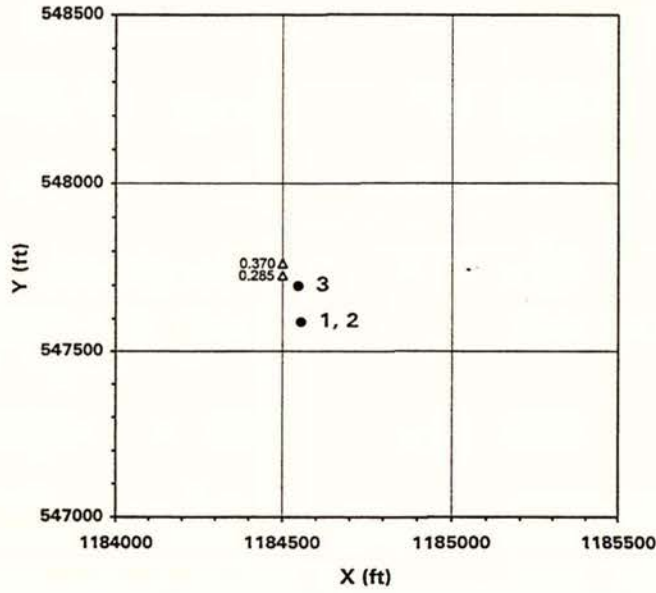
	from	to(m)	comment	D ₅₀ (mm)	C _u	USC	Description	N (raw)	(N ₁) ₆₀	@ (m)
TEST 1,2	1.52	1.98		1.200	5.2	SP	SAND	24	48	1.83
MOS001	1.52	1.98		0.650	3.7	SP	SAND			
MOS002	2.44	2.90	LS					40	70	2.74
[ML14B]	3.35	3.81		0.522	3.5	SP	SAND	22	35	3.66
	3.35	3.81		0.435	2.4	SP	SAND			
	3.35	3.81		0.840	2.5	SP	SAND			
	4.42	4.88		0.270	2.5	SP-SM	SAND with silt	31	44	4.72
WT@	4.42	4.88		0.710	2.7	SP	SAND			
1.53m	5.79	6.25		0.445	2.3	SP	SAND	24	31	6.10
TEST 4	2.90	3.35		0.210	1.7	SP	SAND	23	34	3.20
PAJ001	3.96	4.42		0.219	1.7	SP	SAND			
[PAJ44]	3.96	4.42		0.207	2	SP-SM	SAND with silt	17	23	4.27
	3.96	4.42 top		0.212	1.7	SP	SAND			
	5.49	5.94	LS					11	13	5.79
	6.86	7.32		0.251	1.8	SP	SAND	38	43	7.16
	8.23	8.69		0.002		MH	plastic SILT			
	8.23	8.69		0.240	2					
WT@	8.23	8.69 base		0.002		CH	fat CLAY	5	5	8.53
3.08m	9.14	9.60		0.215	4.2	SP-SM	SAND with silt	25	25	9.45
TEST 5	0.91		auger	0.200	2.1	SP-SM	SAND with silt			
PAJ002	0.76	1.22	middle	0.210	1.7	SP	SAND	27	50	1.07
[PAJ43]	0.76	1.22	top	0.195	36	SM	silty SAND			
	1.52	1.98	base	0.260	2.1	SP-SM	SAND with silt			
	1.52	1.98	middle	0.003		MH	plastic SILT			
	1.52	1.98	top	0.188	51	SM	silty SAND			
	3.35	3.81	top	0.150	17	SM	silty SAND	19	27	3.66
	4.27	4.72		0.275	4.1	SP-SM	SAND with silt	76	99	4.57
	4.27	4.72		0.345	3.3	SP-SM	SAND with silt			
WT@	5.79	6.25		0.248	4.7	SP-SM	SAND with silt	65	77	6.10
3.20m	7.32	7.77		0.455	2.2	SP	SAND with gravel	136	149	7.62
TEST 6	0.00			0.054	42	ML	sandy SILT			
MIL001	1.37	1.83		0.139	26	SM	silty SAND	6	9	1.68
[MIL03]	2.44	2.90		0.071	10	ML	sandy SILT	3	4	2.74
	4.27	4.72		0.154	16	SM	silty SAND	11	13	4.57
	5.33	5.79		0.086	6.5	SM	silty SAND	6	7	5.64
	6.40	6.86		0.120	3.9	SM	silty SAND	13	14	6.71
	7.62	8.08		0.115	3.6	SM	silty SAND	26	27	7.92
	9.75	10.21		0.033	19	ML	sandy SILT	2	2	10.06
	13.72	14.17		0.133	20	SM	silty SAND	23	19	14.02
WT@	14.94	15.39		0.360		SM	silty SAND	30	24	15.24
4.57m	16.46	16.92		0.430	9	SW-SM	SAND with silt	50	39	16.76
TEST 7	0.91	1.07		0.060	27	ML	sandy SILT	5	9	0.91
MIL002	1.52	1.98		0.047	9	ML	SILT with sand	6	10	1.83
[MIL02]	3.81	4.27		0.024		ML	SILT with sand	2	3	4.11
WT@	6.71	7.16		0.036	10	ML	SILT	3	3	7.01
3.66m	10.36	10.82		0.103	31	SM	silty SAND	23	22	10.67
TEST 8	0.30	0.61		0.011		ML	SILT			
MIL003	0.61	1.07		0.048	17	ML	sandy SILT	6	11	0.91
[MIL01]	1.83	2.13		0.038	12	ML	SILT			
	2.13	2.29		0.007		MH	plastic SILT	6	10	2.13
	3.05	3.51		0.002		MH	plastic SILT	17	25	3.35
	4.57	5.03		0.051	12	ML	sandy SILT	3	4	4.88
	7.62	8.08		0.027	8	ML	SILT	3	3	7.92
WT@	10.67	11.13		0.120	16	SM	silty SAND	16	15	10.97
3.05m	14.78	15.24		0.277	13	SM	silty SAND	23	19	15.09
TEST 9	3.05	3.51		0.004		MH	plastic SILT	11	15	3.35
MIL004	6.10	6.55		0.062	48	ML	sandy SILT	5	6	6.40
[MIL10]	7.32	7.77		0.152	9	SM	silty SAND	12	13	7.62
WT@	8.99	9.45		0.115	3	SM	silty SAND	25	25	9.30
3.75m	10.06	10.52		0.180	4	SM	silty SAND	45	43	10.36

	from	to(m)	comment	D ₅₀ (mm)	C _u	USC	Description	N (raw)	(N ₁) ₆₀	@ (m)
TEST 10	2.51	2.97		0.054	7.8	ML	SILT with sand	4	6	2.82
MIL005	3.35	3.66		0.077	17	SM	silty SAND			
[MIL08]	3.96	4.27		0.060	39	ML	sandy SILT			
	4.27	4.72		0.082	7	SM	silty SAND	11	14	4.57
	5.64	6.10		0.143	55	SM	silty SAND	9	10	5.94
	7.16	7.62		0.263		SM	silty SAND	9	10	7.47
	10.06	10.52		0.310	6.3	SW-SM	SAND with silt	44	41	10.36
WT@	10.06	10.21		0.260	2.9	SP-SM	SAND with silt			
4.39m	10.97	11.28		0.255	2.8	SP-SM	SAND with silt	31	28	11.28
TEST 13	1.52	1.98		0.076	14	SM	silty SAND	7	11	1.83
MIL007	3.05	3.51		0.223	3.3	SP-SM	SAND with silt	27	36	3.35
[MIL05]	3.96	4.42		0.244	3.8	SP-SM	SAND with silt	15	19	4.27
	5.03	5.49		0.042	15	ML	SILT			
	5.03	5.49		0.146	3.3	SM	silty SAND	5	6	5.33
WT@	6.71	7.16		0.185	4.3	SM	silty SAND	20	22	7.01
4.30m	10.21	10.67		0.230	3.4	SP-SM	SAND with silt	24	22	10.52
TEST 14	1.60	2.06		0.006		MH	plastic SILT			
MIL008	1.60	2.06		0.008		MH	plastic SILT	12	19	1.91
[MIL12]	2.90	3.35	base	0.032		CL	SILT with sand	19	27	3.20
	2.90	3.35	top 2/3	0.002		CH	fat CLAY			
	3.81	4.27	base	0.028		ML	SILT	2	3	4.11
	3.81	4.27	top 1/3	0.068	12	ML	sandy SILT			
	4.88	5.33	base	0.013		ML	SILT	6	7	5.18
	4.88	5.33	middle	0.038	11	ML	SILT			
	5.94	6.40	base	0.054	35	ML	sandy SILT	7	8	6.25
	5.94	6.40	top	0.114	72	SM	silty SAND			
	8.23	8.69	lower 1/3	0.099	31	SM	silty SAND	11	11	8.53
	8.23	8.69	top 1/3	0.071	24	ML	sandy SILT			
	10.36	10.82		0.003		MH	plastic SILT	6	6	10.67
WT@	10.36	10.82	middle	0.180	70	SM	silty SAND			
3.66m	10.36	10.82	top	0.014	23	ML	SILT			
TEST 15	1.83	2.29		0.200	1.9	SP-SM	SAND with silt	5	9	2.13
AIR002	2.74	3.20		0.380	1.9	SP	SAND	5	8	3.05
[AIR21]	2.74	3.20		0.236	2.7	SP-SM	SAND with silt			
	3.66	4.11		0.910	5.6	SP-SM	SAND with silt	6	9	3.96
	3.66	4.11		0.370	2.6	SP-SM	SAND with silt			
	4.57	5.03		0.540	5	SP-SM	SAND with silt	3	4	4.88
	4.57	5.03		0.391	3	SP-SM	SAND with silt			
	5.49	5.94		0.098	6.8	SM	silty SAND	8	10	5.79
	5.49	5.94		0.285	2	SP	SAND			
	6.40	6.86		0.259	2.3	SP-SM	SAND with silt	12	15	6.71
	6.40	6.86		0.120		SM	silty SAND			
	6.40	6.86		0.278	2.9	SP-SM	SAND with silt			
	7.92	8.38				CH	CLAY	2	2	8.08
	7.92	8.38	top	0.280	3.4					
WT@	7.92	8.38		0.402		SM	silty SAND			
1.92m	10.36	10.82		0.198		SM	silty SAND	17	17	10.67
TEST 16	1.98	2.44		0.153	2.9	SM	silty SAND	3	5	2.29
AIR003	1.98	2.44		0.117	4.3	SM	silty SAND			
[AIR18]	3.05	3.51	base	0.193	3.1	SP-SM	SAND with silt	8	12	3.35
	3.05	3.51		0.087	4.4	SM	silty SAND			
	3.05	3.51		0.148	2.1	SP-SM	SAND with silt			
	4.27	4.72	lower 1/2	0.310	2.2	SP-SM	SAND with silt	5	7	4.57
	4.27	4.72	top 1/2	0.107	5.6	SM	silty SAND			
	6.10	6.55		0.064		ML	sandy SILT	3	4	6.40
	6.10	6.55		0.036	29	ML	sandy SILT			
	7.16	7.62	base	0.140	2.2	SP-SM	SAND with silt	26	30	7.47
	7.16	7.62	top	0.150		SM	silty SAND			
	8.38	9.14		0.112	1.7	SP-SM	SAND with silt	5	5	8.99
	11.28	11.73	lower 2/3	0.005		MH	plastic SILT	5	5	11.58
WT@	11.28	11.73	top 1/3	0.131	85	SM	silty SAND			
2.12m	14.94	15.39		0.050	12	ML	SILT with sand	33	28	15.24

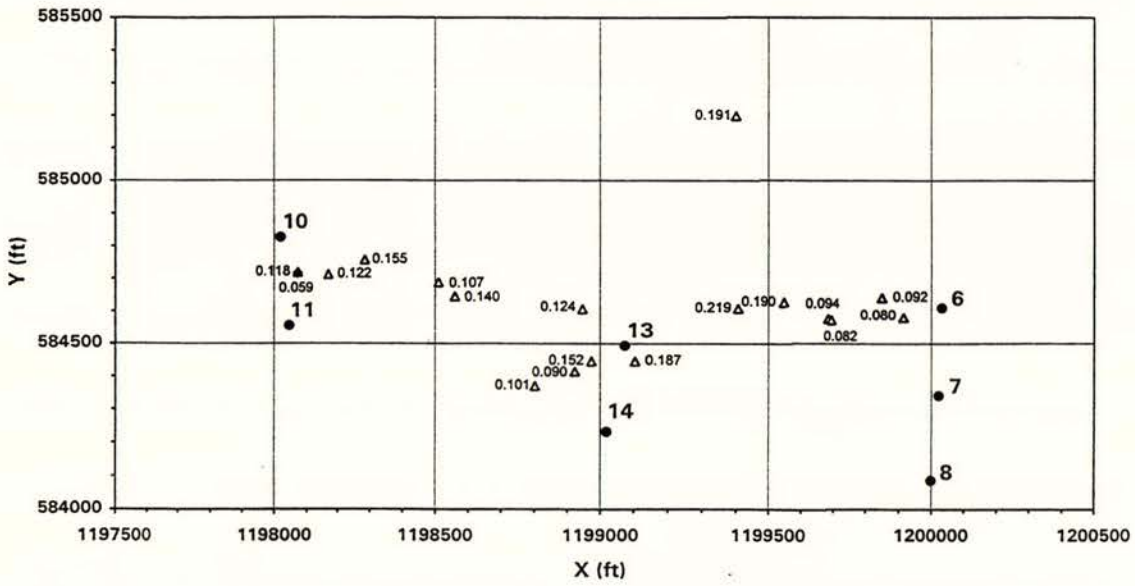
	from	to(m)	comment	D ₅₀ (mm)	C _u	USC	Description	N (raw)	(N ₁) ₆₀	@ (m)
TEST 17	1.98	2.44		0.043	19	ML	SILT with sand	6	11	2.29
AIR004	1.98	2.44		0.014		ML	SILT			
[AIR16]	2.90	3.35		0.019		ML	SILT	5	8	3.20
	4.27	4.72		0.097		SM	silty SAND	9	13	4.57
	6.25	6.71	lower 1/2	0.077	40	ML	sandy SILT	11	14	6.55
WT@	6.25	6.71	top 1/2	0.043	50	ML	SILT with sand			
1.44m	7.16	7.62		0.004		CH	fat CLAY	7	8	7.47
TEST 18	2.13	2.59		0.280	2.5	SP	SAND	9	16	2.44
JEF001	3.05			0.289	2.6	SP	SAND			
[JEF32]	3.35	3.35		0.282	2.4	SP-SM	SAND with silt	12	19	3.35
	5.64	6.10		0.340	3.8	SP-SM	SAND with silt	16	20	5.94
	7.01	7.47		0.245	2.8	SP-SM	SAND with silt	15	18	7.32
	10.97	11.43		0.140	3	SM	silty SAND	30	29	11.28
WT@	13.11	13.56		0.285	2.9	SP-SM	SAND with silt			
1.87m	13.47			0.002				5	5	13.41
TEST 20	1.22	1.68		0.005		MH	plastic SILT	1	2	1.52
SCT001	2.29	2.74		0.680	2.2	SP	SAND	21	41	2.59
[SCT28]	4.27	4.72		0.780	9.8	SP	SAND	33	51	4.57
	6.10	6.55		LS				15	20	6.40
	8.08	8.53		0.640	3	SP-SM	SAND with silt	27	31	8.38
WT@	12.19	12.50		0.410	3.1	SP-SM	SAND with silt			
0.74m	12.50			0.002?			CLAY	5	5	12.50
TEST 21	1.52	1.98		0.096	8.4	SM	silty SAND	9	18	1.83
SCT002	3.66	3.81		0.121	2.2	SM	silty SAND			
[SCT23]	3.81	4.11		0.097	18	SM	silty SAND	11	17	3.96
	4.57	5.03		0.060	27	ML	sandy SILT	3	4	4.88
WT@	6.10	6.55		0.040	15	ML	SILT	1	1	6.40
1.54m	8.23	8.69		0.245	2.5	SP-SM	SAND with silt	21	23	8.53
TEST 22	1.22	1.68		0.330	3.7	SP-SM	SAND with silt	19	40	1.52
JEF003	2.13	2.59		0.380	1.9	SP	SAND	18	33	2.44
[JEF34]	3.35	3.81		0.285	2.7	SP-SM	SAND with silt	20	32	3.66
	4.11	4.42		0.002		MH	plastic SILT	17	25	4.27
	6.16	6.46		0.002		MH	plastic SILT	4	5	6.40
WT@	7.92	8.38		0.002		MH	plastic SILT	9	10	8.23
1.50m	10.06	10.52		0.002		MH	plastic SILT	6	6	10.36
TEST 24	0.91	1.37		0.054	3.9	ML	sandy SILT	5	11	1.22
SEA001	3.05	3.51		0.098	2.5	SM	silty SAND	5	8	3.35
[SEA31]	3.96	4.42		0.123	3	SM	silty SAND	7	11	4.27
	4.88	5.33		0.240		SM	silty SAND	9	13	5.18
	7.01	7.47		0.244		SP-SM	SAND with silt	13	16	7.32
	8.23	8.69		0.258	5.2	SP-SM	SAND with silt	10	11	8.53
	9.14	9.36		0.223	4.4	SP-SM	SAND with silt			
	9.36	9.60		0.003		CL	lean CLAY	9	10	9.45
WT@	11.28	11.73		0.300	3.8	SP-SM	SAND with silt	137	135	11.58
1.19m	11.52			0.040		ML	SILT with sand			
TEST 25	0.61	1.07		0.005		CH	fat CLAY	15	31	0.91
SEA002	2.29	2.74		0.003		MH	plastic SILT	4	7	2.59
[SEA29]	3.35	3.81		0.080		SM	silty SAND	2	3	3.66
WT@	6.10	6.55		0.024	32	ML	SILT	2	2	6.40
2.41m	7.47	7.92		0.262	3.2	SP-SM	SAND with silt	32	36	7.77
TEST 26	1.52	1.98		0.060		ML	sandy SILT	2	4	1.83
LEN001	3.05	3.51		0.185	3	SP-SM	SAND with silt	10	16	3.35
[LEN39]	3.96	4.27		0.188	4	SP-SM	SAND with silt			
WT@	4.27	4.42		0.232	3	SP-SM	SAND with silt	7	10	4.27
1.46m	6.10	6.55		0.305	2.5	SP-SM	SAND with silt	8	10	6.40

	from	to(m)	comment	D ₅₀ (mm)	C _u	USC	Description	N (raw)	(N ₁) ₆₀	@ (m)
TEST 27	1.37	1.83		0.090	3.2	SM	silty SAND	6	12	1.68
LEN002	3.05	3.51		0.105	3	SP-SM	SAND with silt	9	14	3.35
[LEN37]	4.27	4.72		0.170	3.3	SP-SM	SAND with silt			
	6.10	6.55		0.195	2.4	SP-SM	SAND with silt	11	14	6.40
	7.62	8.08		0.197	2.2	SP-SM	SAND with silt	17	19	7.92
	9.75	10.21		0.220	3.5	SP-SM	SAND with silt	23	23	10.06
WT@	11.58	11.83		0.215	1.9	SP	SAND			
2.05m	11.83	12.04		0.003		CH	fat CLAY	4	4	11.89
TEST 28	1.52	1.98		0.004		CH	fat CLAY	15	22	1.83
SPR001	3.05	3.51		0.107	6	SM	silty SAND	7	9	3.35
[SP45]	4.57	5.03		0.167	2	SP-SM	SAND with silt	11	13	4.88
	5.49	5.94		0.171	2.6	SP-SM	SAND with silt	11	13	5.79
	6.71	7.16		0.240	4.3	SP-SM	SAND with silt	19	20	7.01
	7.62	8.08		0.300	3.3	SP-SM	SAND with silt	12	12	7.92
	8.84	9.08		0.005		CH	fat CLAY	8	8	9.14
	9.08	9.30		0.475	5.5	SP-SM	SAND with silt			
	9.75	10.21		0.355	3.3	SP-SM	SAND with silt	41	39	10.06
	10.67	11.13		0.355	4	SP-SM	SAND with silt	22	20	10.97
WT@	9.14			0.007		MH	plastic SILT			
4.54m	11.13			0.020		ML	sandy SILT			
TEST 30	1.52	1.98		0.108	3.4	SM	silty SAND	6	11	1.83
SPR003	3.05	3.51		0.062	15	ML	sandy SILT	7	10	3.35
[SP46]	4.57	5.03		0.158	3	SP-SM	SAND with silt	13	17	4.88
	6.34	6.55		0.168	3.2	SP-SM	SAND with silt	7	8	6.40
	7.01	7.47		LS				10	11	7.32
	8.23	8.69		0.164	3.6	SP-SM	SAND with silt	11	12	8.53
WT@	9.14	9.60		0.623	5.9	SP-SM	SAND with silt	13	13	9.45
2.62m	10.67	11.13		0.225	3.3	SP-SM	SAND with silt	11	11	10.97

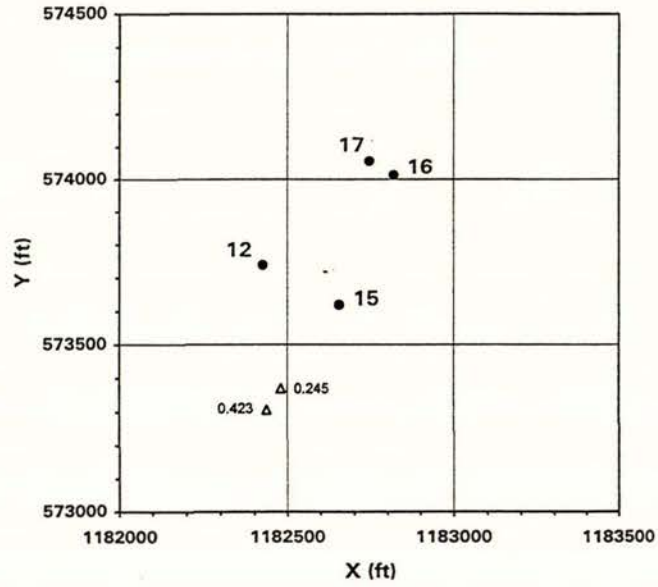
Sand Boil D₅₀ (mm) - Moss Landing



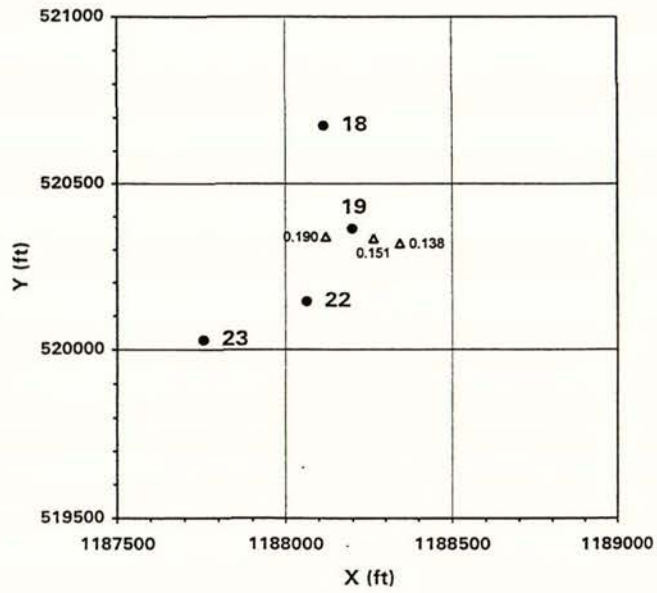
Sand Boil D₅₀ (mm) - Miller's Farm



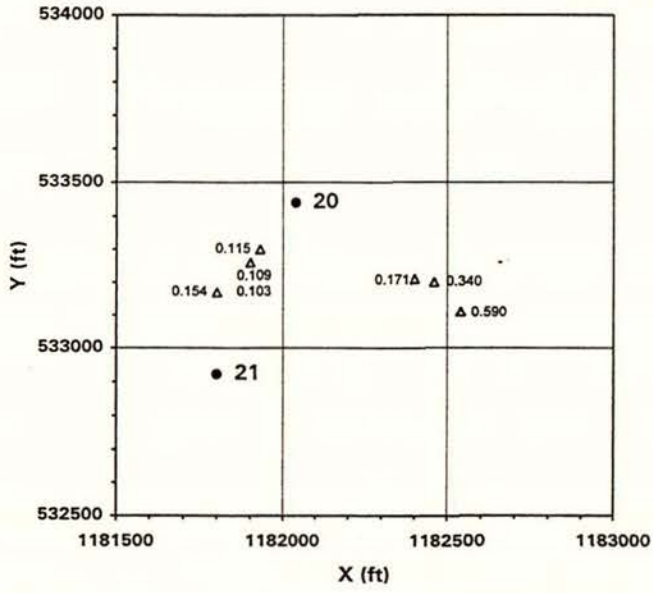
Sand Boil D₅₀ (mm) - Airport Watsonville



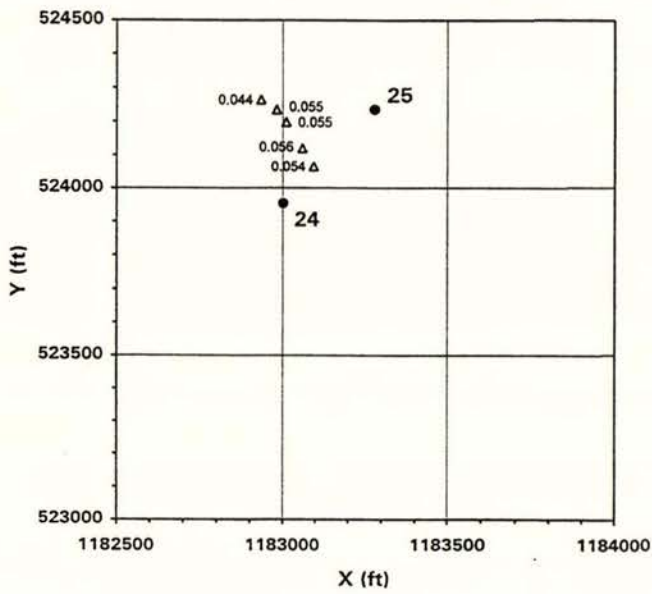
Sand Boil D₅₀ (mm) - Jefferson

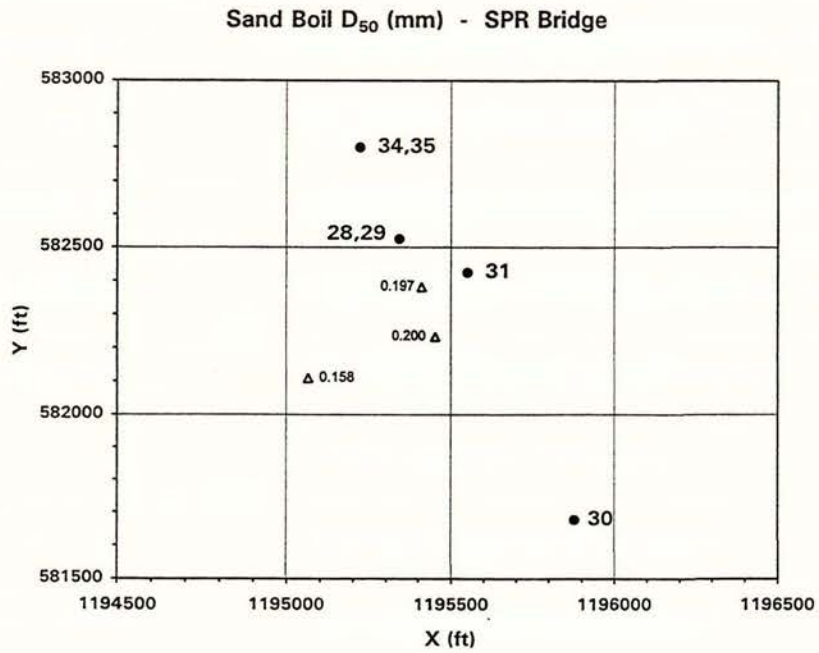
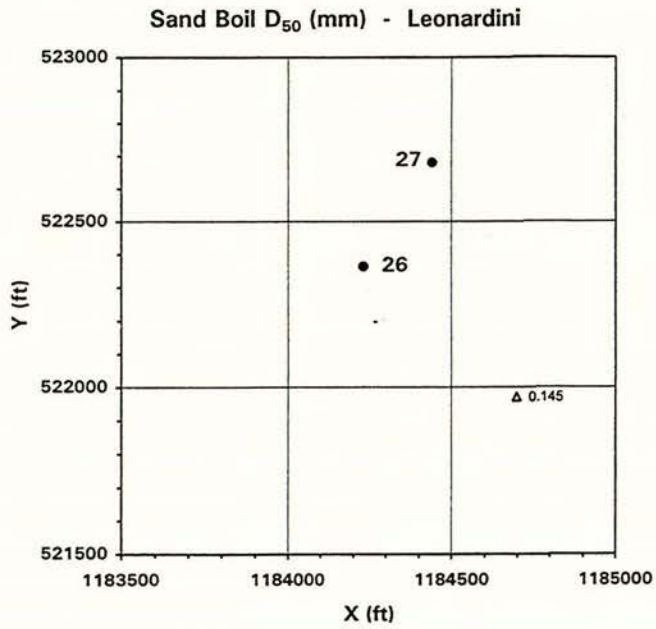


Sand Boil D₅₀ (mm) - Scattini



Sand Boil D₅₀ (mm) - Sea Mist





Appendix B

B.1 DEVELOPMENT OF PLEVAKO SOLUTION

Figure B.1 illustrates the problem of interest solved by Plevako. A vertical point force P is applied within the upper halfspace of a pair of perfectly bonded halfspaces with different elastic constants. The line of action of the force is perpendicular to the interface between materials 1 and 2.

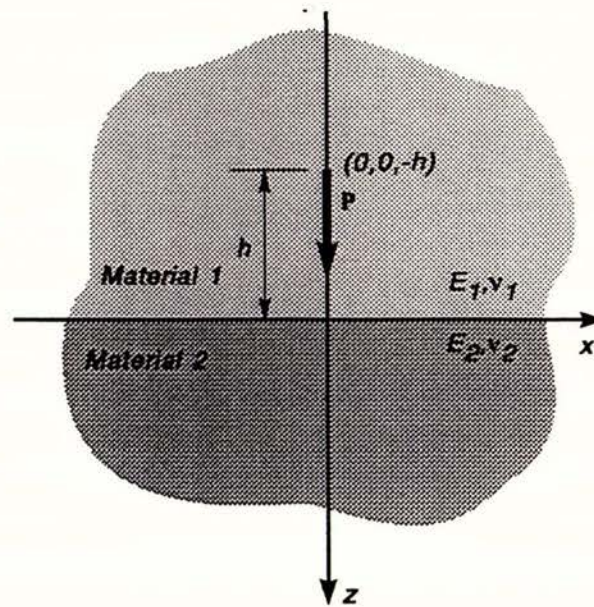


Figure B.1 Vertical point force in two-layered elastic space

Plevako found the vertical displacement u_z in the upper halfspace, due to the point force P applied at the point $(x, y, z) = (0, 0, -h)$ within material 1, to be

$$u_z = \frac{P}{16\pi(1-\nu_1)G_1} \left(\frac{3-4\nu_1}{R_2} + \frac{(z+h)^2}{R_2^3} - \frac{\alpha-1+4(1-\nu_1)(1-2\nu_1)\beta}{R_1} - \frac{\beta[(3-4\nu_1)(z-h)^2+2hz]}{R_1^3} + \frac{6\beta hz(z-h)^2}{R_1^5} \right) \quad (\text{B.1})$$

where ν_i = Poisson's Ratio for material i

G_i = Shear Modulus for material i

h = vertical distance between point load and interface between materials 1 and 2

and z = depth

The lengths R_1 and R_2 are defined as

$$R_1 = \sqrt{x^2 + y^2 + (z-h)^2} \quad R_2 = \sqrt{x^2 + y^2 + (z+h)^2}$$

and, by substituting $r^2 = x^2 + y^2$, they may be expressed as

$$R_1 = \sqrt{r^2 + (z-h)^2} \quad R_2 = \sqrt{r^2 + (z+h)^2}$$

The constants α , β and k are given by the following expressions

$$\alpha = \frac{8k(1-\nu_1) [k(1-\nu_1) + (1-\nu_2)]}{(k+3-4\nu_2) [k(3-4\nu_1) + 1]}$$

$$\beta = \frac{k-1}{k(3-4\nu_1) + 1}$$

$$k = \frac{G_2}{G_1} = \frac{E_2(1+\nu_1)}{E_1(1+\nu_2)}$$

For the special case of incompressibility, where $\nu_1 = \nu_2 = 0.5$, these constants reduce to

$$\alpha = \frac{2k}{k+1}$$

$$\beta = \frac{k-1}{k+1}$$

$$k = \frac{G_2}{G_1} = \frac{E_2}{E_1}$$

Substituting these simplified constants into equation (B.1) reduces the expression for u_z to

$$u_z = \frac{P}{8\pi G_1} \left(\frac{1}{R_2} + \frac{(z+h)^2}{R_2^3} - \frac{\alpha-1}{R_1} - \frac{\beta(z^2+h^2)}{R_1^3} + \frac{6\beta hz(z-h)^2}{R_1^5} \right)$$

Now consider a circular uniform stress p_0 as shown in Figure B.2.

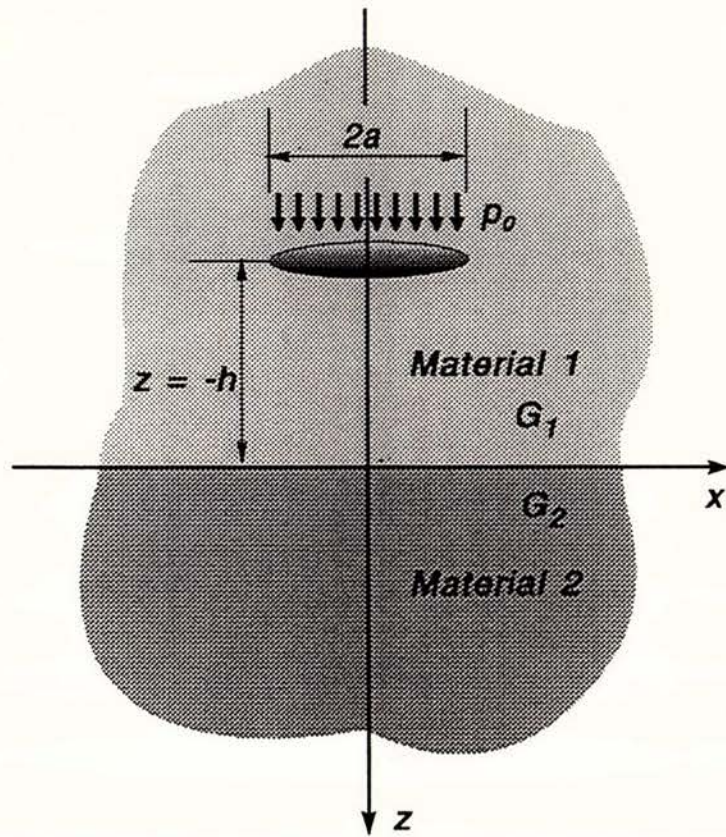


Figure B.2 Loaded disc configuration in two-layered elastic space

We require u_z at the centre of the loaded region. Let $P = p_0 r d\theta dr$, then $u_z(r = 0, z = -h)$ is given by δ_1 where

$$\delta_1 = \int_0^{2\pi} \int_0^a \frac{p_0 r d\theta dr}{8\pi G_1} \left(\frac{1}{R_2} + \frac{(z+h)^2}{R_2^3} - \frac{\alpha-1}{R_1} - \frac{\beta(z^2+h^2)}{R_1^3} + \frac{6\beta h z(z-h)^2}{R_1^5} \right)$$

Now setting $z = -h$ we have

$$R_1 = \sqrt{r^2 + 4h^2} \quad R_2 = r$$

and the equation for the displacement may be recast as

$$\delta_1 = \int_0^{2\pi} \int_0^a \frac{p_0 r d\theta dr}{8\pi G_1} \left(\frac{1}{r} - \frac{\alpha-1}{R_1} - \frac{2\beta h^2}{R_1^3} - \frac{24\beta h^4}{R_1^5} \right)$$

This expression is represented geometrically in Figure B.3.

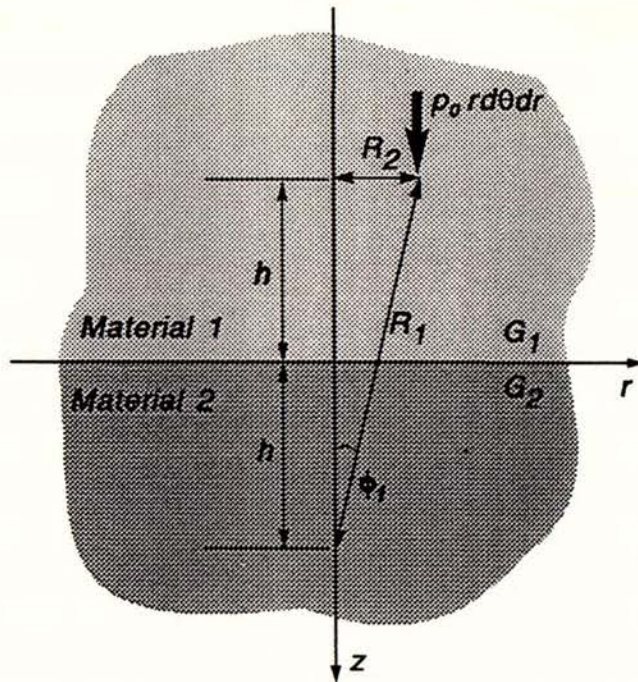


Figure B.3 Geometric representation of equation (B.6)

Evaluating the integral for θ results in the following expression for δ_1

$$\delta_1 = \frac{P_0}{4G_1} \int_0^a \left(1 - \frac{(\alpha-1)r}{R_1} - \frac{2\beta rh^2}{R_1^3} - \frac{24\beta rh^4}{R_1^5} \right) dr$$

Now let

$$\sin\phi = \frac{r}{R_1} \quad \cos\phi = \frac{2h}{R_1} \quad \tan\phi = \frac{r}{2h}$$

From this we have $dr = 2h\sec^2\phi d\phi$. Evaluating the resulting integral for δ_1 gives

$$\begin{aligned} \delta_1 &= \frac{P_0}{4G_1} \left(a - h \int_0^{\phi_1} [2(\alpha-1)\sin\phi + \beta\sin\phi\cos^2\phi + 3\beta\sin\phi\cos^4\phi] \sec^2\phi d\phi \right) \\ &= \frac{P_0 a}{4G_1} \left(1 - \frac{h}{a} \left[2(\alpha-1)\sec\phi - \beta(\cos^3\phi + \cos\phi) \right]_0^{\phi_1} \right) \end{aligned}$$

Finally, the displacement in layer 1 is given as

$$\delta_1 = \frac{P_0 a}{4G_1} \left(1 - \frac{h}{a} \left[2(\alpha - 1)(\sec \phi_1 - 1) - \beta(\cos^3 \phi_1 + \cos \phi_1 - 2) \right] \right) \quad (\text{B.2})$$

Here, ϕ_1 is the Principal Value of the following angle

$$\phi_1 = \tan^{-1} \left(\frac{a}{2h} \right)$$

The limiting cases of the solution are correctly predicted (Florin, 1959). First, consider the case when $h \rightarrow \infty$

$$\text{For } h \rightarrow \infty, \quad \delta_1 \rightarrow \frac{P_0 a}{4G_1}$$

Now consider the remaining limiting case of $h \rightarrow 0$. When $h \rightarrow 0$, the angle $\phi_1 \rightarrow \pi/2$, and therefore $(\cos \phi_1) \rightarrow 1$. The expression for δ_1 given in equation (B.2) then reduces to

$$\delta_1 = \frac{P_0 a}{4G_1} \left(1 - \frac{2h(\alpha - 1)(\sec \phi_1 - 1)}{a} \right)$$

The secant term may be substituted as

$$\sec \phi_1 = \frac{\sqrt{a^2 + 4h^2}}{2h}$$

Thus, for $h \rightarrow 0$, δ_1 is given by

$$\delta_1 \rightarrow \frac{P_0 a}{4G_1} \left(1 - (\alpha - 1) \right) = \frac{P_0 a}{4G_1} (2 - \alpha)$$

From the definition of α we have

$$2 - \alpha = \frac{2G_1}{G_1 + G_2}$$

This may be substituted into the above expression for δ_1 to give the desired limit below.

$$\text{For } h \rightarrow 0, \quad \delta_1 \rightarrow \frac{P_0 a}{2(G_1 + G_2)}$$

Thus, equation (B.2) gives the required stress-displacement relationship for a loaded disc within material 1. From equation (B.2), and by making use of the simplification $\beta = (\alpha - 1)$, we may define the dimensionless penetration resistance, η

$$\eta = \frac{p_0 a}{G_1 \delta} = \frac{4}{1 + \frac{h\beta}{a} [\cos^3 \phi_1 + \cos \phi_1 - 2 \sec \phi_1]} \quad (\text{B.3})$$

Note that we have set $\delta_1 = \delta = \delta_2$, since we are interested in the stress required to displace the disc a constant amount. To determine the displacement δ_2 of the disc within material 2, the roles of the two layers must be reversed and the sign of the applied stress changed. Note that α and β take on different values in material 2. The form of the resulting equation is the same as that of equation (B.2), with G_1 substituted for G_2

$$\delta_2 = \frac{p_0 a}{4G_2} \left(1 - \frac{h}{a} \left[2(\alpha - 1)(\sec \phi_1 - 1) - \beta(\cos^3 \phi_1 + \cos \phi_1 - 2) \right] \right)$$

For this reason, it is necessary to multiply the dimensionless stiffness in material 2 by the factor G_2/G_1 , so that η remains in terms of G_1 . Thus, in material 2, η is given by

$$\eta = \frac{p_0 a}{G_2 \delta} \left(\frac{G_2}{G_1} \right) = \frac{4}{1 + \frac{h\beta}{a} [\cos^3 \phi_1 + \cos \phi_1 - 2 \sec \phi_1]} \left(\frac{G_2}{G_1} \right)$$

B.2 DEVELOPMENT OF APPROXIMATE SOLUTION

Let us determine the equivalent Boussinesq displacement u_z at depth z beneath the centre of a disc in an incompressible elastic halfspace. The general Boussinesq solution is of the form

$$u_z(z) = \frac{q}{4\pi\mu R} \left(2(1-\nu) + \frac{z^2}{R^2} \right) = \frac{q}{4\pi GR} \left(1 + \frac{z^2}{R^2} \right) \quad (\text{B.4})$$

since $\mu = G$ for $\nu = 0.5$. Now let $q = prd\theta dr$, where p is stress and q is a point load, and integrate the resulting expression for a circular load.

$$\begin{aligned}
 u_z(z) &= \int_0^{2\pi} \int_0^a \frac{pr \, d\theta dr}{4\pi GR} \left(1 + \frac{z^2}{R^2}\right) \\
 &= \frac{p}{2G} \int_0^a \frac{r}{R} \left(1 + \frac{z^2}{R^2}\right) dr
 \end{aligned}$$

Holding z constant, let

$$\sin\phi = \frac{r}{R} \quad \cos\phi = \frac{z}{R} \quad \tan\phi = \frac{r}{z}$$

so that $dr = z\sec^2\phi d\phi$. The expression for u_z now reduces to

$$\begin{aligned}
 u_z(z) &= \frac{pz}{2G} \int_0^{\phi_1} \left[\sin\phi \sec^2\phi (1 + \cos^2\phi) \right] d\phi \\
 &= \frac{pz}{2G} \int_0^{\phi_1} \left[\tan\phi \sec\phi + \sin\phi \right] d\phi \\
 &= \frac{pz}{2G} \left[\sec\phi - \cos\phi \right]_0^{\phi_1} \quad \text{where } \phi_1 = \tan^{-1}\left(\frac{a}{z}\right) \\
 &= \frac{pz}{2G} \left[\sec\phi_1 - \cos\phi_1 \right]
 \end{aligned}$$

Here, ϕ_1 is the maximum angle of ϕ possible, as shown in Figure B.4. The cosine of this angle may be expressed as $\cos\phi_1 = z/R'$, where

$$R' = \sqrt{a^2 + z^2}$$

Substituting this into the above expression for u_z gives

$$u_z(z) = \frac{pz}{2G} \left(\frac{R'}{z} - \frac{z}{R'} \right) = \frac{pz}{2G} \left(\frac{a^2 + z^2 - z^2}{z\sqrt{a^2 + z^2}} \right)$$

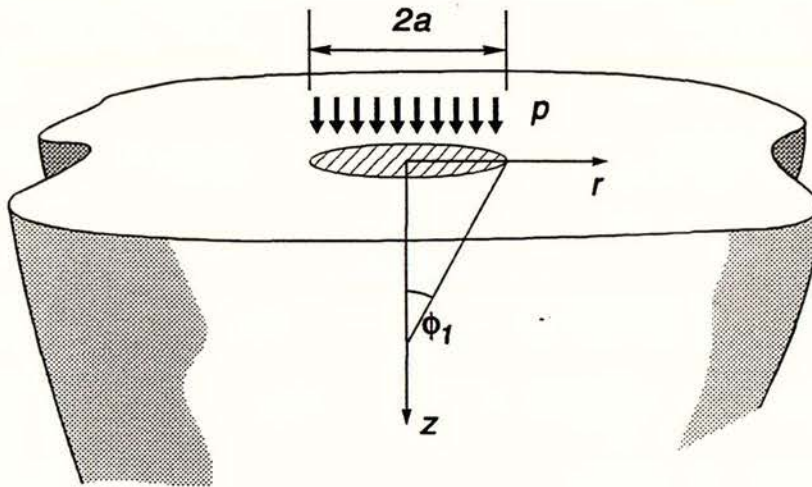


Figure B.4 Circular load on surface of elastic halfspace

Thus, the final expression for u_z is given by

$$u_z(z) = \frac{p}{2G} \left(\frac{a^2}{\sqrt{a^2+z^2}} \right) \quad (\text{B.5})$$

Now let us apply this result to the case of a loaded disc within an incompressible elastic space comprising two different materials, as shown in Figure B.5(a). It is necessary to decompose the layered infinite space in Figure B.5(a) into two elastic half-spaces as shown in Figure B.5(b). Each half-space supports a uniform stress, p_0' or p_0'' , over the disc-shaped region of radius a . The upper half-space is homogeneous, while the lower half-space is layered. For the upper half-space, we may use the result of equation (B.5) to give the displacement δ' at the centre of the disc

$$\delta' = \frac{p_0' a}{2G_1} \quad (\text{B.6})$$

Here G_1 denotes the elastic shear modulus of material 1. For the lower, layered half-space, an approximation can be used, based on Boussinesq's solution in which the relative displacements

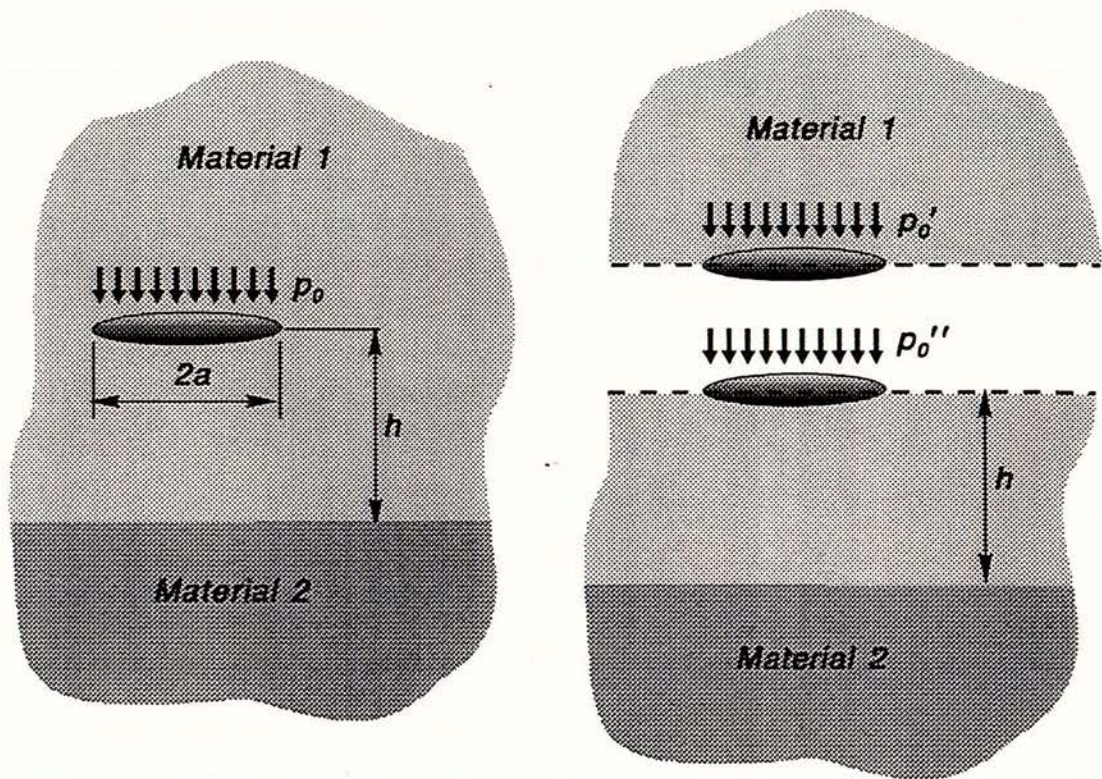


Figure B.5 Method of analysis: (a) representation of CPT by circular uniform load; (b) decomposition of (a) into two half-space problems

in the two layers are combined. The displacement δ'' at the centre of the loaded region is given by

$$\delta'' = \frac{p_0'' a}{2G_1} - \frac{p_0''}{2G_1} \frac{a^2}{\sqrt{a^2+h^2}} + \frac{p_0''}{2G_2} \frac{a^2}{\sqrt{a^2+h^2}} \quad (\text{B.7})$$

The three terms on the right-hand side of this equation represent (i) the surface displacement of a homogeneous half-space composed of material 1, (ii) the displacement at depth h beneath the centre of the loaded disc in a homogeneous half-space composed of material 1, and (iii) the displacement at depth h beneath the centre of the loaded disc in a homogeneous half-space composed of material 2. The difference between terms (i) and (ii) represents the relative shortening in the layer of thickness h . Term (iii) represents the displacement of a half-space of material 2 below the depth h . Equation (B.7) is a well-known approximation for the surface displacement of a layered half-space, and although not exact, it will give a good approximate value for the displacement. It compares favourably with exact solutions based on Burmister's analysis (Poulos, 1967).

It is possible to combine the two half-space solutions in Figure B.5(b) to represent the infinite space problem in Figure 6.1(a). First, we must set $\delta' = \delta'' = \delta$, so that

$$\delta = \frac{p_0' a}{2G_1} = \frac{p_0'' a}{2G_1} \left[1 - \left(1 - \frac{G_1}{G_2} \right) \frac{a}{\sqrt{a^2 + h^2}} \right]$$

$$\text{therefore } p_0' = p_0'' \left[1 - \left(1 - \frac{G_1}{G_2} \right) \frac{a}{\sqrt{a^2 + h^2}} \right]$$

Now, using $p_0' + p_0'' = p_0$, we have

$$p_0 = p_0'' \left[2 - \left(1 - \frac{G_1}{G_2} \right) \frac{a}{\sqrt{a^2 + h^2}} \right]$$

$$\text{therefore } p_0' = p_0 \left[\frac{1 - \left(1 - \frac{G_1}{G_2} \right) \frac{a}{\sqrt{a^2 + h^2}}}{2 - \left(1 - \frac{G_1}{G_2} \right) \frac{a}{\sqrt{a^2 + h^2}}} \right]$$

By substituting this result into equation (B.6), we obtain the required expression for the displacement δ

$$\delta = \frac{p_0 a}{2G_1} \left(\frac{1 - \lambda_1}{2 - \lambda_1} \right) \quad (\text{B.8})$$

where

$$\lambda_1 = \left(1 - \frac{G_1}{G_2} \right) \frac{a}{\sqrt{a^2 + h^2}}$$

Note that the solution becomes exact in the limiting cases (Florin, 1959).

$$\text{For } h \rightarrow \infty, \quad \delta \rightarrow \frac{p_0 a}{4G_1}$$

$$\text{For } h \rightarrow 0, \quad \delta \rightarrow \frac{p_0 a}{2(G_1 + G_2)}$$

In effect, the two half-spaces are being joined on the horizontal plane passing through the loaded region. This approach can be motivated by the fact that, for an incompressible material, Kelvin's solution for a point load in an infinite space gives exactly the same stresses and

displacements in the half-space above or below the load point as does Boussinesq's solution for a half-space with a point load equal to half that used in Kelvin's problem.

It is an easy matter to generalize this analysis to multilayered situations. For example, consider the case of a loaded disc embedded in the upper layer of a three layer elastic space. Following the same method of analysis, equation (B.6) is unchanged while equation (B.7) is replaced by

$$\delta'' = \frac{p_0'' a}{2G_1} \left[1 - \left(1 - \frac{G_1}{G_2}\right) \frac{a}{\sqrt{a^2 + h_1^2}} - \frac{G_1}{G_2} \left(1 - \frac{G_2}{G_3}\right) \frac{a}{\sqrt{a^2 + h_2^2}} \right] \quad (\text{B.9})$$

Here, h_i is the vertical distance between the disc and interface i . The conditions of compatibility of displacements ($\delta' = \delta'' = \delta$) and equilibrium ($p_0' + p_0'' = p_0$) now lead to

$$\delta = \frac{p_0 a}{2G_1} \left[\frac{1 - \lambda_1 - \frac{G_1 \lambda_2}{G_2}}{2 - \lambda_1 - \frac{G_1 \lambda_2}{G_2}} \right] \quad (\text{B.10})$$

where

$$\lambda_j = \left(1 - \frac{G_j}{G_{j+1}}\right) \frac{a}{\sqrt{a^2 + h_j^2}} \quad (\text{B.11})$$

Further layers are easily incorporated if need be, and layering in the upper half-space may be treated by the same approach. In this way the displacement δ at any point in a multilayered infinite space may be estimated. It is necessary to define a more general dimensionless stiffness ratio for the multilayered case

$$k_i = \frac{G_{i+1}}{G_1} \quad i = 0, 1, 2, \dots, N \quad (\text{B.12})$$

Here N is the number of interfaces, so $(N + 1)$ is the number of layers; note that $k_0 = 1$. Finally, recall the dimensionless penetration resistance η , defined in equation (B.3) as

$$\eta = \frac{P_0 a}{G_1 \delta} \quad (\text{B.13})$$

Thus, for any number of layers, η may be defined by a functional relationship of the form $\eta = F(\lambda_1, \lambda_2, \lambda_3, \dots, k_1, k_2, k_3, \dots)$. The exact form of F depends on the number of layers involved and the position at which the load is applied. For example, in the simple single-

interface geometry of Figure B.5(a), the expression for η for load points above the interface (disc in material 1) is

$$\eta = 2 \left(\frac{2 - \lambda_1}{1 - \lambda_1} \right)$$

while for load points below the interface (disc in material 2) the solution is

$$\eta = 2k_1 \left(\frac{2 + k_1\lambda_1}{1 + k_1\lambda_1} \right)$$

Note that when $h = 0$ equation (B.11) shows that

$$\lambda_1 = 1 - \frac{1}{k_1}$$

and the above expressions give the same result for η . For the case of three layers mentioned above, the three expressions for η in materials 1, 2 and 3 are given by

$$\eta = 2 \left(\frac{2 - \lambda_1 - \frac{1}{k_1}\lambda_2}{1 - \lambda_1 - \frac{1}{k_1}\lambda_2} \right) \quad \text{in material 1}$$

$$\eta = 2k_1 \left(\frac{2 + k_1\lambda_1 - \lambda_2}{(1 + k_1\lambda_1)(1 - \lambda_2)} \right) \quad \text{in material 2}$$

$$\eta = 2k_2 \left(\frac{2 + k_2\lambda_1 + \frac{k_2}{k_1}\lambda_2}{1 + k_2\lambda_1 + \frac{k_2}{k_1}\lambda_2} \right) \quad \text{in material 3}$$

For more complex layering, these expressions must be replaced by more complex expressions.

It is convenient to redefine λ_j given in equation (B.11) as $\lambda_j' = \lambda_j / k_{j-1}$, thus

$$\lambda_j' = \left(\frac{1}{k_{j-1}} - \frac{1}{k_j} \right) / \sqrt{1 + \left(\frac{h_j}{a} \right)^2} \quad j = 1, 2, 3, \dots, N \quad \text{(B.14)}$$

where h_j is the vertical distance between the disc and interface j of N . The general form for η in layer i of $(N + 1)$ layers is then given by

$$\eta_i = 2k_{i-1} \left(\frac{2 + A_i - B_i}{(1 + A_i)(1 - B_i)} \right) \quad i = 1, 2, 3, \dots, (N+1) \quad (\text{B.15})$$

where

$$A_1 = 0, \quad A_i = k_{i-1} \sum_{j=1}^{j=i-1} \lambda_j' \quad i = 2, 3, 4, \dots, (N+1)$$

$$B_{N+1} = 0, \quad B_i = k_{i-1} \sum_{j=i}^{j=N} \lambda_j' \quad i = 1, 2, 3, \dots, N$$

The term A_i predicts the influence that layers of different stiffnesses above the disc will have on the dimensionless resistance η , and the term B_i represents the effect of layering below the disc. The calculation is primarily controlled by two dimensionless quantities: the stiffness ratio k_i , and the position of the disc (h_j/a), which is incorporated within λ_j' in equation (B.14).

Classification:

INTERPRETATION OF PIEZOCONE DATA
AND ITS USE IN ESTIMATING
SEISMIC SOIL LIQUEFACTION POTENTIAL

R. A. Vreugdenhil

ABSTRACT: This report documents piezocone (CPTU) testing of ten level-ground sites of liquefaction during the Loma Prieta earthquake of 17 October 1989. The field data have been used to assess the performance of several liquefaction prediction models. An approximate solution is presented for the behaviour of cone resistance in layered soils of different stiffness, based on the superposition of integrated Boussinesq solutions. The approximate solution shows excellent agreement with observed field and calibration chamber data. A genetic algorithm has been employed to optimise the approximate solution to field cone resistance records.

Department of Civil Engineering, University of Canterbury, New Zealand
Research Report 95-7, 1995